# CYRIC

# ANNUAL REPORT

## 2002 (23号)

*(January 2002 - December 2002)*

***CYCLOTRON AND RADIOISOTOPE CENTER***
***TOHOKU UNIVERSITY***
http://www.cyric.tohoku.ac.jp/

# PREFACE

In this twenty-third issue of the CYRIC Annual Report, we summarize the activities for research and development and results of training for radioisotope safe-treatment at Cyclotron and Radioisotope Center (CYRIC) during the calendar year 2002.

Research programs in various fields such as nuclear physics, nuclear chemistry, solid state physics and element analyses by PIXE and activation were carried out, and radioisotopes were produced for use in biology and medicine. Several facility improvements such as installation of the beam-bunching system have been carried out as well. A total of 2060 hours of the K=110MeV cyclotron beam-time was delivered for the scheduled operation for research works.

Synthesis of radiopharmaceuticals for clinical research with PET (Positron Emission Tomography) and other applications have been continuously carried out. Radiopharmaceuticals e. g. FDG, MET, FDOPA, FDGal, FdUrd, YM09151-2, Pyrilamin, Doxepin, Raclopride, and Benzotropine labeled by positron emitting radio-nuclides were provided with the HM-12 cyclotron.

Among the various research programs, studies with PIXE technique have been continuously carried out by using electrostatic accelerator, installed at FNL (Fast Neutron Laboratory) in Graduate School of Technology, Tohoku University, under the scientific tie up between CYRIC and FNL. Indeed, more than nine groups are running under this project using a total of its 300 hours beam-time.

During 2002 school year, 550 of staff members and students of Tohoku University were trained in the beginner's course of safe handling of radiation and radioisotopes, while 257 staff members and students in the "x-ray course". In addition, 101 of staff members and students were trained in the course of safe handling of radiation from a SOR. English course has been opened for 15 foreign beginners.

A quarter of a century has passed since CYRIC was founded in 1977. In the time of this point, we have summarized activities for research and development and results of training for radioisotope safe-treatment during this 25 year. Based on these results we are going to take peer review on coming March 14 and 17, 2003 by Profs. H. Toki (Osaka

University), K. Nishizawa (Nagoya University), H. Saji (Kyoto University) and K. Endoh (Gunma University).

A total of 563 papers have been published in refereed journal written in English based on works in CYRIC, extending over many research fields. Recently we have received news from Elsevier telling that the Journal of Physics Letters is called as "The hottest journal of the Decade". Indeed, 11 papers have been published in Physics Letters by CYRIC, along with those having high “Impact Factors” evaluated in Web of Science. They are Physical Review Letters, Journal of Neurochemistry, Circulation, Journal of Nuclear Medicine, The Lancet, Stroke, Journal of Cerebral Blood Flow and Metabolism, Annals of Neurology, Neurology, etc. A ground total of running sum of the impact factor for the 563 papers is 1020.29.

The other point to be evaluated in the present peer review is the numbers of degrees obtained by the research works closely related to the educational activities of CYRIC. Table lists the numbers of degrees for each Graduate Schools in Tohoku University.

As end of 2002 School-Year.

| | Master's Degree | Doctor's Degree | Mainly joint Division in CYRIC |
|---|---|---|---|
| Graduate Schools Science | 94 | 39 | Accelerator<br>Instrumentations |
| Graduate Schools Medicine | 10 | 53 | Nuclear Medicine<br>Pharmaceutical Chemistry |
| Graduate Schools Engineering | 70 | 18 | Radiation Protection and Safty Control<br>Instrumentations<br>Cyclotron Nuclear Medicine |
| Graduate Schools Pharmaceutical Science | 51 | 7 | Pharmaceutical Chemistry |
| Graduate Schools Agriculture | 4 | 6 | Pharmaceutical Chemistry |
| Other University | 2 | 2 | Accelerator |
| Total | 231 | 125 | |

16 foreigners for Doctor's degree and 9 foreigners for Master's degree

As evaluated in CYRIC Annual Report each year, CYRIC plays an important role in training for the beginner's course of safe handling of radiation and radioisotopes. In addition, CYRIC shares the center of safety control for radiation and radioisotopes under the regulation of related laws.

We are very grateful to Tohoku University and to the Ministry of Education, Sports, Culture, Science and Technology for their continuous support.

January, 2003

*Hikonojo ORIHARA*
Director
*Cyclotron and Radioisotope Center, Tohoku University*

**EDITORS:**

| | |
|---|---|
| *Keizo* | *ISHII* |
| *Tatsuo* | *IDO* |
| *Masatoshi* | *ITOH* |
| *Mamoru* | *BABA* |
| *Ren* | *IWATA* |
| *Hiroyuki* | *OKAMURA* |
| *Tsutomu* | *SHINOZUKA* |

**WORD PROCESSED BY**

*Yu-ko YAMASHITA*

# CONTENTS

## I. PHYSICS AND TECHNOLOGY

## II. CHEMISTRY

## III. MEDICINE AND BIOLOGY (Basic)

## IV. MEDICINE AND BIOLOGY (Clinical)

## V. RADIATION PROTECTION AND TRAINING OF SAFE HANDLING

# I. PHYSICS AND TECHNOLOGY

# I. 1. Nuclear Structure Study of $^{50}$Mn by Charge-exchange (p,n) Reaction on $^{50}$Cr

*Kamurai G., Orihara H., Terakawa A., Yamamoto A., Suzuki H.,
Mizuno H., Kikuchi Y., Kumagai K., G. C. Jon.*, Ishii K.**, and Ohnuma H.****

*Cyclotron and Radioisotope center, Tohoku University
Institute of Physics, Academia Sinica, Nankang Taipei, Taiwan 11592*
Department of Quantum Science and Energy Engineering, Tohoku University**
Department of Physics, Chiba Institute of Technology, Chiba 275-0023, Japan****

The charge-exchange (p,n) reaction is one of the powerful tools to explore the nuclear structure of neutron deficient nuclei, especially selecting spin-isospin excitation in the residual nucleus. The nuclear structure experiment for the neutron deficient $^{50}$Mn nucleus has so far been limited to a few cases with e. g. the ($^3$He,t) reaction, where eleven levels are reported$^{1)}$ and spin-parity assignments for them are limited to only three cases including the ground state.

The (p,n) reaction has provided us with information about spin-isospin, as well as isospin excitation modes in nuclei. One can selectively excite the spin-flip components in the (p,n) reaction at intermediate energies through the relatively strong spin-isospin effective interaction ($V_{\sigma\tau}$). Low energy 35-MeV (p,n) reactions, due to the strong spin non-flip isovector effective interaction ($V_\tau$), give us equivalent information on both excitation modes. Moreover, it gives us a sufficient energy resolution to discuss (p,n) strength for individual nuclear levels$^{2,3)}$, although exchange contributions are important at low energies. Various problems associated with the distorted-wave (DW) analysis of low-energy (p,n) data were discussed in detail by Ohnuma et al$^{4)}$. It has been found possible to obtain basically the same information as that at intermediate energies if careful analysis including exchange terms is carried out.

The other point of the low-energy (p,n) reaction study is higher-L excitation leading e.g. $2^+$ states by which we are able to discuss the isovector deformation parameter$^{5,6)}$. Moreover, Orihara et al. have recently reported a method$^{7)}$ to evaluate Gamow-Teller(GT) matrix elements by (p,n) cross sections for the $\Delta J^\pi=1^+$ transition at 35

MeV.

The experiment was carried out using a 35 MeV proton beam from the AVF cyclotron and the time-of-flight facilities[8,9)] at the Cyclotron and Radioisotope Center at Tohoku University. A beam swinger system was used to measure angular distributions of emitted neutrons between 0° and 140° (lab). The target was a metallic foil of $^{50}$Cr enriched to 99 %. Neutrons were detected by an array of twelve detectors, which were located at 44.3 m from the target and contained a total of 23.2 liters of NE213 scintillator. The detector efficiencies were obtained from Monte Carlo calculations for monoenergetic neutrons with $E \leq 34$ MeV. Absolute detector efficiencies were also measured by counting neutrons from the $^7$Li(p,n)$^7$ Be reaction and comparing its yield with the absolute neutron fluence determined by activation. They were in good agreement with the Monte Carlo calculations. Overall time resolution was typically 1.3 ns corresponding to 174 keV for the most energetic neutrons. Main contributions to this resolution were attributed to the time spread of the beam burst of incident protons. Errors in the absolute scale of the cross sections were estimated to be less than 15%. Further experimental details have been given in a previous report[2,3)].

Figure 1 shows an excitation energy neutron spectrum measured at 25-degrees. Lines are results of peak fitting with eight neutron groups. Figures 2 through and 7 show angular distributions for neutrons leading to the 6 levels discussed in the present report. The data are compared with the DW results calculated by the computer code DWBA-74[10)], which includes knock-on exchange effects in an exact manner. Note that fully antisymmetrized calculations are made in the present DW analysis, in which non-normal parity terms such as $\Delta J(\Delta L, \Delta S) = 1(1, 0)$ for the $0^+ \rightarrow 1^+$ cases. Optical potential parameters of Becchetti and Greenlees[11)] are used for the entrance channel. Those for the exit channel were self-consistent potential parameters derived by Carlson et al[12)]. The effective nucleon-nucleon interactions used in the present DW analysis are those by Bertsch et al. (M3Y)[13)]. Sensitivity of such calculations to the optical-potential parameters is elaborated in Ref. 4. One body transition densities (OBTD) for microscopic DWBA calculation have been obtained by shell-model computer code OXBASH[14)]. However, the present shell-model calculation is tentative, since there are a number of ambiguities including limited model space, effective interactions, etc.

In addition to the 0.0-MeV $0^+$, 0.2229-MeV $5^+$, and 0.651-MeV $1^+$ states, $2^+$ (T=1), $7^+$, ($3^+$), $1^+$ and $5^+$ states have been newly identified at $E_x$= 0.81, 1.04, 1,19, 1.81, 1.94 MeV, respectively. The two $0^+ \rightarrow 1^+$ GT transition have been identified. *N* in the figures denotes the normalization factors introduced to fit the calculated cross sections to experimental cross sections. Since the shell-model calculations are ambiguous, *N*'s are far from unity. Among observed transition, that to the 0.81-MeV $2^+$ (T=1) state is the excited analog (EAS) transition, by which we are able to obtain information about the isovector deformation parameter $\beta_2^{(1)}$. Macroscopic Coupled-Channel (CC) calculations have been carried out by the code CWUCK as illustrated in Fig. 8.

As reported in Refs[5,6], the direct (p,n) process dominates over other CC and CC+DIRECT processes for an EAS transition at $E_p$=35 MeV. Comparison with the theoretical calculation in Fig. 8, indeed, predicts that the direct process describe quite well experimental results. The presently reduced $\beta_2^{(1)}$ value is 0.50. The isoscalar deformation parameter $\beta_2^{(0)}$ obtained with the proton inelastic scattering on $^{50}$Cr by Fabrici et al.[15)] is 0.24. Then, the ratio $\beta_2^{(1)} / \beta_2^{(0)}$ is 2.09, which is reasonable with results of the systematic studies for isovector deformation parameter[5,6)].

A simple but reliable linear relation has been found[7)] to calibrate the (p,n) cross section to the corresponding GT matrix element by the aid of the cross section for the IAS transition in the same reaction as described by the following relation:

$$B(GT) = < N > \frac{\left(\frac{d\sigma}{d\Omega}\right)_{0^+ \rightarrow 1^+, peak}}{\left(\frac{d\sigma}{d\Omega}\right)_{IAS, peak}},$$

with $<N>= 1.96 \pm 0.11$. Now, we are able to extract the GT matrix elements by the (p,n) cross sections of GT- and F-transitions. We have identified two GT-type transition in the present $^{50}$Cr(p,n)$^{50}$Mn reaction to the Ex=0.65 and 1.81-MeV states. As seen Fig2., the deferential cross section for the $0^+ \rightarrow 0^+$ ground state transition is found to be 0.53mb/sr, while those for the $0^+ \rightarrow 1^+$ transition to the 0.65 and 1.81-MeV states are, respectively, 0.14 and 0.068 mb/sr. The GT matrix elements, thus obtained for the $0^+ \rightarrow 1^+$ transitions to the 0.65 and 1.81-MeV states are 0.52 ± 0.09 and 0.25± 0.04, corresponding log*ft* values being 3.88 and 4.20, respectively.

In a summary, we have studied the (p,n) reaction on $^{50}$Cr to find spectroscopic information of neutron deficient $^{50}$Mn nucleus. We have identified eight levels in the residual nucleus. As for the isovector EAS transition to the 0.81-MeV, $2^+$ (T=1) state, isovector deformation parameter was deduced, while GT matrix elements have been obtained for two GT-type $0^+ \rightarrow 1^+$ transitions.

### References

1) Table of Isotope Eigh Edition, ed. by Firestone et al.
2) Orihara H. et al., Phys. Rev. Lett. **47** (1981) 301.
3) Furukawa K. et al., Phys. Rev. C **36** (1987) 1686.
4) Ohnuma H. et al., Nucl. Phys. **A467** (1987) 61.
5) Orihara H. et al., Phys. Lett. **106B** (1981) 171.
6) Maeda K. et al., Nucl. Phys. **A403** (1983) 1.
7) Orihara H. et al., Phys. Lett. **539B** (2002) 40.
8) Orihara H. et al., Nucl Instrum. Methods **188** (1981) 15.
9) Orihara H. et al., Nucl. Instrum. Methods **A257** (1987) 189.
10) Schaeffer R. and Raynal J., the computer program DWBA70 unpublished
11) Becchetti F.D. and Greenlees G.W., Phys. Rev. **182** (1969) 1190.
12) Carlson J.D., Zafiratos C.D. and Lind D.A., Nucl. Phys. **A249** (1975) 29.
13) Bertsch G., Borysowics J., McManus H. and Love W.G., Nucl. Phys. **A284** (1977) 399.
14) Echegoyen A. E. et al., The shell model code OXBASH.
15) Fabrici et al., Phys. Rev. C **21** (1980) 844.

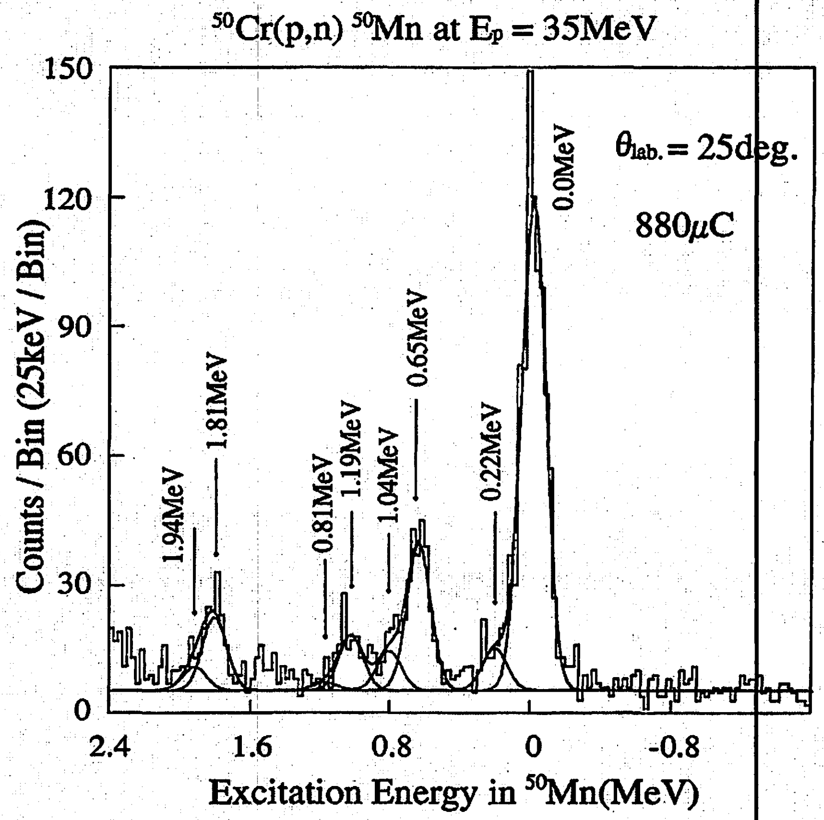

Fig. 1. A sample energy spectrum for the $^{50}$Cr(p,n) $^{50}$Mn reactions at 25° with a flight path of 44.3m. Energy per channel is 25 keV.

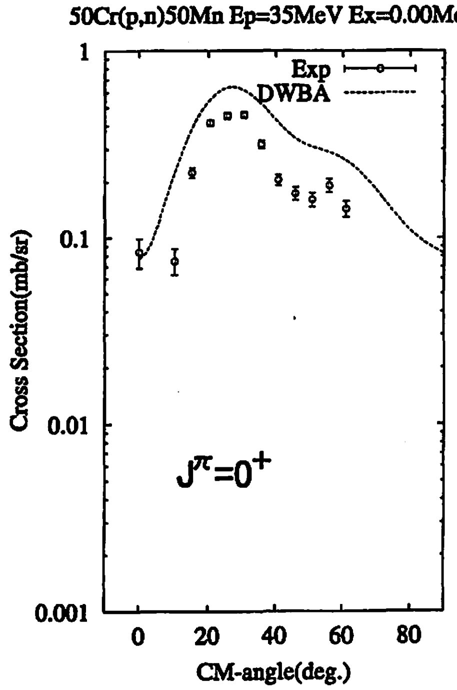

Fig. 2. Differential cross sections for neutrons leading to the ground state in $^{50}$Mn. The curves are microscopic DWBA results described in text. N denotes the normalization factor introduced to fit data.

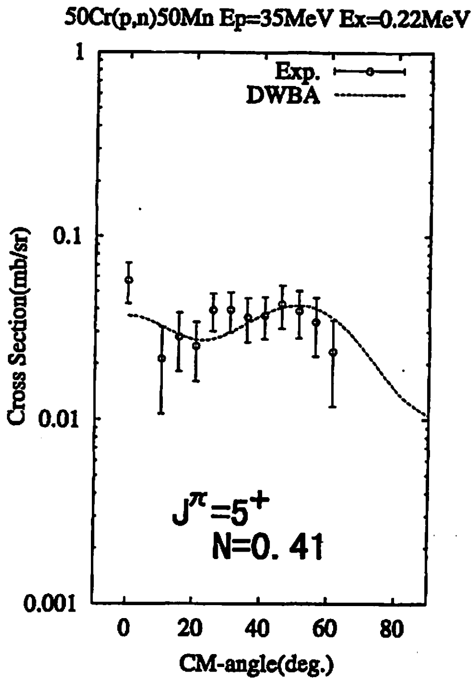

Fig. 3. Same with Fig. 2, but for the 0.22-MeV state in $^{50}$Mn.

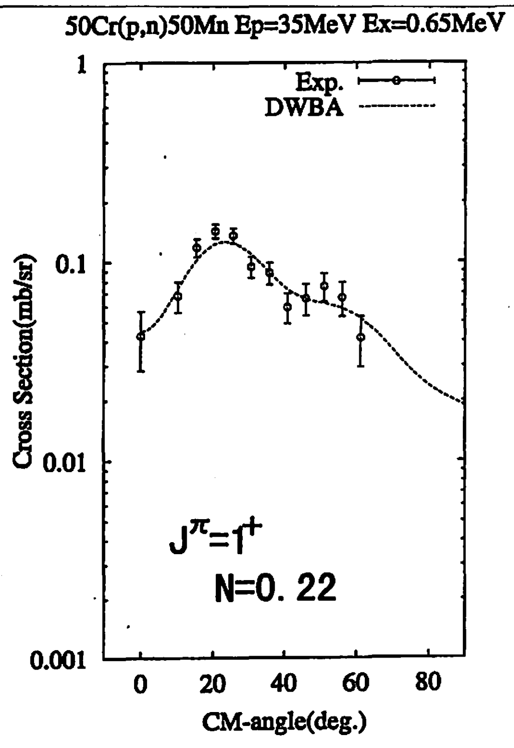

Fig. 4. Same with Fig. 2, but for the 0.65-MeV state in $^{50}$Mn.

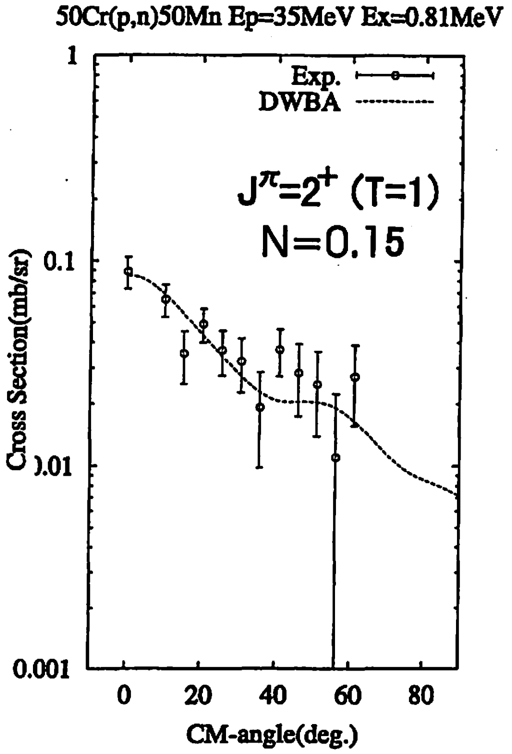

Fig. 5. Same with Fig. 2, but for the 0.81-MeV state in $^{50}$Mn.

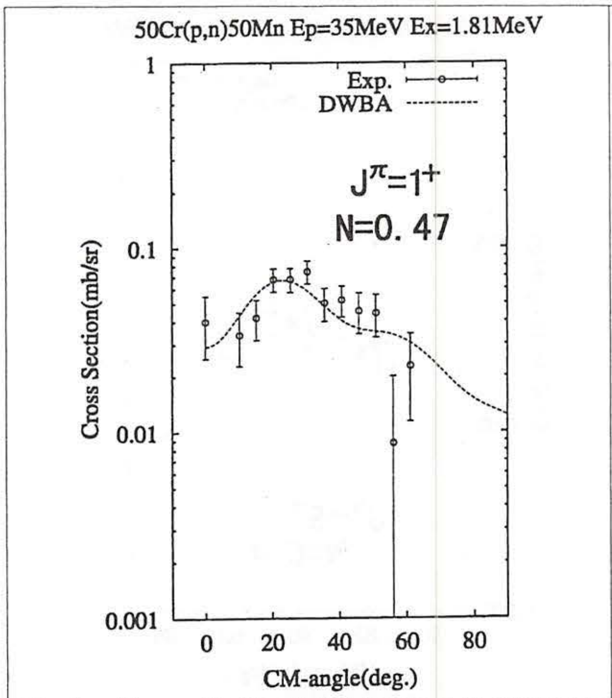

Fig. 6. Same with Fig. 2, but for the 1.81-MeV state in $^{50}$Mn.

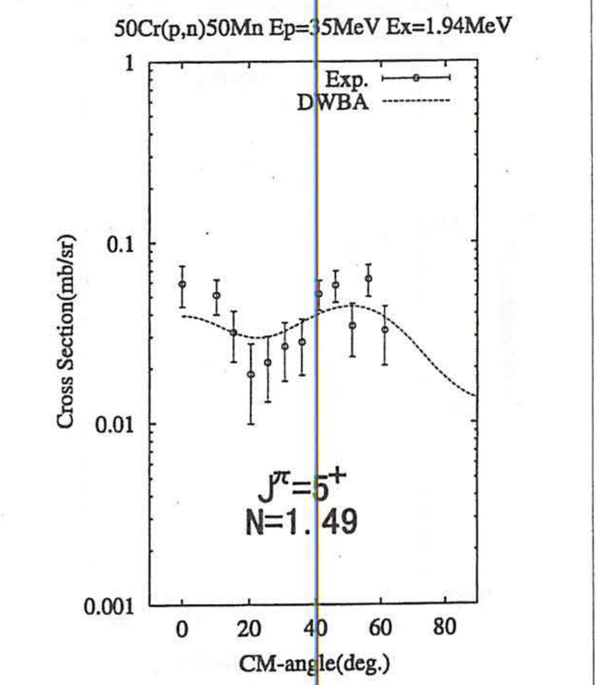

Fig. 7. Same with Fig. 2, but for the 1.94-MeV state in $^{50}$Mn.

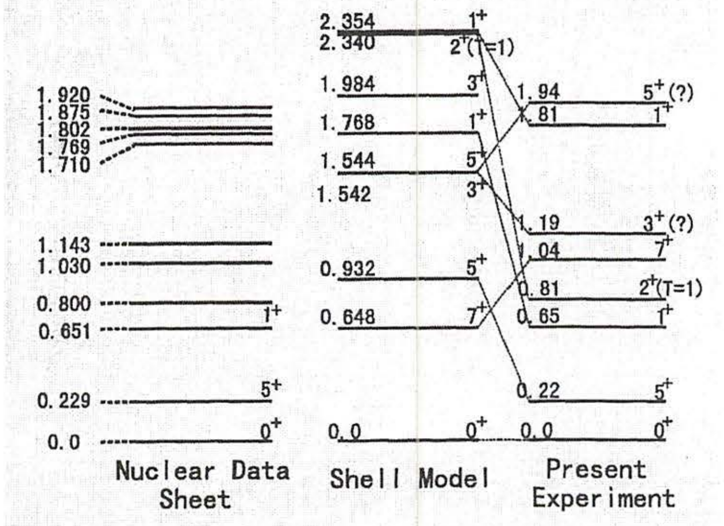

Fig. 8. Comparison for level diagram of $^{50}$Mn.

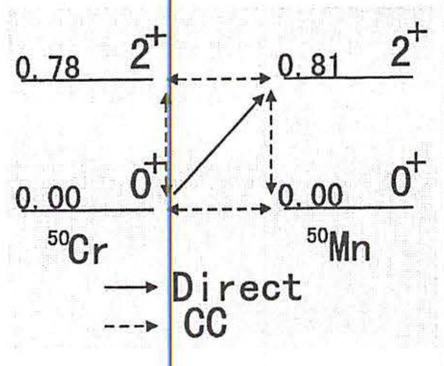

Fig. 9. Coupling scheme applied for CC calculations.

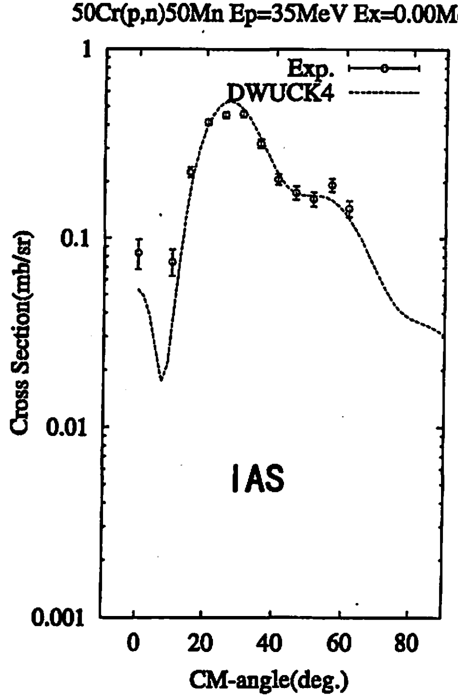

Fig. 10. Same with Fig. 2, but for macroscopic DWBA coparison.

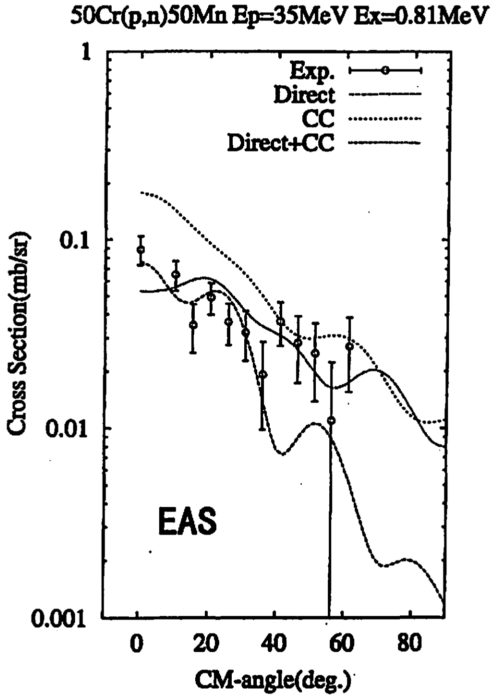

Fig. 11. Same with Fig. 2, but for the 0.65-MeV state in $^{50}$Mn.

# I. 2. Isospin Excitation in $^{22}$Na Studied by the $^{22}$Ne(p,n)$^{22}$Na Reaction at $E_p$=35 MeV

*Orihara H., Terakawa A., Suzuki H. , Kumagai K., G. C. Jon*[*], *Ishii K.*[**],
*and Ohnuma H.*[***]

*Cyclotron and Radioisotope center, Tohoku University*
*Institute of Physics, Academia Sinica, Nankang Taipei, Taiwan 11592*[*]
*Department of Quantum Science and Energy Engineering, Tohoku University*[**]
*Department of Physics, Chiba Institute of Technology, Chiba 275-0023, Japan*[***]

One can selectively excite the spin-flip components in the (p,n) reaction at intermediate energies through the relatively strong spin-isospin effective interaction. Low energy (p,n) reactions, on the other hand, give us a sufficient energy resolution to discuss (p,n) strength for individual nuclear levels$^{1,2)}$. However, spin-nonflip excitation is strong and exchange contributions are important at low energies. Various problems associated with the distorted-wave (DW) analysis of low-energy (p,n) data were discussed in detail by Ohnuma et al$^{3)}$. It has been found possible to obtain basically the same information as that at intermediate energies if careful analysis is carried out.

In the course of the systematic investigation of isospin and spin-isospin excitation in nuclei through the (p,n) reaction at $E_p$ = 35MeV, three reports have been published concerning the $^{22}$Ne(p,n)$^{22}$Na reaction. The first report$^{4)}$ entitled as "$0\hbar\omega$ stretched states observed in the (p, n) reactions on $^{22}$Ne and $^{26}$Mg" describes that cross sections and their angular distribution are well explained by the DWBA analysis based on the precise microscopic transition densities by shell-model in the case of $0\hbar\omega$ stretched state transition. The second one$^{5)}$ is related to isospin excitation and it's topics is "Isovector part of optical potentials studied through analog transitions in the *(p, n)* reaction at 35 MeV". Analog transition in the $^{22}$Ne(p,n)$^{22}$Na reaction has been compiled as well in this report. The last one$^{6)}$ is entitled as "Gamow-Teller matrix-elements in light nuclei and *(p,n)* cross-sections at $E_p$ = 35 MeV". It reports that the peak *(p,n)* cross sections around $\theta \sim 30°$ are proportional to the corresponding $\beta^+$-decay rates of the $T_z$ = -1 partners of the $T$ = 1 multiplets, and proposes a prescription to extract GT matrix elements in light nuclei from *(p,n)* cross sections using such proportionality. The $0^+ \rightarrow 1^+$ Gamow-Teller(GT) type transition to the 1.936-MeV, $1^+$ state in $^{22}$Na has been used for this purpose. In this report, we describe a full outline studied for the $^{22}$Ne(p,n)$^{22}$Na reaction at Ep= 35 MeV, including negative parity state excitation.

The experiment was carried out using a 35 MeV proton beam from the AVF cyclotron and the time-of-flight facilities[7,8)] at the Cyclotron and Radioisotope Center at Tohoku University. A beam swinger system was used to measure angular distributions of emitted neutrons between 0° and 100° (lab). The target was neon gas enriched to 99 % in $^{22}$Ne. Two types of gas-cell were used. One was disk type used for measurements in small angles less than ~30°, while a 20 cm long cylindrical cell which allowed us to shield the neutron detectors against neutrons emitted from the window foils was used for large angle measurements. In all the cases the effective target thickness was in the order of 1 mg/cm$^2$. The window materials were metallic calcium foil for the disk type cell, and Havar foil for the cylindrical cell.

Neutrons were detected by an array of twelve detectors, which were located at 44.3 m from the target and contained a total of 23.2 liters of NE213 scintillator. The detector efficiencies were obtained from Monte Carlo calculations for monoenergetic neutrons with $E \leq 34$ MeV. Absolute detector efficiencies were also measured by counting neutrons from the $^7$Li(p,n)$^7$ Be reaction and comparing its yield with the absolute neutron fluence determined by activation. They were in good agreement with the Monte Carlo calculations. Overall time resolution was typically 1.3 ns corresponding to 184 keV for the most energetic neutrons. Main contributions to this resolution were attributed to the energy loss and straggling of incident protons in the entrance-window of the target gas cell. Errors in the absolute scale of the cross sections were estimated to be less than 15%. Further experimental details have been given in a previous report.

Figure 1 shows an excitation energy neutron spectrum measured at 25-degrees. We discuss for these 10 transitions observed as relatively prominent peaks., and give spin-parity assignments for these levels, as labeled in parentheses in Fig. 1, based on the shell-model calculation and DWBA analysis for the (p,n) cross sections neutron described below.

The data are compared with the DW results calculated by the computer code DWBA-74[9)], which includes knock-on exchange effects in an exact manner. Note that fully antisymmetrized calculations are made in the present DW analysis, in which non-normal parity terms such as $\Delta J(\Delta L, \Delta S) = 1(1, 0)$ for the $0^+ \rightarrow 1^+$ cases. Optical potential parameters of Becchetti and Greenlees[10)] are used for the entrance channel. Those for the exit channel were self-consistent potential parameters derived by Carlson et al[11)]. The effective nucleon-nucleon interactions used in the present DW analysis are those by Bertsch et al. (M3Y)[12)]. Sensitivity of such calculations to the optical-potential parameters is elaborated in Ref. 3. One-body transition densities (OBTD) for microscopic DWBA calculation have been obtained by shell-model computer code OXBASH[13)]. For positive parity transitions, full sd-shell calculations were carried out with the SD-interaction by Brown and Wildenthal[14)] for both initial and final states. As for negative parity transition, on the other hand, OBTD for $1\hbar\omega$-jump into fp-shell were taken into accounts with the PSD model-space and by the SPSDPF interactions[15)]. Note that full sd-shell wave functions were applied for the latter target state.

Figures 2 through 12 show experimental and theoretical angular distribution of emitted neutrons leading to the residual states in $^{22}$Na. Further brief discussions are concerned with those for the individual transition.

### *Analog Transition*

In addition to the $\Delta L=0$ transition to the isobaric analog state at $E_x=0.657$ MeV, an extra $T=T_>$, 2+ excited analog state (EAS) is proposed at $E_x=5.99$MeV. This identification is based on the shell model calculation. Though the shell-model calculations predict two $T=1$, $2^+$ states at lower excitation region. However, the transition densities yield much less cross section to explain this prominent transition.

### *GT-type Transition*

For three GT-type $0^+ \rightarrow 1^+$ transitions, the angular distribution of cross sections have been obtained as illustrated in Figs. 3, 6 and 10. The neutron peak for the lowest 0.583-MeV state is not resolved from that for strong IAS transition to the 0.657-MeV state. The contributions of GT transition, threfor, has been obtained by subtraction of the IAS component from the composite peak. A reliable linear relation has been found[7)] to calibrate the (p,n) cross section to the corresponding GT matrix element by the aid of the cross section for the IAS transition in the same reaction as described by the following relation:

$$B(GT) = <N> \frac{\left(\dfrac{d\sigma}{d\Omega}\right)_{0^+\rightarrow 1^+, peak}}{\left(\dfrac{d\sigma}{d\Omega}\right)_{IAS, peak}},$$

with $<N> = 1.96 \pm 0.11$. Appling this method to the three transitions to the 0.583, 1.936

and 4.00-MeV state, we obtain for the corresponding GT-matrix elements, respectively, 0.8, 1.42 and 0.32.

*Negative Parity Transition*

Two negative parity transitions have been identified at 2.57 and 3.37 MeV as 2- and 3- state, respectively. Prominent $1\hbar\omega$-jump transition to the $2^-$ state was observed as a typical spin-isospin excitation. Reasonable accounts by the shell-model and DWBA theory have been obtained as well.

In summary, experimental study has been carried out in order to make clear the nuclear structure of $^{22}$Na nucleus. Shell-model calculation and analysis by DWBA theory have provided a set of spin-parity assignments over 11 levels.

**References**

1) Orihara H. et al., Phys. Rev. Lett. **47** (1981) 301.
2) Furukawa K. et al., Phys. Rev. C **36** (1987) 1686.
3) Ohnuma H. et al., Nucl. Phys. **A467** (1987) 61.
4) Orihara H. et al., Phys. Rev. C **41** (1990) 2414.
5) Jon G.C. et al., Phys. Rev. C **62** (2000) 044609.
6) Orihara H. et al., Phys. Lett. **539B** (2002) 40.
7) Orihara H. et al., Nucl Instrum. Methods **188** (1981) 15.
8) Orihara H. et al., Nucl. Instrum. Methods **A257** (1987) 189.
9) Schaeffer R. and Raynal J., the computer program DWBA70 unpublished.
10) Becchetti F.D. and Greenlees G.W., Phys. Rev. **182** (1969) 1190.
11) Carlson J.D., Zafiratos C.D. and Lind D.A., Nucl. Phys. **A249** (1975) 29.
12) Bertsch G., Borysowics J., McManus H. and Love W.G., Nucl. Phys. **A284** (1977) 399.
13) Echegoyen A.E. et al., The shell model code OXBASH.
14) Brown B.A. and Wildenthal B. H, Phys. Rev. C **27** (1983) 1296.
15) Warburton E.K. and Brown B.A., Phys. Rev C **46** (1992) 923.

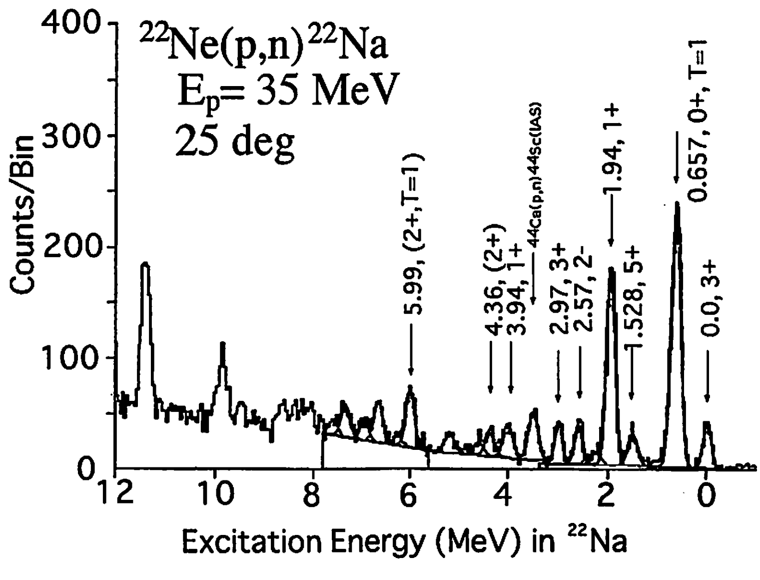

Fig. 1. A sample energy spectrum for the $^{22}$Ne(p,n)$^{22}$Na reactions at 25°. Energy per channel is 25 keV.

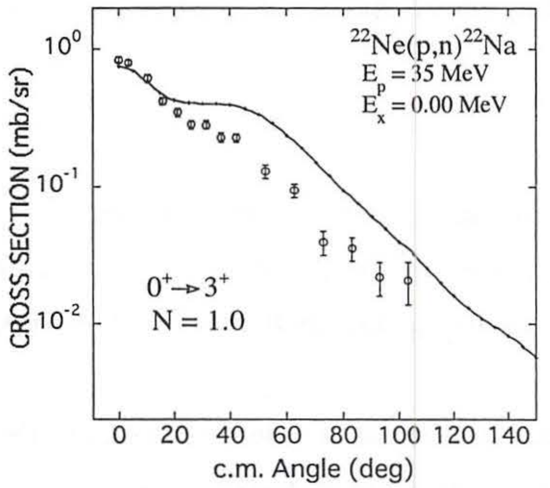

Fig. 2. Differential cross sections for neutrons leading to the ground state in $^{22}$Na. The curves are microscopic DWBA results described in text. N denotes the normalization factor introduced to fit data.

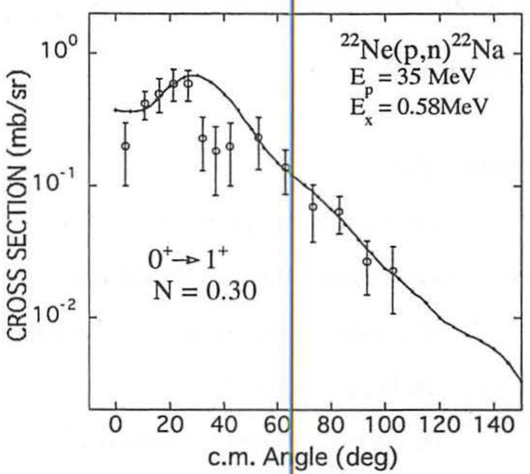

Fig. 3. Same with Fig. 2, but for the 0.58-MeV state in $^{22}$Na.

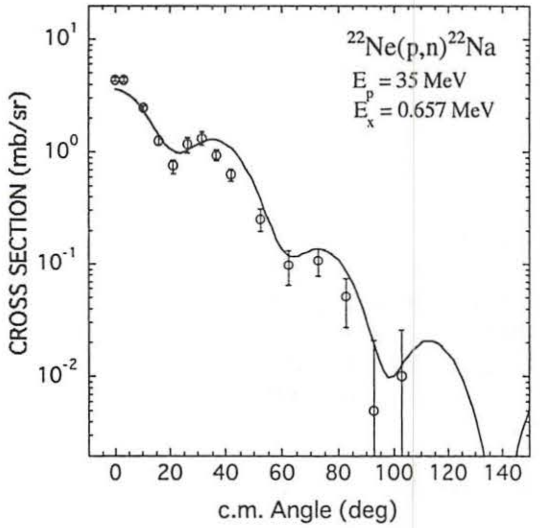

Fig. 4. Same with Fig. 2, but for the 0.657-MeV state in $^{22}$Na, and for macroscopic DWBA results.

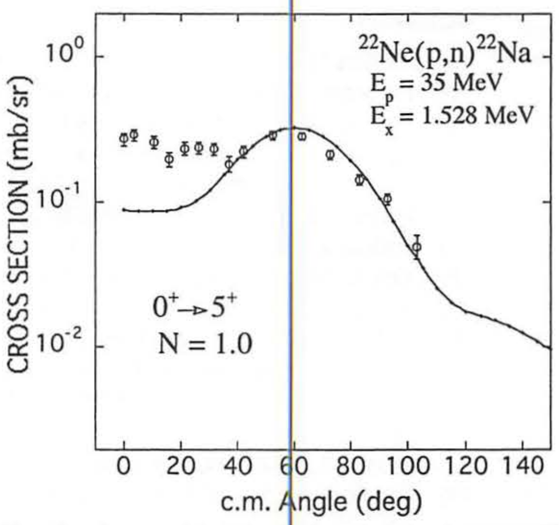

Fig. 5. Same with Fig. 2, but for the 1.528-MeV state in $^{22}$Na.

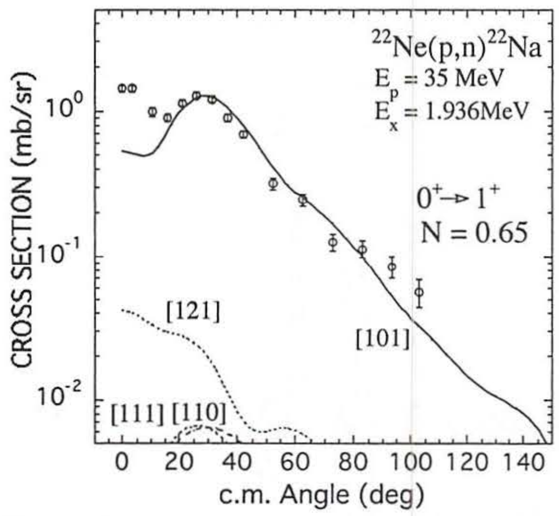

Fig. 6. Same with Fig. 2, but for the 1.936-MeV state in $^{22}$Na.

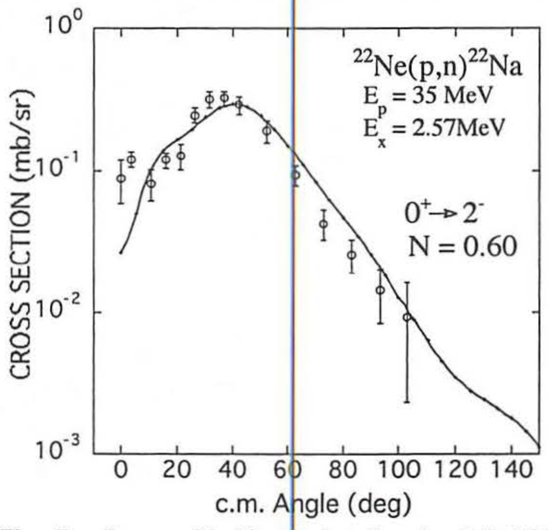

Fig. 7. Same with Fig. 2, but for the 2.57-MeV state in $^{22}$Na.

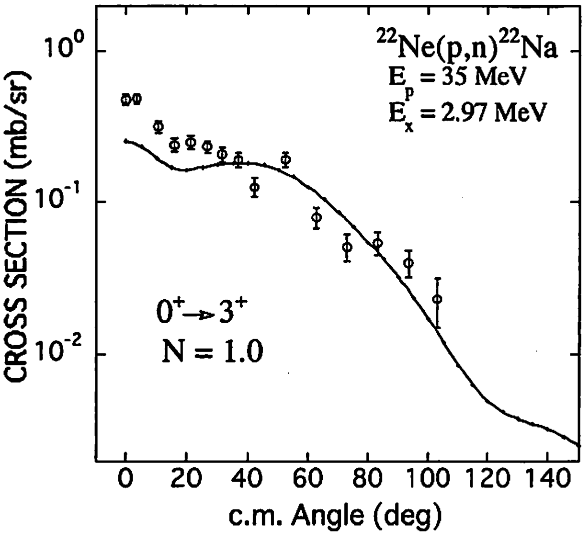

Fig. 8. Same with Fig. 2, but for the 2.99-MeV state in $^{22}$Na.

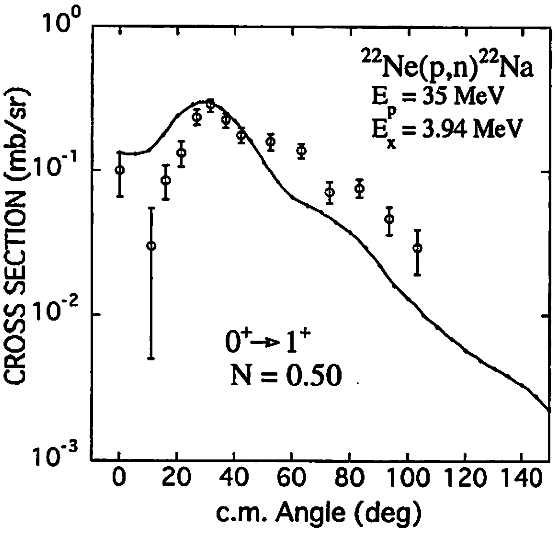

Fig. 9. Same with Fig. 2, but for the 4.00-MeV state in $^{22}$Na.

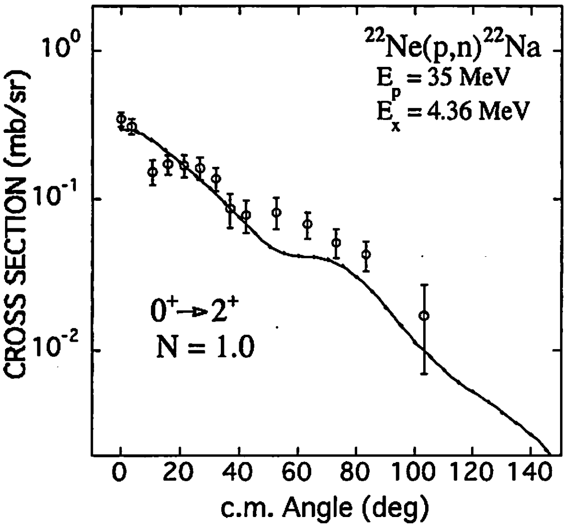

Fig. 10. Same with Fig. 2, but for the 4.36-MeV state in $^{22}$Na.

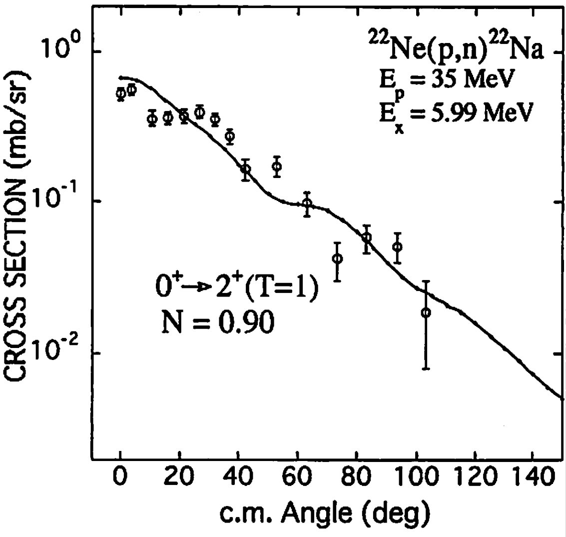

Fig. 11. Same with Fig. 2, but for the 5.99-MeV state in $^{22}$Na.

# I. 3. Improvement on ECR Ion Source for the Production of Highly Charged Ions

*Fujita M., Miyashita Y.*[*]*, Yamazaki A., Tanaka E. and Shinozuka T.*

*Cyclotron and Radioisotope center, Tohoku University*
*Department of physics, Tohoku University*[*]

A 14.5 GHz electron cyclotron resonance (ECR) ion source made of all-permanent-magnet was developed in February 2001[1)] as proto-type. The performance of this source at the initial phase has been enough for the acceleration by 930 new cyclotron to the relatively light ions, such as Carbon, Nitrogen, Oxygen and Neon.

However, for the case of Ar, it was not sufficient to obtain the intensities at the higher charge states. At the beginning of the development of this source, only 0.2 eμA beam of $Ar^{9+}$ could be extracted from the ion source[2)]. Therefore, several improvements have been planned and performed in order to increase beam intensity of highly charged ions.

The first improvement is the increase of the magnetic field for radial confinement. Figure 1 shows the magnetic field intensity of radial direction in the plasma chamber. Originally, the diameter of the plasma chamber was 32 mm, then the radial field strength at the chamber wall was 8052 G. It was suggested[3)] that the radial magnetic field strength at the chamber wall should be 1.5 or more times of ECR resonance magnetic field, which is 5180 G at 14.5 GHz microwave frequency. In order to increase the radial magnetic field strength, therefore, the diameter of the plasma chamber has been enlarged up to 36 mm. As a result, the radial field strength has been increased to 10498 G, and the beam intensity of the $Ar^{8+}$ and $Ar^{9+}$ has been much increased to 9.4 eμA and 1.4 eμA, respectively (see figure 2).

The second one is the tuning of microwave frequency. Figure 3 shows the variation of the highly charged ion production against the frequency scanning. The Traveling Wave Tube Amplifier (TWTA) is used for tuning the microwave frequency. Further more, the partition wall made of SUS has been placed near the entrance window to efficiently confine the microwave power in the plasma chamber. This partition wall is also useful to reduce the gas consumption, because it makes less vaccum conductance. In addition, the position of this wall is controllable from the outside of vacuum, so the fine tuning for decreasing the microwave reflection is available. The position of the partition wall has been set in the optimum conditions at each frequency. As shown in figure 3, the intensity of $Ar^{8+}$ beam has been increased to 10.5 eμA.

The beam intensity of $Ar^{9+}$ has been increased to 10 or more times as a result of these improvements. For further improvement, it is planned for the optimization of the magnetic field distribution in plasma chamber and for the introduction of more precise gas flow control system.

## References

1) Yamazaki A., Fujita M., Tanaka E., Shinozuka T., Yokoi T., Ozawa T. and Tanaka H., Rev. Sci. Instrum. 73 (2002) 589.
2) Yamazaki A., Tanaka E., Fujita M. and Shinozuka T., CYRIC Annual Report (2002).
3) Ciavola G., Gammino S., Antaya T. and Harrison K., Proceedings of the 12th International Workshop on ECR ION SOURCES (1995) 156.

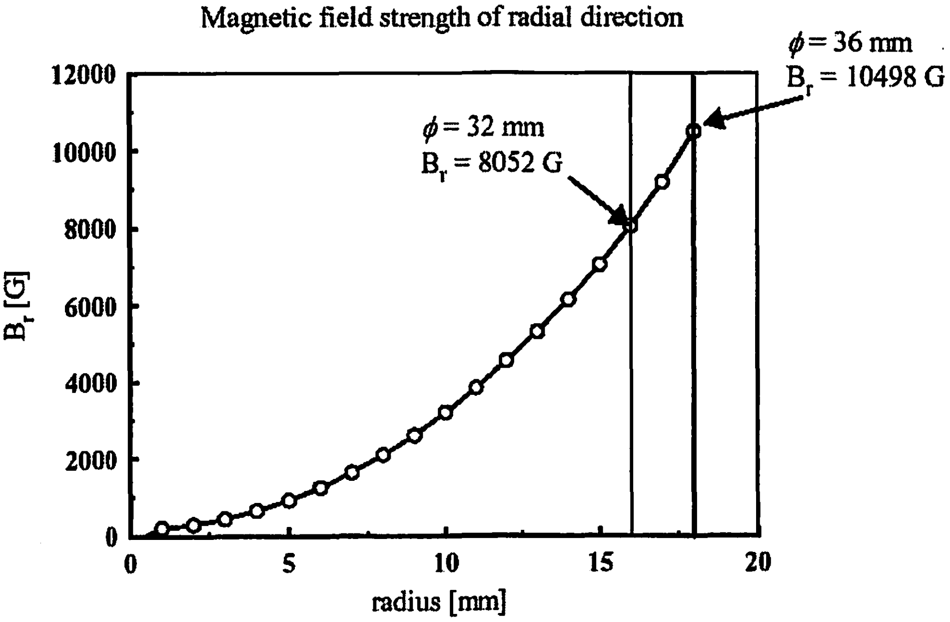

Fig. 1. A magnetic field distribution of radial direction in the plasma chamber.

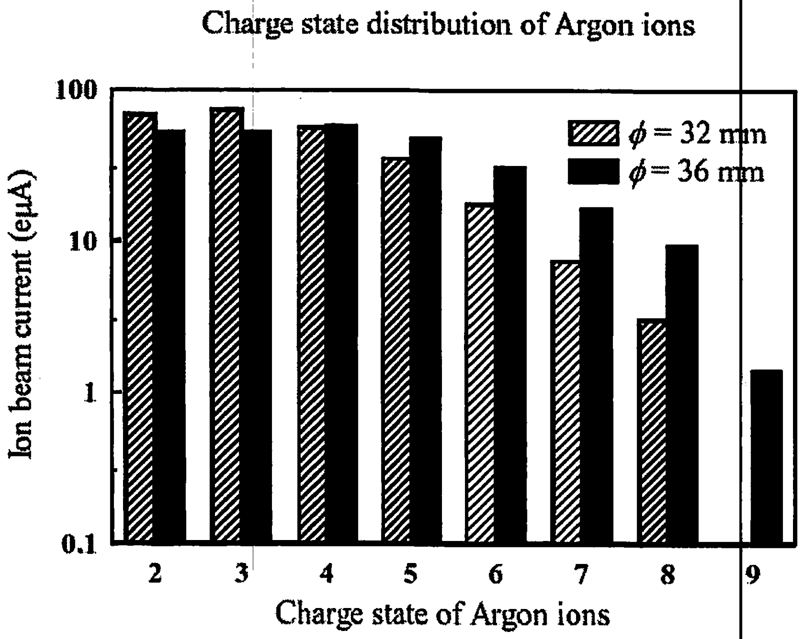

Fig. 2. A charge state distribution of Argon ions after modification of the diameter of plasma chamber in comparison to the original one.

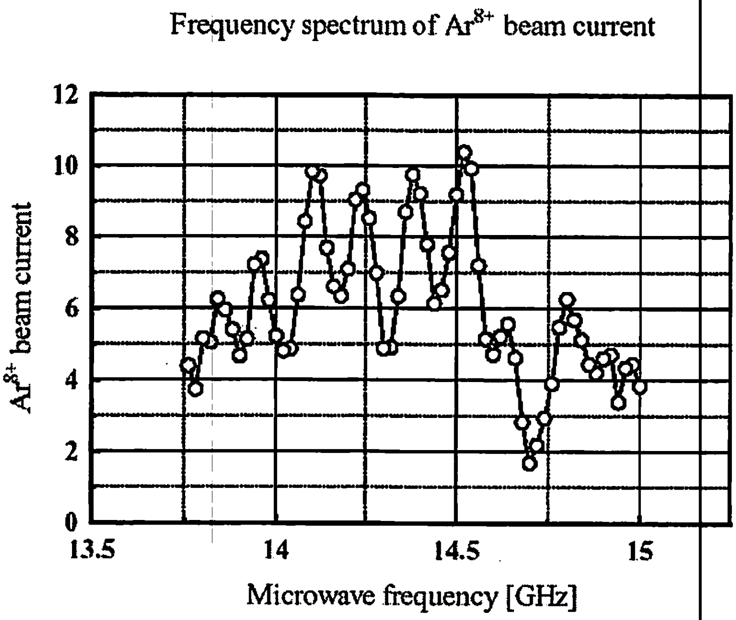

Fig. 3. A frequency dependence of Ar 8+ current. The injected RF power is 200 W.

# I. 4. New Beam Transport System at CYRIC

*Terakawa A., Misu T., Itoh K., Suzuki H., Orihara H., Chiba S.*, Ohmiya Y.*, Takahashi N.*, Kan S.*, Fujita M., and Shinozuka T.*

*Cyclotron and Radioisotope center, Tohoku University*
*Sumitomo Accelerator Service Corporation**

The beam transport system at CYRIC was upgraded during the construction of the new K = 110 MeV AVF cyclotron. Since the maximum beam energy of the new cyclotron is about twice that of the old cyclotron, several dipole and quadrupole magnets for the beam lines were replaced by new ones designed for the high energy beams. Furthermore, new control system for the whole beam lines was built on the basis of the programmable logic controller (PLC) system. In this report the upgraded beam transport system will be described.

The new cyclotron was designed to accelerate not only positive ions but also H- and D- ions for the high intensity beams up to about 300 $\mu$A. The maximum beam energies of the new cyclotron are 90 MeV for a proton beam and 27.5 MeV /u for light ion beams in case of the positive ion acceleration. On the other hand, H- and D- ions are accelerated up to 50 and 25 MeV, respectively, and extracted by foil stripping. The whole beam lines at CYRIC are shown in Fig. 1. There are 4 main beam lines (C1 - C5) leading to additional beam lines (C31 - C51) and 5 experimental rooms (TR1 – TR5). The two beam extraction lines (CP and CN ) were newly built.

Beam transport calculations for the new extraction lines and the subsequent beam lines were carried out with the code TRANSPORT[1]. Fig.2 shows the result of the calculation for the CP-C5-C51 beam lines. The C4 beam line was modified for achromatic beam transport as well as dispersive mode by adding several quadrupole magnets around the analyzing magnets (ANA1, ANA2). The C2 beam line was removed because a small AVF cyclotron for RI production was installed in the TR1 room.

The switching magnets SW1 - SW3 and their power supplies were newly built. In order to perform time-sharing experiments the SW1 was designed to switch one beam line to another one within 2 second. However, the switching mode between the C4 and C5 beam lines is not available at this stage because the power supplies for the magnets are in short.

On the other hand, the analyzing magnets ( ANA1, ANA2, ANA3) were equipped with both the new power supplies and additional 50mm thick iron plates on their yokes to produce sufficient magnetic field without saturation. Several quadrupole magnets were replaced by new ones with the maximum field gradient of 15 or 10 T/m. The specifications of the new magnets are listed in Tables 1-3.

The new control system for the beam lines was also built on the basis of YOKOGAWA FA-M3 controlors (PLC)[2] which consists of the sequence CPU, digital input / output (DI/O), Analog to digital (A/D), digital to analog (A/D) modules. The control programs for the sequence CPU modules were written in the structured-ladder programming method using the WideField2). The Graphical user interface (GUI) for controlling and monitoring the beam transport system was developed using Labview3). The personal computers running the GUI are linked to the PLC system via the local area network.

**References**

1) Brown K. L. et al., A computer program for designing charged particle beam transport system, unpublished.
2) Yokogawa Electric Corporation, Musashino, Tokyo 180-8750, Japan (http://www.yokogawa.co.jp/IA/fam3.htm).
3) National Instruments Corporation, USA (http://www.ni.com).

Table 1. Basic specifications of the new switching magnets.

| Magnets | PSW | SW1 | SW2 | SW3 |
|---|---|---|---|---|
| Pole diameter (mm) | 500 | 400 | 500 | 456 |
| Pole gap (mm) | 47 | 47 | 47 | 47 |
| Maximum field (T) | 1.5 | 1.5 | 1.5 | 1.5 |
| Maximum deflection angle (deg) | 50.7 | 41.3 | 50.0 | 45.0 |

Table 2. Basic specifications of the new dipole magnets.

| Magnets | B1 | B2 | ANA1 | ANA2 | ANA3 | BEND1 | BEND2 |
|---|---|---|---|---|---|---|---|
| Radius(mm) | 1100 | 700 | 1400 | 1400 | 1300 | 1100 | 1100 |
| Deflection angle(deg) | 90 | 60 | 105 | 95 | 60 | 60 | 150 |
| Pole gap (mm) | 56 | 56 | 50 | 50 | 50 | 47 | 47 |
| Entrance angle (deg) | 15.0 | 0.0 | 36.0 | 31.0 | 30.2 | 0.0 | 62.0 |
| Exit angle (deg) | 15.0 | 0.0 | 36.0 | 31.0 | -7.0 | 0.0 | 61.5 |
| Maximum field (T) | 1.5 | 1.5 | 1.3 | 1.3 | 1.3 | 1.5 | 1.5 |

Table 3. Basic specifications of the new quadrupole magnets.

| Magnets | QT15 | QT10 |
|---|---|---|
| Pole gap (mm) | 105 | 105 |
| Pole length (mm) | 240 | 240 |
| Maximum field gradient (T/m) | 15 | 10 |

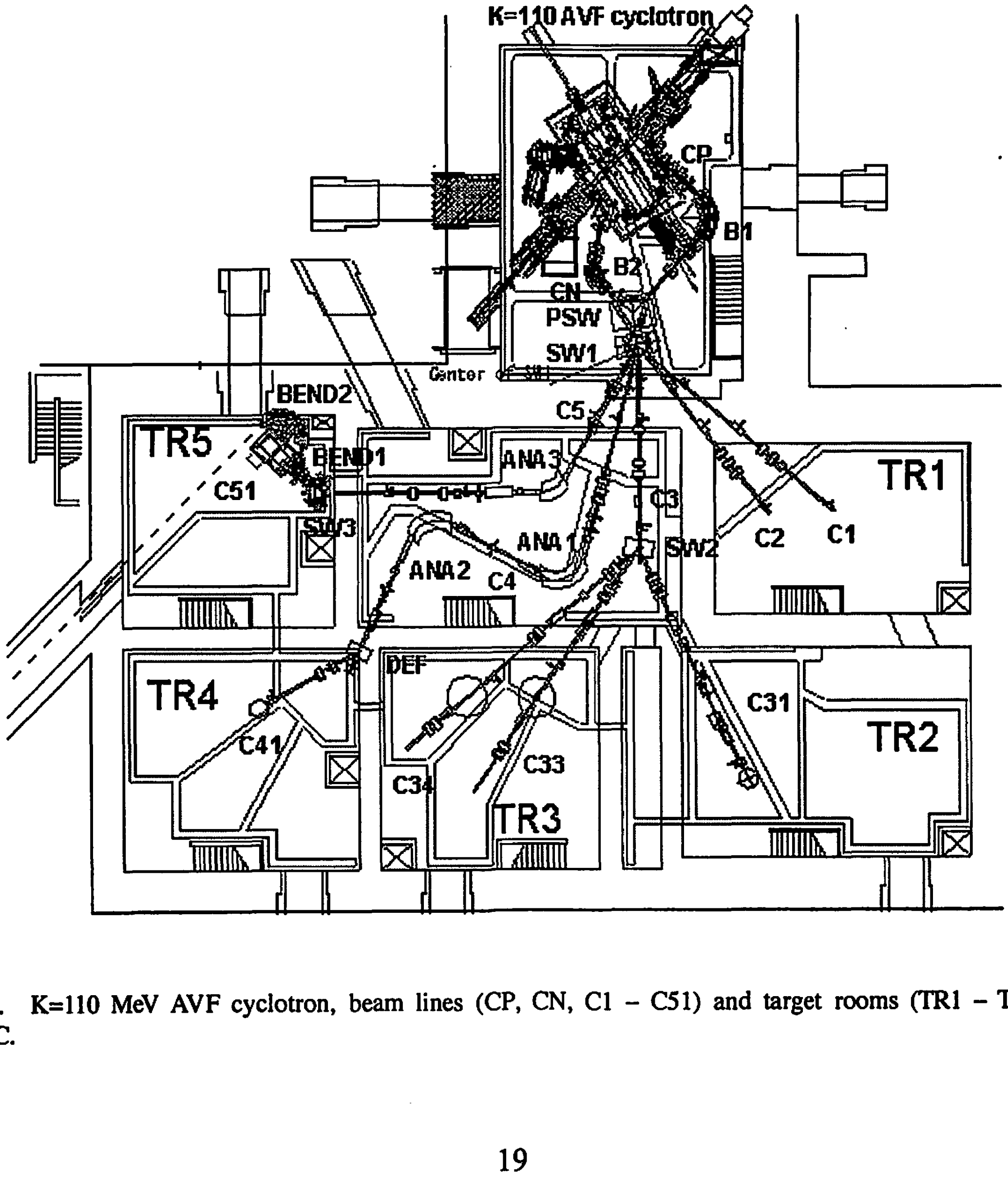

Fig. 1. K=110 MeV AVF cyclotron, beam lines (CP, CN, C1 – C51) and target rooms (TR1 – TR5) at CYRIC.

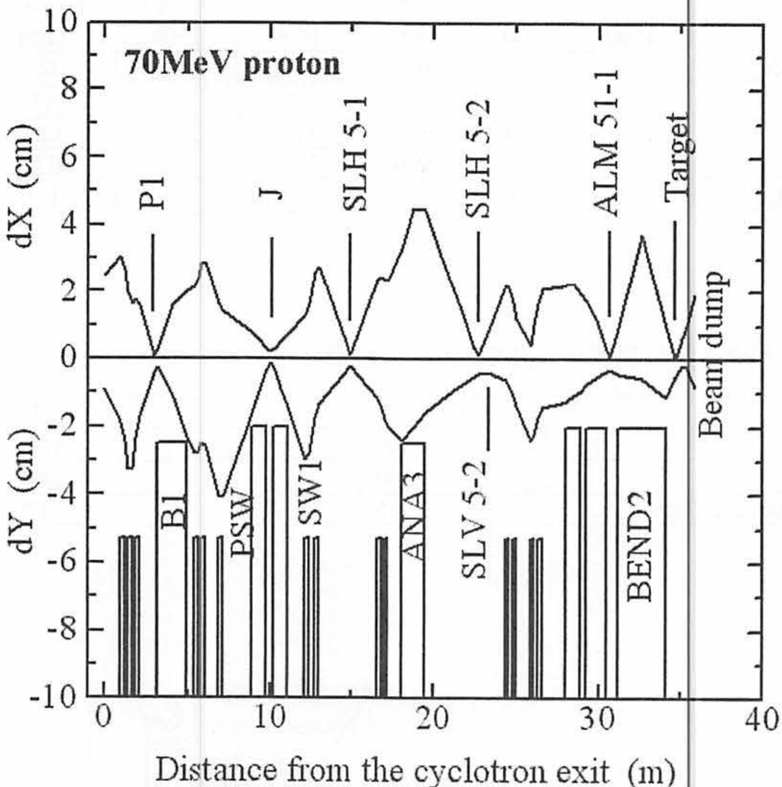

Fig. 2. Result of the beam transport calculation for the CP-C5-C51 beam lines. The horizontal (X) and vertical (Y) beam envelopes are described together with the position and vertical clearance for the magnets.

# I. 5. Development of RF – IGISOL at CYRIC

*Sonoda T., Fujita M.**, *Endo T., Yamazaki A.**,
*Miyake T., Suzuki T., Goto A., Miyashita Y., Sato N.,*
*Tanaka E.**, *Shinozuka T.**, *Mitugasira T.***, *Ohtsuki T.*****,
*Takamiya K.****, *Yuki H.*****

*Department of Physics, Tohoku University*
*Cyclotron and Radioisotope Center, Tohoku University**
*Institute for Materials Research, Tohoku University***
*Research Reactor Institute, Kyoto University****
*Laboratory of Nuclear Science, Tohoku University*****

The Tohoku IGISOL (Ion Guide Isotope Separator On Line) has been used for studying nuclei in the $f_{7/2}$-$p_{3/2}$ shell regions and medium-mass neutron rich nuclei produced by the proton-induced fission reaction with a uranium target since 1987 with the old K=50MeV cyclotron[1,2]. The classical type of an IGISOL chamber has a small stopping volume in order to avoid the loss by diffusion and the recombination with electrons. Jyvaskyla group has recently been reported to have the fission ion guide total efficiency of 0.02 %. It means that the $^{112}$Rh yield using the $^{238}$U( 25 MeV p, fission) reaction has reached $10^5$ ions/sec at a beam intensity of 10 uA. For a cumulative cross section of 30 mb, this corresponds to about 3000 ions/mb[3]. For effective stopping of fission fragments, a large volume and high pressure of the target chamber are required.

A new type of IGISOL has been developed using a large gas cell equipped with DC and RF electric field. The new rf ion guide gas cell (off and on-line setup respectively) is shown in Fig. 1. In a 30 cm long gas cell, 80 electrodes were arranged to form a parabolic structure with different dc voltage being applied to each electrode. The bottom electrode consists of planar type of printed circuit board. It has a diameter of 6 cm with 100 ring type electrodes and an exit nozzle of 1.6 mm. This type of electrodes was originally developed by Wada[4] and named rf-carpet. The DC field guides the ions to the exit hole and the RF field push out the ions from the surface of electrodes.

The first off line tests of this new approach, using a $^{227}$Ac alpha-decay-recoil source, are performed. The $^{227}$Ac has a recoiled $^{219}$Rn ions. It placed at the tip of a movable stick along the symmetry axis of the chamber. This allows absolute efficiency measurement as a function of the distance between extraction hole and source. Figure 2 shows measured from $^{219}$Rn and $^{215}$Po alpha spectra with SSD detector which is placed at ISOL collector station.

It clearly revealed the effect of DC and RF electric field. The extraction yield of recoiled atoms is 20 times higher than the gas transportation without electric field in the chamber. Figure 3 shows the extraction efficiency related to the position of source. Even for the 15cm transportation in gas, it has over 1% efficiency by the effect of electric field. However, the efficiency has come to down at a longer than 15 cm, presumable due to the fact that ions are lost the formation of molecular ions and/or with impurities in the gas (~ 10 ppm no purification).

Further experiments are planed for systematic measurements of efficiency for recoils from the $^{227}$Ac source in presence of the cyclotron beam. This involves a need to extrapolate the knowledge of plasma effect that lead to a repulsive space charge effect.

**References**

1) Yoshii M. et al., Nucl. Instrum. Methods **B26** (1987) 410.
2) Kudo H. et al., Nucl. Instrum. Methods **B126** (1997) 209.
3) Aysto J., Nuclear Physics **A693** (2001) 477.
4) Wada M. et al., Nucl. Instrum. Methods **B204** (2003) 570.

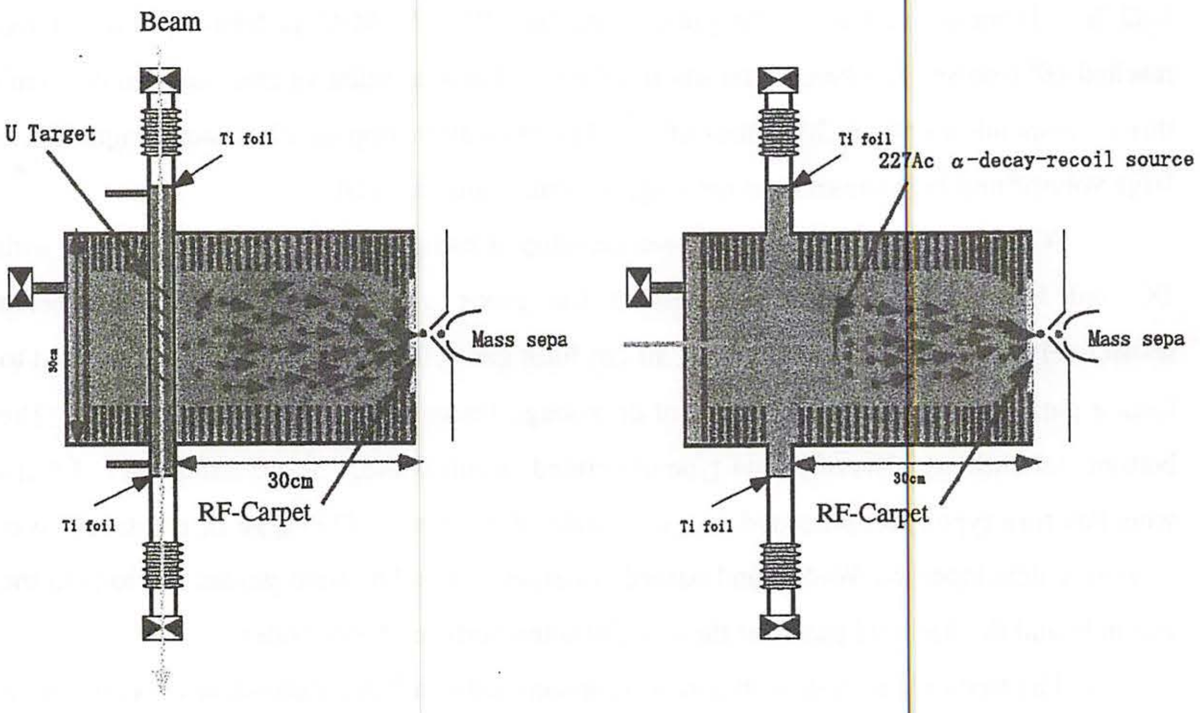

TYPE 1 TYPE 2

Fig. 1. Cross-sectional view of RF Ion guide gas cell of the on line setup ( Type 1), off line setup ( Type 2 ).

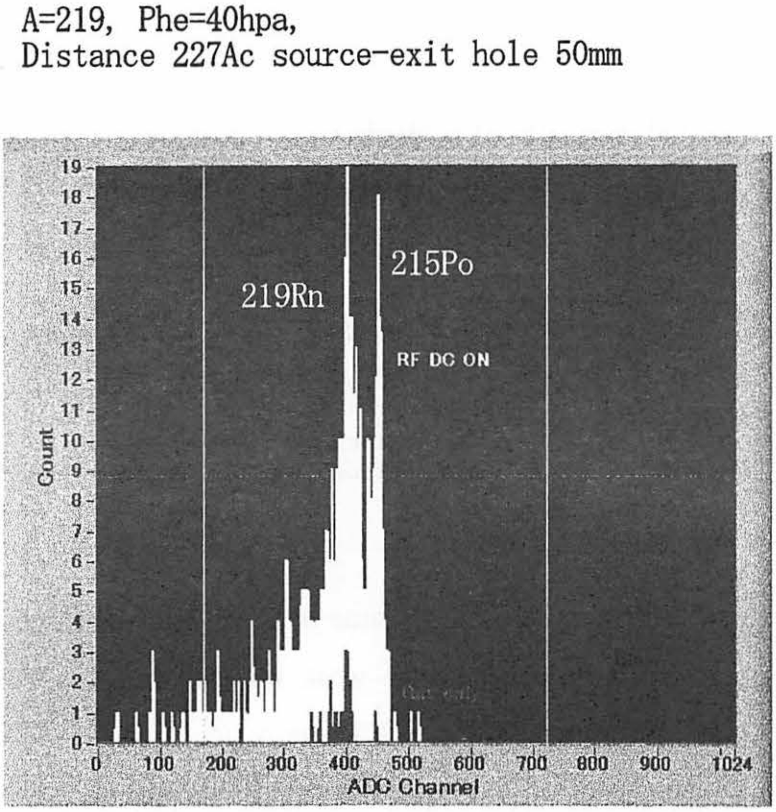
A=219, Phe=40hpa,
Distance 227Ac source-exit hole 50mm

Fig. 2. Alpha spectra measured by SSD detector where is placed at ISOL collector station. The peaks marked as "Rn","Po" are the alpha particles from $^{219}$Rn, $^{215}$Po nuclei on the aluminum catcher foil in front of the detector.

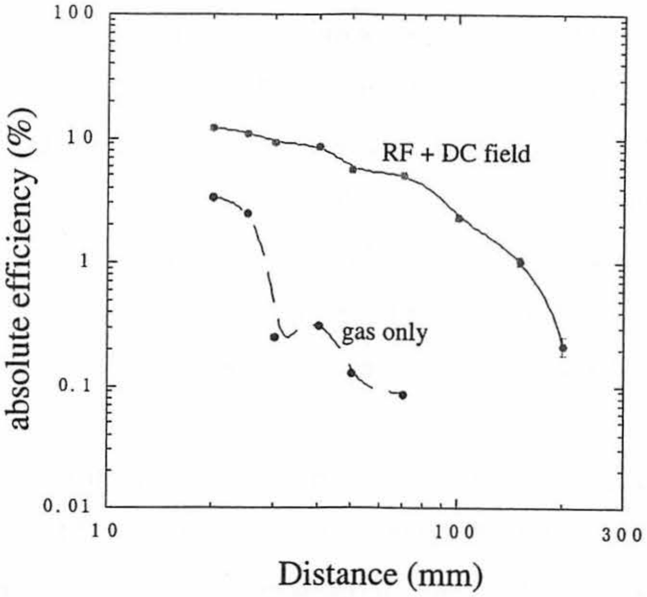

Fig. 3. Absolute efficiency for $^{219}$Rn recoils as a function of exit hole-source distance.

# I. 6. Developments of a High-speed Target Transfer System for the Short-lived Nuclei

*Suzuki T.*[*,**], *Miyake T.*[*], *Fujita M.*[*], *Endo T.*[*], *Sonoda T.*[*], *Goto A., Miyashita Y.*
*Tanaka E.*[*], *Takahashi Y.*[**] *and Shinozuka T.*[*]

*Cyclotron and Radioisotope Center, Tohoku University*[*]
*Department of Physics, Yamagata University, Yamagata, Japan, 990-8560*[**]

Precise measurements for the *ft* value of $0^+ \rightarrow 0^+$ superallowed Fermi beta decays are effective tools for testing the electro weak standard model. This value has been determined in good precision less than 1% at the region of lighter nuclei (e.g. $^{10}\mathrm{C}$, $^{38m}\mathrm{K}$, $^{50}\mathrm{Mn}$, $^{54}\mathrm{Co}$)[1]. The *ft* value provides the vector coupling constant $G_V$, which is linked to $V_{ud}$ up-down element of the Cabbibo-Kobayashi-Maskawa (CKM) matrix[2,3]. In combination with $V_{us}$ and $V_{ub}$, $V_{ud}$ gives the check of the unitarity of CKM matrix. However, in the $A \geq 62$ region, only few measurements were exist, ie. Chiba *et. al.*[4], because of the experimental difficulties, the small cross section and short half-lives. In this region, the precise measurements of *ft* values are desired in order to evaluate the radiative corrections for nuclear parts at the beta decay, ie. the isospin symmetry braking correction. Recently, the *ft* value of $^{74}\mathrm{Rb}$ was measured at ISOLDE[5] and TRIUMF[6]. But it is not enough data to discuss these corrections at the measurements of precise Q-beta values and precise branching ratios including the non-analog $0^+$-$0^+$ transitions[7,8].

The ISOL (Isotope Separator On-Line) is one of the most elaborate technique to select an isotope with a high purity, but this technique does not suit the measurement which needs high statistics because of low efficiency. The target transport methods with high efficiency has been utilized as one of the complementary ways. In the past work at CYRIC target rotation system[9] was used to measure the half life of $^{57}\mathrm{Cu}$, but the target rotation time was not short enough in comparison with the half life of the target nucleus. In order to achieve high statistics a new target transfer system faster than TARO. In the present system, a target mounted on cart has been linearly transported to a detector position at low background area, which is 37cm from beam position. Fig. 1. shows a new system.

The design goal is set for 50msec transfer time, which is shorter than the half-life of $^{74}$Rb.

In this system, a necessary torque is 7.1N·m. To satisfy this condition, Mitsubishi HC-KFS73 servomotor (750W), which has a performance of 2.4N·m effective torque, 7.2N·m maximum instantaneous torque and effective speed 3000rpm is chosen. The target cart is moved in the vacuum chamber, and the 0.2mm thickness milar window is placed at the detector position. The operation is totally controlled by computer using YOKOGAWA FA-03 PLC modules. The position resolution for step and move is less than 3mm by 3-bit laser sensor. The time-sequence of measurement (i) An irradiation during for about 3 half-lives of a target nuclei by the cyclotron beam. (ii) The beam is switched off and irradiated target is transported to detector position about 50msec. (iii) The radiation measurement during about 10 half-lives. (iv) The target is back to the beam position with a lower speed.

The test experiment using this new system has been done for the beta decay of $^{62}$Ga produced $^{64}$Ga(p,3n) reaction. A 19.5mg/cm$^2$-thick natural zinc target is bombarded by 110nA, 45MeV protons from 930 Cyclotron at CYRIC. After beam irradiation, the target was transported to detector position by 51msec. The irradiation time was 400msec and measurement time was 1200msec. The emitted beta particles have been detected by a counter-tellescope which consisted of 2mm-thick NE102A and 5cm-thick BC408 plastic scintillators. For gamma rays measurement, HP-Ge detector was placed opposite sides of the beta counters (Fig. 2). The measured half-life is 110.1±17.6msec and is consistent with old data[10,11].

Measurements for heavier nuclei having $0^+$-$0^+$ superallowed Fermi decays $^{70}$Br and soon $^{66}$As are progressing on.

## References

1) Hardy J.C. and Towner I.S., Hyperfine Interactions **132** (2001) 115.
2) Cabbibo N., Phys. Rev. **104** (1956) 895.
3) Kobayashi M. and Maskawa T., Prog. Theor. Phys. **49** (1973) 652.
4) Chiba R. et. al., Phys. Rev. **C17** (1978) 2219.
5) Oinonen M. et. al., Phys. Lett. **B511** (2001) 145.
6) Ball G.C., et. al. Phys. Rev. Lett. **86** (2001) 1454.
7) Zganjar E.F. et. al., Eur. Phys. J. **A15** (2002) 229.
8) Blank B., Eur. Phys. J. **A15** (2002) 121.
9) Miyatake H. et. al., Nucl. Instrum. Methods Phys Res. A **245** (1986) 271.
10) Daves C.N., et. al., Phys Rev. **C19** (1979) 1463.
11) Alburger D.E., et. al., Phys Rev. **C18** (1978) 1875

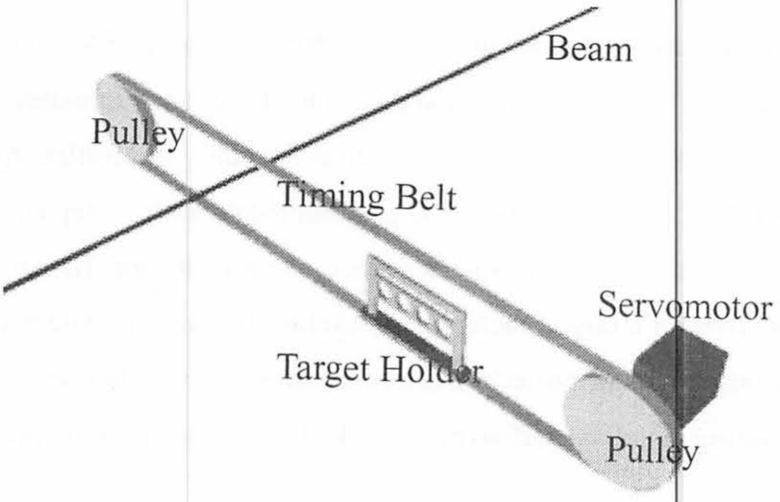

Fig. 1. The schematic of new target transfer system.

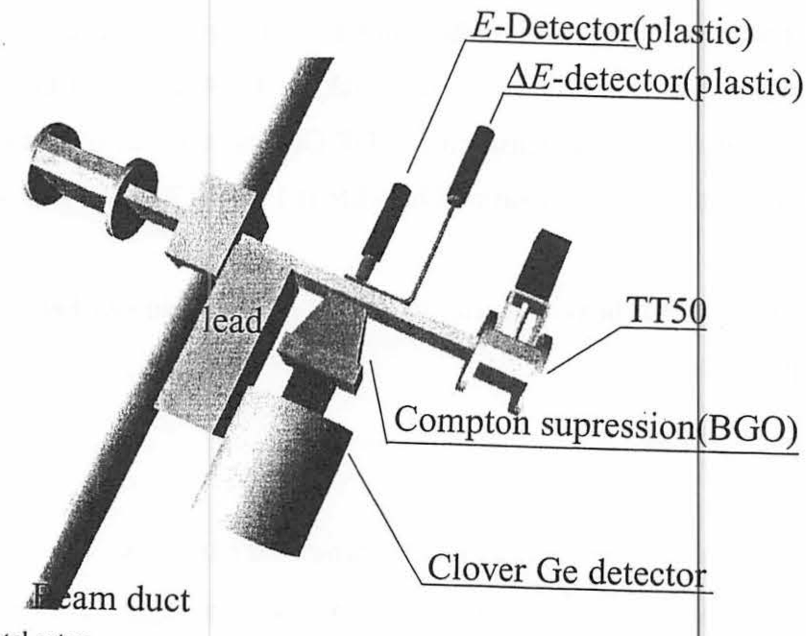

Fig. 2. Experimental setup.

# I. 7. Effect of He Pre-implantation and Neutron Irradiation on Mechanical Properties of SiC/SiC Composite

*Hasegawa A., Nogami S., Snead L.L.*[*]*, Jones R.H.*[**]*, and Abe K.*

*Department of Quantum Science and Energy Engineering, Tohoku University*
*Oak Ridge National Laboratory, Oak Ridge, TN 37831 6138, USA*[*]
*Pacific Northwest National Laboratory, Richland, WA 99352, USA*[**]

## Introduction

Silicon carbide (SiC) fiber-reinforced SiC-matrix composites (SiC/SiC composites) are being considered as a structural material for a fusion reactor blanket component1,2). Displacement damage and transmutation products such as helium (He) will be produced in these materials during high energy (about 14 MeV) neutron irradiation. The displacement damage and He concentration in the SiC component of ARIES-AT were calculated to be approximately 57 dpa and 15380 at.ppm in a full power year, respectively2). The He concentration per dpa in SiC will be about ten times larger than that in other candidate materials (ferritic steels and vanadium alloys).

There has been relatively abundant study of the displacement damage effect on the mechanical properties of SiC/SiC composites. Advanced SiC/SiC composites developed in recent years using stoichiometric and high crystalline SiC-fibers such as Hi-Nicalon Type-S3) and Tyranno SA4) have exhibited improved radiation resistance up to about 7.7 x $10^{25}$ n/m2,5). While, the study of the transmutant He effect on the mechanical properties SiC/SiC composites has not been limited6-8). For the case of study using bend test, the ultimate fracture strength of Nicalon CG/C/SiC composite (C: carbon6) and Hi-Nicalon/C/SiC composite7)) decreased after He-implantation up to 2500 at.ppm at 900°C and up to 150-170 at.ppm at 400-800°C, respectively. For the case of study using nano-indentation test, the decreased hardness and elastic modulus of the SiC-matrix, Hi-Nicalon fiber and Hi-Nicalon Type-S fiber were observed after He-implantation up to 20000 at.ppm below 100°C8). However, effect of He, effect of displacement damage and their synergistic effect on the mechanical property changes of SiC/SiC composites were not clearly distinguished in all cases.

The purpose of this study is to investigate the effect of He pre-implantation followed by neutron irradiation on the mechanical properties of SiC/SiC composite. The bend properties of SiC/SiC composite, the hardness and elastic modulus of the SiC-matrix and SiC-fiber in the composite after He pre-implantation and neutron irradiation were investigated.

## Experimental

SiC/SiC composite with Hi-Nicalon fibers (0°/90° plain-weave) manufactured by DuPont Lanxide (now Honeywell Advanced Composites)[9] was examined in this study. SiC-matrix (crystalline β-SiC) was fabricated by an ICVI (isothermal chemical vapor infiltration) process. The interface material between SiC-fibers and SiC-matrix was a pyrolytic carbon (approximately 150 nm thickness), which was fabricated by a CVD (chemical vapor deposition) process. Hi-Nicalon is composed of β-SiC grains whose size is about 5-10 nm and substantial residual oxygen (<0.5 wt.%) and carbon (C/Si atomic ratio ~ 1.39)[3]. The geometry of specimens for irradiation and bend tests was approximately $4^w$ x $1^t$ x $20^l$ mm$^3$, which was machined from specimens with the geometry of $6^w$ x $2^t$ x $20^l$ mm$^3$. Compression side in bend test was machined to 1 mm thickness, while tension side was not machined. Therefore CVI β-SiC is remained in the tension side. Figure 1 shows the schematic illustration of the specimen configurations in this study.Helium pre-implantation test followed by neutron irradiation test was performed using the cyclotron accelerator at Tohoku University. The acceleration energy of He-ions was 36 MeV. The projected range of 36 MeV He-ions in SiC was calculated to be about 470 μm by TRIM code[10]. Tandem type energy degrader wheels were used to obtain uniform depth distribution of He-atoms. The nominal He concentration was about 170 at.ppm. The displacement damage in the He implanted region was calculated to be about 0.009 dpa using threshold displacement energy of 45 eV. The implantation temperature was 400-800°C, which was measured by an infrared pyrometer. He-ions were implanted to the tension side in the bend test. He-implanted area was about $4^w$ x $4^l$ mm$^2$ at the center of the specimens as shown in Fig. 1. After the implantation, these specimens were shipped to Oak Ridge National Laboratory(ORNL) to irradiate neutron.

Neutron irradiation was performed in the HFIR (High Flux Isotope Reactor) at ORNL. Specimens were irradiated at 800°C up to about $7.7 \times 10^{25}$ n/m$^2$ ($E_n > 0.1$ MeV), which is corresponds to about 7.7 dpa using an assumption that 1 x $10^{25}$ n/m$^2$ ($E_n$ > 0.1 MeV) corresponds to about 1 dpa. Thermocouples embedded in specimen holders were used to monitor irradiation temperature.

Three points bend test was performed at room temperature in air. Support span length and cross head speed were 10 mm and 0.5 mm/min, respectively. Bend tests #1-1 and #1-2 in Fig.1 are for the measurement of non-He-implanted and neutron-irradiated region. While bend test #2 in in Fig.1 is for the measurement of He-implanted and neutron-irradiated region. Fractography observation was performed by a scanning electron microscope (SEM) after the bend test.

Cross-sectional nano-indentation test was performed by using NANO INDENTER® II (Nano-instruments). This machine is equipped with a Berkovich diamond tip. Indentation depth and loading (unloading) rate were constant, 50 nm and 50 mN/s, respectively. Specimens were mechanically sliced perpendicular to the He-implanted surface as shown in Fig.1. The cross-section of the cut specimens for indentation was mechanically polished by fine diamond slurry. These post irradiation experiments were carried out in hot laboratories of ORNL.

## Results

Figure 2 shows the typical stress-strain curves of the bend tests for non-He-implanted and non-neutron-irradiated (Non-He / Non-irr) composite, non-He-implanted and neutron-irradiated (Non-He / Neutron) composite and He-implanted and neutron-irradiated (He / Neutron) composite. Figure 3 shows the summary of the bend test results for the "Non-He / Non-irr" composite, "Non-He / Neutron" composite and "He / Neutron" composite, which gives ultimate fracture strength, elastic modulus and proportional limit stress (PLS). The elastic modulus was calculated using the slope of the linear range of the stress-strain curves. It is noted that, since calculated strain in this study is affected by elastic deformation of the bend machine during testing, the elastic modulus of the specimens is not quantitative but qualitative in nature. The proportional limit stress was the value when offset strain was about 0.0005. The number of the bend test for the "Non-He / Non-irr" composite, the "Non-He / Neutron" composite and "He / Neutron" composite were 6, 4 and 2, respectively. The ultimate fracture strength, elastic modulus and proportional limit stress decreased due to neutron irradiation by about 50%, 10% and 55%, respectively. Effect of He pre-implantation followed by neutron irradiation on the bend properties was almost negligible.

Figure 4 shows the typical observation of fracture surface by SEM for the "Non-He / Non-irr" composite, "Non-He / Neutron" composite and "He / Neutron" composite. He-ions were implanted from the lower side of the pictures. Pull-out length of Hi-Nicalon fibers for "Non-He / Neutron" composite was longer than that for the "Non-He / Non-irr" composite. Almost no difference of the pull-out length of Hi-Nicalon fibers was observed between "Non-He / Neutron" composite and "He / Neutron" composite.

Figure 5 and Figure 6 show the hardness and elastic modulus of the SiC-matrix and Hi-Nicalon fiber of the "Non-He / Non-irr" composite, "Non-He / Neutron" composite and "He / Neutron" composite. The number of the indentation for the SiC-matrix and Hi-Nicalon fiber was 37-41 and 13-27 for each irradiation condition, respectively. The hardness and elastic modulus for non-He-implanted and neutron-irradiated region and He-implanted and neutron-irradiated region were the average value of the data points at the depth of 0-470 μm and 470-1000 μm from the He-implanted surface, respectively. The error bars denote the plus or minus of one standard deviation calculated from the data points. The hardness showed about 30% increase by neutron irradiation for both SiC-matrix and Hi-Nicalon fiber. While, almost no change of the elastic modulus for SiC-matrix and about 30% increase for Hi-Nicalon fiber by neutron irradiation were observed. Effect of He pre-implantation followed by neutron irradiation on the hardness and elastic modulus was almost negligible for both SiC-matrix and Hi-Nicalon fiber.

## Summary

Mechanical property changes of SiC/SiC composite, its matrix and fiber (Hi-Nicalon) due to He pre-implantation up to about 170 at.ppm at 400-800°C and neutron irradiation up to about 7.7 x $10^{25}$ n/m$^2$ ($E_n > 0.1$ MeV) at 800°C in HFIR were investigated by the bend test and nano-indentation. The following results were obtained;

(1) The ultimate fracture strength, elastic modulus and proportional limit stress decreased due to neutron irradiation by about 50%, 10% and 55%. Effect of He pre-implantation followed by neutron irradiation on the bend properties was almost negligible.

(2) Pull-out length of Hi-Nicalon fibers for non-He-implanted and neutron-irradiated composite was longer than that for non-He-implanted and non-neutron-irradiated composite. Almost no difference of the pull-out length of Hi-Nicalon fibers was observed between non-He-implanted and neutron-irradiated composite and He-

implanted and neutron-irradiated composite.

(3) The hardness showed about 30% increase by neutron irradiation for both SiC-matrix and Hi-Nicalon fiber. Effect of He pre-implantation followed by neutron irradiation on the hardness was almost negligible for both SiC-matrix and Hi-Nicalon fiber.

(4) Almost no change of the elastic modulus for SiC-matrix and about 30% increase for Hi-Nicalon fiber by neutron irradiation was observed. Effect of He pre-implantation followed by neutron irradiation on the elastic modulus was almost negligible for both SiC-matrix and Hi-Nicalon fiber.

## Acknowledgements

The authors are grateful to the staffs in the CYRIC of Tohoku University relating to the He implantation test and to the staffs in Oak Ridge National Laboratory relating to the irradiation test and post-irradiation experiments. This work was supported by the JUPITER (Japan-USA Program of Irradiation Testing for Fusion Research) and JUPITER-II program.

### References

1) Ueda S., Nishio S., Seki Y., Kurihara R., Adachi J., Yamazaki S. and DREAM Design Team, J. Nucl. Mater. **258-263** (1998) 1589.
2) El-Guebaly L.A., Fus. Eng. Des. **28** (1995) 658.
3) Takeda M., Urano A., Sakamoto J. and Imai Y., J. Nucl. Mater. **258-263** (1998) 1594.
4) Ishikawa T., Kohtoku Y., Kumagawa K., Yamaura T. and Nagasawa T., Nature **391** (1998) 773.
5) Hinoki T., Snead L.L., Katoh Y., Hasegawa A., Nozawa T. and Kohyama A., J. Nucl. Mater. **307-311** (2002) 1157.
6) Frias Rebelo A.J., Scholz H.W., Kolbe H., Tartaglia G.P. and Fenici P., J. Nucl. Mater. **258** (1998) 1582.
7) Hasegawa A., Saito M., Abe K. and Jones R.H., J. Nucl. Mater. **253** (1998) 31.
8) Nogami S., Miwa S., Hasegawa A. and Abe K., to be published in Effects of Radiation on Materials, ASTM STP 1447.
9) Youngblood G.E., Henager C.H. Jr. and Jones R.H., DOE/ER-0313/20 (1996)140.
10) Ziegler J.F., Biersack J.P. and Littmark U., The Stopping and Ranges of Ions in Mater. Vol. 1, Pergamon, New York, 1985.

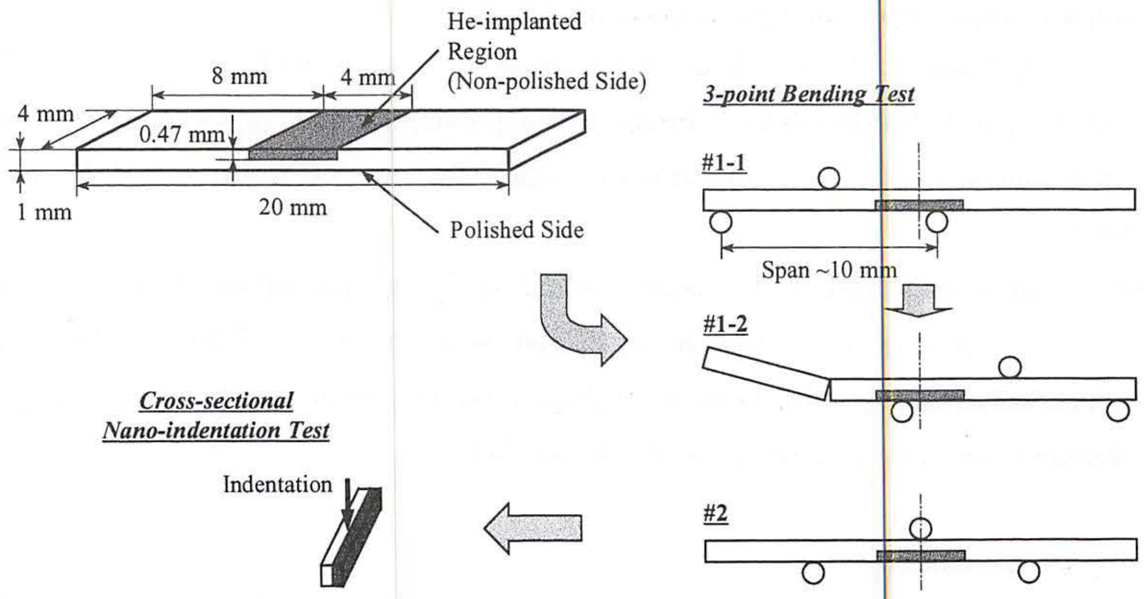

Fig. 1. The schematic illustration of the specimen configurations in this study.

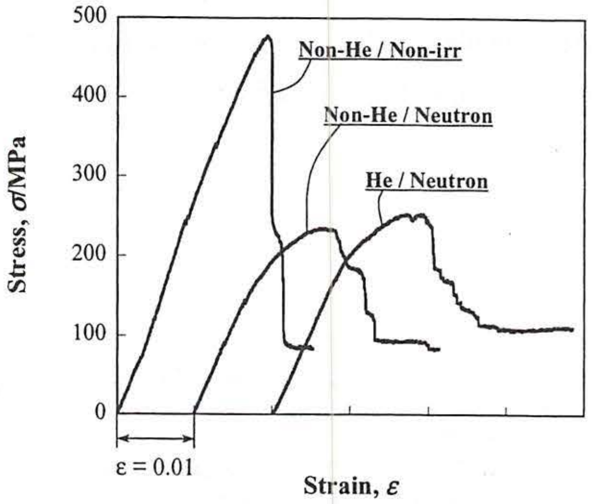

Fig. 2. The typical stress-strain curves of the bend tests for non-He-implanted and non-neutron-irradiated (Non-He / Non-irr) composite, non-He-implanted and neutron-irradiated (Non-He / Neutron) composite and He-implanted and neutron-irradiated (He / Neutron) composite

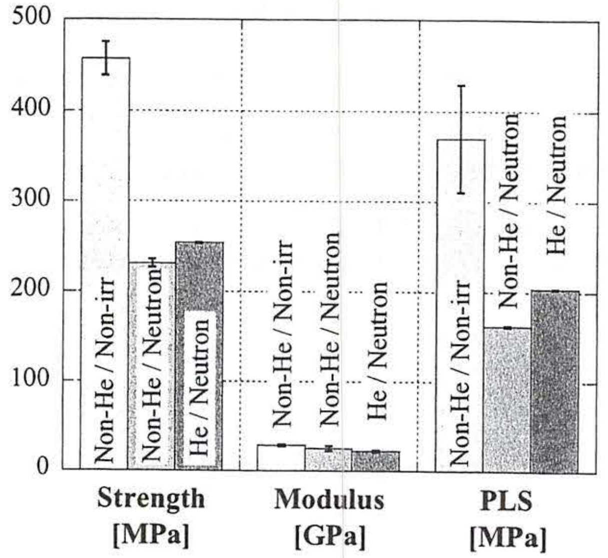

Fig. 3. The ultimate fracture strength, elastic modulus and proportional limit stress (PLS, offset strain ~ 0.0005) in the three-points bend test for non-He-implanted and non-neutron-irradiated (Non-He / Non-irr) composite, non-He-implanted and neutron-irradiated (Non-He / Neutron) composite and He-implanted and neutron-irradiated (He / Neutron) composite.

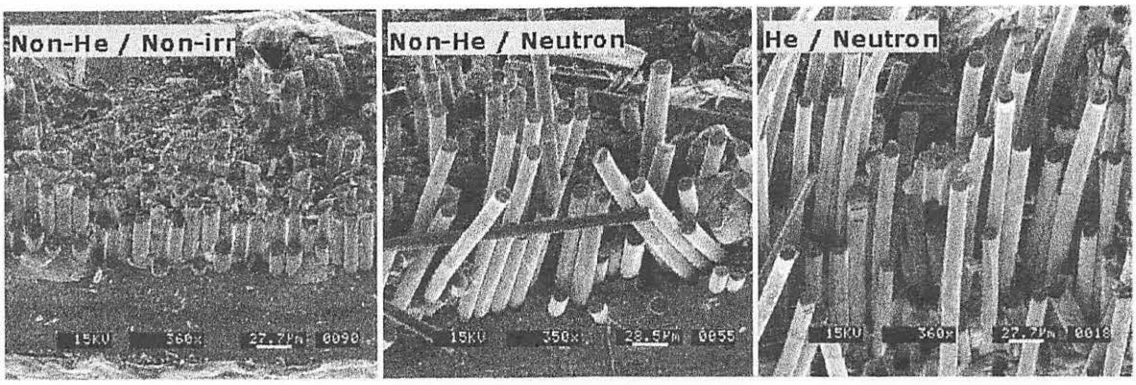

Fig. 4. The typical observations of fracture surface by SEM for non-He-implanted and non-neutron-irradiated (Non-He / Non-irr) composite, non-He-implanted and neutron-irradiated (Non-He / Neutron) composite and He-implanted and neutron-irradiated (He / Neutron) composite. He-ions were implanted from the lower side of the pictures

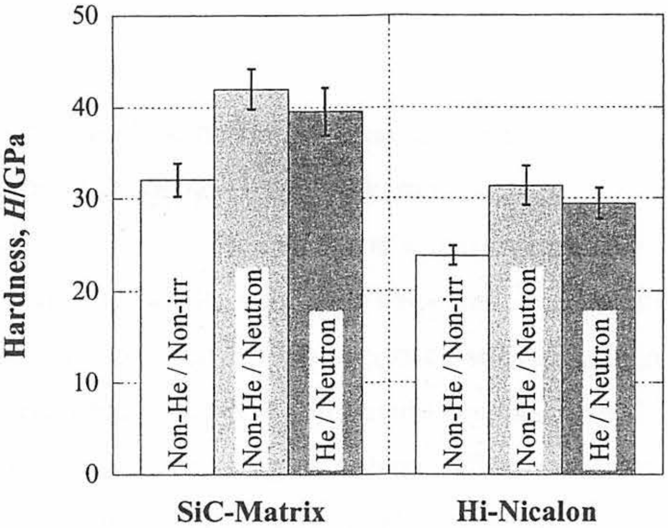

Fig. 5 The hardness of the SiC-matrix and Hi-Nicalon fiber of non-He-implanted and non-neutron-irradiated (Non-He / Non-irr) composite, non-He-implanted and neutron-irradiated (Non-He / Neutron) composite and He-implanted and neutron-irradiated (He / Neutron) composite.

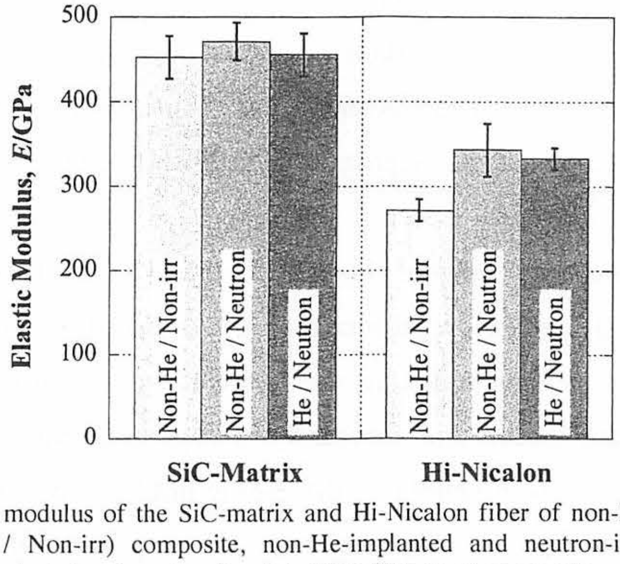

Fig. 6. The elastic modulus of the SiC-matrix and Hi-Nicalon fiber of non-He-implanted and non-neutron-irradiated (Non-He / Non-irr) composite, non-He-implanted and neutron-irradiated (Non-He / Neutron) composite and He-implanted and neutron-irradiated (He / Neutron) composite.

# I. 8. Evaluation of Ductile-brittle Transition Behavior of Helium-Implanted Reduced Activation Martensitic Steel F82H by Miniature Charpy Specimens

*Hasegawa A., Wakabayashi E., Tanaka K., Abe K., and Jitsukawa S.**

*Department of Quantum Science and Energy Engineering, Tohoku University*
*Japan Atomic Energy Research Institute, Tokai Lab., Shirakata-shirane, Tokai, Japan**

## Introduction

Helium induced embrittlement is one of the critical issues of fusion structural materials in which several thousands at.ppm of helium is estimated to be generated during reactor operation. It is well known that a small amount of helium enhances irradiation embrittlement of austenitic steels[1-3] and some vanadium alloys[4,5] in the tests at relatively high temperatures accompanied by the change in the fracture mode from transgranular to intergarnular cracking. Microstructural observations revealed that many bubbles, which were considered to be helium bubbles, existed at grain boundaries, indicating that the helium atoms in the matrix of these materials diffused to form bubbles at grain boundaries during irradiation and/or testing at a high temperature. In contrast, it was reported that the martensitic steels were highly resistant to helium bubble-induced grain boundary embrittlement[6-8] at high temperatures. High resistance to the bubble formation in the martensitic steels is considered to be attributed to trapping of helium atoms and point defects in the martensitic structure or dislocations, lath boundaries and carbides in high density which prevent helium atoms segregating to form helium bubbles at grain boundaries.

Ductile-brittle transition behavior is characteristic to martensitic steels, and irradiation hardening usually results in an increase in the transition temperature. It is expected that the trapped helium atoms in the martensitic structure would enhance irradiation hardening of the matrix and resultantly transgranular embrittlement at low temperatures. As for the effects of helium on the ductile-brittle transition behavior of the martensitic steels, there have been done several studies relating to the effects of so called transmutation helium. Isotope tailoring experiments on helium effects utilizing nuclear transmutation helium from nickel^9-12) and boron^13) showed that the increase in the composition of nickel or boron caused severer irradiation embrittlement in the martensitic steels, and the enhanced embrittlement, which was usually accompanied by severer irradiation hardening, was attributed to the helium transmuted from nickel or boron. It is, however, not made clear that the transmutation helium in itself really induces low temperature embrittlement, since the addition of boron or nickel results in the change in the martensitic structure or properties of the steel^14).

Helium implantation technique is more effective to evaluate helium effects directly and many investigations have been performed for the martensitic steels. Since the range of the implantation is usually smaller than 0.2 mm, the experiments have been often limited to microstructural observation, hardness measurement and tensile test with thin specimens. We had already reported the He effect of DBTT of martensitic steels JLF-1 using 650 appm He implanted TEM disks by means of small punch test^15). Increase of DBTT caused by irradiation hardening was observed, however, grainboundary embrittlement was not observed. It is well known that charpy impact test is more appropriate to estimate DBTT behavior, but relatively larger specimen volume is needed for charpy impact test. Small specimen test technique have been developed to evaluate mechanical properties of irradiated specimen. Miniature charpy test method is one of example of the small specimen test technique. Specimen size is almost 1/10 of the standard specimen such as ASTM standard or JIS standard. This methods have already been applied to neutron irradiation studies but not been applied to high energy ion-beam irradiation experiments.

In this study, to study the DBTT behavior of reduced activation martensitic steels by means of charpy impact test method, we improved irradiation apparatus of materials irradiation course of CYRIC, and evaluate the effects the DBTT behavior.

## Experimental

Figure 1 shows a overview of 42-beam course for material irradiation in target room 4. Irradiation chamber was installed at the end of this beam line. The chamber is evacuated up to 1 x $10^{-6}$ Torr by a turbo pump. Various type of material irradiation experiments are available. Figure 2 shows a specimen loading system which has four different stage positions. Two specimen holders are installed in this picture. Upper position is for room temperature irradiation, lower position is for high temperature irradiation up to 600°C. Water cooling system is installed at upper two positions and heating system using a sheath heater are available at all positions. Specimen temperature is monitored using thermocouples and an infrared pyrometer. A tandem type energy degrader system are also installed in this irradiation chamber. This system consists two rotating wheels. The first wheel consists of 5 different thickness of aluminum foils, and the second wheel consists of 105 different thickness of aluminum foils. Therefore total 525 different thickness aluminum foils across the incident beam line. Figure 3 shows drawings of a rotating wheel, and Fig. 4 shows a schematic illustration of a tandem type energy degrader system. Using this energy degrader system, irradiated ions can be implanted almost homogeneously from the irradiated surface to its projected range.

In order to evaluate DBTT behavior, a small charpy specimen were used. The size and shape, and its notch configuration are shown in Fig. 5 and Fig. 6, respectively. F82H, a 8Cr-2W base martensitic steels, was used as sample. It is reference material of RAM in IEA research activities for fusion rector materials. An ingot of IEA heat F82H heat-treated by standard procedures were supplied from JAERI. Charpy specimens were fabricated from this ingot. Nine charpy specimens were loaded in a specimen holder at once. Thermocouples were welded on the specimen.

Alpha particles beam accelerated to 50 MeV was used for He implantation. The projected range of this ion beam in Iron was about 380 $\mu$m. Implanted He concentration of the specimen was about 50 appm and the displacement damage was about 0.04 dpa after 10 h irradiation. In order to obtain higher implanted He concentration during a limited irradiation time, the ion beam was scanned horizontally only the periphery of center V notch area of the specimens. Irradiation temperature of the irradiated specimen area were below 90°C in the room temperature irradiation, and 500°C in the high temperature irradiation. The specimen temperature control system, temperature monitoring system, specimen loading system and energy degrader system were controlled by a computer through internet using PLC system.

After the irradiation, these specimens were moved to RI laboratory of Faculty of Engineering of Tohoku University to measure hardness using a Vickers hardness tester, and then these were shipped to hot laboratory of Oarai branch of IMR, Tohoku University to carry out impact test. The instrumented charpy impact test were conducted in a hot cell of Oarai laboratory at temperature between -140°C and -100°C. After the charpy impact test, these specimens were shipped to Alpha-emitter laboratory of IMR (Sendai), and fracture surface observation was conducted using a scanning electron microscope.

## Results

Figure 7 shows result of hardness before and after irradiation. Hardness increased after room temperature irradiation. The hardness of implanted specimen almost recovered after heat treatment at 550℃ for 1hour. The hardening was also observed clearly in the specimen which were irradiated at 500℃.

Typical examples of load / displacement curves obtained by the charpy impact test at various test temperature is shown in Fig. 8-(a). The area below each load/displacement curve corresponds to the absorbed energy to rupture at each test temperature. Figure 8-(b) summarizes test temperature dependence of absorbed energy of unimplanted specimen. Fracture mode transient from ductile mode to brittle mode are clearly observed in this figure. In Fig. 8-(b) ductile brittle transient temperature(DBTT) is about -125°C. Below -140°C, specimen ruptured brittle. The typical fracture surface of the specimen is shown in Fig. 9. The rupture mode was cleavage. The temperature above -100°C, specimen ruptured ductile. The dimple pattern was observed on fracture surface. Figure 11 shows the typical ductile fracture pattern of specimen. Between -140°C and -100°C is transient temperature region. Specimen tested and ruptured at this temperature region shows mix fracture mode. Figure 10 shows typical fracture surface tested at the transient temperature

Figure 12 is a summary of DBTT curves of He implanted/unimplanted specimens. DBTT increased about 10°C after the He implantation at 30°C. In the case of higher temperature irradiation, temperature range of transient mode increased but brittle mode area still remains at lower temperature. The detail analysis using fracture analysis is in progress. Considering about the temperature shift and data dispersion, implantation up to higher concentration of He (more than 1000 appm) is needed to clarify the He effects on fracture mode change of reduced activation martensitic steels.

## Summary

(1) Material irradiation chamber was moved and improved for higher temperature irradiation. Energy degrader system and multi-stage specimen loading stage with cooling and heating system controlled by PC were installed. This system can be applied for higher energy and higher current beam irradiation.

(2) Helium implantation to 50 appm at RT and 500°C were conducted. Irradiation

hardening was detected and DBTT shift by He implantation was observed. The effect of He on fracture mode change was not observed.

## Acknowledgements

The authors are grateful to the staffs in the CYRIC of Tohoku University relating to beam transport and irradiation experiments. The authors are also grateful to Mr. T. Takahashi, Mr. K. Komatsu and Mr.T. Nagaya of machine shop of Dept. of Quantum Science and Energy Engineering, Tohoku University for fabrication of specimen loading system and energy degrader.

### References

1) Schroeder H. and Batfalsky P., J. Nucl. Mater. **117** (1983) 287.
2) Trinkaus H., J. Nucl. Mater. **133&134** (1985) 105.
3) Schroeder H., J. Nucl. Mater. **155-157** (1988) 1032.
4) Braski D.N. and Ramey D.W., Effects Radiation on Materials, ASTM STP **870** (1985) 1211.
5) Satou M., Koide H., Hasegawa A., Abe K., Kayano H. and Matsui H., J. Nucl. Mater. **233-237** (1996) 447.
6) Stamm U. and Schroeder H., J. Nucl. Mater. **155-157** (1988) 1059.
7) Moslang A. and Preininger D., J. Nucl. Mater. **155-157** (1988) 1064.
8) Moslang A. and Preininger D., J. Nucl. Mater. **191-194** (1992) 910.
9) Klueh R.L. and Vitek J.M., J. Nucl. Mater. **150** (1987) 272.
10) Klueh R.L. and Vitek J.M., J. Nucl. Mater. **161** (1989) 13.
11) Klueh R.L. and Alexander D.J., J. Nucl. Mater. **179-181** (1991)733.
12) Klueh R.L. and Maziasz P.J., J. Nucl. Mater. **187** (1992) 43.
13) Lindau R., Moslang A., Preininger D., Rieth M. and Rohrig H.D., J. Nucl. Mater. **271-272** (1999) 450.
14) Heinisch H. L., J. Nucl. Mater. **155-157** (1988) 121.
15) Kimura A., Morimura T., Kasada R., Matsui H., Hasegawa A. and Abe K., *Effects of Radiation on Materials, $19^{th}$ International Symposium, ASTM STP 1366*, M.L. Hamilton, A.S. Kumar, S.T. Rosinski and M.L. Grossbeck, Eds., American Society for Testing and Materials, 1999.

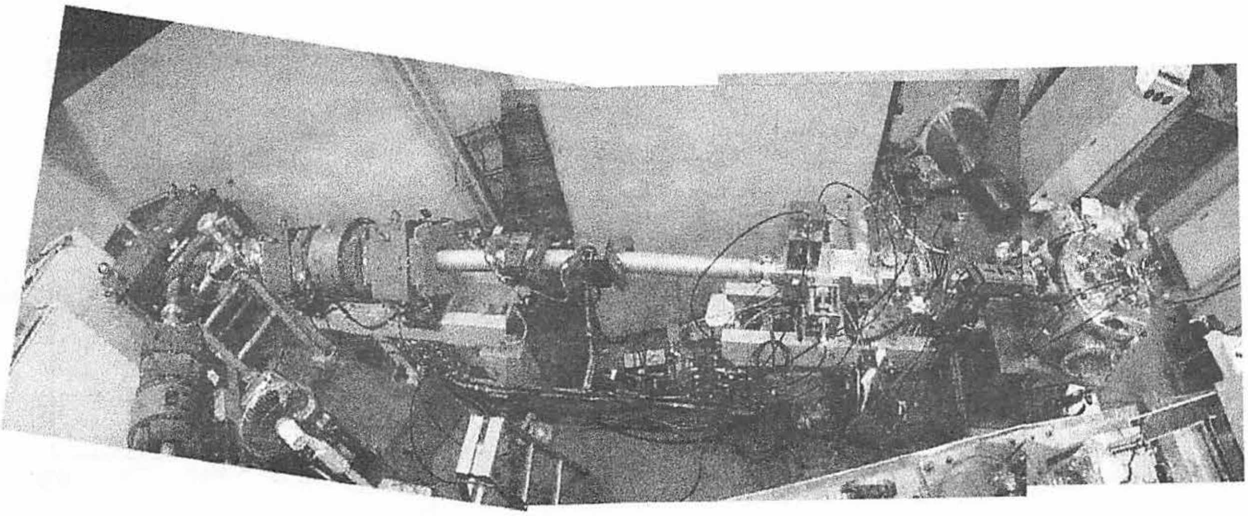

Fig. 1. Overview of Irradiation chamber of 42 beam course.

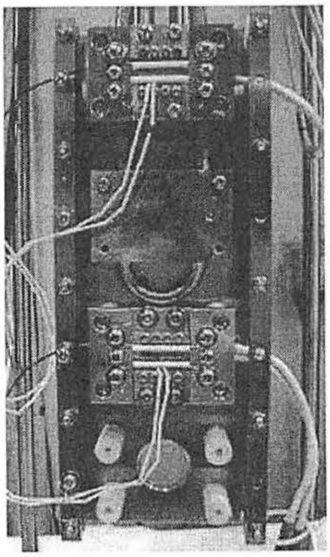

Fig. 2. Specimen loading system.

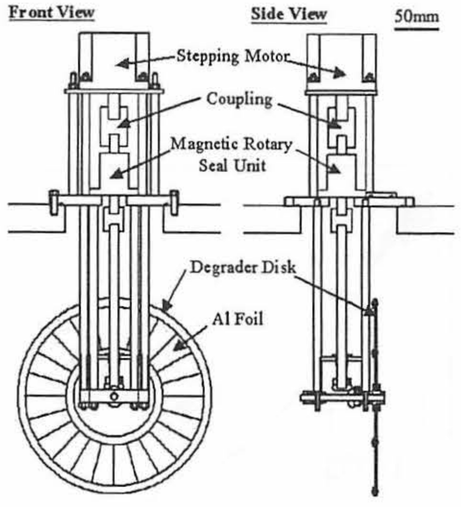

Fig. 3. Energy degrader.

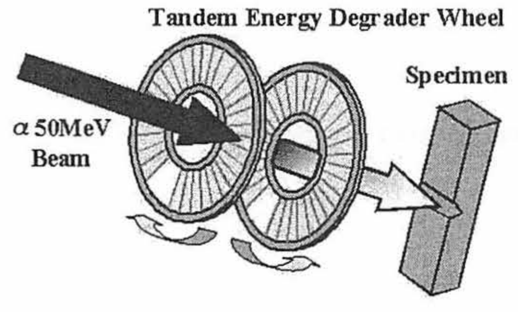

Fig. 4. Schematic view of a tandem degrader system.

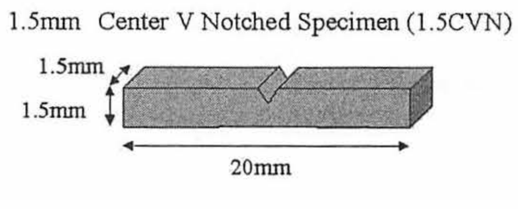

Fig. 5. Specimen size.

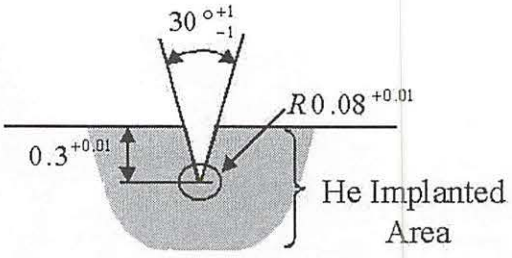

Fig. 6. Detail of V notch of the specimens.

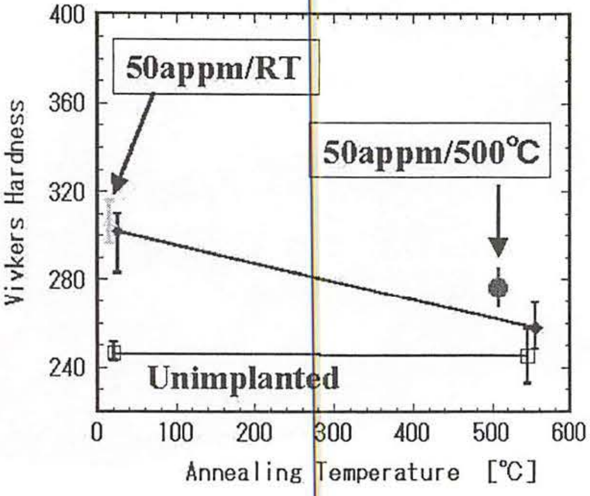

Fig. 7. Hardness of He implanted specimen.

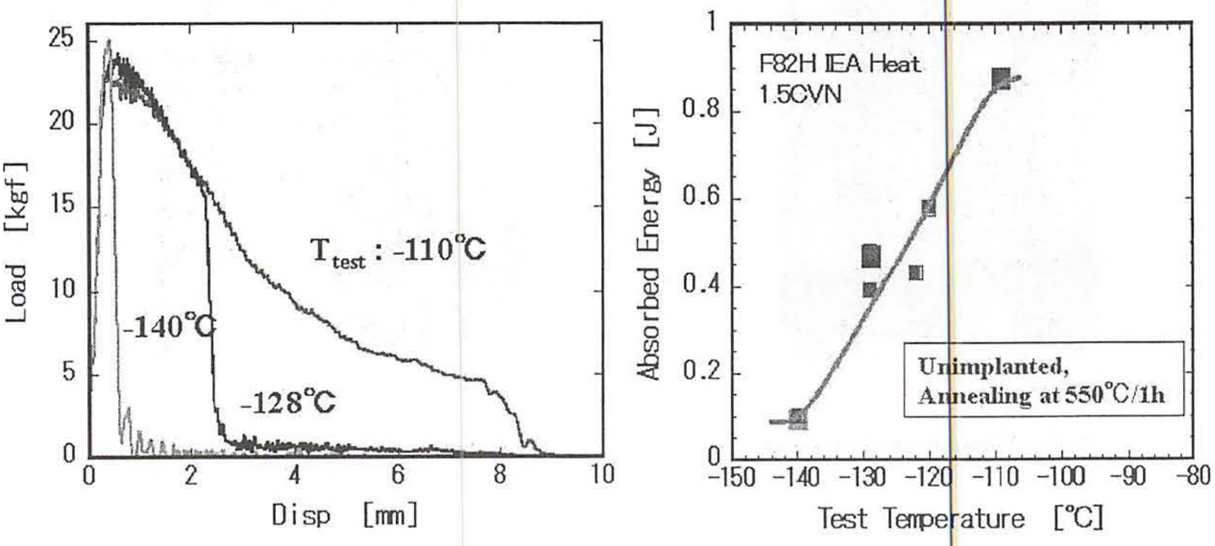

(a)

(b)

Fig. 8. Load / Displacement curves by charpy test and absorbed energy / Test temperature curve of unimplanted sample.

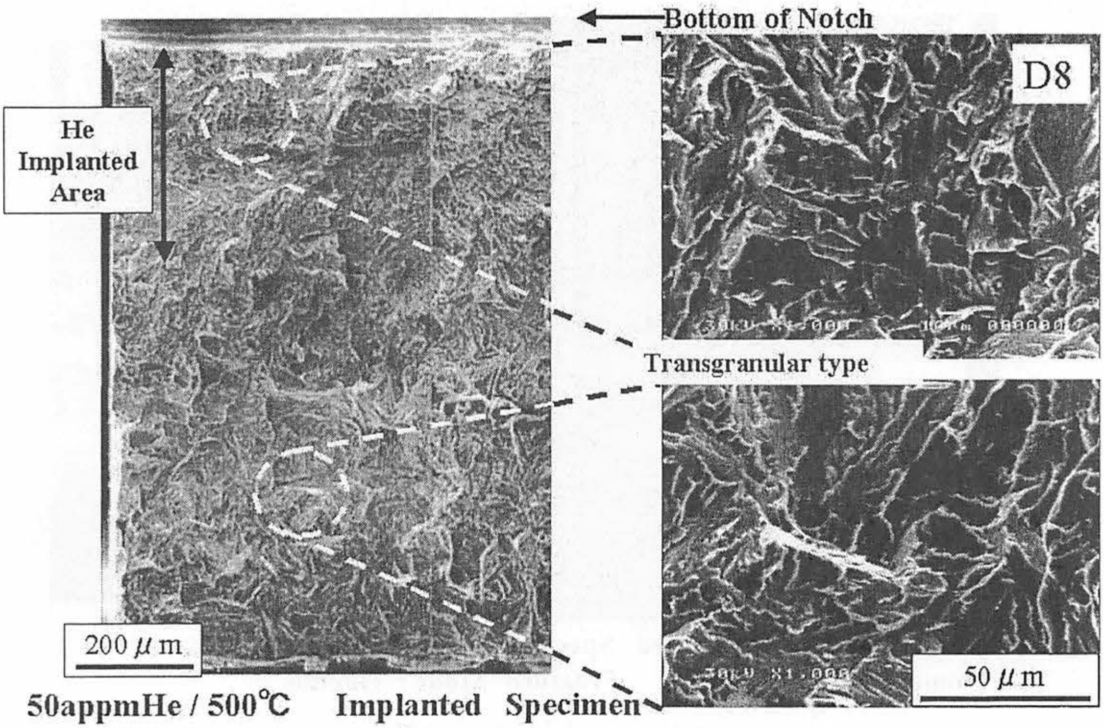

50appmHe / 500℃ Implanted Specimen
Test temperature : -120℃ Fracture Mode : Brittle

Fig. 9. Surface observation of ruptured 1.5CVN specimen in brittle mode.

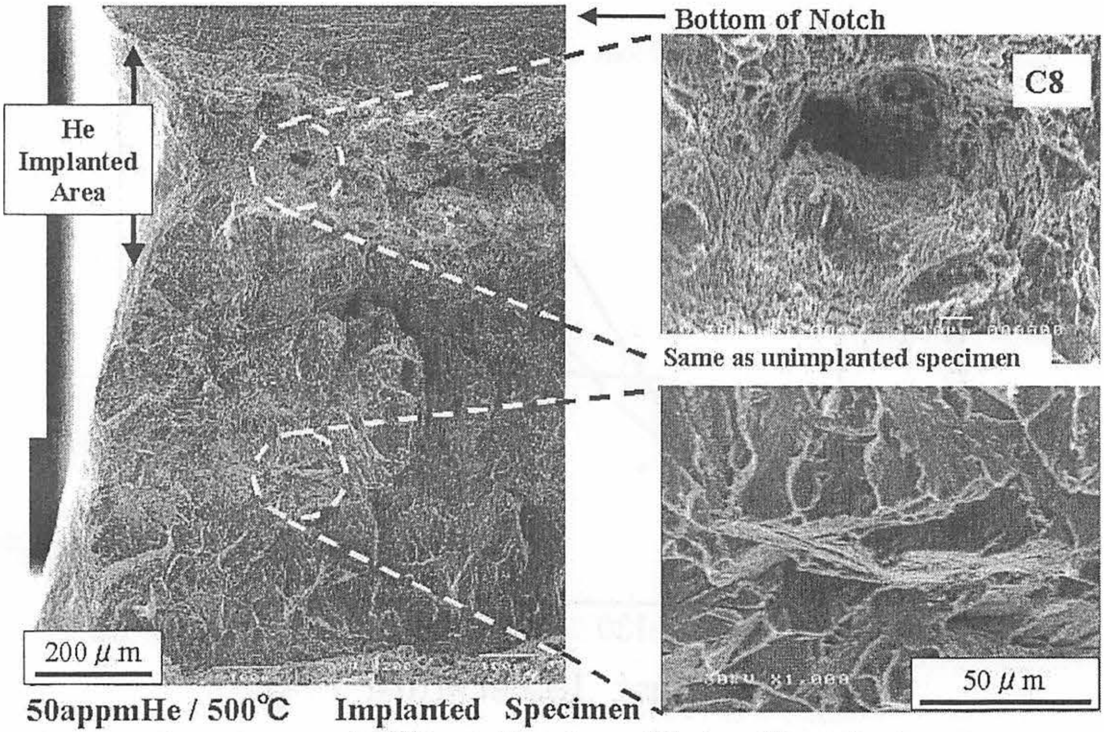

50appmHe / 500℃ Implanted Specimen
Test temperature : -112℃ Fracture Mode : Transient

Fig. 10. Surface observation of ruptured 1.5CVN specimen in transient mode.

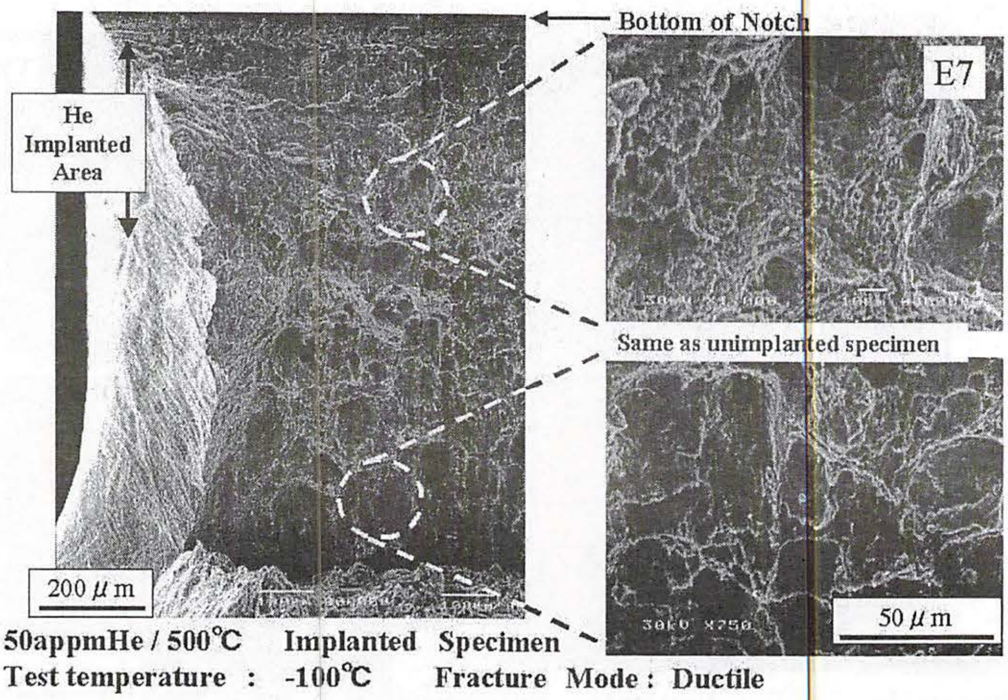

Fig. 11. Surface observation of ruptured 1.5CVN specimen in transient mode.

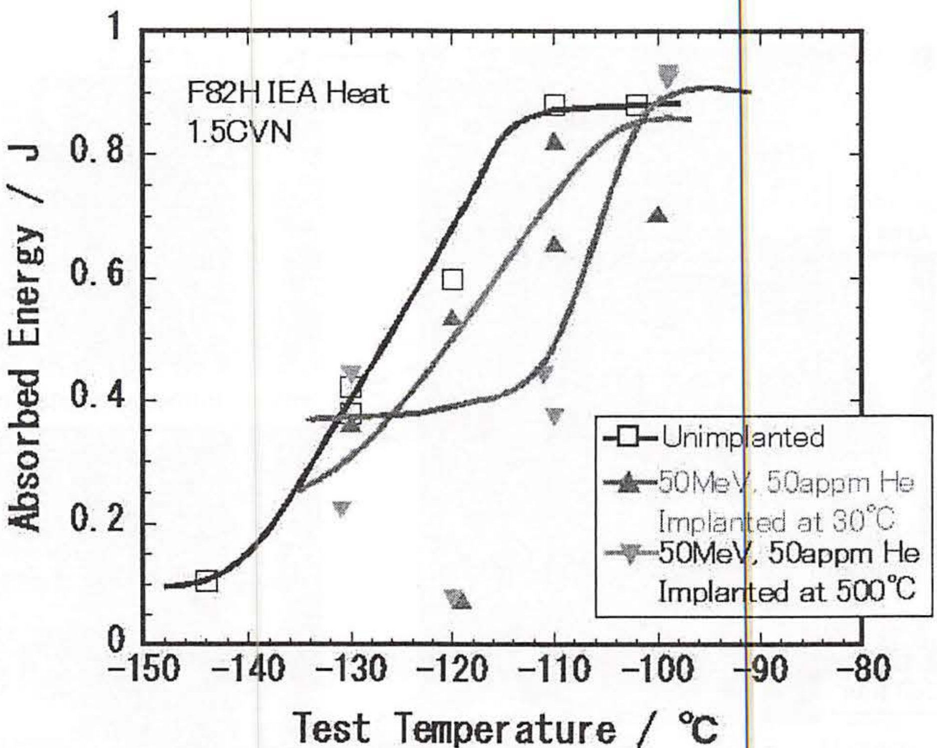

Fig. 12. Absorbed energy / Test temperature curves of He implanted samaple.

# I. 9. Preliminary Results on Estimating the Attenuation Coefficients in PET using the Single Events

*Rodriguez M., Ishii K., Yamazaki H., Matsuyama S., Kikuchi Y., Oishi Y., Suzuki A., Yamaguchi T., Watanuki S.*, and Itoh M.**

*Department of Quantum Science and Energy Engineering, Tohoku University*
*Cyclotron and Radioisotope Center, Tohoku University**

## Introduction

During a Positron Emission Tomography (PET) scan, there are several physical effects arising from the interaction photon-matter. The main two interactions are attenuation and scattering of photons. Their effects on total coincidence counting should be evaluated and corrected, if reliable quantitative results are a goal1). The photon attenuation has several detrimental effects like overall loss of counts, higher image noise, image non-uniformity due to non-uniform photon attenuation. Overall losses of counts in the body due to attenuation can be as high as 85% for a moderately large body, but the loss varies substantially with the body size, resulting in varying noise levels2). Development of attenuation correction techniques is a very active field in PET and, recently, it has been developed a scanner that allows simultaneous acquisition of attenuation images (X-ray CT) and PET. In general, the choices for attenuation correction can be divided in two groups: calculated and measured attenuation correction3). The first one uses an image segmentation technique and assigns a uniform attenuation coefficient to each segment4). The measured attenuation is performed by scanning the patient with an external radiation source (transmission scan), thus the total attenuation for each coincidence line (LOR) is measured. These methods have advantages and disadvantages. The calculated attenuation is easy to apply and does not require a transmission scan. However, the assumption that the segments have homogeneous attenuation properties, leads to errors in some types of scan. For brain imaging it gives good results, but the skull attenuation properties cannot be completely recovered4). The transmission scan detect attenuation discontinuities, which is desirable for whole body or thorax imaging. However, it introduces statistical errors since transmitted photons must also be measured. This can be improved by high counting but it will imply either larger scanning time or higher activity transmission sources. This research presents the preliminary results on determining the attenuation properties of the imaged object by using the single event rates. Only simulated data were used for this report.

### Description of the method

The conventional PET images are reconstructed from coincidence events originated from electron-positron annihilation. However, if one of the photon forming the coincidence pair is absorbed or scattered out of the gantry, only one photon will be counted, hence producing a single count. Several PET systems can measure the single events for each detector, since they are useful for estimating the accidental coincidence. Moreover, the single events also carry valuable information on the attenuation properties of the imaged object.

It is assumed to have a ring system with M (m=1,…,M) detectors defining L (l=1,…,L) coincidence pairs, as shown in Fig.1. The image is divided into B (b=1,…,B) image elements. Each image element is thought of as having an average attenuation coefficient $\mu_b$. Each radiation detector $m$ counts $S_m^{data}$ single events and each coincidence pair $l$ receives $\rho_l$ coincidence counts, however due to the effect of the dead time ($\tau$) it counts $\gamma_l$ events. Assuming a paralyzable behavior of the dead time, it is known that:

$$\gamma_l = \rho_l \exp(-\rho_l \tau) \qquad (1)$$

It is defined $p_{mb}$ and $c_{lb}$ as the geometrical probability for single and coincidence detection, respectively. $g_{bb'}$ are the elements of the inverted $L \times B$ matrix defined by $c_{lb}$. A simple work on the mathematics involved in the coincidence and single detection models, it is reasonable to say that the mathematical model that allows us to determine the attenuation properties of the imaged object is written as:

$$S_m^{\text{model}} = \sum_{b=1}^{B} \sum_{b'=1}^{B} \sum_{l=1}^{L} p_{mb} A_{mb} g_{bb'} c_{lb'} \rho_l A_l^{-1} \qquad (2)$$

where $A_{mb} = \exp\left( - \sum_{b'=1}^{B} \mu_{b'} r_{mbb'} \right)$ and $A_l = \exp\left( - \sum_{b'=1}^{B} \mu_{b'} r_{lb'} \right)$. It means that the single counting can be modeled by the coincidence events (after dead time correction), attenuation properties of the object and the geometrical characteristics of the imaging system. The determination of attenuation properties can be treated as a least square minimization problem where the figure to be minimized is

$$\sum_{m=1}^{M}\left[\frac{S_m^{data}-S_m^{\text{model}}}{\sigma_m^{data}}\right]^2 \tag{3}$$

The Newton-Raphson method for non-linear systems of equation was tested in a first trial to solve the non-linear system provided by (3). This method needs a function $F_m$ is defined as:

$$F_m=\frac{S_m^{data}-S_m^{\text{model}}}{\sigma_m^{data}} \tag{4}$$

The objective is to minimize $F_m$. It can be achieved setting $F_m=0$. The Taylor expansion series tell us that

$$F_m(\mu+\Delta\mu)=F_m(\mu)+\sum_{b=1}^{B}\frac{\partial F_m}{\partial \mu_b}\Delta\mu_b \tag{5}$$

where

$$\mu_b=\begin{bmatrix}\mu_1\\ \mu_2\\ \cdot\\ \mu_B\end{bmatrix} \tag{6}$$

The iterative algorithm to update each $\mu_b$ until $F_m$ reaches a minimum value is written as:

$$\Delta\mu=-\frac{F}{J} \tag{7}$$

where F is the vector of functions $F_m$ and J is the jacobian of F respect to $\mu$. Therefore,

$$\mu^{new}=\mu^{old}+\Delta\mu \tag{8}$$

When the iterative process converges, the resulting vector $\mu$ will represent a rough estimation of the attenuation properties of the imaged object.

## Simulations

In order to test the convergence of the described method, two different distributions of attenuation coefficients ($cm^{-1}$) were used to simulate the coincidence and single data. These data were used as input for the iterative process which estimates the attenuation coefficients that were previously used to simulate the data. The image was divided into a 4 x 4 matrix. It means the image has of 16 image elements (pixels). An attenuation coefficient and activity value is assigned to each pixel. The distributions are sketched in Fig. 2.

The distribution A is uniform (the attenuation coefficients are the same for every image pixel). Several coefficients were tested for this distribution. The distribution B shows different attenuation coefficients for different pixels. Several values were tested for this distribution as well. The activity distribution chosen for data simulation was to assign an activity of 750000 cps to the four central pixels. The activity for all other pixels is assumed to be zero.

## Results and Discussion

The results are summarized in the table 1. The main interest is to know if the iteration process converged to the expected attenuation coefficients.

It is clear that this method does not converge for high attenuation coefficients (>0.25 $cm^{-1}$). This tendency does not depend on the distribution. However, this technique is mainly addressed for brain imaging where the attenuation coefficients are not so large, except for the skull (around 0.26 $cm^{-1}$). Therefore, the probability to have a high attenuation coefficient is low since the attenuation coefficient for each pixel represents the average attenuation within the pixel whose size is very large. In general, the iterative algorithm converged after a maximum of 12 iterations and the results showed a maximum deviation of 5% with respect to the expected values.

## Conclusion

This report describes the preliminary results for a method aiming to estimate the attenuation correction coefficients for each LOR by using the single photon counting rate for each detector. The method is an iterative algorithm based on the Newton-Raphson method for solving non linear equations. For cases where simulated data was obtained using attenuation coefficients larger than 0.25 $cm^{-1}$, the method did not converge to the expected attenuation coefficients. At this point we do not have an explanation for this behavior. This method clearly offers a very rough estimation of the attenuation coefficients compared to the transmission scan. However, attenuation coefficients within the brain do not change too drastically. Hence, this technique could give satisfactory estimations for brain imaging. As presented in this report, the technique has several restrictions. The first one is the method is only useful for 2D imaging. Extension to 3D imaging is only possible if the Compton scattering effect is included. For 2D imaging, scatter photons contribution is around 10-15% which is expected to cause a small deviation from the true attenuation coefficients. However, scatter contribution increases to 40% in 3D imaging. If this effect is not modeled, the estimated values will not be reliable. The second restriction is related to the scanner hardware. This technique is only useful if the scanner provides simultaneously, single and coincidence rates.

## References

1) Huang S. et al., J. Nucl. Med. 22 (1981) 627.
2) Harkness B., Comparison of currently available PET scanners, Society of Nuclear Medicine, 47th annual meeting, June 2000.
3) Turkington T., J. Nucl. Med.Technology 29 (2001) 1.
4) Mizuta T. et al., Attenuation Correction in 3D PET, CYRIC annual report 1998, 165.

Table 1. Results of the iteration for estimating the attenuation coefficients.

| Distribution | Higher Coefficient | Smaller Coefficient | Convergence |
|---|---|---|---|
| A | 0.05 | 0.05 | yes |
| A | 0.1 | 0.1 | yes |
| A | 0.15 | 0.15 | yes |
| A | 0.2 | 0.2 | yes |
| A | 0.25 | 0.25 | no |
| A | 0.3 | 0.3 | no |
| B | 0.3 | 0.08 | no |
| B | 0.25 | 0.08 | no |
| B | 0.22 | 0.08 | yes |
| B | 0.2 | 0.05 | yes |
| B | 0.2 | 0.1 | yes |

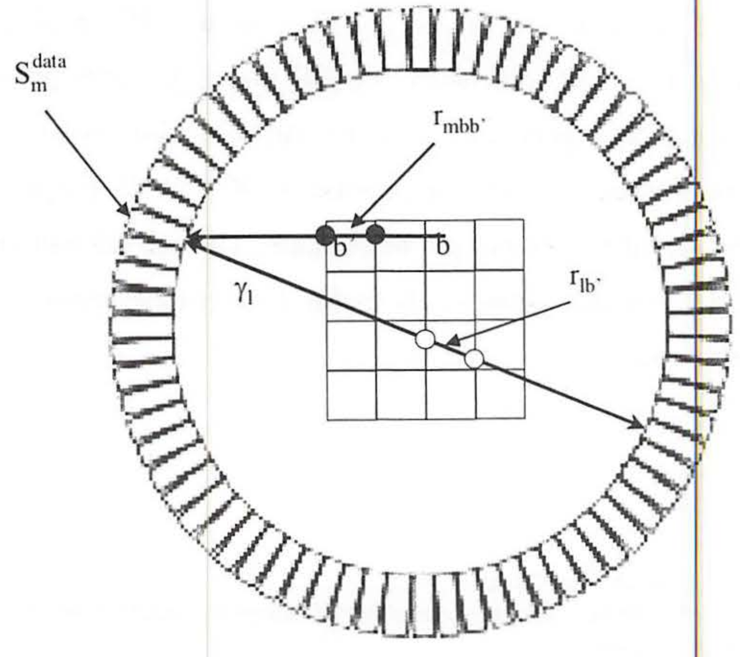

Fig. 1. 2D-PET scanner and discretized imaged.

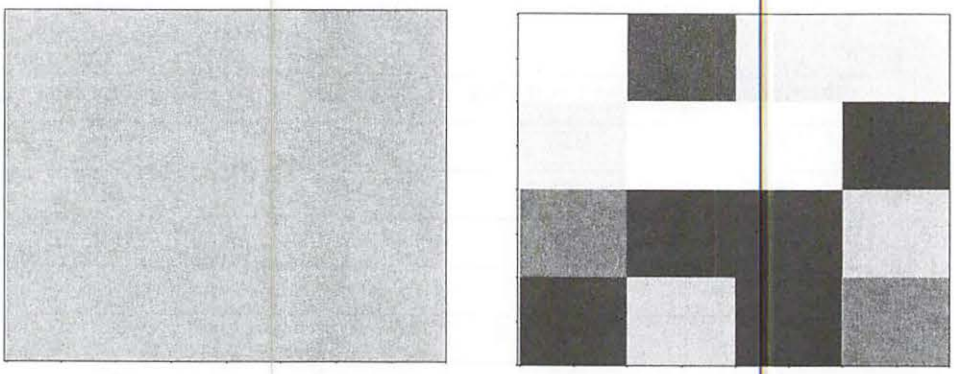

Distribution A

Distribution B

Fig. 2. Distribution of attenuation coefficients in the imaged object.

# I. 10. Stopping Rule for EM Algorithm Based on the Image Reconstructed by FBP Algorithm

*Oishi Y., Ishii K., Yamazaki H., Matsuyama S., Kikuchi Y., Rodriguez M., Suzuki A., Yamaguchi T., Watanuki S.*, and Itoh M.**

*Department of Quantum Science and Energy Engineering, Tohoku University*
*Cyclotron and Radioisotope Center, Tohoku University**

## Introduction

Nowadays the Expectation Maximization (EM) algorithm is used instead of the Filtered Backprojection (FBP) algorithm in a lot of PET facilities. The reason of this shift is that EM algorithm provides better quality images compared to FBP algorithm. Images reconstructed by FBP algorithm have many streak artifacts and are poor to make clinical diagnosis. In contrast, EM algorithm does not exhibit such artifacts and provides clearer images. However, EM algorithm does not guarantee reliable quantification which is an important factor in PET imaging. Therefore, many PET facilities use images reconstructed by FBP algorithm when PET images are analyzed by compartment models. When analyzing by compartment models, the images require not only reliable quantification but also quality because good quality is essential to decide regions of interest (ROIs). The quantification problem for EM algorithm lies on the lack of a suitable stopping rule for the iteration procedure: Namely, it is indispensable to estimate how many iterations are required to guarantee good quantification. For such stopping rule, many methods are discussed and proposed(1,2). In this paper, we propose a new approach of stopping rule by using the images reconstructed by FBP algorithm.

It is well-known that FBP algorithm shows reliable quantification properties for the chosen ROIs. If a stopping rule to guarantee the quantification is derived from images reconstructed by FBP algorithm, images reconstructed by EM algorithm are expected to have good quantification properties characterized by FBP algorithm and good quality originated from EM algorithm. Together, FBP and EM algorithm procedure take long time, but recent computer developments allow good performance to reconstruct images with both algorithms in 2D mode. From these viewpoints, a stopping rule by using images reconstructed by FBP algorithm is expected to become a powerful method for reconstructing appropriate quantitative images by EM algorithm.

## Method

Sinograms were acquired by a Monte Carlo simulation of a one ring PET scanner. Detector efficiency, scatter components and absorption were neglected in this simulation. Two kinds of phantom were used and their shape and radioactivity ratio are shown in Fig. 1. Each phantom is to evaluate the convergence tendency for radioactivity ratio (phantom 1) and hotspot size (phantom 2). The events were generated according with the radioactivity ratio by using random numbers and the total events assumed in this simulation were $10^6$ and $10^7$.

Images were reconstructed, from these sinograms, by FBP algorithm using Shepp-Logan filter and EM algorithm iterated till 50 times. For each image, after taking several ROIs covering all hotspot areas, the mean value and standard deviation of images were examined. A method to derive a stopping rule, from those values, was evaluated.

## Result and Discussion

Fig. 2 (left) shows the ROI position of phantom 1. Fig. 3 shows the mean value and standard deviation of the images in each ROI at the case of total events $10^7$ and Fig. 4 shows at the case of total events $10^6$. Square points indicate the value obtained from the EM algorithm. Dashed and solid lines are the FBP and true values respectively.

When the number of iterations is increased, the mean value of images, reconstructed by EM algorithm, in each ROI converges to the one of true images regardless of the total events. At the case of total events $10^7$, the mean value of images reconstructed by EM algorithm for the ROI 3 is the fastest to converge and the one for the ROI 1 is the slowest. The mean value of images reconstructed by EM algorithm reached the one by FBP algorithm at 19 iterations in ROI 3 and 27 iterations in ROI 1. At the case of total events $10^6$, the convergence of mean value is same as at the case of total events $10^7$ and the mean value of images by EM algorithm reached the one by FBP algorithm at 20 iterations in ROI 3 and 30 iterations in ROI 1. Therefore, the necessary number of iterations for the mean value convergence becomes ROI 3<ROI 2<ROI 1.

At the case of total events $10^7$, though the standard deviation, in ROI 2 and 3, of images after a few of iteration is higher than the one by FBP algorithm, this result can be neglected because it appears at a very early stage of the image reconstruction process. Thus, the standard deviation of images by EM algorithm till 50 iterations is less than the one by FBP algorithm. However, at the case of total events $10^6$, the standard deviation of images by EM algorithm in ROI 1 after 11 iterations is larger than the one by FBP algorithm and the ones in ROI 2 and 3 are considered as becoming larger than the one by FBP algorithm for more than 50 iterations because the shape of graph is upward-sloping curve. Thus, when total amount of events is small, it is understood that EM algorithm provides images reflecting the bad counting statistics and emphasizes the statistical noise according with the increase of iteration procedures. The case of few total events, in other words, when decreasing data acquisition time or radioactivity injected to patients, suggests the importance of a stopping rule.

Fig. 2 (right) shows the ROI position of phantom 2 and Fig. 5 shows the mean value and standard deviation of images in each ROI at the case of total events $10^6$ and Fig. 6 shows at the case of total events $10^7$. Details in figures are the same as above-mentioned Fig. 3 and 4.

When the number of iterations increases, the mean value of images by EM algorithm converges to the true one as the case of phantom 1. Necessary iteration number for the mean value of images by EM algorithm to converge to the one by FBP algorithm is ROI 2<ROI 1<=ROI 3 regardless of the difference of total events. For the standard deviation of images by EM algorithm, the importance of a stopping rule is shown for few total events because the shape of graph is upward-sloping curve same as the phantom 1.

A stopping rule should be derived from the dependence on the convergence tendency of the phantom shape and radioactivity ratio. However, only the fact that the hotspot with higher radioactivity ratio converges faster than the one with lower radioactivity ratio could be observed (Fig. 3 and 4) and the relation between convergence and phantom shape could not be observed (Fig. 6 and 7). At this point, a stopping rule results as follows: 1. Taking the ROI included all pixels in all hotspots and 2. Iteration procedure should be stopped when the mean value of images by EM algorithm reaches the one by FBP algorithm and then 3. If the standard deviation of images by EM algorithm is not a minimum, more iteration is necessary. However, attention must be paid not to increase the standard deviation in other ROIs after more iteration processes. Therefore, the comprehensive judgment for all ROIs or another solution is needed. For this problem, we are now considering a new algorithm such that some weighted factors are applied to the update pixels which have already converged.

## Conclusion

In this paper, we performed Monte Carlo simulation and tried to derive a stopping rule for EM algorithm based on the images reconstructed by FBP algorithm. We proposed the stopping rule that iteration procedures should be stopped when the mean values of images by EM algorithm in the region of all hotspots arrive at the one by FBP algorithm. Fig. 7 shows, at the case of total events $10^6$, the true image of phantom 1, the images reconstructed by FBP algorithm and by EM algorithm according with the proposed stopping rule. The image reconstructed by EM algorithm has good quantification properties as the one by FBP algorithm and better quality than the one by FBP algorithm. However, when the image is analyzed more detailed, the standard deviation of images in B.G region has already become larger than the one at a few iterations before. For example, the standard deviation after 20 iterations (when the mean value of images by EM algorithm only at ROI 3 has converged to the FBP one) was about 14% and after global convergence was about 20%. This means that the image by EM algorithm at the proposed adequate iteration number was already degraded in the B.G region. For this point, we will make a new algorithm such as weighted EM algorithm. Moreover, the ROI selection and how many ROIs are needed in this stopping rule should be discussed more. We plan to develop automatically ROI taking system and judging the stopping rule.

### References

1) Selivanov V. V. et al., IEEE Trans. Nucl. Sci. **48** (2001).
2) Veklerov E. and Llacer J., IEEE Trans.Med.Imag. **MI-6** (1987).

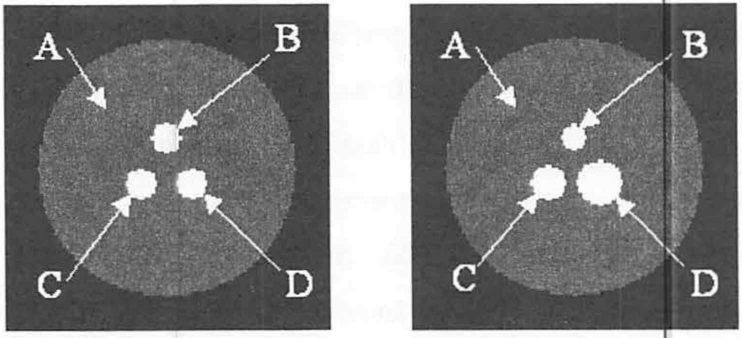

Fig. 1. Phantom 1 (left) and 2 (right). Radioactivity ratios A:B:C:D are 1:3:4:5 (phantom 1) and 1:3:3:3 (phantom 2).

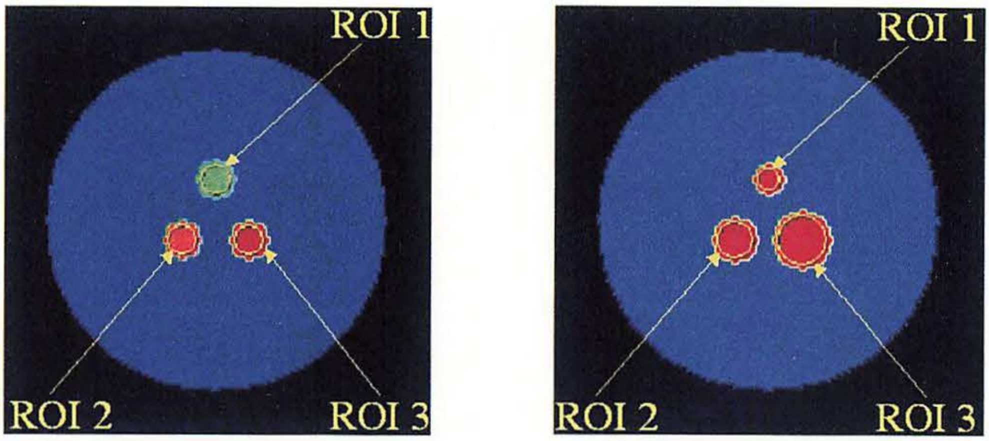

Fig. 2. The ROI positions of phantom 1 (left) and 2 (right).

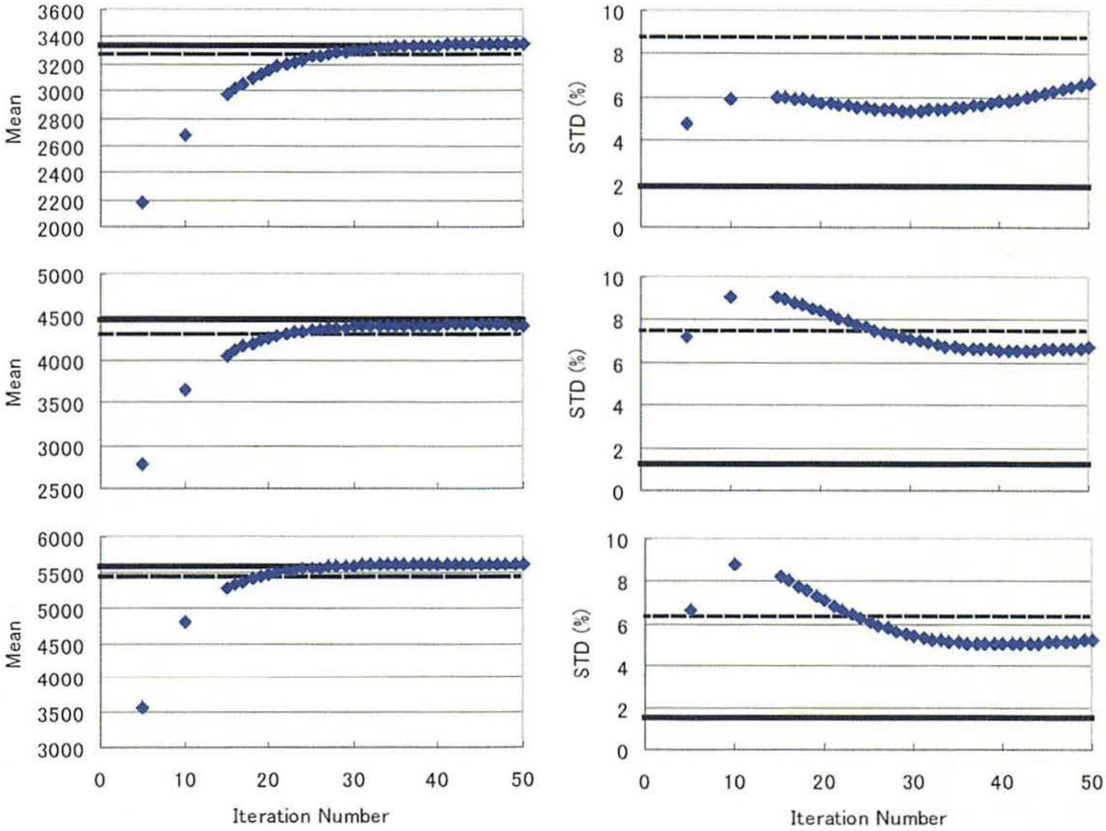

Fig. 3. The mean value (left column) and standard deviation (right column) of phantom 1 for total events $10^7$. Top row is for ROI 1, middle for ROI 2 and bottom for ROI 3. Solid line is for true, dashed line is for FBP algorithm and square points are for EM algorithm.

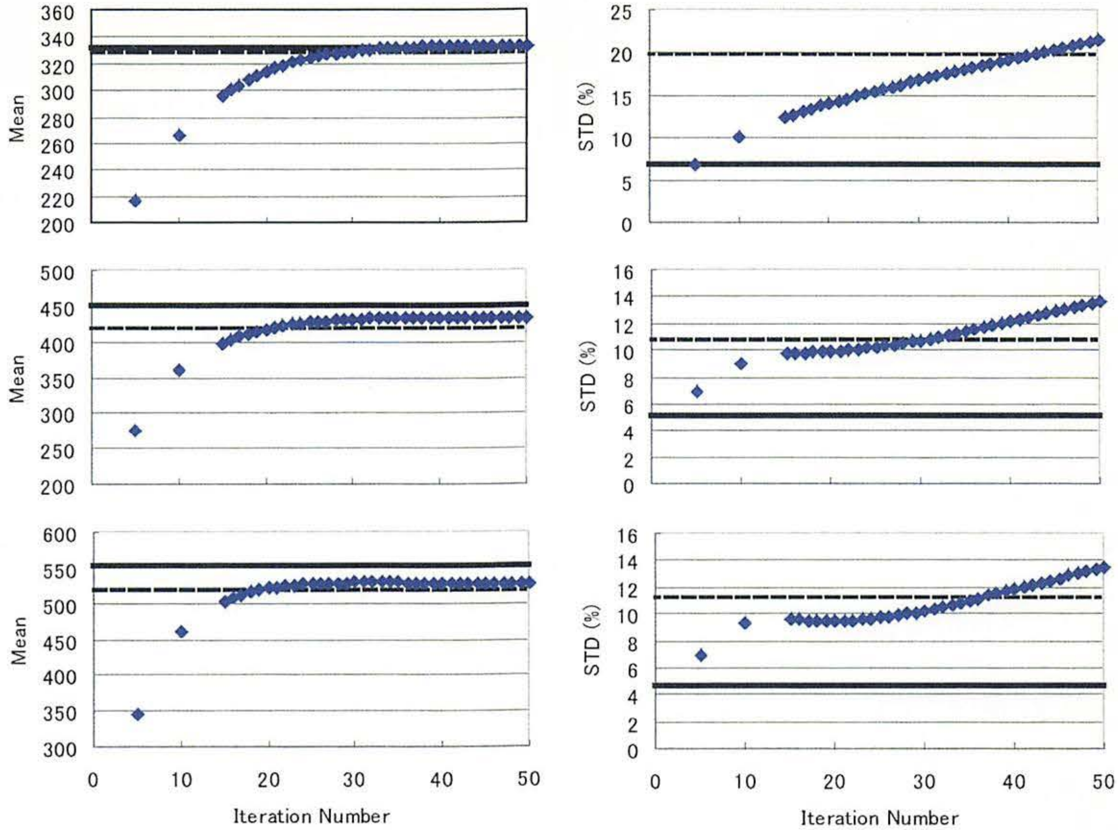

Fig. 4. The mean value (left column) and standard deviation (right column) of phantom 1 for total events $10^6$ Top row is for ROI 1, middle for ROI 2 and bottom for ROI 3. Solid line is for true, dashed line is for FBP algorithm and square points are for EM algorithm.

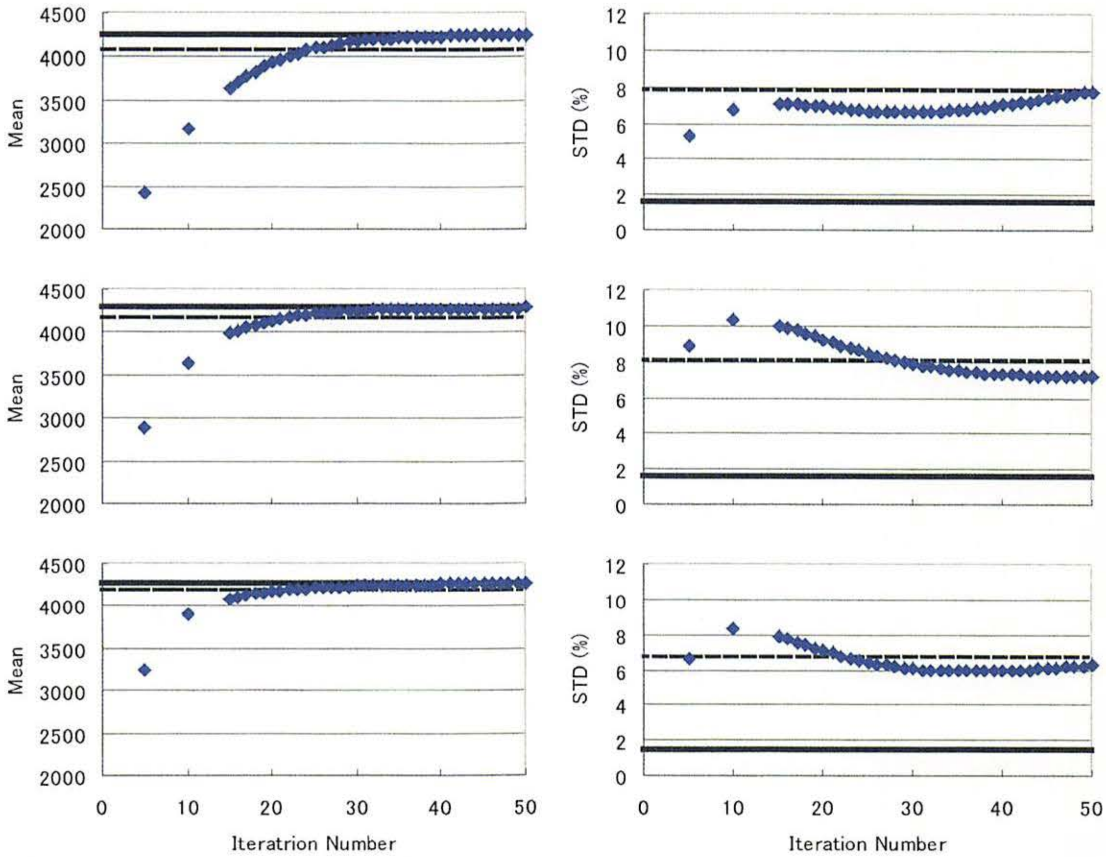

Fig. 5. The mean value (left column) and standard deviation (right column) of phantom 2 for total events $10^7$ Top row is for ROI 1, middle for ROI 2 and bottom for ROI 3. Solid line is for true, dashed line is for FBP algorithm and square points are for EM algorithm.

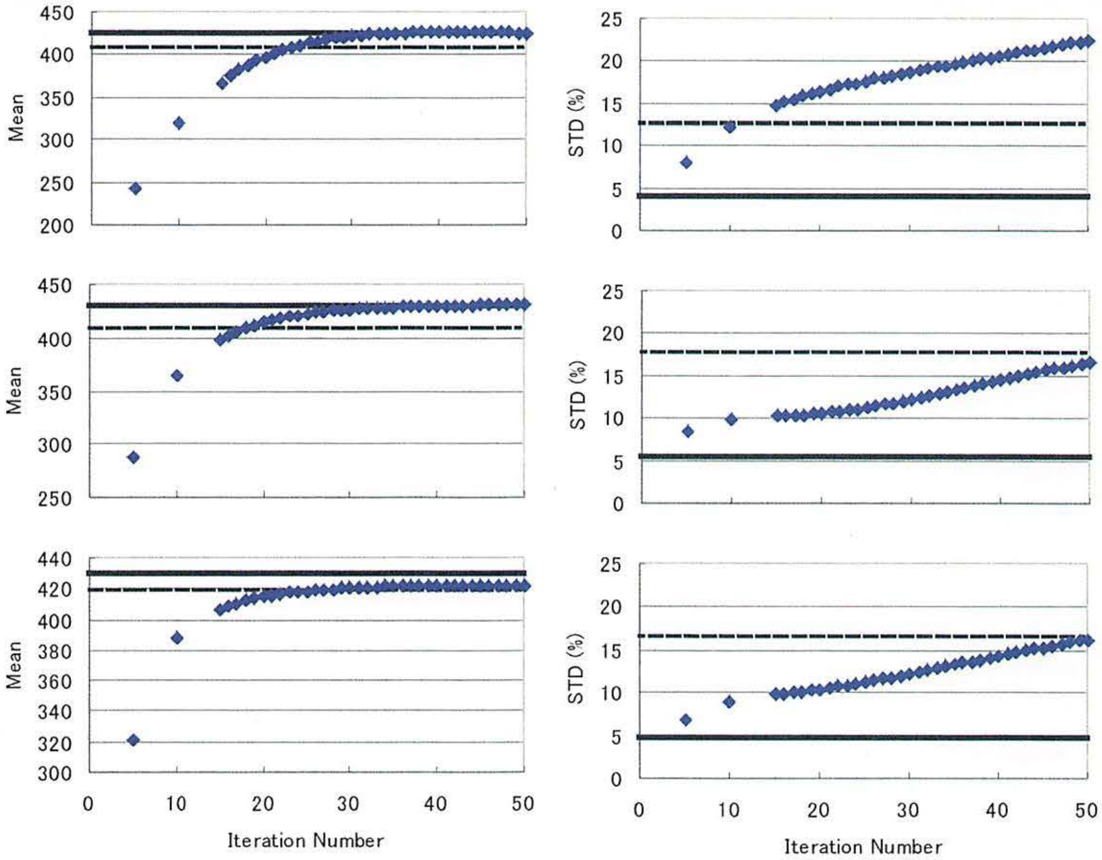

Fig. 6. The mean value (left column) and standard deviation (right column) of phantom 2 for total events $10^6$. Top row is for ROI 1, middle for ROI 2 and bottom for ROI 3. Solid line is for true, dashed line is for FBP algorithm and square points are for EM algorithm.

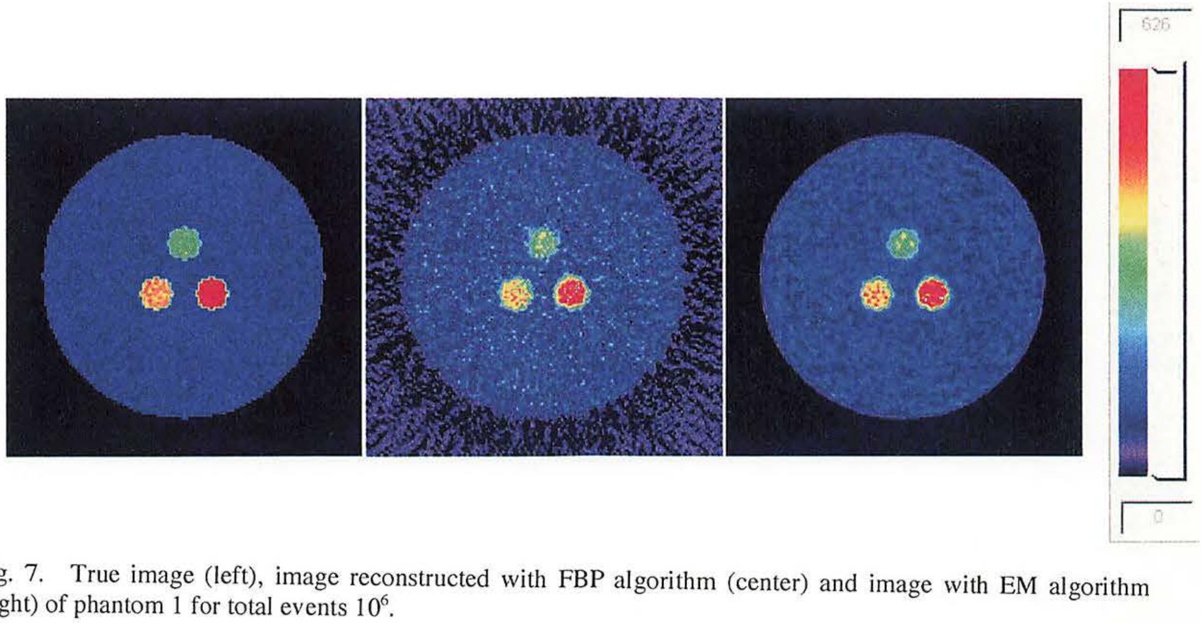

Fig. 7. True image (left), image reconstructed with FBP algorithm (center) and image with EM algorithm (right) of phantom 1 for total events $10^6$.

# I. 11. NEC Evaluation of the Front Shield in Rejecting Annihilation Photons from Out Side of Field of View in 3D Brain PET Study

*Watanuki S., Ishii K.* and Itoh M.*

*Cyclotron and Radioisotope center, Tohoku University*
*Department of Quantum Sience and Energy Engineering, Tohoku University**

## Introduction

In a 3D positron emission tomography (PET) study, the PET detectors are exposed to the undesirable annihilation photons from the outside of the field of view, since the detector has the relatively wide opening angle in the axial direction with inter-slice septa retracted. The image quality of a 3D PET is substantially degraded by increasing of scatters and random coincidences[1-2]. An additional lead shield (Figure 1) was used for 3D brain studies to reduce the annihilation photons from the outside of field of view (FOV) in case of SET-2400W[2]. In this study, we examined the shield performance in terms of noise equivalent count (NEC) measured in phantom experiments and clinical studies.

## Materials and methods

### *PET system and shield*

Experiments were carried out with a 3D PET system (SET-2400W, Shimadzu Co., Kyoto, Japan). The system has a 20 cm axial FOV and produces a set of 63 slice images at one scan[3)]. The front shield was designed to be installed in front of the gantry (Figure 1 a). The shield was made of a pair of half annular 7mm thick lead plate lined with 2 mm thick steel with aperture diameter of 30 cm. It can be opened along two lateral hinges for a whole body scans (Figure 1 b).

### *Phantom experiment*

A cylindrical phantom (60 cm internal length, 15 cm bore) was used for the experiments. The phantom was filled with 7.4 kBq/ml of $^{18}$F (Fluorine) solution, and was located as shown in Figure 2. Twenty-two frames of 20 minutes scan (each) were performed in a 3D mode. A total (true, scatter and random) coincidence rate and a random coincidence rate were recorded during the scan. The measurements were carried out twice, i.e., with and without the shield. The transmission scan was done one-hour after decayed out of radioactivity. The transmission scan was used for the attenuation corrections in images reconstruction.

*Clinical studies*

Two healthy normal volunteers were scanned with $^{15}O$ labeled $H_2O$ injection, with or without the lead shield. A 70 seconds' scan was performed in 3D mode. A total coincidence rate and a random coincidence rate were recorded during the scan. Injected activities in the experiments with and without the shield study were 180 MBq and 195 MBq, respectively.

*NEC*

NEC rates for the phantom and for the patient's measurements were obtained by using the following equation4).

$$NECr = \frac{T^2(1\text{-}SF)^2}{T+2fR} \qquad (1)$$

Where, T corresponds true coincidence rates (including scatter), SF, R, f means the scatter fraction, the random coincidence rate and the fraction of the sinogram covered by the object respectively. In this study the value of SF and f were set to 0.3 and 2.5 respectively.

## Results and discussion

Figure 3 shows the count rate of true + scatter, random and NEC, in a phantom measurement as a function of the mean radioactivity concentration with and without the shield. Concerning about the result of decreasing of random coincidence and increasing of true coincidence, the NEC was improved with use of the shield compared to the NEC without the shield as the result of decreases in-random coincidences and increases in true coincidence. This improvement was more pronounced with higher the count rates. However NECs became plateau or no improvement at the activity concentrations over 6 kBq/ml in both conditions; with and without the shield. Consequently, the ratio between the NEC with the shield and the NEC without the shield became almost constant. The improvement of NEC by using of the shield can be count as an increasing of efficiency of a PET system. Then we approximate the increasing of the efficiency will be 23% at maximum using the shield when activity distributes uniformly. The total coincidence count rate with the shield was about 300Kcps at 6 kBq/ml of activity concentration.

Figure 4 shows the count rate of true + scatter, random and NEC, in clinical studies, as function of the time after the start of the scan. The random coincidence rates in the scan without the shield was 3.7-5.4 times higher than the true rates in the initial 10 seconds. The scan was started at the initial rise point of the PET system counts. The radioactivity in the chest, i.e., lung and heart were higher than in the brain at this period. Many of random coincidence events at early phase of the scan came from organs in the outside of the FOV especially in the lung and heart. On the other hand, the random coincidence rate with the shield is 1.2-2.3 times higher than the true plus scatter rate at the same period. Furthermore, the ratio of random and true plus scatter coincidence rate with the shield was lower than without the shield throughout the scanning. These results indicated that the shield substantially reduced random coincidences induced by annihilation ray from the outside of FOV actually in clinical studies. The dose corrected average NEC rates in scanning with and without the shield were 0.22 and 0.27 kcps/MBq respectively. The corrected NEC rate with the shield is 27% higher than the efficiency without the shield. The peak of true plus scatter coincidence rate was obtained at 30-40 seconds after a scan start time, and the rate decreases slowly after the peak. The NEC rate not increases over than 300 kcps of total coincidence during the scanning with the shield in phantom experiment. We decided to control the injection dose of $^{15}O$-$H_2O$ for brain studies at 3D mode to have total coincidence rate less than 300 kcps at peak after 30 seconds. Slow injection such as 30 seconds was also preferred.

Both the phantom and clinical studies demonstrated that the lead front shield was effective and expected a practical improvement of efficiency about 20% at least.

## References

1) Sossi V., Barncy JS. et al., IEEE Trans. Nucl. Sci. **46** (1995) 1157.
2) Yamamot S., Miura S. et al., Jpn. J. Nucl. Med. **33** (1996) 641.
3) Fujiwara T., Watanuki S. et al., Anna. Nucl. Med. **11** (1997) 307.
4) Holm S., Toft P. et al., IEEE Trans. Nucl. Sci. **43** (1996) 2285.

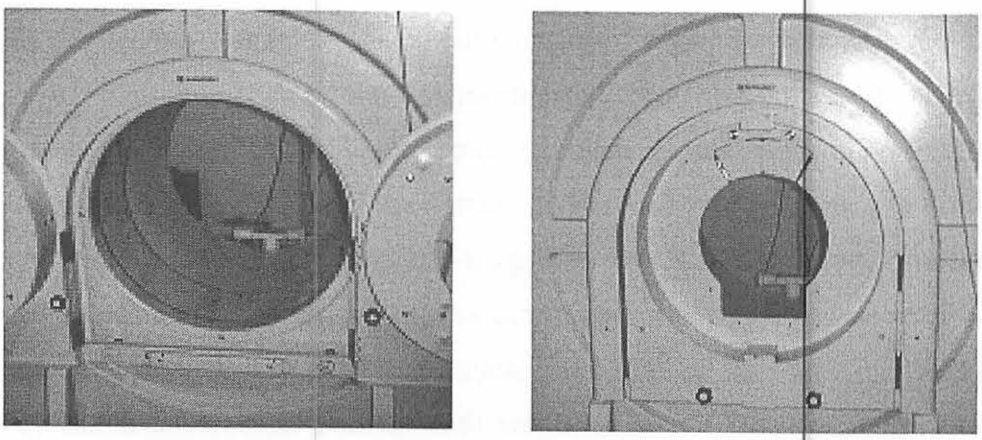

a

b

Fig. 1. Photograph of a shield of annihilation ray from outside of scanner FOV. The Photograph (**a**) is the shield not in installed position and (**b**) is the shield in installed position in the SET-2400W PET scanner gantry.

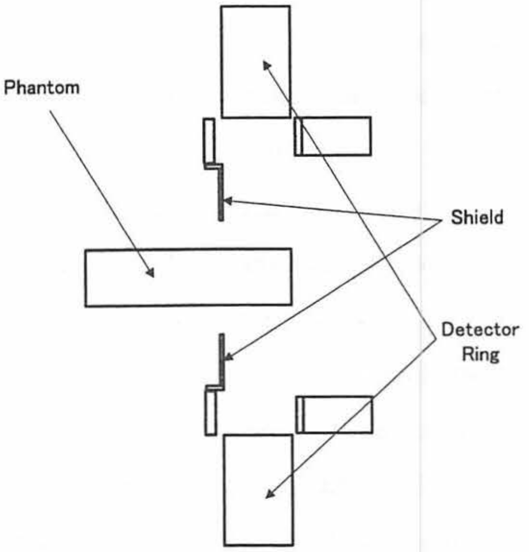

Fig. 2. Arrangement for the shield and the andphantom in a SET-2400W gantry.

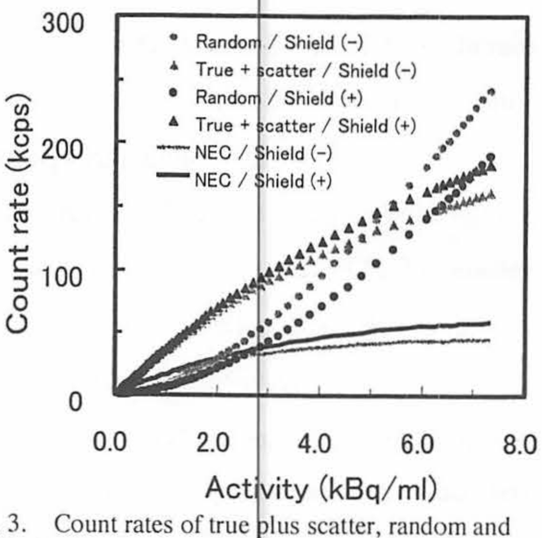

Fig. 3. Count rates of true plus scatter, random and NEC with the phantom as a function of the mean activity concentration obtained in scanning with without the shield.

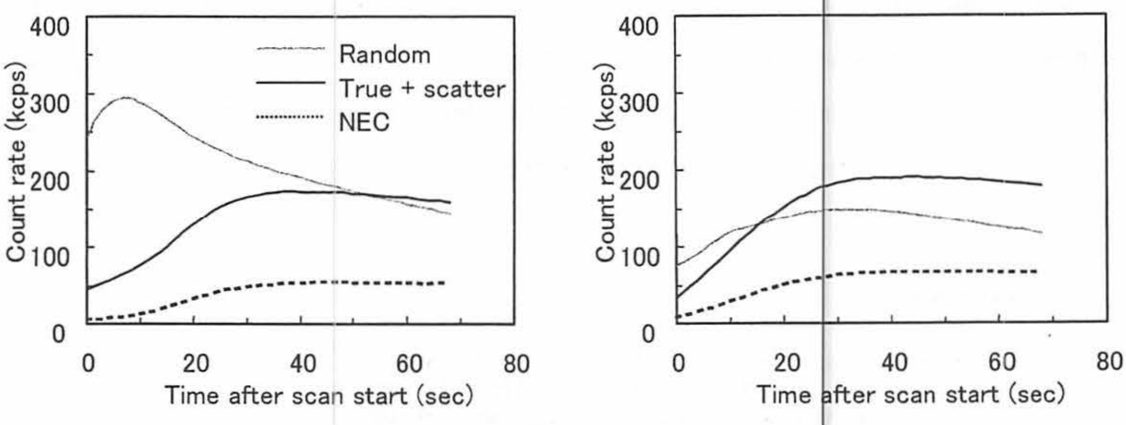

a

b

Fig. 4. Comparison between with lead shield (**a**) and without lead shield (**b**) for the count rate of true plus scatter, random and NEC for the patient head as a function of time after scan started.

# I. 12. Multi-site Aerosol Monitoring Using Mini Step Sampler

*Matsuyama S., Katoh K., Sugihara S., Ishii K., Yamazaki H., Satoh T., Amartaivan Ts., Tanaka A., Komori H., Hotta K., Izukawa D., Mizuma K., Orihara H.[*], Nakamura E.[**], Satoh N.[**], Futatsugawa S.[***], and Sera K.[****]*

*Department of Quantum Science and Energy Engineering, Tohoku University*
*Cyclotron and Radioisotope Center, Tohoku University[*]*
*Miyagi Prefectural Institute of Public Health and Environment, Sendai 983-0836, Japan[**]*
*Nishina Memorial Cyclotron Center, Japan Radioisotope Association, Takizawa, Iwate 020-0173, Japan[***]*
*Department of Cyclotron Research Center, Iwate Medical University, Takizawa, Iwate 020-0173, Japan[****]*

## Introduction

Atmospheric aerosol consists of small particulate matter and are often deformed by photo chemical reactions in the atmosphere[1-3)]. Elemental concentrations in atmospheric aerosol reflect the processes generating air pollution. Therefore, elemental analysis of atmospheric aerosols is useful to detect the sources of aerosols. The combination of aerosol collection on thin filters and PIXE analysis is one of the most effective methods for analyzing atmospheric aerosols[1)]. Many studies have focused on aerosol monitoring[4-8)]. In some of these studies, statistical models, such as the principal components analysis (PCA) and the chemical mass balance (CMB), were used to determine the contribution of aerosol sources[5-8)]. Back trajectory analysis has been used to delimitate aerosol sources[1)]. The dependence of elemental concentrations on the wind direction has been investigated and was found to be influenced by aerosol source locations[10,11)]. In our previous study, we performed a successive collection of aerosol samples in correlation with meteorological data and carried out PIXE analysis. The concentrations of Mn, Fe, Zn and Pb depended strongly on the wind direction and their intensity distributions reflected the position of the aerosol sources[10)]. This result suggests that the aerosol source location can be determined by measuring the elemental concentration of aerosols simultaneously with wind direction at several positions with short sampling time during long sampling periods. Thus, we need an inexpensive way to construct a local area air-pollution monitoring system. For this purpose, we have developed a compact sampler with low manufacturing and running costs for simultaneous sampling at several positions. In this study, we applied them to outdoor multi-site aerosol monitoring in the local area close to our daily life.

### Mini step samplers

The samplers matched to PIXE analysis have been reviewed by K.R. Akselsso[12] and R.O.Nelson et. al. have developed streaker air samplers[13,14]. The two stage streaker sampler has continuous and discrete modes. In the continuous mode, one month of sampling period can be achieved with 4-hour time resolution. However, aerosol samples overlap in time and time resolution is strongly dependent on beam size. Since synchronization of the sampling time at multi points is very important, this mode is not appropriate. In the discrete mode, the sampling period is too short for our intended use. The step sampler (Green-blue Co. LTD), which we used in previous studies, can collect samples for 9 days with 3-hour time resolution[15]. The suction nozzle of the sampler is 4 mm in diameter. Here, we developed a sampler with smaller suction nozzle diameter for continuous sampling over extended periods with lower running costs. It has been reported that a loading distribution of aerosols collected on 47 mm diameter, 0.8 μm pore size, cellulose nitrate filter paper is not uniform[16]. In this case, a beam with uniform intensity across its cross sectional area is required for quantitative analysis. A small sample size is appropriate for quantitative analysis, since a uniform beam intensity is easy to obtain from accelerators.

We tested samplers of 2 mm-suction nozzle diameter and of 4 mm-suction nozzle diameter from the view point of non-uniformity, choke of filter and high detection limit. Air at atmospheric pressure is sucked through a Nuclepore filter[17] of 10 μm pore size, and aerosols are collected on the surface of this filter. Since the size of collected aerosols depends on the filter face velocity as well as on pore size[18], these parameters must be determined, when the sampler is designed. Sampling was performed at the same time using the two samplers with 2 and 4 mm nozzle for 3 hours on the campus of Tohoku University. Elemental concentration ratios for both cases were consistent to within ±20 %, except for a few cases. While sample uniformity did not vary significantly, high-density areas are seen 40% above mean density. This causes a problem in quantitative analysis using a beam with small spot size, but it does not cause a significant variation when analysis is carried out using a beam, which covers over 50 % of the sample area. Therefore, sampling with small suction nozzle does not adversely affect aerosol collection and is preferable for quantitative analysis, because of lower costs. Then, we developed two types of mini step samplers with 2 mm-diameter suction nozzle. The suction nozzle of the mini sampler moves in one dimension. It comprises a sampling unit, mass flow meter, fine control valve, vacuum pump, programmable control unit and a shelter. A small reversible motor moves the suction nozzle. The programmable controller controls the movement of the suction nozzle one-dimensionally and the vacuum pump. Filter is pasted on a frame of 34×265 $mm^2$. Sampling is made step by step for a preset sampling time. The pump is stopped after the preset sampling time, the suction nozzle is moved to the next position and sampling starts again. Sampling time can be set arbitrarily from a few minutes up to several hours. Travel distance of the suction nozzle is determined by the operation time of the motor. The sampler collects more than 70 samples and operates for more than one week with a sampling resolution of 3-hours.

Fig.1 shows the sampler whose suction nozzle moves in 2-dimensions with the main direction like the 1 dimensional sampler. It collects more than 900 aerosol samples. The sampling period is in excess of one month with a sampling resolution of one-hour.

Our mini step samplers and commercial step sampler (Green-blue Co. LTD) were operated side by side at Tohoku University campus using 3-hours time resolution. The collected samples were analyzed by the Vertical in-air PIXE (ViaPIXE) system at Tohoku University[19)]. The beam spot size was 1.5 mm in diameter and covered 60 % of the sample area. Detection limits were ~37, ~8 and ~10 $ng/m^3$ for Ca, Mn and Pb for an irradiation time of 5 min with a beam current of ~1.5 nA. The elemental concentrations obtained by these samplers were consistent. We conclude the newly developed mini step sampler is applicable to aerosol monitoring.

## Multi-site monitoring

A program of simultaneous multi-site (A, B, C and D site) aerosol sampling was conducted during two periods from July 25, 2002 to August 7, 2002 and from December 11, 2002 to December 25, 2002 for two weeks, respectively. The sampling sites are the outskirts of Sendai City, where strong air pollution might be expected (Site D was used only in December). Fig.2 shows the map of sampling sites. The sampling sites are located along the national road No.4. Two factories are surrounded by sites B, C and D. The meteorological data (wind direction, and velocity) at the sites A and B during sampling periods were provided by the Prefectural Institute of Public Health and Environment. The meteorological data used at site C and D were those of site B. The aerosol samples were collected every 3-hours by using the mini step samplers and the commercial step sampler. The aerosol samples were consecutively analyzed by the ViaPIXE system[10,19].

Elemental concentrations of eight elements (Ca, Ti, Mn, Fe, Ni, Cu, Zn, Pb) were obtained as a function of sampling time. Fig.3 shows the elemental concentration of Fe as a function of time. A cyclical change in concentrations is evident, which is thought to be caused by human activity and all sites showed similar patterns. Some elements (Ca, Ti, Mn, Pb), which would be a soil origin, also showed similar trends. Fig.4 and Fig.5 show the elemental concentrations of Cu and Zn. The concentration of Cu strongly increased in the last part of July exhibiting narrow concentration spikes and returning to normal levels later on. The concentration of Zn also showed irregular concentration spikes during the time of sampling and its pattern varied with sites. Cu spikes reached values of up to 90 times the average concentration of Cu in Japan, and Zn exceeded the average concentrations by 45 times. These two elements were analyzed in more detail by using the data of wind directions.

Average Concentration of Cu, Zn and Fe as a function of wind directions, superimposed on the map, are shown in Figs.6- 8 for the summer period. The patterns in these figures give the average values over the sampling period. We conclude that Cu had been transported to the sites from the northeast. The concentration of Zn appears to be influenced by two big factories encircled by the three sites B, C, and D. In contrast, the concentration of Fe does not depend on the wind direction. In order to identify the pollution sources, the wind direction and the elemental concentrations at each sampling site are displayed on the map, and the trends are shown as optical images every 3 hours. Figs. 9 and 10 display typical results. The direction of arrows gives the wind direction and the arrow length and width are related to the elemental concentration. The relation between wind direction and increase in elemental concentration is evident and indicates that Cu was transported to the sampling sites in southwesterly direction possibly from a big source of pollution in far distance. Concerning Zn, it is not known to be contained in soil dust in high concentrations. This indicates that Zn is most likely a man made pollution source. We suspect it to arise from factory emission. It is clear that the pollution source is located between the sites B, C and D which was confirmed by analyzing the ash samples collected at the factories that the pollution source is factory A. In conclusion, it has been demonstrated that the multi-site system of mini step samplers combined with meteorological data is well suited to identify sources of pollution.

## Conclusion

We applied the mini step samplers to multi-site aerosol sampling during two periods tagging the concentrations with meteorological data (wind direction, and velocity). The elemental concentrations of some soil origin elements changed periodically. In contrast, the concentrations of Cu and Zn showed irregular concentration spikes with patterns varying according to the sites. Analysis using the data of wind directions showed that Cu had been transported to the sites from the northeast and the concentration of Zn was dominated by emission from one of the factories near the monitoring sites. In conclusion, it was been demonstrated that the multi-site system combined with meteorological data is well suited to identify sources of pollution.

## Acknowledgements

This study was partly supported by funds from the Grant-in-Aid for Scientific Research in Priority Areas under Grant No.14048205 from the Ministry of Education, Science, Sport and Culture. The authors would like to acknowledge the assistance of Messrs. R.Sakamoto and M.Fujisawa for maintenance of the Dynamitron accelerator. We also appreciate the help of T.Takahashi, K.Komatsu and T.Nagaya for their help on manufacturing the mini sampler. We are deeply indebted to Prof. W.Galster for fruitful discussion during this work.

### References

1) S.A.E.Johansson and J.L.Campbell, *PIXE:A Novel Technique for Elemental Analysis*,(JohnWiley and Sons, 1988).
2) M.Kasahara, J.H.Park and K.Yamamoto, *Nuclear Instruments and Method*, **B109/110**, 471-475 (1996).
3) T.A.Cahill, *Nuclear Instruments and Method*, **B49**, 345-350 (1990).
4) V.Ariola et. al., *Nuclear Instruments and Method*, **B190**, 471-476 (2002).
5) P.Parti et. Al., *Atmospheric Environment*, **34**, 3149-3157 (2000).
6) S.F.Bongiovanni et. al., *Nuclear Instruments and Method*, **B161-163**, 786-791 (2000).
7) D.D Cohen, *Nuclear Instruments and Method*, **B136-138**, 14-22 (1998).
8) P.Formenti, H.J.Annegarnand S.J.Piketh, *Nuclear Instruments and Method*, **B136-138**, 948-954 (1998).
9) A.Sturman and P.Zawar-Reza, *Atmospheric Environment*, **36**, 3339-3350 (2002).
10) S.Matsuyama et.al., *International Journal of PIXE*, **9**, 51-56 (1999).
11) I.Borbely-Kiss et.al., *Nuclear Instruments and Method*, **B150**, 339-344 (1999).
12) K.R.Akselsson, *Nuclear Instruments and Method*, **B3**, 425-430 (1984).
13) R.O.Nelson and J.W.Nelson, *Nuclear Instruments and Method*, **B22**, 353-355 (1987).
14) PIXE International, P.O.Box 7744, Tallahassee, FL32316, USA.

15) Y.Hashimoto et. al., "Development of a new air surveillance system by a step sampler-PIXE technique", *Proc. 7th World Clean Air Congress (II)*, (1986) pp.11-13.
16) H.K.Bandhu et.al., *Nuclear Instruments and Method*, **B160**, 126-138 (2000).
17) K.R.Spurny et. al., *Environmental Science and Technology*, **3**, 453-464 (1969).
18) K.Kemp and L.Kownacka, *Nuclear Instruments and Method*, **B22**, 340-343 (1987).
19) S.Iwasaki et. al., *International Journal of PIXE*, **5**, 163-173 (1995).

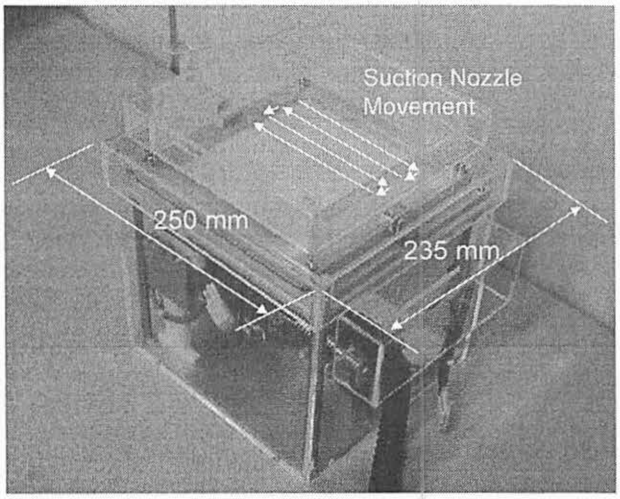

Fig. 1 Mini step sampler whose suction nozzle moves in 2 dimentions.

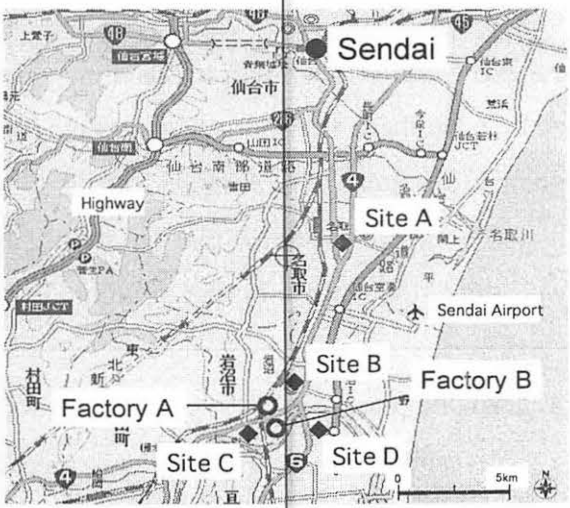

Fig. 2. Map around sampling sites.

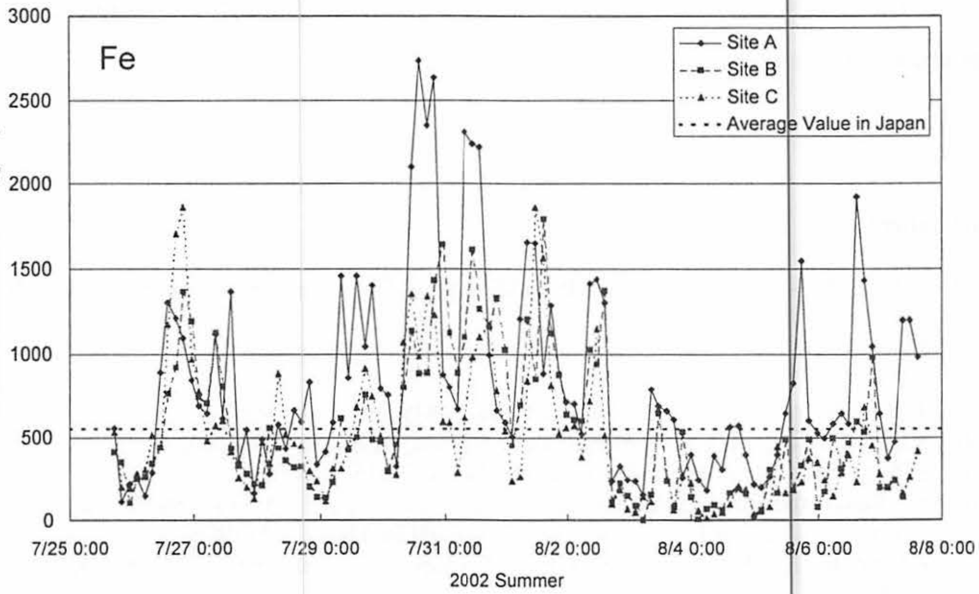

Fig. 3. Elemental concentrations of Fe as a function of time.

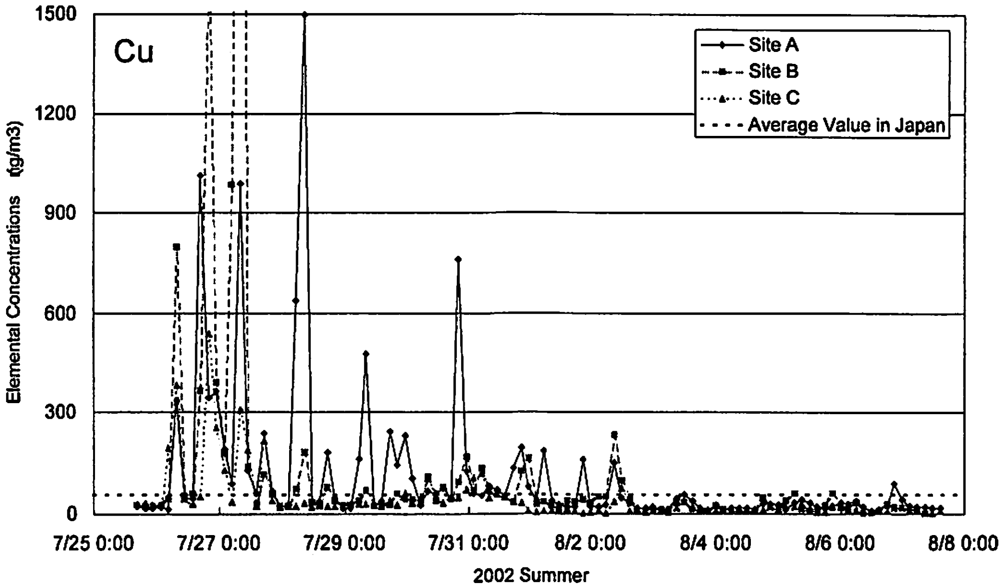

Fig. 4. Elemental concentration of Cu as a function of time.

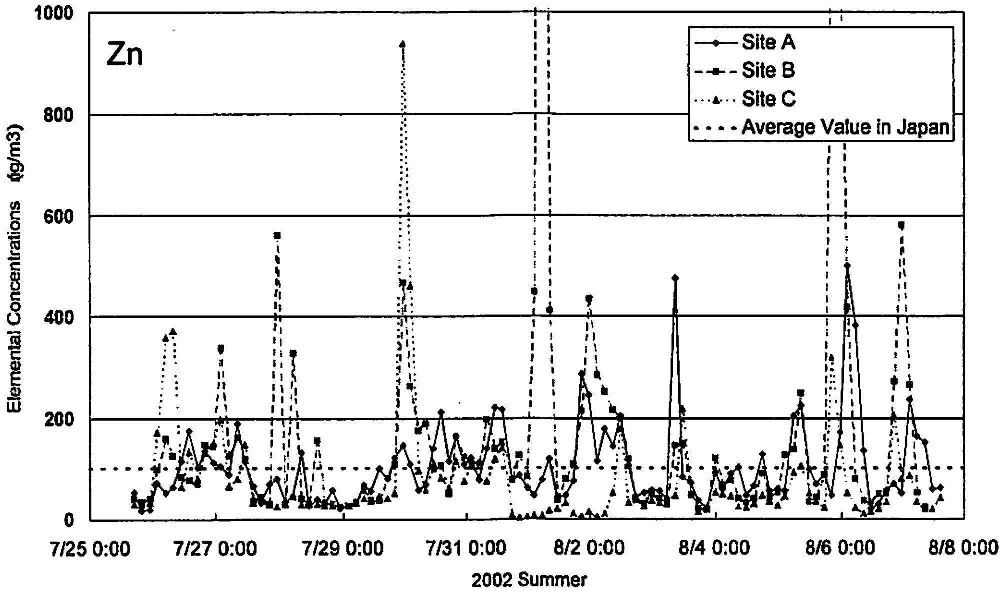

Fig. 5. Elemental concentration of Zn as a function of time.

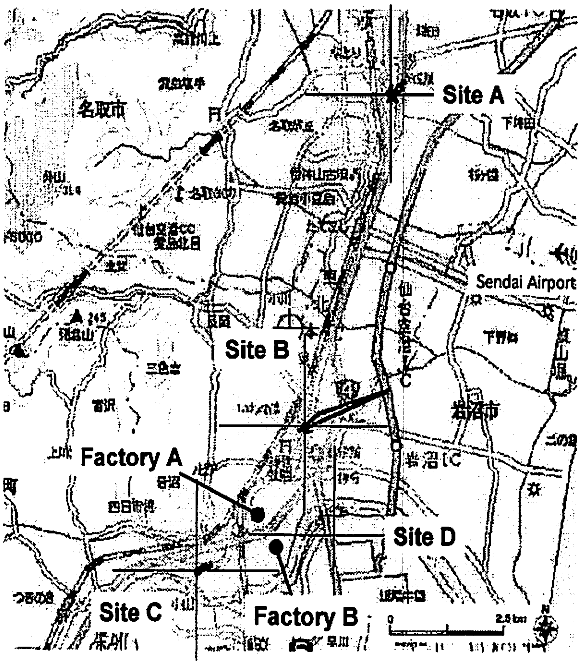

Fig. 6. Concentration of Cu as a function of wind directions. (Summer period)

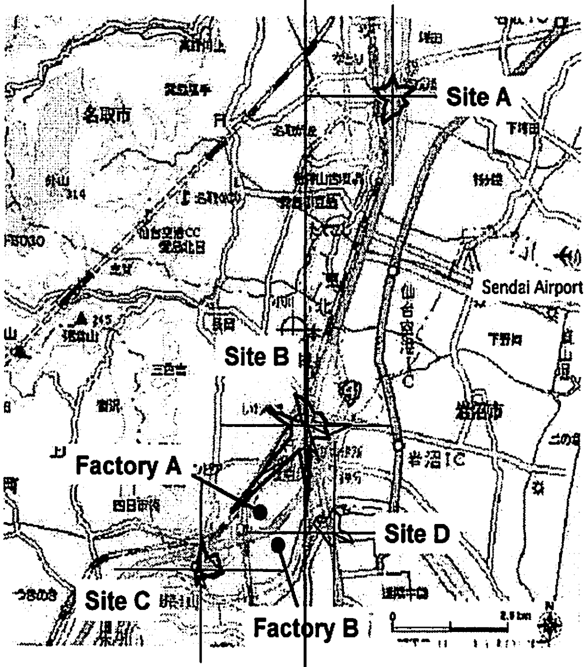

Fig. 7. Concentration of Zn as a function of wind dire ctions. (Summer( — ) and Winter( — ) periods)

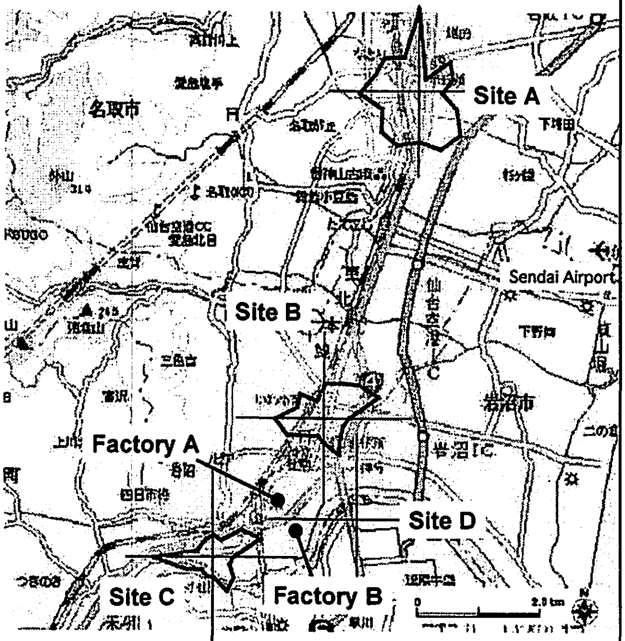

Fig. 8. Concentration of Fe as a function of wind directions. (Summer period)

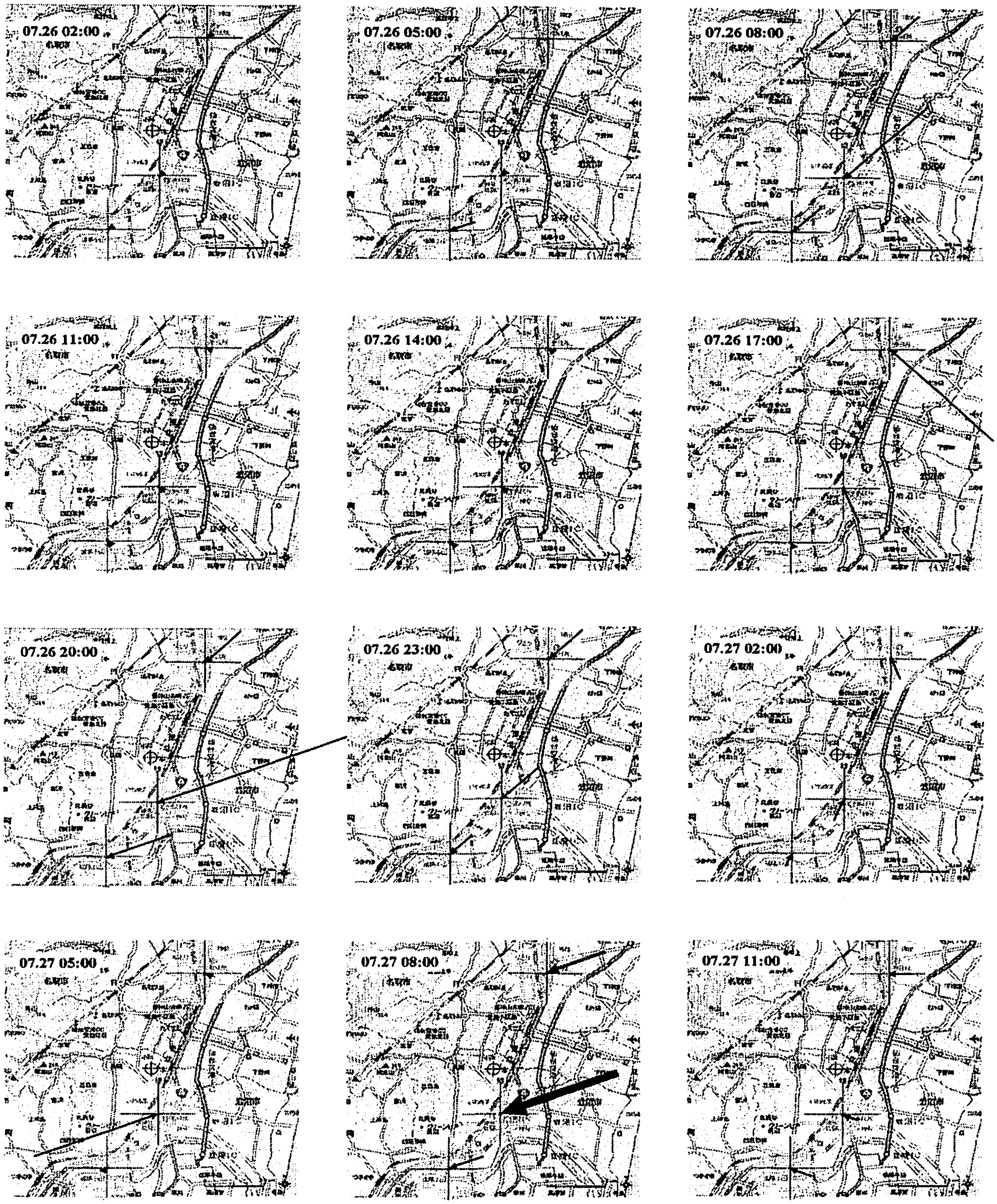

Fig. 9. Concentration of Cu with wind direction (all ↑ N up).

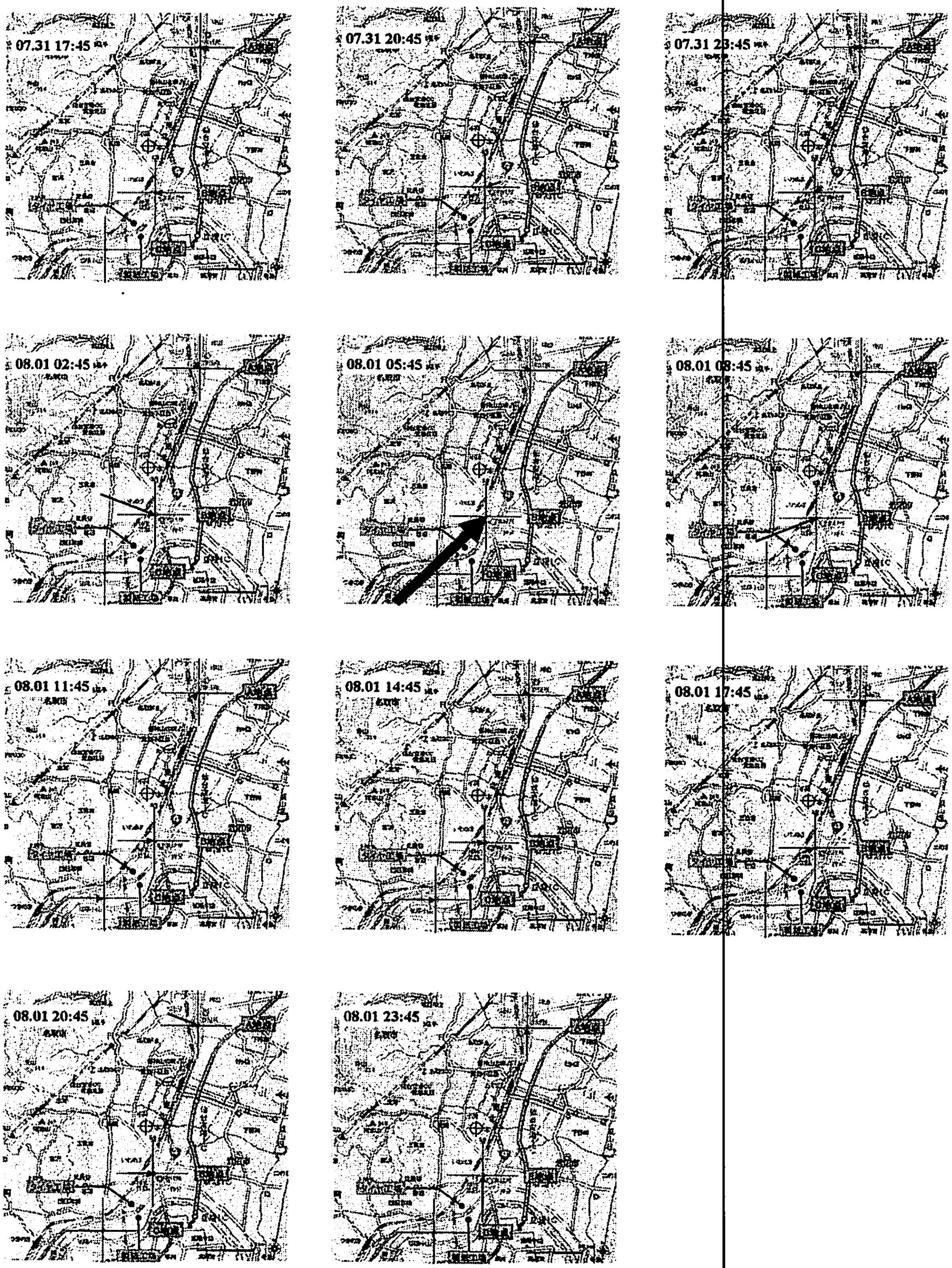

Fig. 10. Concentration of Zn with wind direction (all ↑ N up).

# II. CHEMISTRY

# II. 1. Technetium-99 Concentrations in Japanese Rice Paddy Fields

*Tagami, K., Uchida, S. and Sekine, T.*[*]

*Environmental and Toxicological Sciences Research Group,*
*National Institute of Radiological Sciences*
*Department of Chemistry, Graduate School of Science, Tohoku University*[*]

## INTRODUCTION

Technetium-99 is a long-lived radionuclide with a half-life of 2.111 x $10^5$ y. It is produced in appreciable amounts (6.1 %) by nuclear fission. Because of its long half-life, the migration of $^{99}$Tc in the environment is of great importance from a viewpoint of dose assessment. It is well known that pertechnetate ions ($TcO_4^-$) have a high geochemical mobility under oxidative condition and the uptake of $TcO_4^-$ into plants is quite high. From a radioecological viewpoint, analysis data on global fallout $^{99}$Tc in environmental samples should give useful information to know the migration of $^{99}$Tc. At present, however, due to very low concentration and analytical difficulties for determination of the nuclide in environmental samples, knowledge on $^{99}$Tc levels is quite limited.

In this study, we determined concentrations of $^{99}$Tc in surface soil samples of paddy fields collected at several sites in Japan (Table 1). Radioacitivity of $^{137}$Cs in the samples was also determined as a comparative indicator, because the fission yields from $^{235}$U and $^{239}$Pu are about the same (ca. 6%) for the two nuclides, and the behavior and distribution of $^{137}$Cs in the environment are well understood. The activity ratio of $^{99}$Tc/$^{137}$Cs was calculated to understand Tc mobility in the soil.

## EXPERIMENTAL

Nine soil samples were collected from the surface layer (< 20 cm) of paddy fields in Japan (Table 1). For the $^{99}$Tc determination, air-dried samples were incinerated for 8 h at 450°C to decompose organic matter before chemical separation. The separation procedure used for $^{99}$Tc determination in soil samples was reported previously$^{1)}$. Some amounts of the air-dried soil were used for the analysis of soil characteristics. A 100 mL

(85-140 g) portion of each sample was used for $^{137}$Cs determination with a Ge detecting system (Seiko EG&G).

A standard $^{99}$Tc solution (Amersham, TCZ.44) was used for calibrating ICP-MS. Technetium-95m (half-life: 61 d) was used as a yield monitor. It was prepared by irradiation of Nb in a cyclotron to avoid any $^{99}$Tc contamination[2]. The radiochemical recovery of Tc was determined by comparing the counts of $^{95m}$Tc in the sample with that in the reference solution using a NaI (Tl) scintillation counter (Aloka, ARC-380). The $^{99}$Tc content of the sample solution was then determined by ICP-MS (Yokogawa, PMS-2000). To check levels of potential interference elements (e.g., Ru, Mo), m/z = 98, 101 and 102 were also scanned at the same time. The average radiochemical recovery of $^{95m}$Tc from the soil samples was 63 ± 6% by the present method. The instrumental detection limit for $^{99}$Tc by ICP-MS was 0.03 mBq/mL of the sample solution, corresponding to 0.014 mBq/g-dry of soil sample under the operational conditions.

## RESULTS AND DISCUSSION

The concentrations of $^{99}$Tc and $^{137}$Cs in paddy field soils are listed in Table 1. The ranges of $^{99}$Tc and $^{137}$Cs concentrations are 6 – 88 mBq/kg-dry (average: 29 mBq/kg-dry) and 1.4 – 14 Bq/kg-dry (average: 6.3 Bq/kg-dry), respectively. The activity ratios of $^{99}$Tc to $^{137}$Cs are given in the last column of the Table, ranging from $1.1 \times 10^{-3}$ to $7.0 \times 10^{-3}$. Theoretically, the activity ratio from nuclear fission yield is presently calculated as $3.3 \times 10^{-4}$ with correction for radioactive decay, because the major source of $^{99}$Tc and $^{137}$Cs in Japan should be attributed to global fallout from nuclear tests. Compared to the theoretical ratio, the activity ratios in the paddy field soils are one order of magnitude higher, suggesting that $^{99}$Tc has been accumulated in the soils[3]. The concentration of $^{99}$Tc was compared with several characteristics of the soils, e.g., cation exchange capacity, pH, active-Fe, total carbon and so on, but there was no correlation. Presumably, immobilization of Tc in soil was mainly controlled by redox conditions and was not affected by soil characteristics.

The high $^{99}$Tc/$^{137}$Cs activity ratio in soil would be influenced by several factors, i.e., the ratios in depositions containing rain and dry fallout and the change of Tc chemical form in soil under environmental conditions. Paddy fields are generally waterlogged during the planting period and subsequently, the redox potential decreases because of a decrease of oxygen concentration by microorganisms' activity[4]. Although $^{99}$Tc is expected to be in a soluble form of $TcO_4^-$ in surface soils and water under aerobic conditions, Tc changes its chemical form under reducing condition from $Tc^{VII}O_4^-$ to a lower oxidation form such as $Tc^{IV}O(OH)_2$, having lower solubility and strong absorption ability onto soil. Thus, Tc would be immobilized on the soils. Then, the paddy fields are kept dry after harvesting rice, and the redox potential of the soils gradually increases. In our previous radiotracer study, however, we found that most of the Tc retained in the soil was not in a readily soluble form even under aerobic conditions[5]. When Tc was transformed from $TcO_4^-$ to other chemical forms that have a low bioavailability, plants would not absorb Tc in the soil. Thus, $^{99}$Tc would be accumulated in the paddy field soils.

Relatively high $^{99}$Tc concentrations (Table 1) in paddy fields compared to those in other soils[3] suggest that $^{99}$Tc was immobilized not only from direct deposition but also from irrigation water through the mechanism as mentioned above. The average Japanese paddy field receives 1800 mm of irrigation water during the irrigation season, which is twice as much as the water supply from precipitation. The irrigation water would contain $^{99}$Tc leached from other soil sites, e.g., forest soils. Some part of the $^{99}$Tc in the water could be trapped onto the paddy field soil surface, though there are no data on $^{99}$Tc in water for irrigation. Further studies are needed to understand $^{99}$Tc behavior in the terrestrial environment.

## References

1) Tagami K. and Uchida S., Radioact. Radiochem. **10** (1999) 30.
2) Sekine T., Konishi M., Kudo H., Tagami K. and Uchida S., J. Radioanal. Nucl. Chem. **239** (1999) 483
3) Tagami K. and Uchida S., J. Nucl. Radiochem. Sci. **3** (2002) 1.
4) Tagami K. and Uchida S., Chemosphere **33** (1996) 217.
5) Tagami K. and Uchida S., Chemosphere **38** (1999) 963.

Table 1. Concentrations of $^{137}$Cs and $^{99}$Tc in paddy field soils in Japan on a dry weight basis and activity ratio of $^{99}$Tc to $^{137}$Cs.

| Sampling site<br>Prefecture / City or Town | $^{137}$Cs (Bq/kg)<br>Decay corrected to 2001.1.1 | $^{99}$Tc (mBq/kg) | Activity ratio<br>$^{99}$Tc/$^{137}$Cs (x $10^{-3}$) |
|---|---|---|---|
| Ibaraki / Mito | 2.7 ± 0.3 | 8.4 ± 1.3 | 3.2 ± 0.6 |
| Hiroshima / Fukuyama | 1.4 ± 0.7 | 6.1 ± 0.5 | 4.4 ± 2.3 |
| Saga / Imari | 14.0 ± 0.6 | 88 ± 15 | 6.3 ± 1.1 |
| Saga / Kawazoe | 4.1 ± 0.4 | 22 ± 3 | 5.4 ± 0.9 |
| Akita / Omagari | 14.0 ± 0.5 | 34 ± 5 | 2.4 ± 0.4 |
| Aomori / Misawa | 6.3 ± 0.5 | 6.8 ± 0.7 | 1.1 ± 0.1 |
| Iwate / Morioka | 8.4 ± 0.5 | 52 ± 10 | 6.2 ± 1.3 |
| Fukushima / Koriyama | 1.7 ± 0.2 | 12 ± 1.7 | 7.0 ± 1.4 |
| Fukushima / Koriyama | 4.2 ± 0.4 | 29 ± 4 | 7.0 ± 1.1 |

Note) Error shows statistical errors in calculation (1 σ)

# II. 2. Preparation of *O*-[$^{18}$F]Fluoromethyl-L-Tyrosine as a Potential Tumor Imaging Agent

*Iwata R., Furumoto S.*[*], *Pascali C.*[**], *Bogni A.*[**], *and Ishiwata K.*[***]

*CYRIC Tohoku University*
*Institute of Development, Aging and Cancer, Tohoku University*[*]
*National Cancer Institute, Milan, Italy*[**]
*Tokyo Metropolitan Institute of Gerontology*[***]

Many positron-emitting amino acids have so far been developed for imaging tumor by PET. Among them, *O*-[$^{18}$F]fluoroethyl-L-tyrosine ([$^{18}$F]FET)[1)] is expected to be the most promising tracer currently under investigation[2)]. It can be produced in large quantities owing to the preparation from [$^{18}$F]fluoride and its high radiochemical yield. Although this synthesis has recently been improved using a new precursor[3)], it was originally prepared by the reaction of 2-[$^{18}$F]fluoroethyl tosylate with tyrosine disodium salt in DMSO. Noting this method, we have developed a convenient method for the preparation of *O*-[$^{18}$F]fluoromethyl-L-tyrosine as a novel $^{18}$F-labeled tyrosine analogue from [$^{18}$F]fluoromethyl triflate, which was introduced as a versatile, reactive [$^{18}$F]fluoromethylating agent[4)].

[$^{18}$F]Fluoromethyl triflate ([$^{18}$F]$CH_2FOTf$) was synthesized from [$^{18}$F]fluoride via [$^{18}$F]fluoromethyl bromide according to the reaction scheme shown in Fig. 1. Briefly, [$^{18}$F]fluoromethyl bromide was prepared by the K.222-supported substitution of [$^{18}$F]fluoride with $CH_2Br_2$ (Aldrich, 50 μL) and distilled from a reaction vessel with a He flow (100 mL/min)[4)]. It was then passed through a AgOTf column heated at 200°C and converted to [$^{18}$F]fluoromethyl triflate in decay-corrected radiochemical yields of 47±8% based on [$^{18}$F]fluoride. The [$^{18}$F]$CH_2FOTf$ was introduced under the He current into DMSO (0.5 mL) containing L-tyrosine disodium (Aldrich, 0.5-2.3 mg) at room temperature. After bubbling the reaction solution was diluted with an HPLC solvent (water-ethanol-acetic acid=875/100/25, 0.5 mL) and the mixture injected onto an HPLC column (YMC ODS A-324, 10 x 300 mm, see Fig. 2). A fraction of the desired product eluting between 10 and 12 min was collected and evaporated to dryness. The residue was finally dissolved in saline. The overall synthesis time was 50 min from the EOB.

One of the main advantage in using triflates as labeling agents in nucleophilic substitution reactions is their higher reactivity than that of the corresponding halides, a favorable feature which allows the reaction to proceed rapidly even at room temperature. As seen in Table 1, [$^{18}$F]CH$_2$FOTf showed reasonable conversion rates at room temperature even after just one minute, while the production yield showed a dependence on the amount of precursor used. The higher boiling point of [$^{18}$F]CH$_2$FOTf is also advantageous to efficient trapping of flowing [$^{18}$F]CH$_2$FOTf. It was trapped in 75-87% yields with 0.5 mL DMSO.

*O*-[$^{18}$F]Fluoromethyl-L-tyrosine was obtained in overall decay-corrected radiochemical yields of >50% within 50 min. It turned out that *O*-[$^{18}$F]fluoromethyl-L-tyrosine was stable in saline over 2 hr.

**References**

1) Wester H.J., Herz M., Weber W., Heiss P., Senekowitsch-Schmidtke R., Schwaiger M. and Stöcklin G., J. Nucl. Med. **40** (1999) 205.
2) Laverman P., Boerman O.C., Corstens F.H.M. and Oyen W.J.G., Eur. J. Nucl. Med. **29** (2002) 681.
3) Hamacher K. and Coenen H.H., Appl. Radiat. Isot. **57** (2002) 853.
4) Iwata R., Pascali C., Bogni A., Furumoto S., Terasaki K. and Yanai K., Appl Radiat Isot. **57** (2002) 347.

Table 1. Radiochemical yields of *O*-[$^{18}$F]fluoromethyl-L-tyrosine.

| Precursor amount*1 | Reaction time*2 | RCY*3 |
|---|---|---|
| 0.5 mg | 1 min | 51% |
| 0.5 mg | 5 min | 66% |
| 0.5 mg | 10 min | 71% |
| 1 mg | 1 min | 78% |
| 1 mg | 5 min | 87% |
| 2.3 mg | 1 min | 84% |

*1Dissolved in 0.5 mL DMSO. *2Additional reaction time after bubbling at room temperature. *3Decay-corrected radiochemical yield, based on the labeling agent.

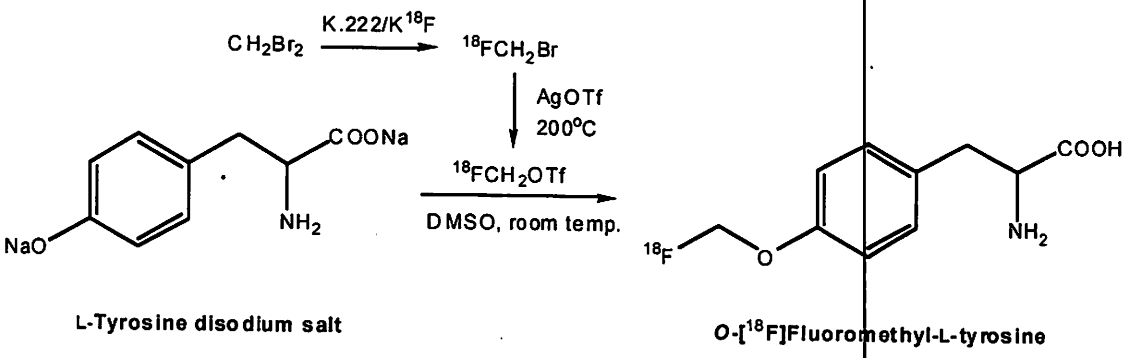

Figure 1. A synthetic scheme of *O*-[$^{18}$F]fluoromethyl-L-tyrosine from [$^{18}$F]fluoride.

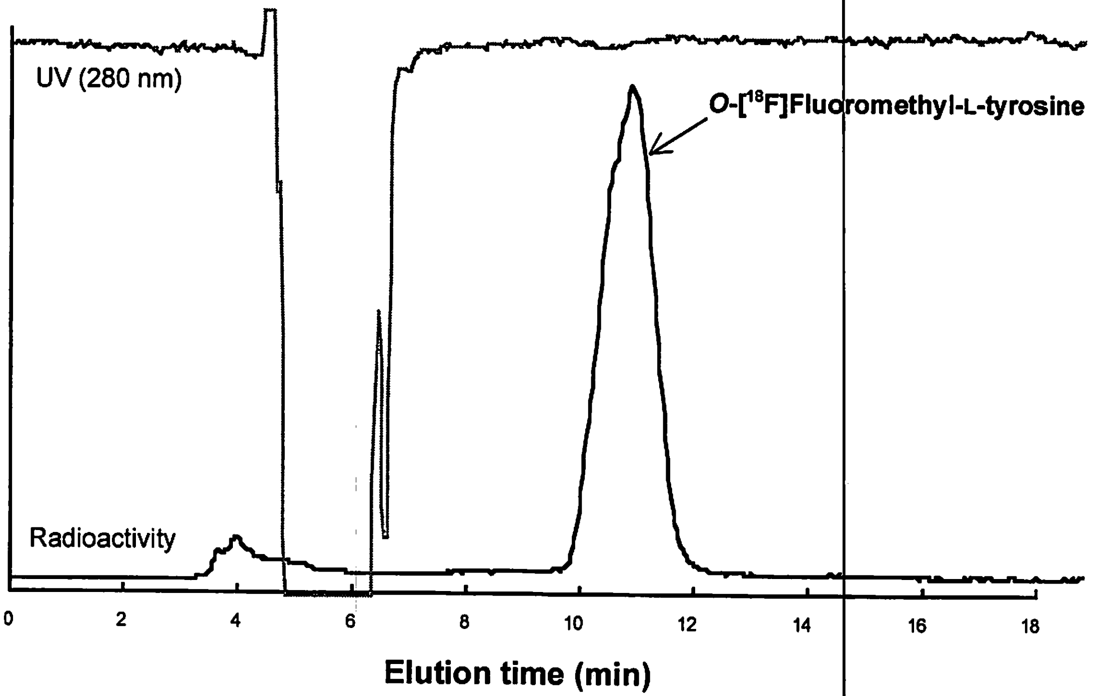

Figure 2. A typical HPLC purification profile

- Column: YMC A-324
- Solvent: water-EtOH-AcOH (875/100/25)
- Flow rate: 4.0 mL/min

# III. MEDICINE AND BIOLOGY (Basic)

# III. 1. Changes of Brain Distribution of [$^{11}$C]methamphetamine by Pentobarbital Anesthesia in Mice

*Hishinuma T.*[*,**], *Nakagawa N.*[**], *Nakamura H.*[***], *Iwata R.*[****], *and Goto J.*[*,**]

*Division of Clinical Pharmacy, Graduate school of Pharmacy, Tohoku University*[*]
*Department of Pharmaceutical Science, Tohoku University Hospital*[**]
*Information Science Center, Tohoku Pharmaceutical University*[***]
*Cyclotron Radioisotope Center, Tohoku University*[****]

## Introduction

We previously studied the variation of the brain distribution of methamphetamine (MAP) following the repeated administration of MAP and found the significant increase in [$^{11}$C]MAP uptake in the brains both of MAP-sensitized mouse$^{1)}$ and rat$^{2)}$. In addition, we reported that the accumulation of [$^{11}$C]MAP in the MAP-sensitized dog brain was 1.4 times higher than that in the control using the positron emission tomography (PET) study$^{3)}$. These results suggested that the uptake of MAP increased in the brain of MAP-sensitized animals. However, studying [$^{11}$C]MAP uptake in a MAP-sensitized rhesus monkey using PET, [$^{11}$C]MAP uptake significantly decreased. We considered whether this result related to the anesthesia. Then we investigated the influence of anesthesia on the brain distribution of [$^{11}$C]MAP by PET using two normal rhesus monkeys under intravenous anesthesia or inhalation anesthesia$^{4)}$. As a result, the uptake of [$^{11}$C]MAP in the brain under halothane anesthesia was faster and higher than that under pentobarbital anesthesia$^{4)}$.

In the present study, since it is not clear whether the effect of anesthesia in the MAP-sensitized animals influences to the brain distribution of MAP, we examined the effect of pentobarbital anesthesia on the brain distribution of [$^{11}$C]MAP in the MAP-sensitized mice. We report here the over-accumulation of [$^{11}$C]MAP in the MAP-sensitized mice brain might be masked under pentobarbital anesthesia.

## Material and methods

Male ddY mice, 12 weeks old and weighing 37.0 – 47.5 g each, were used. They were maintained on a 12 h light-dark cycle and given free access to food and water. The investigations using the mice described in this report conformed to the provisions of the Animal Care Committee, cyclotron and radioisotope center, Tohoku University.

The mice in MAP sensitization model were intraperitoneally injected with 4 mg/kg of MAP once daily for 7 consecutive days. The mice in the control model received an equal volume of saline for the same length of time. After 7 consecutive days of withdrawal in each model, stereotyped behavior was scored using a stereotypy rating scale of Creese and Iversen[5], after the administration of the drug, and we confirmed the expression of behavioral sensitization in MAP sensitization model. Respective mice models were divided in no anesthesia group and pentobarbital anesthesia group. The mice in pentobarbital anesthesia group were intraperitoneally administered 60 mg/kg of pentobarbital 20 min before injection of [$^{11}$C]MAP. We used 4 mice in each group and model.

Synthesis of [$^{11}$C]MAP was carried out by modifying the on-line [$^{11}$C]methylation method[6]. A 0.2 mL (7.4 MBq) of [$^{11}$C]MAP was intravenously injected in each mouse. Mice were decapitated at 15 min after injection and the brains were immediately removed. Eight brain regions included the striatum, frontal cortex, hypothalamus, posterior cortex, hippocampus, midbrain, cerebellum and medulla oblongata were analyzed according to the method of Glowinski and Iversen[7]. The radioactivity of $^{11}$C in each area was counted and weighed. [$^{11}$C]MAP distribution in each area was represented as the differential absorption ratio (DAR). DAR was calculated as (observed tissue radioactivity / tissue weight) / (injected radioactivity / body weight). The statistical analysis was performed using Stat View software (Abacus Concepts Inc. Berkeley, CA, USA). Student t-test was used to analyze the findings. Differences were considered significant at $p<0.05$.

## Results

Figure 1 shows the result of the influence of pentobarbital anesthesia on the distribution of [$^{11}$C]MAP in 8 brain regions in mice. The pentobarbital anesthesia groups showed the significant decrease compared with no anesthesia groups. The extents of decrease were greater in MAP-sensitized mice than those of the control mice.

## Discussion

In the present study, we suggested that the pentobarbital anesthesia made decreased the uptake of [$^{11}$C]MAP in the mouse brain. Moreover it significantly made decreased the distributions of [$^{11}$C]MAP in the MAP-sensitized mice brain compared with the control mice, implying that the pentobarbital anesthesia could mask the over-accumulation of MAP in the MAP-sensitized mice in no anesthesia. Gjedde and Rasmussen reported that the pentobarbital anesthesia (40 mg/kg) resulted in a 50% decrease in cerebral blood flow (CBF) of the rat brain and that unidirectional blood-brain glucose transfer decreased in proportion to CBF in pentobarbital anesthesia8). Linde et al. measured CBF using the Kety-Schmidt technique that enables repetitive simultaneous determination of CBF on awake, non-stressed animals, obtaining the data that anesthesia with pentobarbital induced a uniform reduction of CBF by 40%, during halothane anesthesia CBF increased by 50%9). Therefore we consider that the decrease of distribution of [$^{11}$C]MAP might depend on the variation of CBF due to the pentobarbital anesthesia.

It has been reported that cardiac muscle lesions are associated with the chronic administration of MAP in rats10), the cardiomyopathy was associated with the amphetamine administration in humans11) and MAP directly induced cellular hypertrophy and might lead to cardiac functional disorder12). In addition, Bachmann *et al.* reported the cardiac potassium currents were inhibited by pentobarbital13) and Wartenberg *et al.* reported the human cardiac sodium channel was blocked by pentobarbital14). Taking these reports, it is considered that the pentobarbital further makes diminished the cardiac function of MAP-sensitized mice which have already been inhibited due to the chronic administration of MAP. The inhibition of cardiac function both by MAP-sensitization and pentobarbital anesthesia is possible to cause the decrease of blood-output to the brain and to make decrease the CBF. Therefore we consider the uptake of [$^{11}$C]MAP was significantly decreased depending on the decrease of CBF in the MAP-sensitized model with pentobarbital anesthesia. As Yang pointed out15), there is a difficulty in interpreting data obtained from anesthetized mice.

As a result, it suggest that the uptake of [$^{11}$C]MAP was significantly decreased depend on the reduce of CBF in the MAP-sensitized mice in the pentobarbital anesthesia. There is some possibility to masking the over-accumulation of MAP to MAP-sensitized mice. The effect of anesthesia is an important problem in pharmacokinetic study.

## References

1) Mizugaki M., HishinumaT., Nakamura H. et al., Nucl. Med. Biol. **20** (1993) 487.
2) Numachi Y., Yoshida S., Inosaka T. et al., Ann. N. Y. Acad. Sci. **654** (1992) 153.
3) Mizugaki M., Nakamura H., Hishinuma T. et al., Nucl. Med. Biol. **22** (1995) 803.
4) Mizugaki M., Nakagawa N., Nakamura H. et al., Brain Res. **911** (2001) 173.
5) Creese I. and Iversen S. D., Brain Res.,**55** (1973) 369.
6) Mizugaki M. et al., CYRIC Annual Report (1993) 93.
7) Glowinski J. and Iversen L.L., J. Neurochem. **13** (1966) 655.
8) Gjedde A., Rasmussen M., J. Neurochem. **35** (1980) 1382.
9) Linde R., Schmalbruch I.K., Paulson OB. et al., Acta. Physiol. Scand. **165** (1999) 395.
10) He S.Y., Matoba R., Fujitani N. et al., Am. J. Forensic. Med. Pathol., **17** (1996) 155.
11) Smith H. J., Roche A. H., Jausch M. F. et al., Am Heart J. **91** (1976) 792.
12) Maeno Y., Iwasa M., Inoue H. et al., Forensic. Sci. Int. **113** (2000) 239.
13) Bachmann A., Mueller S, Kopp K. et al., Naunyn. Schmiedebergs Arch. Pharmacol. 365 (2002) 29.
14) Wartenberg H. C., Wartenberg J. P. and Urban B. W., Eur. J. Anaesthesiol. **18** (2001) 306.
15) Yang X. P., Liu Y. H., Rhaleb N. E. et al., Am. J. Physiol. **277** (1999) 1967.

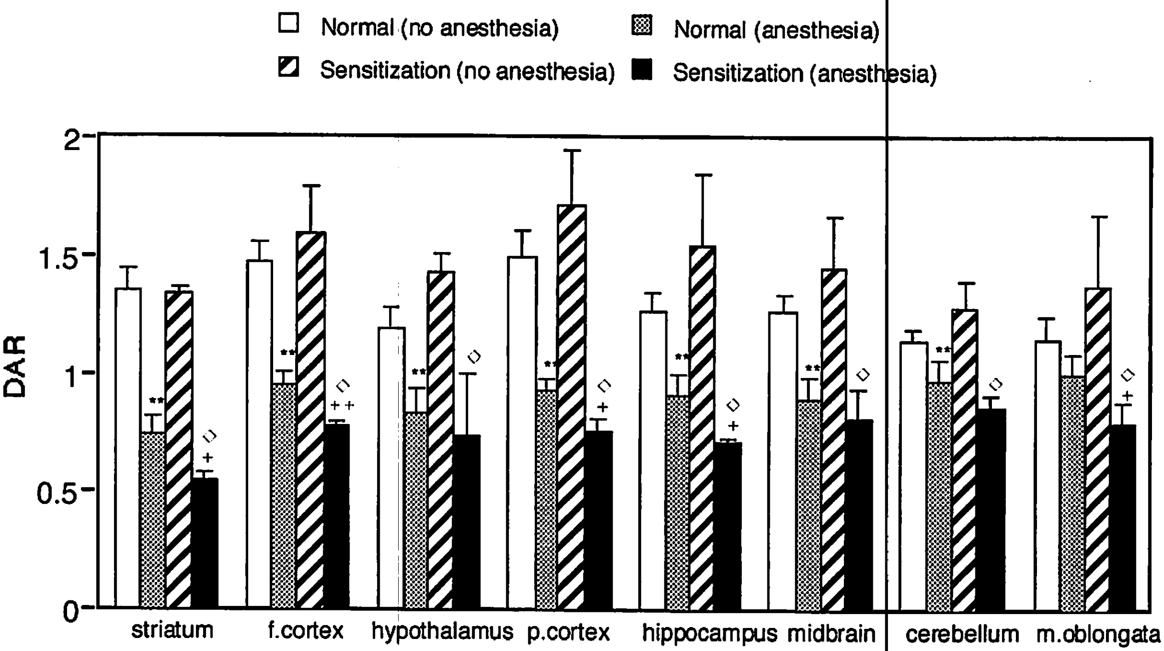

Fig. 1. The influence of pentobarbital anesthesia on brain distribution of [$^{11}$C]methamphetamine in mice. The values represent means ± S. E. M. of 4 animals per group. $^{**}$ p<0.01 vs normal (no anesthesia). $^{+}$p<0.05, $^{++}$p<0.01 vs normal (anesthesia). $^{\diamond}$p<0.01 vs sensitization (no anesthesia).

# III. 2 Biological Evaluation of [5-$^{11}$C-*methoxy*]Donepezil in the Rat Brain

*Funaki Y., Kato M.*, Iwata R., Sakurai E.*, Sakurai E.**, Tashiro M., Ido T., and Yanai K.**

*Cyclotron and Radioisotope Center, Tohoku University*
*Graduate School of Medicine, Tohoku University**
*Tohoku Pharmaceutical University***

## Introduction

Alzheimer's disease (AD) is an age-related and progressive neurodegenerative disease of the central nervous system. At the cellular levels, there were marked neurodegenerative changes accompanied with a reduction in many neurotransmitters and neuropeptides. A remarkable dysfunction of the cholinergic system, characterized by deficits in memory and cognitive functions, has been observed in several brain regions of patients suffering from AD[1,2,3] Especially, acetylcholinesterase (AChE, EC 3.1.1.7) activities in the neocortex and the hippocampus is reported to be lowered in AD[4], and decreased activity correlates with the severity of cognitive impairment[5]. These pathological findings have led to the hypothesis that enhancement cholinergic neurotransmission with cholinergic agent, either AChE inhibitors or cholinergic agonists, may ameliorate the cognitive impairment in AD. Although many attempts have been made to reverse cognitive impairment using cholinergic agents, AChE inhibitors are the only class of drugs for the treatment of AD. Recently, one promising AChE inhibitor, donepezil, was developed and has been successfully used for treatment of AD. It is reported that this agent has a high affinity and selectivity for AChE with an excellent efficacy and fewer undesired pharmacological effects[6].

In the present study, we describe the synthesis of [5-$^{11}$C-*methoxy*]donepezil using [$^{11}$C]methyl triflate from 5'-*O*-desmethylprecursor, and the biological evaluation of [5-$^{11}$C-*methoxy*]donepezil.

## Materials and Methods

Male Wistar rats (Japan SLC, Shizuoka, Japan; 5 weeks) were used in these studies. They were fed food and water *ad libitum*. The animal study was carried out according to the protocol approved by the Animal Care Committees of Cyclotron and Radioisotope Center.

The rats were injected intravenously with 7.4 MBq (200 $\mu$Ci) of [$^{11}$C]donepezil in 0.2 mL of physiological saline via tail vein. The rats were killed at the four time points (10, 20, 40 and 60 min). Samples of blood and six brain tissues (cerebral cortex, striatum, hippocampus, cerebellum, midbrain and brain stem) were quickly removed, weighed, and counted. The amount of radioactivity was expressed as DAR (differential absorption ratio). DAR is defined as follows; [observed radioactivity in the tissue] x [body weight] / [weight of tissue] / [injected radioactivity].

The saturation experiments were performed in order to demonstrate the reversibility of [$^{11}$C]donepezil binding *in vivo*. A large amount of unlabeled donepezil (0.1, 1 or 5 mg/kg) was intraperitoneally (i.p) administered with rats 20 min before [$^{11}$C]donepezil injection. The rats were sacrificed 40 min after the injection.

## Results and discussion

The radio-synthesis was carried out by the loop-SPE method described in our previous paper[7,8,9]. [$^{11}$C]Donepezil was successfully synthesized by *O*-methylation of 5'-*O*-desmethylprecursor (M2) using the loop method with [$^{11}$C]MeOTf (Fig.1). The radioactivity of [$^{11}$C]donepezil was approximately 92.5-814 MBq (2.5-22 mCi) after 20 min irradiation and radiochemical yield was calculated to be 25-30% based on [$^{11}$C]MeOTf after decay-correction. The specific activity of [$^{11}$C]donepezil was 19-122 GBq/$\mu$mol (0.51-3.30 Ci/$\mu$mol) at the end of synthesis (30-40 min after the bombardment). The radiochemical purity was more than 99%.

Table 1 demonstrates the time course of [$^{11}$C]donepezil binding *in vivo*. The values of DAR in brain tissues were higher than that in the blood, suggesting that [$^{11}$C]donepezil easily penetrates through the blood-brain barrier. Forty min after injection, the distribution of [$^{11}$C]donepezil was heterogeneous in the brain; it was especially higher in the striatum and brain stem. Our *in vitro* binding study demonstrated [$^{11}$C]donepezil binding was the lowest in the cortex[9]. Therefore, the data of *in vivo* binding was calculated as the ratio of tissue to cortex. The ratios of striatum-to-cortex and brain stem-to-cortex were approximately 1.4 and 1.5 respectively.

In the blocking study, the distribution was measured 40 min after [$^{11}$C]donepezil injection. The ratios of striatum-to-cortex and brain stem-to-cortex were significantly reduced from 1.4 ± 0.2 to 1.0 ± 0.1 (n=4, $p<0.05$) and 1.5 ± 0.1 to 1.1 ± 0.1 (n=4, $p<0.01$), respectively, by the administration of donepezil (5 mg/kg, i.p). To confirm the reversibility of [$^{11}$C]donepezil binding *in vivo*, the dose effects on tissue to cortex ratios were examined 40 min after the injection of [$^{11}$C]donepezil. As shown in Fig.2, the striatum-to-cortex and the brain stem-to-cortex ratios were reduced with increasing amounts of donepezil, whereas the hippocampus-to-cortex ratio did not change with the injected dose. This result indicates that [$^{11}$C]donepezil specifically binds to the AChE rich regions. On the other hand, the binding in the hippocampus was not displaced by unlabeled donepezil, indicating the higher nonspecific binding of [$^{11}$C]donepezil to the hippocampus.

In conclusion, we have successfully synthesized [5-$^{11}$C-*methoxy*]donepezil using [$^{11}$C]MeOTf. *In vivo* brain distribution of [$^{11}$C]donepezil in the rat brain was heterogeneous, and it was displaced by unlabeled donepezil. Although further studies are needed, this study clearly demonstrates that this strategy is useful to visualize AChE in the living human brain and to evaluate the efficacy of therapy of AChE inhibitors.

**References**

1) Bowen D.M., Smith C.B., White P. and Davison A.N., Brain **99** (1976) 459.
2) Cummings J.L. and Kaufer D., Neurology **47** (1996) 876.
3) Engelborghs S. and De Deyn P. P., Acta Neurol. Belg. **97** (1997) 67.
4) Davis P. and Maloney A.J.F., Lancet **2** (1976) 1403.
5) Perry E.K., Tomlinson B.E., Blessed G., Bergman K., Gibson P.H. and Perry R.H., Br. Med. J. **2** (1978) 1456.
6) Sugimoto H., Iimura Y., Yamanishi Y. and Yamatsu K., J. Med. Chem. **38** (1995) 4821.
7) Iwata R., Pascali C., Bogni A., Miyake Y., Yanai K. and Ido T., Appl. Radiat. Isot. **55** (2001) 17.
8) Iwata R., Pascali C., Bogni A., Yanai K, Kato M., Ido T. and Ishiwata K., J. Labelled Cpd. Radiopharm. **45** (2002) 271.
9) Funaki Y., Kato M., Iwata R., Sakurai E., Sakurai E., Tashiro M., Ido T. and Yanai K., J. Pharmacol. Sci. **92** (2003) 105.

Table 1. *In vivo* distribution of [$^{11}$C]donepezil in the rat blood and brain.

| **Tissue** | **Time after injection** | | | |
|---|---|---|---|---|
| | 10 min | 20 min | 40 min | 60 min |
| Blood | 0.23 ± 0.02 | 0.17 ± 0.01 | 0.10 ± 0.00 | 0.13 ± 0.00 |
| Cortex | 0.48 ± 0.09 | 0.53 ± 0.02 | 0.57 ± 0.08 | 0.29 ± 0.01 |
| Striatum | 0.74 ± 0.09 | 0.61 ± 0.06 | 0.72 ± 0.08 | 0.37 ± 0.03 |
| Hippocampus | 0.41 ± 0.06 | 0.49 ± 0.01 | 0.58 ± 0.07 | 0.33 ± 0.06 |
| Cerebellum | 0.49 ± 0.07 | 0.56 ± 0.02 | 0.64 ± 0.07 | 0.38 ± 0.01 |
| Midbrain | 0.47 ± 0.07 | 0.56 ± 0.02 | 0.65 ± 0.07 | 0.36 ± 0.01 |
| Brain stem | 0.53 ± 0.04 | 0.65 ± 0.03 | 0.85 ± 0.14 | 0.55 ± 0.02 |

DAR values are expressed as means ± S.E.M (n=3~8)

Fig. 1. Radio-synthesis of [$^{11}$C]donepezil.

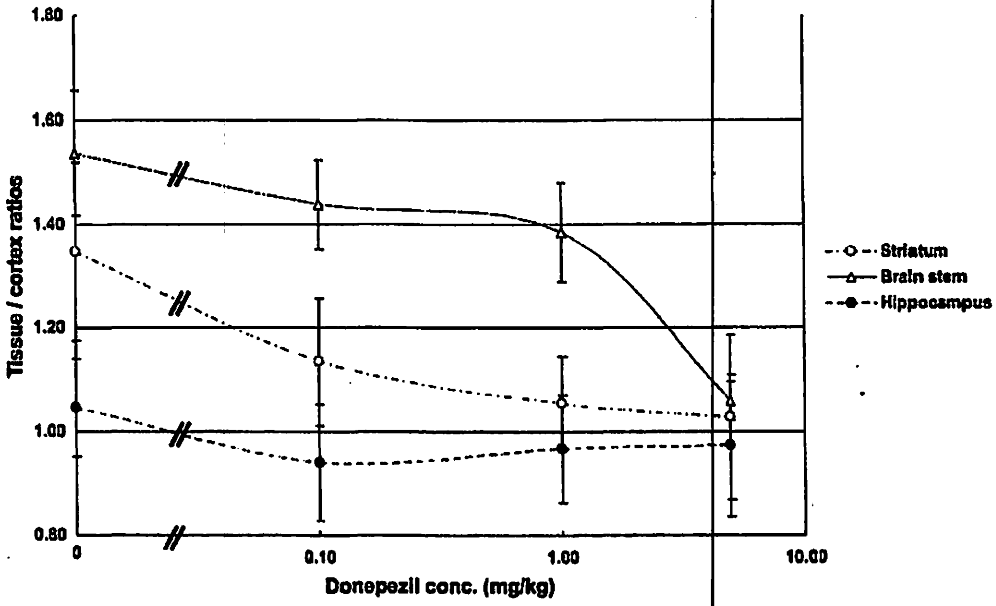

Fig. 2. The *in vivo* binding of [$^{11}$C]donepezil. Dose-dependent inhibition of [$^{11}$C]donepezil binding *in vivo*. Tissue-to-cortex ratios as a function of donepezil dose at 40 min after [$^{11}$C]donepezil injection.

# III. 3. Preliminary Biological Evaluation of Fluorine-18 Labeled MMP-2 Inhibitor for Cancer Imaging by PET

*Furumoto S.*[*, **], *Takashima K.*[**], *Kubota K.*[*], *Iwata R.*[**], *Ido T.*[**],
*and Fukuda H.*[*]

*Institute of Development, Aging, and Cancer*[*]
*Cyclotron and Radioisotope Center Tohoku University*[**]

## Introduction

Matrix metalloproteinases (MMPs) are a family of zinc-dependent enzymes that degrade specific components of the extracellular matrix. At present, they are known to include at least 20 enzymes and are classified into five groups according to their domain structure and substrate specificity: collagenases, gelatinases, stromelysins, membrane-type MMPs and others[1)]. Among MMPs, gelatinases (MMP-2 and MMP-9) have been shown to be involved in tumor invasiveness, metastasis, and angiogenesis, and increased expressions of them, especially MMP-2, have been found in a variety of malignant tumors.

To date, many types of PET tracers for tumor imaging have been developed. For example, [$^{18}$F]2-deoxy-2-fluoro-D-glucose and L-[methyl-$^{11}$C]methionine are the most widely and successfully used for clinical diagnosis of cancers[2)]. Tumor uptake of both tracers is considered to be correlated to tumor proliferation, which is an important feature of tumor malignancy. Another critical aspect of malignancy is tumor invasiveness. However, there is no PET tracer that is directly applicable for evaluating the invasiveness. Tracers that target MMPs should be clinically useful for predicting cancer invasiveness by PET. Furthermore, the imaging of MMP expression and/or activity by PET would be beneficial for clinical evaluation of pharmacological effects and therapeutic usefulness of MMP inhibitors. We recently reported the design of a fluorine-18 labeled MMP inhibitor, [$^{18}$F]SAV03, and established a method for radiosynthesis[3)]. In an extension to that study, we describe here the results of biodistribution studies on [$^{18}$F]SAV03 and on its methyl ester derivative, [$^{18}$F]SAV03M, used as a prodrug[4)].

## Results and Discussion

Biodistribution studies on [$^{18}$F]SAV03 were performed using Ehrlich tumor bearing mice as a tumor model, because Ehrlich ascites cells growing *in vivo* have the potential to produce MMP-2 during tumor growth. Tissue distribution data of [$^{18}$F]SAV03 and [$^{18}$F]SAV03M at 30 and 120 min post-injection are summarized in Table 1. [$^{18}$F]SAV03 showed higher uptake in tumor compared with muscles, heart, lung, spleen, kidney, and blood. Tumor/blood and tumor/muscle ratios were 2.31 ± 1.09 and 8.42 ± 3.31 at 120 min, respectively. However, a considerable radioactivity uptake was observed in the tissues of small intestine, liver, and bone. On the other hand, The biodistribution of [$^{18}$F]SAV03M in Ehrlich tumor-bearing mice was different from that of [$^{18}$F]SAV03. The radioactivity uptake in liver was approximately halved ($p<0.01$), and thus the uptake in blood, heart, lung, spleen, muscle, and brain showed statistically significant increase at 30 min after injection. The radioactivity uptake in tumor showed about 2.4 fold increase at 120 min after injection.

The time course study on [$^{18}$F]SAV03M biodistribution showed that the radioactivity uptake in the small intestine increased to a peak level at 30 min post-injection, indicating clearance of the tracer by biliary excretion (Fig 2). The uptake in bone increased time-dependently, suggesting accumulation of fluorine-18 anion eliminated from the alkyl terminal of [$^{18}$F]SAV03M. The radioactivity uptake in tumor tissue showed a slight decrease with time, whereas the uptake in the liver, blood, lung, and muscle decreased gradually during 120-min period. Such tumor specific uptake of the radioactivity resulted in higher tumor/muscle ratio of 13.9.

In support of the above conclusion, whole body ARG using [$^{18}$F]SAV03M demonstrated relatively higher radioactivity uptake in the tumor than in other organs and tissues, except for bone and intestine (Fig 1). Considerable accumulation of radioactivity was observed within the intestine, indicating that most of the tracer and/or its metabolites were eliminated rapidly from the body through biliary excretion.

## Conclusion

The biodistribution studies on [$^{18}$F]SAV03 and [$^{18}$F]SAV03M, a carboxylic acid based MMP-2 inhibitor and its methyl ester derivative, demonstrated that the uptake was significantly higher in tumor tissue than in most of other organs and tissues. Specifically, the biodistribution properties of [$^{18}$F]SAV03M, which served as a prodrug of [$^{18}$F]SAV03, were superior to those of [$^{18}$F]SAV03, resulting in high tumor/organ uptake ratios of %ID/g in blood, heart, lung, spleen, muscle, and brain at 120 min post-injection. In addition, the tumor accumulation of radioactivity observed in whole body ARG suggests that [$^{18}$F]SAV03M is potentially suitable for visualizing tumors by PET.

**References**

1) Cawston T. E., Pharmacol. Ther. **70** (1996) 163.
2) Kubota K., Ann. Nucl. Med. **15** (2001) 471.
3) Furumoto S., Iwata R. and Ido T., J. Label. Compd. Radiopharm. **45** (2002) 975.
4) Furumoto S. *et al.*, Nucl. Med. Biol. **30** (2003) 119.

Table 1. Tissue distributions of [$^{18}$F]SAV03 and [$^{18}$F]SAV03M in Ehrlich tumor bearing-mice at 30min and 120 min after i.v. injection.

| | [$^{18}$F]SAV03 | | [$^{18}$F]SAV03M | |
|---|---|---|---|---|
| | **30 min (n=6)** | **120 min (n=5)** | **30 min (n=5)** | **120 min (n=4)** |
| Blood | 0.43 ± 0.08 | 0.10 ± 0.03 | 0.56 ± 0.09* | 0.19 ± 0.02** |
| Heart | 0.22 ± 0.03 | 0.05 ± 0.01 | 0.49 ± 0.07** | 0.08 ± 0.03 |
| Lung | 0.17 ± 0.07 | 0.04 ± 0.03 | 0.48 ± 0.14** | 0.08 ± 0.02 |
| Liver | 6.54 ± 1.66 | 1.29 ± 0.18 | 3.08 ± 0.18** | 1.06 ± 0.27 |
| Spleen | 0.16 ± 0.03 | 0.05 ± 0.01 | 0.28 ± 0.03** | 0.07 ± 0.01* |
| Kidney | 1.25 ± 0.48 | 0.28 ± 0.08 | 1.60 ± 0.39 | 0.39 ± 0.07 |
| Small Intestine | 12.3 ± 9.37 | 2.60 ± 1.13 | 15.1 ± 5.51 | 2.08 ± 0.28 |
| Bladder | 0.53 ± 0.28 | 0.11 ± 0.07 | 0.70 ± 0.29 | 0.20 ± 0.10 |
| Muscle | 0.12 ± 0.01 | 0.03 ± 0.01 | 0.31 ± 0.11* | 0.04 ± 0.01 |
| Bone | 5.13 ± 1.05 | 7.27 ± 1.31 | 3.28 ± 1.38* | 5.90 ± 0.90 |
| Brain | 0.04 ± 0.01 | 0.03 ± 0.01 | 0.54 ± 0.11** | 0.22 ± 0.03** |
| Tumor | 0.52 ± 0.16 | 0.22 ± 0.07 | 0.61 ± 0.18 | 0.53 ± 0.07** |
| T/B[a] | 1.21 ± 0.35 | 2.31 ± 1.09 | 1.12 ± 0.33 | 2.72 ± 0.27 |
| T/M[b] | 4.33 ± 1.62 | 8.42 ± 3.31 | 2.24 ± 1.34 | 13.9 ± 4.94 |

Values are mean ±SD of %ID/g. [a] The tumor/blood ratio of %ID/g. [b] The tumor/muscle ratio of %ID/g. * $p<0.05$, ** $p<0.01$ (Comparison of the uptake between [$^{18}$F]SAV03M and [$^{18}$F]SAV03 at each time point by Student's *t*-test)

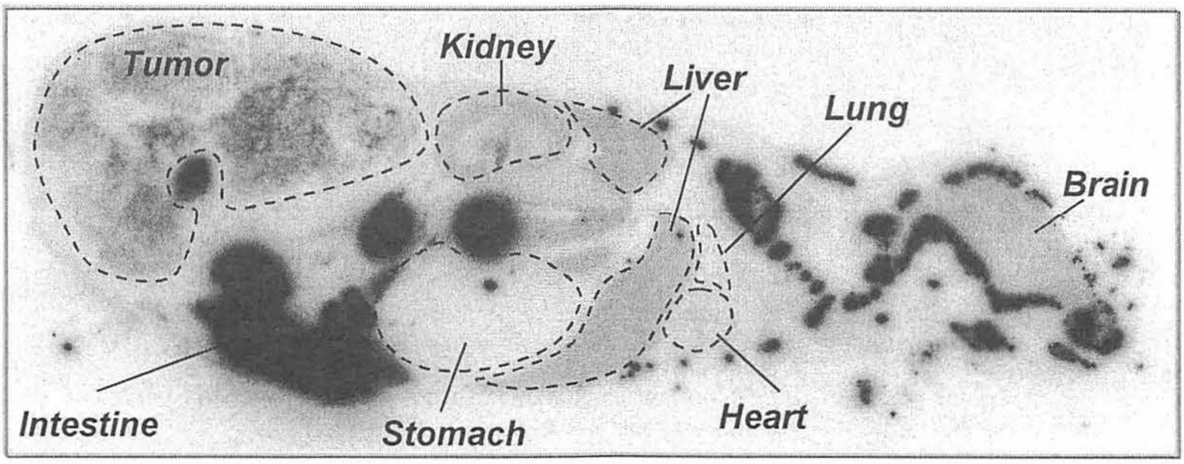

Fig. 1. Autoradiograph of whole body section of a mouse bearing an Ehrlich tumor. The section was prepared at 120 min after i.v. injection of [$^{18}$F]SAV03M. Gastric and intestinal contents were not removing during processing.

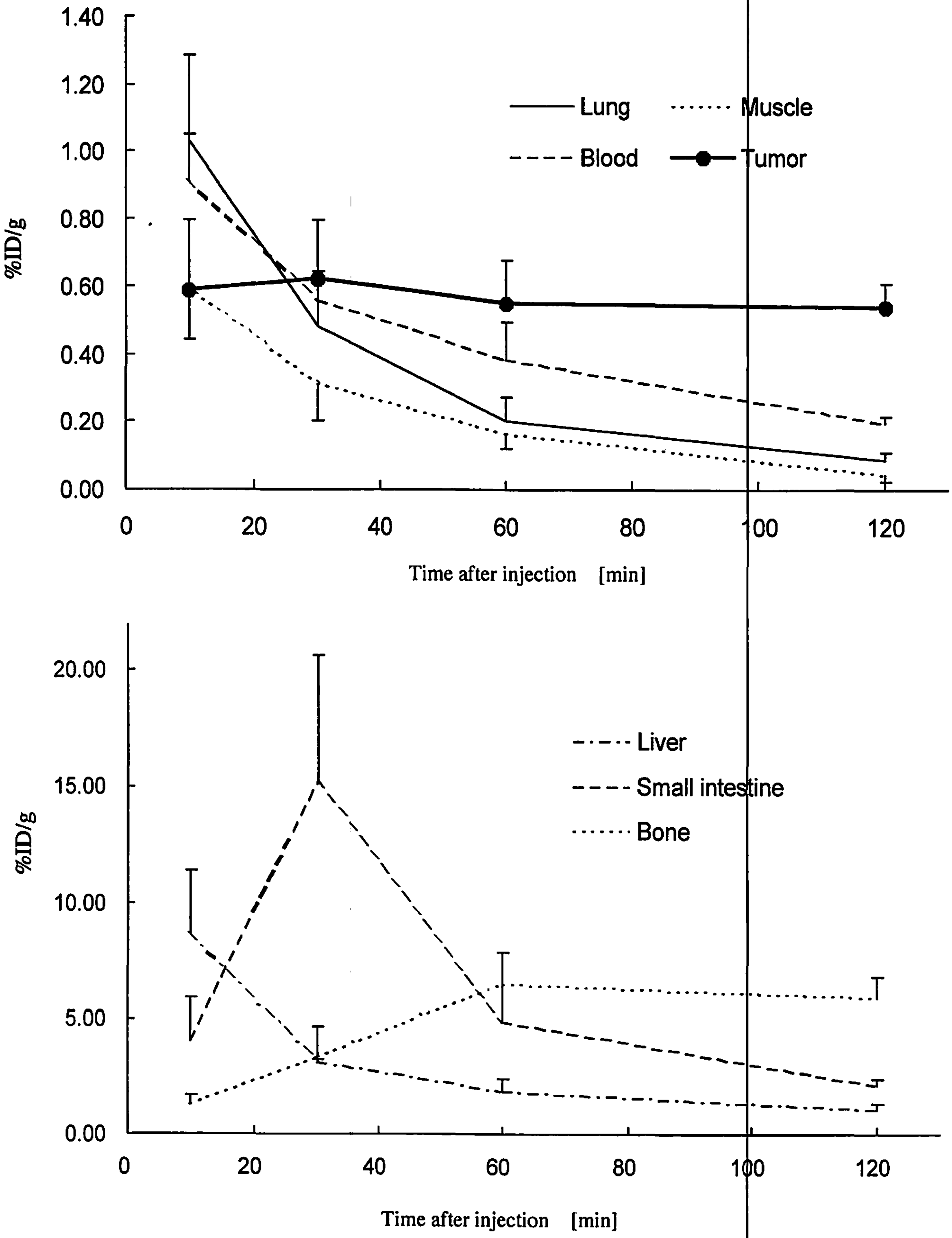

Fig. 2. Time course of radioactivity uptake after i.v. injection of [$^{18}$F]SAV03M in Ehrlich tumor-bearing mice (n=4-5). Values are mean ± SD.

# III. 4. Immunohistochemical Changes of S100 Protein in MPTP-Treated Mice

*Muramatsu Y.*[*], *Kurosaki R.*[*,**], *Harasawa T.*[*], *Hara A.*[*], *Kimura S.*[**], *Imai Y.*[*]
*and Araki T.*[*]

*Department of Clinical Pharmacology and Therapeutics, Tohoku University Graduate School of Pharmaceutical Science and Medicine*[*]
*Department of Human Life Science, Graduate School of Showa Women's University*[**]

## INTRODUCTION

Parkinson's disease is one of the major neurodegenerative disorders of middle and old age, involving progressive degeneration of dopaminergic neurons in the substantia nigra, resulting in deficiency of dopamine in the brain[1,2]. Dopamine replacement therapy has been used for decades and alleviates major symptoms of the disease, but the underlying cause of Parkinson's disease is enigmatic and available therapies do not halt the degeneration of dopaminergic neurons[3]. A critical goal is to find the cause of this desease and to develop new protective drugs designed to halt the progressive degeneration of the dopaminergic neurons or even to reverse the process.

1-Methyl-4-phenyl-1,2,3,6-tetrahydropyridine (MPTP) is a neurotoxin that produces a parkinsonian syndrome in both humans and experimental animals[4,5]. Its neurotoxic effects also appear to involve energy depletion and free radical generation. MPTP is converted to its metabolite 1-methyl-4-phenylpyridinium ion ($MPP^+$) by monoamine oxidase B[6]. $MPP^+$ is selectively accumulated by high affinity dopamine transporters and taken up by the mitochondria of dopaminergic neurons, where it disrupts oxidative phosphorylation by inhibiting complex I of the mitochondrial electron transport chain[7]. This leads to impairment of ATP production, elevated intracellular calcium levels, and free radical generation[8,9].

S100B is a calcium binding protein synthesized essentially in astroglial cells in the central nervous system (CNS) and Schwann cells[10,11]. Interestingly, a recent report suggests that increased S100B protein may contribute to the early diagnosis of brain death and is a promising serum outcome predictor for severe head injury victims[12]. However, little is known about the role of S100B protein during neuronal damage caused by MPTP. In the present study, therefore, we investigated immunohistochemical changes of S100 in relation to changes of neurons and glial cells after MPTP treatment.

## MATERIALS AND METHODS

Male C57BL/6 mice (Nihon SLC Co., Shizuoka, Japan), 8 weeks of age, were used in this study. The animals were housed in a controlled environment (23±1°C, 50±5% humidity) and were allowed food and tap water *ad libitum*. All experiments were performed in accordance with the Guidelines for Animal Experiments of the Tohoku University School of Medicine.

The mice were injected intraperitoneally (i.p.) with four administrations of MPTP (20 mg/kg) at 2-h intervals, the total dose per mouse being 80 mg/kg. The control animals were injected i.p. in the same manner with saline treatment instead of MPTP. The mice were anesthetized with sodium pentobarbital (50 mg/kg, i.p.) at 5 hours, 1, 3 and 7 days after MPTP treatment, and the brains were perfusion-fixed with 4% paraformaldehyde in 0.1M phosphate buffer (pH 7.4) following a heparinized saline flush. The brains were removed 1 h after perfusion fixation at 4°C and were immersed in the same fixative until they were embedded in paraffin. Paraffin sections, 5 μm in thickness, of the striatum and substantia nigra were used for immunohistochemistry. Each group consisted of five animals.

For immunostainings, rabbit anti-S100 polyclonal antibody (DAKO, Carpintera, CA, USA), mouse anti-glial fibrillary acidic protein (GFAP) monoclonal antibody (Chemicon International, Inc., Temecula, CA, USA), and Vectastain *elite* ABC kit (Vector Lab., Burlingame, USA) were used. The immunohistochemical staining with anti-S100 antibody (1:150) or anti-GFAP antibody (1:200) was carried out as described previously[13, 14]. Negative control sections were treated similarly, except that each antibody was omitted. Immunoreactions for S100 and GFAP staining were visualized using Vector DAB (3',3'-diaminobenzidine) substrate kit; some sections were then counterstained with hematoxylin. The immunostaining for S100 and GFAP was graded semiquantitatively as intense and swollen (grade 4), intense (grade 3), moderate (grade 2), weak (grade 1) and not detectable (grade 0). The number of S100-positive or GFAP-positive cells was also counted under light microscopy at a magnification of X400. The mean values of S100-positive or GFAP-positive cells were calculated. The average of right and left cells was regarded as the cell number of each animal. Values were expressed as means ± SD. Statistical significance was evaluated using the nonparametric Dunnett's multiple comparison test.

Double-labeled immunostaining with anti-S100 and anti-GFAP antibodies was performed in some brain sections of mice after MPTP treatment. The immunohistochemical staining with anti-GFAP antibody was carried out as described above. The next day, double-labeled immunostaining with anti-S100 antibody was performed as described above. Immunoreactions for GFAP and S100 staining were visualized using Vector DAB substrate kit and Vector SG substrate kit, respectively. Some brain sections of mice after MPTP treatment were also double-label immunostained with anti-S100 antibody and alpha-D-galactosyl-specific isolectin $B_4$ conjugated with horseradish peroxidase derived from *Griffonia simplicifolia seeds* (Isolectin $B_4$) (Sigma, St Louis, MO, USA). Histochemical staining with isolectin $B_4$ for the visualization of microglia was performed as described previously[15,16)]. The next day, double-labeled immunostaining with anti-S100 antibody was performed as described above. Immunoreactions for isolectin $B_4$ and S100 staining were visualized using Vector DAB substrate kit and Vector SG substrate kit, respectively.

## RESULTS

Alterations of S100 and GFAP immunostaining in the striatum and substantia nigra of mice after MPTP treatment are summarized in Table 1. Representative microphotographs of S100 immunostaining in the striatum and substantia nigra of MPTP-treated mice are shown in Fig. 1. S100-immunoreactive cells were detectable in the striatum and substantia nigra of control mice. S100-immunoreactive cells were stained with evident immunopositive processes. In the striatum, the number of S100-immunopositive cells increased from 1 day after MPTP treatment. Three days after MPTP treatment, S100-immunopositive cells exhibited a ramified form in the striatum, which showed a marked increase in the number of the cells in this region. Thereafter, a reduction in the number of S100-immunopositive cells was observed in mice 7 days after MPTP treatment. In the substantia nigra, the number of S100-immunopositive cells with a ramified form increased from 3 days after MPTP treatment. Thereafter, a decrease in the number of S100-immunopositive cells was found 7 days after MPTP treatment (Table 1).

Representative microphotographs of GFAP immunostaining in the striatum and substantia nigra of MPTP-treated mice are shown in Fig. 2. Few GFAP-immunopositive astrocytes were observed in the striatum of control mice. In the substantia nigra of control mice, however, GFAP-immunopositive astrocytes had a ramified form with many fine processes. In the striatum, the number of GFAP-immunopositive astrocytes increased gradually from 1 day after MPTP treatment. Thereafter, the levels of staining for GFAP-immunopositive astrocytes increased slightly in the striatum 3 days after MPTP treatment. Seven days after MPTP treatment, GFAP-immunopositive astrocytes in the striatum exhibited a ramified form with many fine processes, with a marked increase in the number of the cells in this region. In the substantia nigra, the number of GFAP-immunopositive astrocytes increased gradually from 5 hours after MPTP treatment. Thereafter, a marked increase in the number of GFAP-immunopositive astrocytes was noted in mice 3 and 7 days after MPTP treatment (Table 1).

Representative microphotographs of double-labeled immunostainings with anti-S100 and anti-GFAP antibodies in the substantia nigra after MPTP treatment are shown in Fig. 3 a,b. Representative microphotographs of double-labeled immunostainings with anti-S100 and anti-isolectin $B_4$ antibodies in the substantia nigra after MPTP treatment are shown in Fig. 3 c,d. S100 immunoreactivity was found mainly in the cytoplasm of GFAP-immunopositive astrocytes. In contrast, S100 immunoreactivity was not observed in isolectin $B_4$-immunopositive glial cells.

## DISCUSSION

S100B is a calcium binding protein produced and secreted by astrocytes. S100B protein is expressed throughout the brain and is observed primarily in the cytoplasm of astrocytes[17]. Interestingly, a previous study reported that overexpression of S100B protein can cause chronic neuronal damage[18]. Several reports also demonstrated that overexpression of S100B protein might be an exacerbating factor in some neuronal diseases, such as Down's syndrome and Alzheimer's disease[19,20]. A recent study reported that the enhanced synthesis of S100B protein by reactive astrocytes participates in the inflammatory responses within the periinfarct area, which may be related to the occurrence of delayed infarct expansion after permanent focal ischemia in rat[21]. In contrast, Migheli et al.[22] suggested that S100B expression was unrelated to neuronal apoptosis, but might be involved in cellular defense mechanism against oxidative stress. S100B protein has also been demonstrated to stimulate neurite outgrowth, proliferation of melanoma cells and induction of apoptosis in PC12 pheochromocytoma cells[11,23]. Furthermore, S100B protein is known to have trophic effects on both glial and neuronal cells[24,25]. Thus, there is no consensus regarding the significance of the precise role of S100B expression in neuronal cell damage. The reason for these phenomena is presently unclear. However, a recent, interesting study using permanent focal ischemia in rats suggested that ONO-2506, a novel astrocyte modulating agent, can mitigate delayed infarct expansion and neurologic deficits, presumably through modulation of astrocytic activation within the periinfarct area, and the inhibition of astrocytic S100B synthesis by this agent may play a major role[26]. These findings suggest that pharmacological modulation of astrocytic activation may provide a novel therapeutic strategy against ischemic neuronal damage. However, further studies are needed to investigate the exact mechanisms for the role of astrocytic S100B synthesis against ischemic neuronal cell damage. Furthermore, little is known about the exact relationship between S100B overexpression and neurodegeneration in MPTP-treated mice as a useful model of Parkinson's disease.

In the present study, S100-immunopositive cells were found in the striatum and substantia nigra of control mice. The increase in the number of S100-immunopositive cells was observed in the striatum from 1 day after MPTP treatment. Thereafter, a marked increase in the number of S100-immunopositive cells was noted 3 days after MPTP treatment. In the substantia nigra, the number of S100-immunopositive cells also increased 3 days after MPTP treatment. However, the number of S100-immunopositive cells was reduced in the striatum and substantia nigra 7 days after MPTP treatment. Additionally, we observed changes of GFAP-immunopositive astrocytes in the striatum and substantia nigra of MPTP-treated mice. GFAP is well known to be a marker for reactive astrocytes in response to CNS injury, due to its specificity for astrocytes[27]. In our study, an increase in the number of GFAP-immunopositive astrocytes was observed in the striatum and substantia nigra of mice from 1 day after MPTP treatment. Thereafter, a marked increase in the number of GFAP-immunopositive astrocytes was noted in these regions 3 and 7 days after MPTP treatment. From these findings, it is conceivable that the time course patterns of the expression of S100-immunopositive cells are, at least in part, similar to these of GFAP-immunopositive cells after MPTP treatment. Thus, the present study suggests that the activation of S100-immunopositive cells may reflect that of reactive astrocytes after MPTP treatment.

In our double-labeled immunostaining with anti-S100 and anti-GFAP antibodies, S100 immunoreactivity was observed in GFAP-immunopositive astrocytes. In contrast, however, S100 immunoreactivity was not observed in isolectin $B_4$-positive glial cells as a marker of microglia as shown in Fig. 3. These findings demonstrate that S100 protein is expressed selectively by reactive astrocytes, but not microglia. In the present study, we used the rabbit anti-cow polyclonal antibody of S100, that reacts with S100B and S100A proteins. In the central nervous system, S100A1, although not secreted, is found in neurons, S100A4 in astrocytes beside S100B. Further, S100A8 and S100A9 are found in resident, activated microglial cells in brain inflammatory processes, Alzheimer's disease and in ischemic brain lesions[23,28]. However, several arguments support the assumption that, in the present study, the antibody detected mainly S100B protein. (i) S100B is known to be one of the proteins upregulated on astrocytic activation. (ii) S100 was colocalized with GFAP. (iii) Microglial cells were not stained by the S100 antibody. Thus, the antibody did not detect S100A8 and S100A9. (iV) S100B has a much (12.5 times) higher concentration in the brain in comparison with the S100A proteins[29]. Interestingly, a recent study demonstrates that S100B cells possessed attributes typical of astrocytes in rats[30]. The findings were, at least in part, consistent with our immunohistochemical results. These observations seem to suggest that S100-immunoreactive cells in the present study reflect mainly reactive astrocytes after MPTP treatment. However, further studies should be performed to investigate the precise mechanisms for our findings.

Of particular interest in the present study is that the expression of S100 protein was closely related to decreases in tyrosine hydroxylase-immunopositive neurons after MPTP treatment[31]. Although the reason for this phenomenon is presently unclear, we speculate that the overexpression of S100B protein produced by reactive astrocytes may play a key role in the pathogenesis of degeneration of dopaminegic neurons at the acute phase after MPTP treatment. However, the precise mechanisms responsible for such findings should be investigated in further studies.

In conclusion, the present results provide evidence that astrocytic activation may play some role in the pathogenesis of MPTP-induced degeneration of dopaminergic neurons. Furthermore, the present study demonstrates that S100 protein is expressed selectively by astrocytes, but not microglia after MPTP treatment. Thus our study provides valuable information for the pathogenesis of acute stage of Parkinson's disease.

## REFERENCES

1) Hornykiewicz O. and Kish S.J., Adv. Neurol. **45** (1986) 19.
2) Kish S., Shannak J.K. and Hornykiewicz. N., Engl. J. Med. **318** (1988) 876.
3) Kostic V., Przedbrorski S., Flaster E, et al., Neurolog, **41** (1991) 202.
4) Bloem B.R., Irwin I., Buruma O.J.S, et al., J. Neurol. Sci. **97** (1990) 273.
5) Hantraye P., Varastet M., Peschanski D. et al., Neuroscience **53** (1993) 169.
6) Heikkila R.E., Manzino L., Cabbat F.S. et al., Nature **311** (1984) 467.
7) Tipton K.F. and Singer T.P., J. Neurochem. **61** (1993) 1191.
8) Hasegawa E., Takeshige K., Oishi T. et al., Biochem. Biophys. Res. Commun. **170** (1990) 1049.
9) Sriram K., Pai K.S., Boyd M.R. et al., Brain Res. **749** (1997) 44.
10) Heizmann C.W., Gen. Physiol. Biophys. **11** (1992) 411.
11) Zimmer D.B., Cornwall E.H., Landar A. et al., Brain Res. Bull. **37** (1995) 417.
12) Regner A., Kaufman M., Friedman G. et al., NeuroReport **12** (2001) 691.
13) Araki T., Kumagai T., Tanaka K. et al., Brain Res. **918** (2001) 176.
14) Muramatsu Y., Kurosaki R., Mikami T. et al., Metab. Brain Dis. **17** (2002) 169.
15) Streit W.J., J. Histochem. Cytochem. **38** (1990) 1683.
16) Kato H., Kogure K., Araki T. et al., J. Cereb. Blood Flow Metab., **15** (1995) 60.
17) Van Eldik L.J., Ehrenfried B. and Jensen R.A., Proc. Natl. Acad. Sci. U.S.A. **81** (1984) 6034.
18) Reeves R.H., Yao J., Crowley M.R. et al., Proc. Natl. Acad. Sci. U.S.A. **91** (1994) 5359.
19) Griffin W.S.T., Stanley L.C., Ling C. et al., Proc Natl. Acad. Sci. U.S.A. **86** (1989) 7611.
20) Sheng J.G., Mrak R.E. and Griffin W.S.T., J. Neuropathol. Exp. Neurol. **56** (1997) 285.
21) Matsui T., Mori T., Tateishi N. et al., J. Cereb. Blood Flow Metab. **22** (2002) 711.
22) Migheli A., Cordera S., Bendotti C. et al., Neurosci. Lett. **261** (1999) 25.
23) Schäfer B.W. and Heizmann C.W., Trends Biochem. Sci. **21** (1996) 134.
24) Selinfreud R.H., Barger S.W., Pledger W.J. et al., Proc. Natl. Acad. Sci. U.S.A.,**88** (1991) 3554.
25) Whitaker-Azmitia P.M., Wingate M., Borella A. et al., Brain Res. **776** (1997) 51.
26) Tateishi N., Mori T., Kagamiishi Y. et al., J. Cereb. Blood Flow Metab. **22** (2002) 723.
27) Lin R.C., Polsky K. and Matesic D.F., Brain Res. **600** (1993) 1.
28) Donato R., Int. J. Biochem. Cell Biol. **33** (2001) 637.
29) Haimoto H., Hosoda S. and Kato K., Lab. Invest. **57** (1987) 489.
30) Melzer P., Savchenko V. and McKanna J.A., Exp. Neurol. **168** (2001) 63.
31) Muramatsu Y., Kurosaki R. and Watanabe H., Glia **42** (2003) 307.

Table 1. Alterations of S100 and GFAP immunostaining in the striatum and substantia nigra of mice after MPTP treatment.

| | Striatum | Substantia nigra |
|---|---|---|
| | Grade | (cell number) |
| *S100 immunostaining* | | |
| Control | 1.4±0.3 (114.4±24.5) | 1.6±0.4 (51.4±8.0) |
| 5 hours | 1.6±0.4 (124.6±19.3) | 1.6±0.3 (63.6±13.3) |
| 1 day | 2.8±0.7**(161.9±30.5$^{\dagger}$) | 2.6±0.4* (65.1±11.9) |
| 3 days | 3.1±1.0**(171.0±54.4$^{\dagger}$) | 3.2±0.2**(79.8±17.4$^{\dagger}$) |
| 7 days | 1.7±0.1 (137.8±18.7) | 2.0±0.3 (63.9±12.7) |
| *GFAP immunostaining* | | |
| Control | 0.2±0.1 (4.7±1.1) | 1.4±0.5 (62.5±5.6) |
| 5 hours | 0.6±0.5 (8.3±3.4) | 2.0±1.0 (72.0±14.0) |
| 1 day | 1.2±0.5** (24.1±17.7) | 1.6±0.9 (69.5±16.9) |
| 3 days | 3.2±0.5**(139.9±49.2$^{\ddagger}$) | 3.6±0.5**(110.5±16.0$^{\ddagger}$) |
| 7 days | 3.3±0.5**(143.3±41.1$^{\ddagger}$) | 3.2±0.8**(112.0±21.0$^{\ddagger}$) |

The immunoreactivity was semiquantitatively graded as intense and swollen (grade 4), intense (grade 3), moderate (grade 2), weak (grade 1) and not detectable (grade 0). Values were expressed means ± SD. $^{*,\dagger}$ $P<0.05$, $^{**,\ddagger}$ $P<0.01$ vs. the corresponding control group (non-parametric Dunnett's multiple comparison test). Each group contained 5 animals. Figures in parenthesis indicate the number of S100-immunopositive or GFAP-immunopositive cells.

## RESULTS

The striatal dopamine, DOPAC and HVA content showed a severe reduction from 1 day to 14 days post-treatment except for the DOPAC level 14 days post-treatment. Thereafter, the striatal dopamine level showed a significant decline (59% loss) even 21 days after MPTP treatment. A significant reduction was also found in the striatal DOPAC (48% loss) and HVA (58% loss) level 21 days after MPTP treatment (Table 1).

The measurement of motor activity had a significant prolongation of Tturn, TLA and cataleptic effect 7 days after MPTP treatment. After 14 days, a significant prolongation of TLA and cataleptic effect was still observed in these mice. However, a significant prolongation of Tturn was not evident in these mice (Table 2).

Representative photographs of TH immunostaining in the striatum and substantia nigra are shown in Fig. 1. Dopaminergic neurons with the TH antibody were easily detectable in control mice. One day after MPTP treatment, TH immunopositive fibers and cell bodies were reduced in the striatum and substantia nigra, respectively. Thereafter, the TH immunopositive fibers and cell bodies were markedly decreased in the striatum and substantia nigra up to 7 days after MPTP treatment.

Representative photographs of GFAP immunostaining in the striatum and substantia nigra are shown in Fig. 2. GFAP positive astrocytes were evident in the substantia nigra. One day after MPTP treatment, GFAP immunopositive astrocytes were increased in the striatum and substantia nigra. Thereafter, GFAP positive astrocytes were markedly increased in the striatum and substantia nigra 3 and 7 days after MPTP treatment.

Representative photographs of isolectin $B_4$ staining in the striatum and substantia nigra are shown in Fig. 3. Isolecton $B_4$ positive cells were evident in the striatum and substantia nigra. One day after MPTP treatment, isolectin $B_4$ positive cells were increased in the striatum and substantia nigra. Thereafter, isolectin $B_4$ positive cells were markedly increased in the substantia nigra 3 and 7 days after MPTP treatment.

## DISCUSSION

To clarify the pathophysiological mechanisms of Parkinson's disease, first we investigated a close correlation between neurochemical and behavioral manifestation using mice with several studies. This study is the first report using mice in several experimental studies to test the close correlation between neurochemical and behavioral manifestation.

Since the discovery that MPTP selectively destroys nigrostriatal dopaminergic neurons in humans, a wide range of animal models for parkinsonism have been extensively studied. Mice are susceptible to MPTP neurotoxicity and the animals make excellent conventional models for Parkinson's disease. In general, MPTP is usually administered to mice either by an acute or a subacute regimen[7,18]. In the acute and subacute mice models, MPTP can produce depletions in the striatal level of dopamine and its metabolites (DOPAC and HVA) along with a reduction in the striatal synaptosomal dopamine uptake[18,19]. However, when survival times in mice are extended, the neurotoxic effects of MPTP are reversible[20]. Furthermore, despite evidence of dopamine reductions, animals that receive MPTP acutely or subacutely do not always exhibit motor dysfunctions or motor abnormalities[4,21]. Therefore, we examined the exact neurotoxic effects of acute or consecutive treatment of MPTP in mice.

In the present study, we investigated the striatal dopamine, DOPAC and HVA levels from 1 day to 21 days after acute MPTP treatment. As shown in Table 1, the acute MPTP treatment showed a severe reduction in the striatal dopamine, DOPAC and HVA content in mice from 1 day to 14 days post-treatment. Thereafter, the striatal dopamine level showed a significant decline (59% loss) even 21 days after MPTP treatment. In our behavioral studies, the acute MPTP treatment caused severe motor deficits in mice 7 and 14 days post-treatment (Table 2). From the present findings, we suggest that the model with acute MPTP treatment can cause a severe dopamine depletion and motor deficiency in mice. Based on these present results, we speculate that the acute treatment with MPTP is a very useful model of Parkinson's disease. Our study also suggests that continuous and excessive production of endogenous MPTP-like substrates in the brain may be one of the mechanisms in the development of Parkinson's disease[22].

In our immunohistological study, we observed loss of TH immunoreactivity in the striatal fibers and nigral cells from 1 day after the acute MPTP treatment. Thereafter, the severe loss of TH immunoreactivity was observed in the striatum and substantia nigra up to 7 days post-treatment (Fig. 1). In contrast, 1 day after acute MPTP treatment, GFAP immunopositive astrocytes were increased in the striatum and substantia nigra. Thereafter, GFAP positive astrocytes were markedly increased in the striatum and substantia nigra 3 and 7 days after MPTP treatment (Fig. 2). These results suggest that an increase in GFAP immunostaining produced by MPTP in the striatum and substantia nigra is linked to decrements in TH immunostaining, suggesting that factors originating in the damaged dopamine neurons initiated the astrocyte reaction to MPTP. For histochemical staining of isolectin $B_4$, which specifically combines with terminal alpha-D-galactose residues located on the cell surface of microglia[23,24)], isolectin $B_4$ staining was weak in the striatum and substantia nigra of control mice. One day after acute MPTP treatment, isolectin $B_4$-positive microglia were increased markedly in the striatum and substantia nigra. Thereafter, the increase of isolectin $B_4$-positive microglia lasted up to 7 days after MPTP treatment. It is known that activated microglia exert cytotoxic effects in the brain through two different, yet complementary processes[25)]. First, activated microglia can act as phagocytes, which involve direct cell-to-cell contact. Second, they are capable of releasing a large variety of potentially neurotoxic substances[25)]. Therefore, it is believed that activated microglia may sometimes be associated with beneficial effects and often they may appear to be deleterious[26)]. A recent interesting study suggested that inhibition of microglial activation by minocycline can protect the nigrostriatal dopaminergic pathway against neurotoxic effects of MPTP in mice[27)]. These findings seem to suggest that activated microglia plays an important role in the pathogenesis of MPTP-induced degeneration of dopaminergic neurons. In the present study, the number of activated microglia appeared in the striatum and substantia nigra earlier than that of reactive astrocytes, as shown in Fig. 3. These results were, at least in part, consistent with the previous report[28)]. Based on these observations, we also suggest that microglial activation may play a key role in the MPTP neurotoxic process.

In conclusion, we have shown that the acute treatment of mice with MPTP is accompanied by sustained nigral degeneration and motor abnormalities relatively resembling Parkinson's disease. Furthermore, our results show that continuous and excess production of endogenous MPTP-like substrates in the brain may be one of the mechanisms in the development of Parkinson's disease. Thus our findings provide valuable information for explorations of age-related disease progression, mechanisms of neurodegeneration and neuroprotection.

## REFERENCES

1) Tipton, K.F. and Singer, T.P., J. Neurochem. **61** (1993) 1191.
2) Turski L., Bressler K., Rettig K.J. et al., Nature **349** (1991) 414.
3) Gerlach M. and Richerer P., J. Neural. Transm. **103** (1996) 987.
4) Heikkila R.E., Sieber B.A., Manzino L. and Sonsalla P.K., Mol. Chem. Neuropathol. **10** (1989) 171.
5) Tanji H., Araki T., Nagasawa H.,and Itoyama Y., Brain Res. **824** (1999) 224.

6) Zuddas A., Fascetti F., Corsini,G.U. and Piccardi M.P., Exp. Neurol. **127** (1994) 54.
7) Sonsalla P.K. and Heikklia R.E., Eur. J. Pharmacol. **129** (2001) 231.
9) Araki T., Kumagaya T., Tanaka K. et al., Brain Res. **918** (2001) 176.
10) Araki T., Mizutani H., Matsubara M. et al., Eur. Neuropsychopharmacol. **11** ( 2001) 125.
11) Ogawa N., Mizukawa K., Hirose Y. et al., Eur. Neurol. **26** (1987) 16.
12) Kobayashi T., Araki T., Itoyama Y. et al., Life Sci. **61** (1997) 2529.
13) Kurosaki R., Akasaka M., Michimata,M. et al., Neurobiol. Aging. **24** (2003) 315.
14) Kurosaki R., Muramatsu Y., Watanabe H. et al., Metab. Brain Dis. **18** (2003) 139.
15) Muramatsu Y., Kurosaki R., Mikami T. et al., Metab. Brain Dis. **17** (2002) 169.
16) Kurosaki R., Muramatsu Y., Michimata M. et al., Neurol. Res. **24** (2002) 655.
17) Muramatsu Y., Kurosaki R., Watanabe H. et al., Glia **42** (2003) 307.
18) Heikkila R.E., Hes A. and Duvoison,R.C., Science **224** (1984) 1451.
19) Ricaurte G.A., Langston J.W. Delanncy L.E., et al., Brain Res. **376** (1986) 117.
20) Hallman H., Lange J., Olson I. et al., J. Neurochem. **44** (1985) 117.
21) Gerlach M., Ben-Schachar D., Riederer P. and Youdim M.B.H., J. Neurochem. **63** (1994) 793.
22) Tasaki Y., Makino Y., Ohta S. and Hirobe M., J. Neurochem. **57** (1991) 1940.
23) Morinaka T., Kalehua A.N. and Streit W.J., J. Cereb. Blood Flow Metab. **11** (1991) 966.
24) Streit W.J., J. Histochem. Cytochem. **38** (1990) 1683.
25) Banati R.B., Gehrmann J., Schbert P. and Kreuzberg G.W., Glia **7** (1993) 111.
26) Vila M., Jakson-Lewis V., Guégan C. et al., Curr. Opin. Neurol. **14** (2001) 483.
27) Wu D.C., Jackson-Lewis V., Vila M. et al., J. Neurosci. **22** (2002) 1763.
28) Liberatore G.T., Jackson-Lewis V., Vukosavic S. et al., Nat. Med. **5** (1999) 1403.

Table 1. Time course effects of MPTP (20 mg/kg,i.p.) treatment four times a day at 2-hr intervals on the striatal dopamine, DOPAC and HVA levels in mice.

| Days after MPTP treatment | Dopamine ($\mu$g/g tissue) | DOPAC ($\mu$g/g tissue) | HVA ($\mu$g/g tissue) |
|---|---|---|---|
| Control | 16.22±0.57 | 2.99±0.26 | 1.73±0.14 |
| 1 day | 2.63±0.53** | 1.21±0.25** | 0.82±0.17** |
| 3 days | 3.03±0.62** | 1.24±0.23** | 0.56±0.06** |
| 7 days | 2.91±0.37** | 1.39±0.18** | 0.63±0.06** |
| 14 days | 3.46±0.32** | 3.20±0.20 | 1.11±0.02** |
| 21 days | 6.58±0.51** | 1.55±0.18** | 0.73±0.06** |

Values are expressed as means±S.E.M. $*p<0.05$, $**p<0.01$ compared with control (Dunnett's multiple range test). n=5-6 mice.

Table 2. Effects of MPTP (20 mg/kg,i.p.) treatment four times a day at 2-hr intervals on the motor activity in mice.

| Days after MPTP treatment | Pole test (sec) |  | Catalepsy test (sec) |
|---|---|---|---|
|  | Tturn | TLA |  |
| Control | 1.74±0.10 | 4.02±0.29 | 2.03±0.21 |
| 7 days | 2.69±0.20** | 5.80±0.60** | 4.07±0.54** |
| Control | 1.77±0.16 | 3.75±0.33 | 2.17±0.40 |
| 14 days | 2.13±0.18 | 5.25±0.65* | 3.11±0.34* |

Values are expressed as means±S.E.M. $*p<0.05$, $**p<0.01$ compared with control (Student's *t*-test). n=8-10 mice.

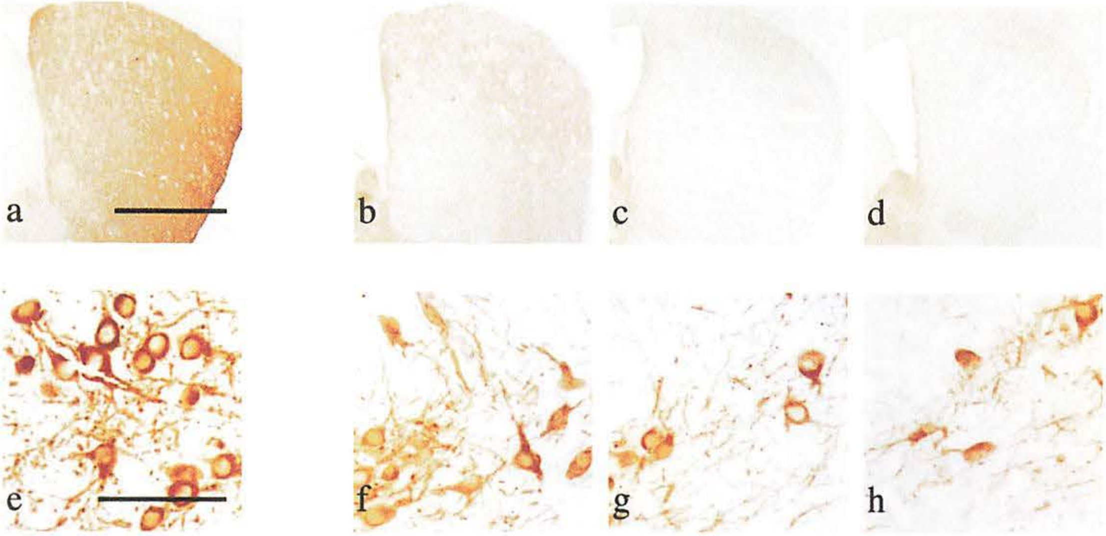

Fig. 1. Representative microphotographs of tyrosine hydroxylase (TH) immunostaining in the striatum and substantia nigra of mice after MPTP (20 mg/kg,i.p.) treatment four times a day at 2-hr intervals within a day. (a,e): Control. (b,f,): 1 day after MPTP treatment. (c,g): 3 days after MPTP treatment. (d,h): 7 days after MPTP treatment. Striatum (a-d), bar=100 mm; Substantia nigra (e-h), bar=100 $\mu$m. n=5.

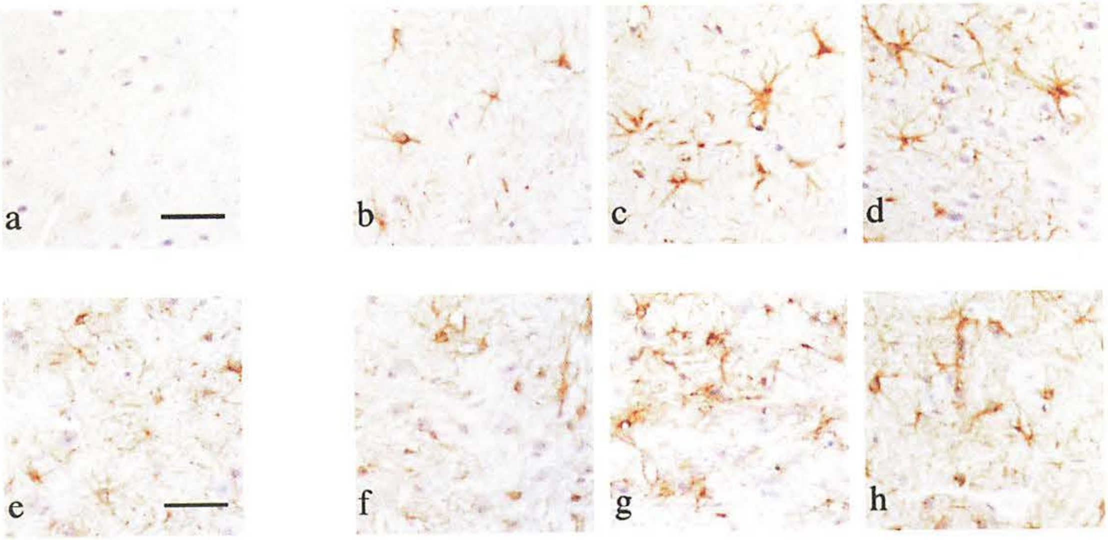

Fig. 2. Representative microphotographs of glial fibrillary acidic protein (GFAP) immunostaining in the striatum and substantia nigra of mice after MPTP (20 mg/kg,i.p.) treatment four times a day at 2-hr intervals within a day. (a,e): Control. (b,f): 1 day after MPTP treatment. (c,g): 3 days after MPTP treatment. (d,h): 7 days after MPTP treatment. Striatum (a-d), bar=100 $\mu$m; Substantia nigra (e-h), bar=100 $\mu$m. n=5.

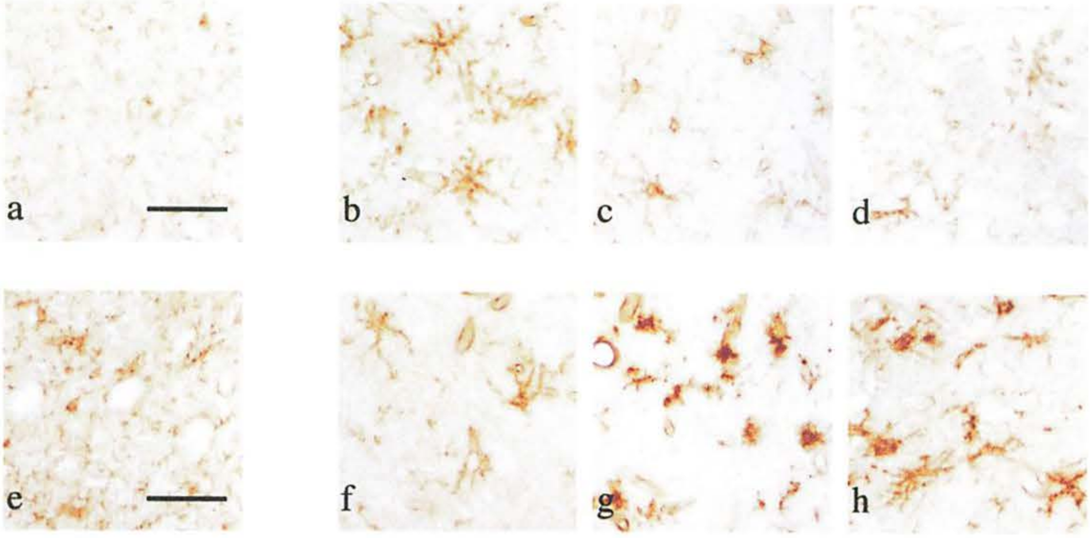

Fig. 3. Representative microphotographs of isolectin $B_4$ immunostaining in the striatum and substantia nigra of mice after MPTP (20 mg/kg,i.p.) treatment four times a day at 2-hr intervals within a day. (a,e): Control. (b,f): 1 day after MPTP treatment. (c,g): 3 days after MPTP treatment. (d,h): 7 days after MPTP treatment. Striatum (a-d), bar=100 $\mu$m; Substantia nigra (e-h), bar=100 $\mu$m. n=5.

# IV. MEDICINE AND BIOLOGY (Clinical)

# IV. 1 Functional Module of the Brain Correlates the Trait Anxiety by Colonic Distention

*Hamaguchi T., Kano M.*, Rikimaru H.**, Kanazawa M., Itoh M.**, Yanai K.*, and Fukudo S.*

*Department of Behavioral Medicine, Tohoku University Graduate School of Medicine*
*Department of Pharmacology, Tohoku University Graduate School of Medicine**
*Division of Nuclear Medicine, Tohoku University, Cyclotron Radio Isotope Center***

## Introduction

Psychological factors may play an important role in visceral perception. A close relationship between emotional state and gastrointestinal function is reported in patients with functional gastrointestinal disorders, including irritable bowel syndrome (IBS)[1). There is increasing experimental evidence to suggest an interaction between emotional context, cognition and sensory processing[2,3). The cerebral evoked potential to gastrointestinal stimulation has been shown to be modulated by attentional processes[4), it may reflect such higher level processing of painful stimuli[5).

Psychological stress response induces gastrointestinal symptoms such as abdominal pain, diarrhea or constipation in humans[6). These phenomena are explained by stress-induced colonic motility[7) and visceral perception abhorred by the stress[8). IBS is a functional gastrointestinal disorder characterized with chronic abdominal pain and abdominal bowel habituation. Functional relation between central nervous system and gastrointestinal tract begins to be clarified and brain-gut interactions are considered to be major pathophysiology of IBS[9,10).

Personality property is closely related to stress response. The processing of the information about perception from the gastrointestinal tract to the brain may be related to personality traits[11). However, brain regions of personality traits as well as anxiety trait that relate to stress response is uncertain. We are imaging that the multiple control sites are interconnected so that stress responses can be organized, at varied degrees of complexity, some involving the recruitment of just a few brain sites, others requiring a concerted large-scale operation, but often involving both cortical and subcortical sites.

To vilify the following hypotheses, we examined the brain images and personality trait during colonic distention in humans.

## Method

### *Subjects*

Fifteen volunteers participated in this study. Their were all male, right-handed, and aged 22±2 (mean±SE). All subjects were free from gastrointestinal symptoms or signs. Each underwent a basic evaluation to exclude organic disease including a history and physical examination and colonoscopy. All subjects gave informed consent as approved by the Ethics Committee in Tohoku University School of Medicine.

### *Distention Protocol*

On the day before examination, the subjects took the low residue diet. At 21: 00 before the examination, they ingested 17g (13.6%) of magnesium citrate, 75mg of sodium picosulfate, and 24mg of sennoside A & B to cleanse the colon. Subjects were tested in the fasted state at 8: 15. Colonoscope was inserted to the splenic flexure and splinting device was inserted along the scope. After the removal of the scope, a thin plastic bag (Svnestics Medical, Stockholm) of maximal volume (700ml, 10cm diameter when fully inflated) was advanced into the descending colon. The location of the bag was confirmed with X-ray fluoroscopy. The splinting device was removed and the bag was taped in place. Subjects were laid in bed at 9: 15 for the rest.

The colonic distention stimuli were provided with computerized barostat equipment (maximal inflation rate, 38ml/s [Medtronics Synectics, Shoreview, MN]). The sham stimulation with 0 mmHg was given at first. The colon was then stimulated with the bag pressure of 40 mmHg for 80 seconds.

### *Psychological measurement*

Before the stimulation, subjects were required the answer to questioner in the State Trait Anxiety Inventory (STAI)[12].

### *PET scanning*

Plaster head support was set for each subject to minimize head movements during the PET imaging. By using 68Ge/68Ga radiation source, transmission scan for the $\gamma$-ray absorptive correction was done before positron emission tomography (PET) scanning. The PET scan room was made to be under the gloom. The subjects closed their eyes with waking.

[$^{15}$O] labeled water which was synthesized by the cyclotron was injected from the right arm vein with the beginning of colonic distention. At 10 seconds after the beginning of [$^{15}$O] labeled water injection and colonic distention, both radioactivity and peak pressure of the bag reach plateau. The PET scanning then started and continued for 70 seconds. We measured regional cerebral blood flow (rCBF) during 4 scans (70 seconds each) using a PET scanner in three-dimension sampling mode (HEADTOME V SET-2400W, Shimadzu, Japan).

### *Analysis*

The PET image analyzed for brain image analysis software (Statistical Parametric Mapping; SPM99, The Wellcome Department of Cognitive Neurology, London) according to the method of Friston et al$^{14)}$. All slices (63 sheet) including the brain images were extracted. The PET images were realigned, spatially normalized and transformed into an approximate Talairach-Tournoux stereotactic space$^{13)}$, 3D Gaussian filtered (FWHM = 13 mm), and proportionally scaled to account for global confounders. The size of each voxel was set at 2×2×2mm.

To clarify the region where the rCBF fluctuates by correlating with trait anxiety in the colonic distention, we examined by using the 'simple regression analysis' option in SPM. We set 0.18 % level of significance or less (uncorrected, $Z \geqq 3.00$) as the region of significant correlation.

## Results

### *Trait anxiety score of subjects*

Trait anxiety scores of subjects were 44.33±8.65 (mean ± SD, minima 26 to maxima 58). The normal score range in trait anxiety was 25 to 75. After the colonic distention, all subjects reported their emotion and visceral perception during the distention protocol. They reported increasing the negative emotion such as anxiety and perceived stress, and the visceral perception such as abdominal distention, abdominal pain, and urgency for defecation.

*Brain activity correlates the trait anxiety by colonic distention*

The simple regression analysis showed positive relation between trait anxiety and rCBF during the colonic distention (uncorrected p = 0.0018, Table 1). They were the left middle frontal gyrus (BA 10, Fig. 1-A), the left orbitofrontal gyrus (BA11, Fig. 1-B), the left prefrontal gyrus (Fig. 1-C), and the right inferior temporal gyrus (BA20, Fig. 1-D). Conversely, there were no regions of significantly negative correlation with the trait anxiety by colonic distention.

## Discussion

The most important part of this study is that the prefrontal cortexes were significantly correlated to the trait anxiety by colonic distention in human. Our results suggest that trait anxiety may be related to central processing of visceral perception by colonic distention in humans. The prefrontal cortex participates in linking perception of stimuli to the guidance of behavior(15), including the flexible execution of strategies for obtaining rewards and punishments(16). Regions in the medial and ventral aspects of the frontal lobe seem especially important in relating information about external sensory stimuli to interoceptive information that represents emotional significance. The prefrontal area checks the given stimulation with experience and memory accumulated and may be the position which finally determines the meaning of stimulation; comfort or discomfort(17,18).

Recently, the significant negative correlation between late peak latency of cerebral evoked potential and hypochondriasis in Minnesota Multiphasic Personality Inventory by esophageal electro stimulation was reported(11). Previously finding suggested the cognitive pattern associated with some personality variables might promote visceral hypersensitivity via cortical processing.

Our results also suggest that cognitive patterns associated with neurotic variables such as depression and anxiety might promote visceral hyper and/or hyposensitivity via cortical processing.

## Acknowledgements

Grant Support: This research was supported by Grant-in-Aid for Scientific Research No. 833-5020-11680778 and No. 622-5637-13897021 from the Ministry of Education, Science, and Culture of Japan and Grant-in-Aid for Scientific Research No. H11-Nou-003, No. H13-Chouju-028, and H14-Si-9 from the Ministry of Health, Welfare, and Labor of Japan.

## References

1) Whitehead W.E., Bosmajian L., Zonderman A.B., Costa P.T. Jr. and Schuster M.M., Castroenterology **95** (1988) 709.
2) Kaviani H., Gray J.A., Checkley S.A., Kumari V. and Wilson D.G., Int. J. Psychophysiol **32** (1999) 47.
3) Vrana S.R. and Lang P.J., J. Abnorm. Psychol. **99** (1990) 189.
4) Hollerbach S., Tougas G., Frieling T., Enck P., Fitzpatrick D. and Upton A.R., Crit. Rev. Biomed. Eng. **25** (1997) 203.
5) Hobson A.R., Aziz Q., Furlong P.L., Barlow J.D., Bancewicz J. and Thompson D.G., Neurogastroenterol Motil. **10** (1998) 421.
6) Drossman D.A., Sandler R.S., McKee D.C. and Lovitz A.J., Gastroenterology **83** (1982) 529.
7) Fukudo S., Nomura T., Murakawa M. and Taguchi F., J. Clin. Gastroenteol. **16** (1993) 133.
8) Accarino A.M., Azpiroz F. and Malagelada J.R., Gastroenterology **113** (1997) 415.
9) Silverman D.H., Munakata J.A., Ennes H., Mandelkern M.A., Hoh C.K. and Mayer E.A., Gastroenterology **112** (1997) 64.
10) Mertz H., Morgan V., Tanner G., Pickens D., Price R., Shyr Y., et al., Gastroenterology **118** (2000) 842.
11) Kanazawa M., Fukudo S., Nomura T. and Hongo M., JAMA **286** (2001) 1974.
12) Spielberger C.D., Goursh R. and Lushene R., In: Manual for the Sate-Trait Anxiety Inventory. (1970) Consulting Psychologist Press, Palo Alto CA.
13) Friston K.J., Frith C.D., Liddle P.F., Dolan R.J., Lammertsma A.A. and Frackowiak R. S. J., J Cereb. Blood Flow Metab. **10** (1990) 458.
14) Talairach J. and Tournoux P., In: Co-Planar stereotaxic atlas of the human brain (1998) pp. 37-110 Thieme, Medical Publishers, New York.
15) Resenkilde C.E., Behav. Neural. Biol. **25** (1979) 301.
16) O'Doherty J., Kringelbach M.L., Rolls E.T., Hornak J. and Andrews C., Nature Neurosci. **4** (2001) 95.
17) Blood J.A., Zatorre J.R., Bermudez P. and Evans A.C., Nature Neurosci. **92** (1999) 382.
18) Dolan R.J. and Fletcher P.C., Nature **358** (1997) 582.

Table 1. Covariation of rCBF with STAI (positive correlation).

| Region | Side | BA | Coodinates | | | Z | p | Voxels in |
|---|---|---|---|---|---|---|---|---|
| | | | x | y | z | score | value | Cluster |
| Middle Frontal Gyrus | L | 10 | -34 | 64 | -6 | 3.37 | < 0.001 | 44 |
| Orbitofrontal Gyrus | L | 11 | -18 | 52 | -22 | 3.07 | 0.001 | 133 |
| Precentral Gyrus | L | | -30 | 4 | 28 | 3.10 | 0.001 | 77 |
| Inferior Temporal Gyrus | R | 20 | 52 | -12 | -46 | 3.07 | 0.001 | 35 |

Coodinate refer to location in stereotaxic space. Table shows at Maxima in the seach value defined a priori. Height threshould P = 0.0018, Extent threshould k = 20 Voxels (uncorrected). BA: Brodmann Area.

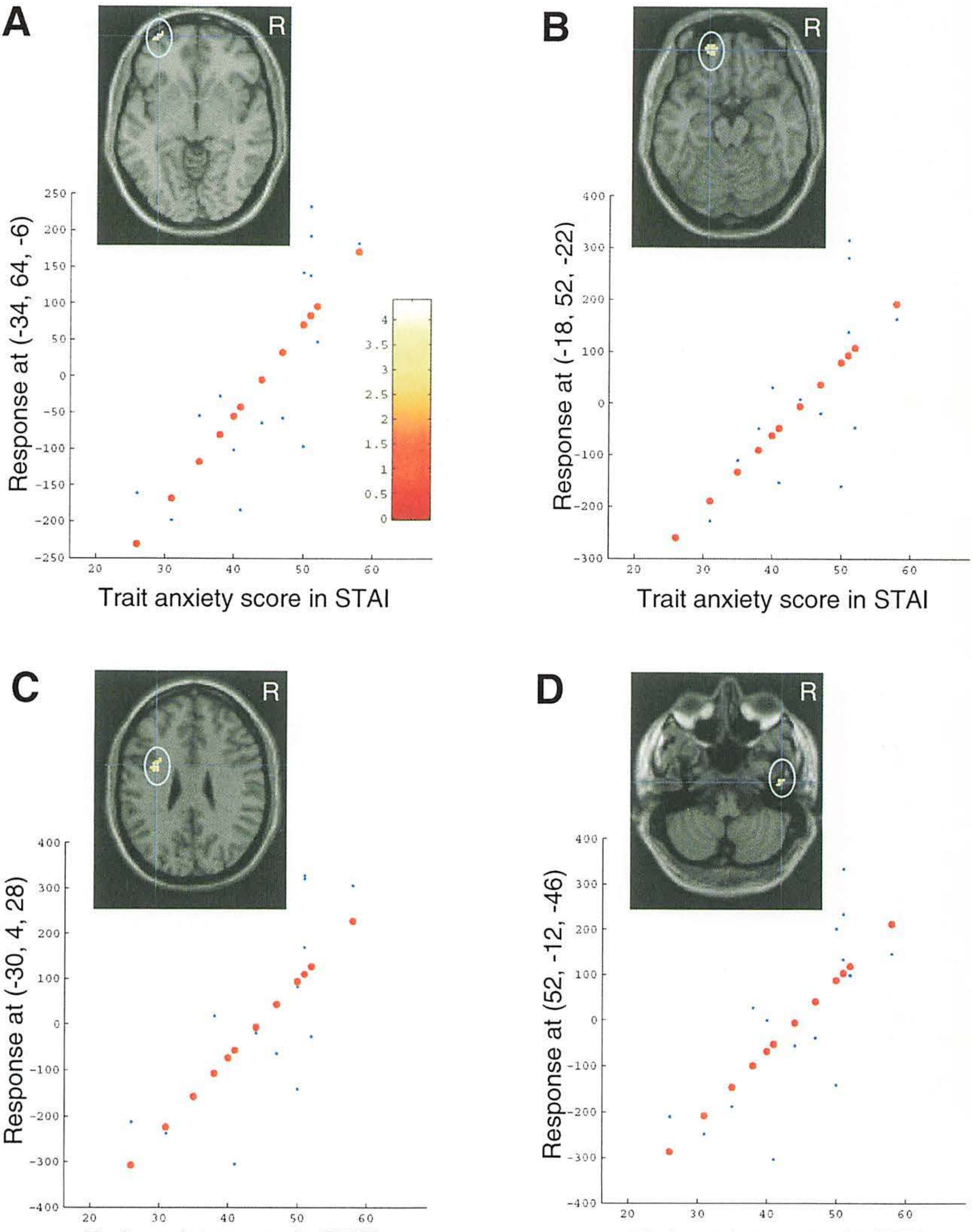

Fig. 1. Brain regions of positive correlation between rCBF and STAI by the simple regression analysis ($p < 0.0018$ uncorrected). (A) showed demonstrating voxels in the left middle frontal gyrus, (x y z), (-34 64 -6), (B) the left orbitofrontal gyrus, (x y z), (-18 52 -22), (C) the left precentral gyrus, (x y z), (-30 4 28), and (D) the right inferior temporal gyrus (x y z), (52 -12 -46) that significant correlated to trait anxiety. There were superimposed on the structural MRI scan of a single subject. Bottom showed the linear regression between PET signal across subjects and trait anxiety in STAI. Blue dots were indicated the subject data, and red were linear regression lines. Color bar indicated T-score by the simple regression analysis option in SPM99.

# IV. 2. Time-Dependent Contribution of the Hippocampal Complex during Remembering the Past: A PET Study

*Tsukiura, T.*[*]*, Fujii, T.*[†]*, Okuda, J.*[†]*, Ohtake, H.*[†]*, Kawashima, R.*[‡§]*, Itoh, M.*[¶]*,*
*Fukuda, H.*[§] *and Yamadori, A.*[†]

*Brain Architecture Analysis Group, Neuroscience Research Institute, National Institute of Advanced Industrial Science and Technology*[*]
*Division of Neuropsychology, Department of Disability Medicine, Tohoku University Graduate School of Medicine*[†]
*New Industry Creation Hatchery Center, Tohoku University*[‡]
*Department of Nuclear Medicine and Radiology, IDAC, Tohoku University*[§]
*Cyclotron and Radioisotope Center, Tohoku University*[¶]

## Introduction

Since the report of an amnesic case H.M.[1], a number of neuropsychological studies demonstrated that damage to the medial temporal lobe produces anterograde amnesia as well as retrograde amnesia[2]. This fact shows that the hippocampal complex (hippocampus, entorhinal, perirhinal, and parahippocampal cortices) plays a role not only in memory encoding but also in memory storage or retrieval, or both. The hippocampal retrograde amnesia usually shows a temporal gradient with impairment of recall being more difficult for episodes of the recent past than the remote one. This phenomenon has supported the idea called memory consolidation that neurophysiological processes occurring after the initial encoding of information contribute to the permanent storage of memory.

Regarding the roles of this region on memory consolidation, two theories have been proposed. One of the two currently dominant theories maintains that it works to consolidate a newly acquired memory for a temporal period of time[3], while the other believes its involvement in memory is life-long[2,4]. Although both theories stress dynamic reorganization of memory store over time, the functional role assigned to the hippocampal complex is incompatible to each other.

In the present study, we investigated whether patterns of brain activation during memory retrieval as measured by positron emission tomography (PET) is the same or different when the oldness of a to-be-retrieved episode is manipulated. The task-related PET signal changes detected from these tasks demonstrate the neural correlates depending on the retention time of autobiographical memories.

## Methods

### *Subjects*

Nine healthy male volunteers (mean 20.6 years) participated in the present study. They were all right-handers and their Edinburgh handedness scores were all above +90⁵⁾. All subjects were informed of the nature of the experiment and gave written consent in accordance with the guidelines approved by Tohoku University and the Declaration of Human Rights, Helsinki 1975.

### *Task procedures*

We employed the Crovitz technique to assess the ability to remember personally experienced episodes⁶⁾. Subjects were presented with a cue word and were required to recall a personal episode related to the word. Six cue words were visually presented one by one at the rate of one word per 20 seconds through virtual i-glasses controlled by Windows PC (Virtual i.o., Seattle, USA). These cue words were chosen from the list used in a previous study⁷⁾ and had been confirmed by a pilot study performed on another group of young normal subjects to be appropriate stimuli for evoking personal memories. The performance was scored according to the criteria of episodicity proposed by Baddeley and Wilson⁸⁾. It is a 4-step rating from 3 to 0. When subjects recalled a personal event with a specific time and place, it was rated 3. If a recalled event was personal but lacked specific information about time and place, it was rated 2. If they responded with only a vague description referring to no specific event, it was rated 1. When no response, or only semantic explanation of a cue was produced, a score of 0 was allotted. The full score in one session was 18. They participated in three experimental tasks and one control task during PET scanning. The same six words were presented in all tasks. In the first task, they were asked to recall personal episodes from childhood (CH), in the second task, episodes from adolescence (AD), and in the third, events from recent day (RE). In the control task (CN), they were asked to retrieve the lexical meaning of the words. The order of the tasks was counterbalanced across the subjects. In total, three sets of scores of episodicity were obtained from each subject. A schematic representation of the task procedures is shown in Figure 1.

*PET Measurements*

The rCBFs were measured using a PET scanner (SET2400W Shimadzu, FWHM 4.0mm) and $^{15}O$ labeled water (approximately 180 MBq for each injection)[9]. The transaxial sampling FOV was 256 mm, and the axial FOV was 190 mm. The thickness of the slices measured was 3.125 mm. Prior to the PET experiments, subjects had a catheter inserted into the right brachial vein for tracer administration. Each task was started at the same time with a bolus injection of $H_2{}^{15}O$, and lasted 120 seconds. PET data acquisition was started 40 seconds after the injection and lasted 60 seconds. The time schedule for the experiment is shown in Figure 1. A transmission scan was performed before the experiment and the data were used to obtain corrected emission images. All PET data were reconstructed by using a convolution filter (cut-off value 8 mm). They also received a T1-weighted MRI scan (0.5 T) on a separate occasion.

*Data Analyses*

The scan data were analyzed by statistical parametric mapping (SPM99) implemented by MATLAB 5.3. First, all rCBF images acquired from each subject were corrected for motion artifacts by realignment to the first image of the experiment. The realigned images were resliced by a sinc interpolation method. Second, a T1-weighted structural MRI was coregistered to the mean image of the realigned images. Third, all images were then spatially normalized into a standard space[10] and smoothed with Gaussian kernel of FWHM of 11 mm. Finally, the effects of the task on the rCBF were estimated using a general linear model. The effects of each comparison were estimated using linear contrasts, which yielded a t-statistic for a given comparison at each voxel. Activation was considered significant if it had a cluster of voxel thresholded above $p<0.005$ (uncorrected, $k>10$ voxels).

## Results

We calculated mean scores for each experimental task and analyzed these scores by a one-way ANOVA. The ANOVA showed no significant difference among these mean scores of the three experimental tasks [CH=12.8, AD=12.6, RE=12.8 (full score=18); $F_{2,24}=0.02$, $p>0.9$].

First, the regional cerebral blood flows (rCBFs) in each experimental condition (CH, AD and RE) were compared to those in CN. All activation foci and their coordinates on a standard brain template are shown in Table 1. Activation areas yielded from the comparison of CH and CN included the inferior frontal (Brodmann area; BA 45), superior temporal (BA 21), and parahippocampal gyri (BA 36) of the right hemisphere, and the medial parietal lobe (BA 18 and 31) and cerebellar vermis of the left hemisphere. Comparison of AD and CN showed activations in the anterior and posterior cingulate (BA 32 and 31), superior temporal (BA 38) and fusiform gyri of the right hemisphere, and in the precuneus (BA 18), cuneus (BA 18) and cerebellar vermis of the left hemisphere. Comparison between RE and CN revealed rather diffuse activations involving the inferior frontal (BA 45), middle temporal (BA 21), and parahippocampal gyri (BA 36) of the right hemisphere, and the medial frontal lobe (BA 9) and precuneus (BA 31) of the left hemisphere. Activation images of the right parahippocamal areas are illustrated in Figure 2.

## Discussion

Previous studies of brain-damaged patients and functional neuroimaging have consistently shown the importance of the hippocampal complex in episodic memory retrieval. The right parahippocampal activation shown in our study reinforces the importance of the parahippocampal area in episodic memory recall, but its differential activation and rCBF patterns based on the oldness of to-be-recalled episode requires explanation.

According to Squire's hypothesis, the medial temporal system continues to consolidate a newly encoded episodic memory for a specific period of time[3)]. Once this critical period is passed, its neural organization stabilizes, and episodes can be retrieved even without the help of the medial temporal system. According to the model proposed by Nadel and Moscovitch, the role of the medial temporal system for consolidation is not temporary but lifelong[2,4)]. The temporal gradient is a reflection of the frequency of retrieval of an episode through the hippocampo-parahippocampal system. Older memories are more frequently recalled resulting in more nodes, and thus become more resistant to destruction than recently encoded ones. Squire's temporal consolidation theory would predict no or little parahippocampal activation during the recall of episodes from the remote past, i.e. CH and AD period. However, our data showed strong

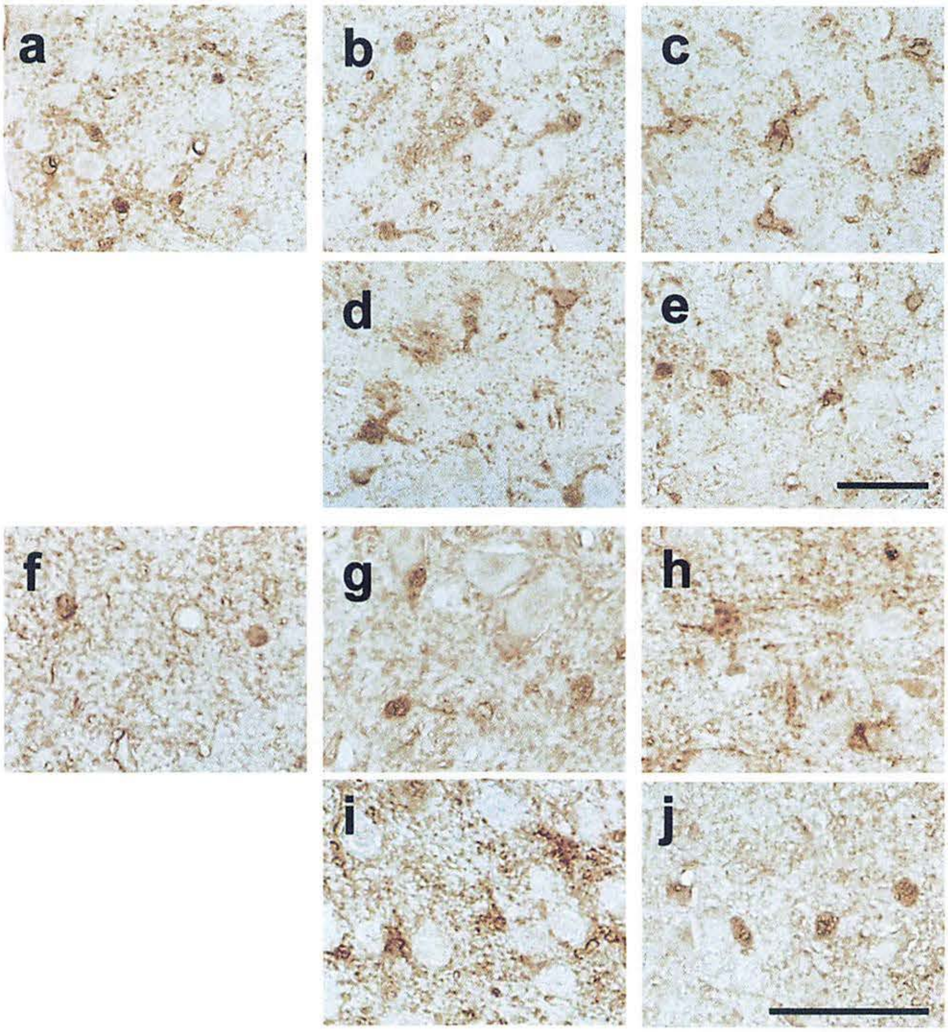

Fig. 1. Representative microphotographs of S100 immunostainig in the striatum (a-e) and substantia nigra (f-j) of mice after MPTP treatment. a,f: Control mice. b,g: Mice at 5 h after MPTP treatment. c,h: Mice at 1 day after MPTP treatment. d,i: Mice at 3 days after MPTP treatment. e,j: Mice 7 days after MPTP treatment. Scale bars = 50 μm.

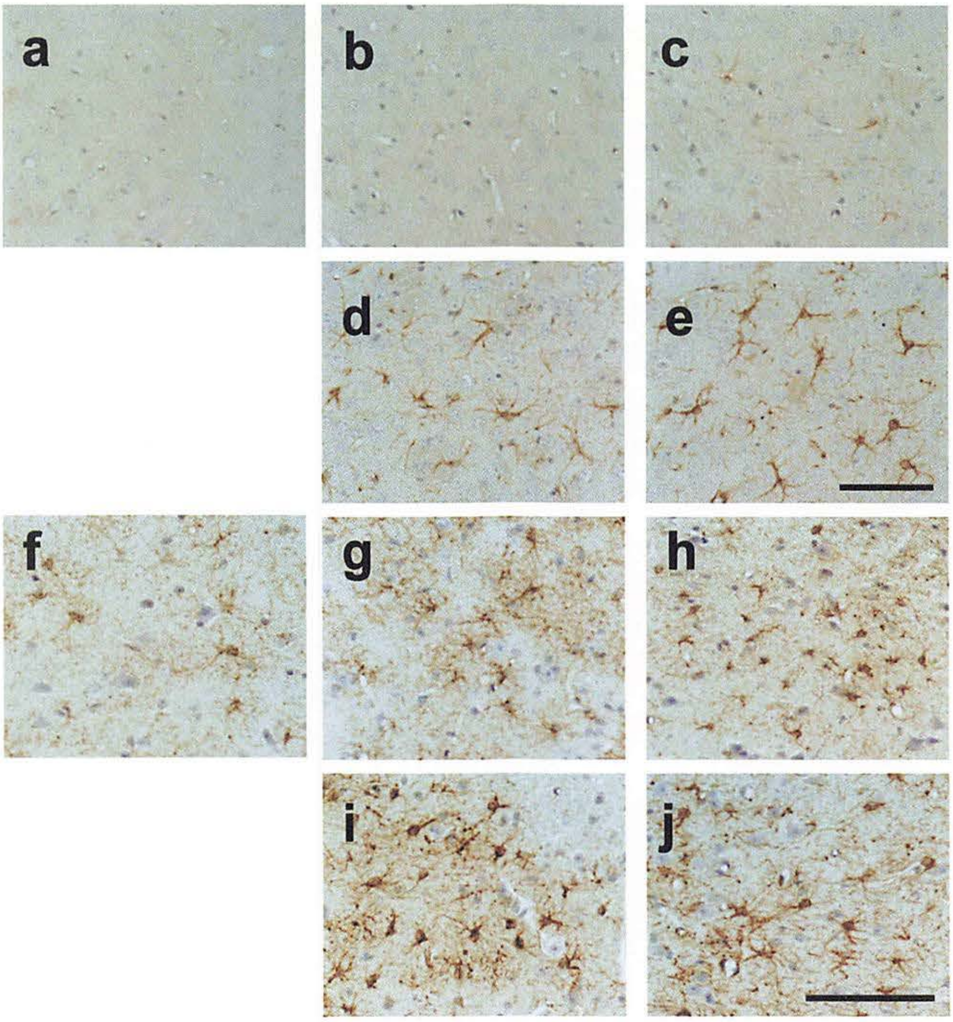

Fig. 2. Representative microphotographs of GFAP immunostainig in the striatum (a-e) and substantia nigra (f-j) of mice after MPTP treatment. a,f: Control mice. b,g: Mice at 5 h after MPTP treatment. c,h: Mice at 1 day after MPTP treatment. d,i: Mice at 3 days after MPTP treatment. e,j: Mice 7 days after MPTP treatment. Scale bars = 100 μm.

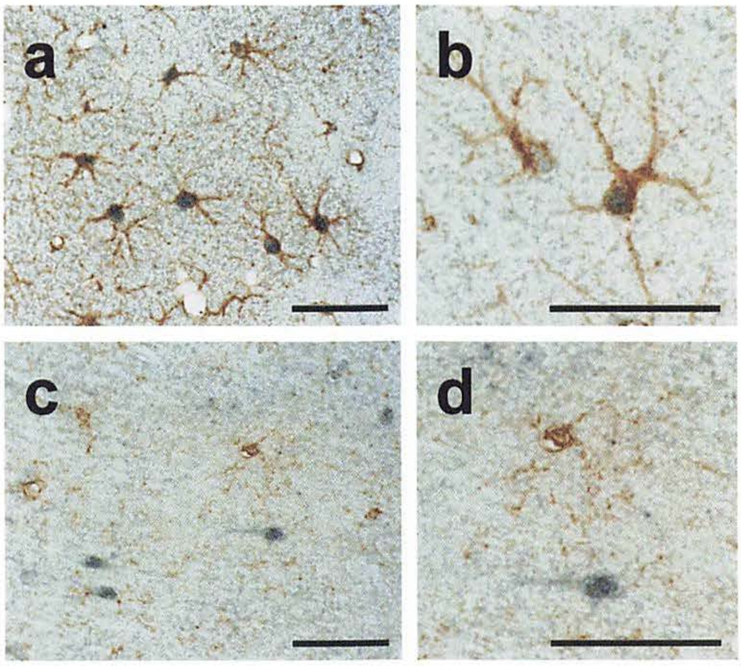

Fig. 3. Representative microphotographs of double-labeled immunostainig with anti-S100 and anti-GFAP antibodies (a,b), and anti-S100 and anti-isolectin $B_4$ antibodies (c,d) in the substantia nigra of mice after MPTP treatment. Scale bars = 50 μm.

# III. 5. Biochemical, Behavioral and Immunohistochemical Study in the Brain of MPTP-treated Mouse Model

*Kurosaki R.*[*,**], *Muramatsu Y.*[*], *Hara A.*[*], *Harasawa T.*[*],
*Kimura S.*[**], *Imai Y.*[*] *and Araki T.*[*]

*Department of Clinical Pharmacology and Therapeutics, Tohoku University Graduate School of Pharmaceutical Science and Medicine*[*]
*Department of Human Life Science, Graduate School of Showa Women's University*[**]

## INTRODUCTION

The neurotoxin 1-methyl-4-phenyl-1,2,3,6-tetrahydropyridine (MPTP) is known to cause degeneration of mesencephalic dopaminergic neurons in several species including monkeys, dogs, cats and mice. The neurotoxic effects of MPTP are thought to be initiated by 1-methyl-4-phenyl-pyridinium ion ($MPP^+$) which is a major metabolite formed by the monoamine oxidase (MAO) B-mediated oxidation of MPTP. $MPP^+$ is taken up by high-affinity dopamine and noradrenaline uptake systems and is subsequently accumulated within mitochondria of nigrostriatal dopaminergic cells[1,2]. This can lead to a number of deleterious effects on cellular function, resulting in neuronal cell death. Therefore, MPTP-treated animals are widely used as one of models for Parkinson's disease[3,4,5,6].

Induction of parkinsonism by MPTP in mice has generated a wealth of neurochemical, pharmacological and anatomical findings. However, in order to deplete striatal dopamine in mice, large doses of MPTP and frequent injections are required[7]. Although the magnitude of the striatal dopamine loss can be increased under some circumstances, progressive and persistent dopamine depletion over a relatively long period has yet to be demonstrated. Furthermore, little is known about the relationship between motor abnormalities and dopamine depletion in MPTP-treated mice.

In the present study, therefore, we investigated the relationship between motor deficit and dopamine depletion in mice after MPTP treatment. Furthermore, we examined immunohistochemically changes of neurons and glial cells in the striatum and substantia nigra of mice after MPTP treatment.

## MATERIALS AND METHODS

Male C57BL/6 mice (Nihon SLC Co., Shizuoka, Japan), 8 weeks of age, were used in this study. All experiments were performed in accordance with Guidelines for Animal Experiments of the Tohoku University School of Medicine.

The mice were injected intraperitoneally MPTP hydrochloride (20 mg/kg in saline) four times at 2-hr intervals within a day. The mice were killed by cervical dislocation at 1, 3, 7, 14 or 21 days after MPTP treatment. The striata were rapidly dissected and were then sonicated in ice-cold 0.2 M perchloric acid containing 100 ng/ml isoproterenol as an internal standard. Dopamine, DOPAC and HVA were quantified by high-performance liquid chromatography (HPLC) with an electrochemical detector (ECD) (Eicom, Kyoto, Japan), as described previously[8,9)].

To measure cataleptic symptoms such as akinesia and rigidity, bar-test catalepsy was evaluated by placing both forepaws of the mouse over a horizontal bar (diameter: 0.2 cm), elevated 15 cm from floor, as described previously[10)]. The time during which the animals maintained this position was recorded. To determine the degree of bradykinesia, a typical symptom of parkinsonism, pole test was performed according to the method of Ogawa *et al.*[11)] with minor modifications[10,12,13)]. The mouse was placed head upward on the top of a rough-surfaced pole (8 mm in diameter and 50 cm in height) which was wrapped doubly with gauze to prevent slipping: the time until it turned completely downward (Tturn) and the time until it climbed down to the floor (TLA) were examined.

For immunohistochemical study, the paraffin sections of the striatum and substantia nigra were used as described previously[14,15)]. For tyrosine hydroxylase (TH) and glial fibrillary acidic protein (GFAP) immunostainings, a rabbit anti-TH polyclonal antibody (Chemicon International, Inc., Temecula, CA, USA), a mouse anti-GFAP monoclonal antibody (Chemicon International, Inc., Temecula, CA, USA) and a Vectastain elite ABC kit (Vector Lab., Burlingame, USA) were used. The immunohistochemical stainings with anti-TH antibody (1:200) or anti-GFAP antibody (1:200) were performed as described previously[14,15,16)].

Microglial cells were histochemically stained with alpha-D-galactosyl-specific isolectin $B_4$ conjugated with horseradish peroxidase derived from Griffonia simplication seeds (GSA I-$B_4$-HRP, isolectin $B_4$) (Sigma, St Louis, MO, USA), as described previously[17)].

activation during recall from CH period. If Nadel and Moscovitch's model was correct, we should expect the same amount of, if not stronger, activation of the parahippocampal region during the CH and AD tasks compared with the RE task. On the contrary, our data showed a curious dip of the parahippocampal activation in the AD task. Therefore, neither of the theories can fully explain the activation pattern of parahippocampal region in the present study.

It has been well established that the myelination process of neurons in association cortices continues well into the late period of the second decade from birth[11]. This fact may suggest that episodes experienced in childhood are encoded when the brain is not fully mature, resulting in rather fragile network formation. This weak organization of early memories may require active hippocampal contribution for their retrieval. For episodes experienced after adolescence, Squire's explanation may be valid. Memories acquired in the adolescence might have been old enough to be established in neocortical systems requiring less participation of the medial temporal lobe system. Episodes more recently acquired in the recent period, are in the midst of consolidation, still requiring hippocampal participation.

It has also been well established that secretion of growth hormone increases during adolescence[12]. There have been suggestions that the rate of growth hormone secretion and such cognitive activities as memory are positively correlated[13,14]. In line with this argument, adolescent subjects were reported to have scored better than other age groups on the Wechsler Memory Scale-Revised (WMS-R)[15]. Well-established memory in the neocortex during this period may not need the strong participation of the hippocampal system for its retrieval, resulting in less activation.

## References

1) Scoville W.B. and Milner B., J Neurol Neurosurg Psychiatry **20** (1957) 11.
2) Fujii T., Moscovitch M. and Nadal L., In: Handbook of Neuropsychology. Cermak L.S. (ed). Amsterdam: Elsevier; 2000, p. 223.
3) Squire L.R. and Alvarez P., Curr Opin Neurobiol **5** (1995) 169.
4) Nadel L. and Moscovitch M., Curr Opin Neurobiol **7** (1997) 217.
5) Oldfield R.C., Neuropsychologia **9** (1971) 97.
6) Crovitz H.F. and Schiffman H., Bull Psychonom Soc **4** (1974) 517.
7) Robinson J.A., Cogn Psychol **8** (1976) 578.
8) Baddeley A.D. and Wilson B.A., In: Autobiographical memory. Rubin D.C. (ed) Cambridge: Cambridge University Press; 1986, p. 225.
9) Fujiwara T., Watanuki S., Yamamoto S. Miyake M., Seo S., Itoh M., Ishii K., Orihara H., Fukuda H., Satoh T., Kitamura K., Tanaka K. and Takahashi S., Ann Nucl Med **11** (1997) 307.
10) Talairach J. and Tournoux P., In: An Approach to Cerebral Imaging. Stuttgart: Thieme, 1988.
11) Yakovlev P.I. and Lecours A.R., In: Regional Development of the Brain in Early Life.

Minkowski A (ed). Oxford: Blackwell; 1967, p. 3.
12) Finkelstein J.W., Roffwarg H.P., Boyar R.M., Kream J. and Hellman L., J Clin Endocrinol Metab **35** (1972) 665.
13) Aleman A., de Vries W.R., de Haan E.H., Verhaar H.J., Samson M.M. and Koppeschaar H.P., Neuropsychobiology **41** (2000) 73.
14) Deijen J.B., de Boer H. and van der Veen E.A., Psychoneuroendocrinology **23** (1998) 45.
15) Wechsler D., In: Wechsler memory scale-revised. New York: The Psychological Corporation; 1987.

Table 1. Activation foci in three experimental tasks compared to the control task.

| Region | | *BA | Talairach Coordinations | | | t-value |
|---|---|---|---|---|---|---|
| | | | x | y | z | |
| 1. CH minus Control | | | | | | |
| Right | inferior frontal gyrus | 45 | 37 | 24 | 4 | 3.32 |
| | superior temporal gyrus | 21 | 65 | -14 | 2 | 3.51 |
| | parahippocampal gyrus | 36 | 25 | -32 | -13 | 5.04 |
| | fusiform gyrus | 19 | 29 | -72 | -11 | 4.47 |
| | lingual gyrus | 19 | 32 | -49 | -3 | 3.01 |
| | supramarginal gyrus | 40 | 58 | -37 | 33 | 3.60 |
| | cerebellar hemisphere | | 47 | -49 | -3 | |
| Left | precuneus | 18 | -2 | -64 | 24 | 3.12 |
| | | 31 | -21 | -64 | 21 | 3.10 |
| | cerebellar vermis | | -9 | -68 | -15 | 3.90 |
| | | | -21 | -67 | -23 | 3.00 |
| 2. AD minus Control | | | | | | |
| Right | cingulate gyrus | 32 | 6 | 36 | -9 | 3.80 |
| | | 31 | 1 | -62 | 10 | 3.00 |
| | superior temporal gyrus | 38 | 44 | 20 | -34 | 3.18 |
| | fusiform gyrus | 19 | 30 | -74 | -10 | 3.85 |
| Left | precuneus | 18 | -2 | -63 | 27 | 3.83 |
| | cuneus | 18 | -3 | -85 | 13 | 3.38 |
| | cerebellar vermis | | -12 | -66 | -14 | 3.33 |
| 3. RE minus Control | | | | | | |
| Right | inferior frontal gyrus | 45 | 37 | 25 | -1 | 3.09 |
| | middle temporal gyrus | 21 | 44 | -5 | -15 | 3.32 |
| | parahippocampal gyrus | 36 | 25 | -32 | -13 | 4.51 |
| | precuneus | 7 | 5 | -47 | 31 | 3.22 |
| | cerebellar vermis | | 10 | -54 | -40 | 3.74 |
| Left | medial frontal lobe | 9 | -18 | 40 | 18 | 3.06 |
| | cingulate gyrus | 29 | -1 | -44 | 8 | 3.24 |
| | precuneus | 31 | -2 | -62 | 23 | 3.74 |

* BA; Brodmann area

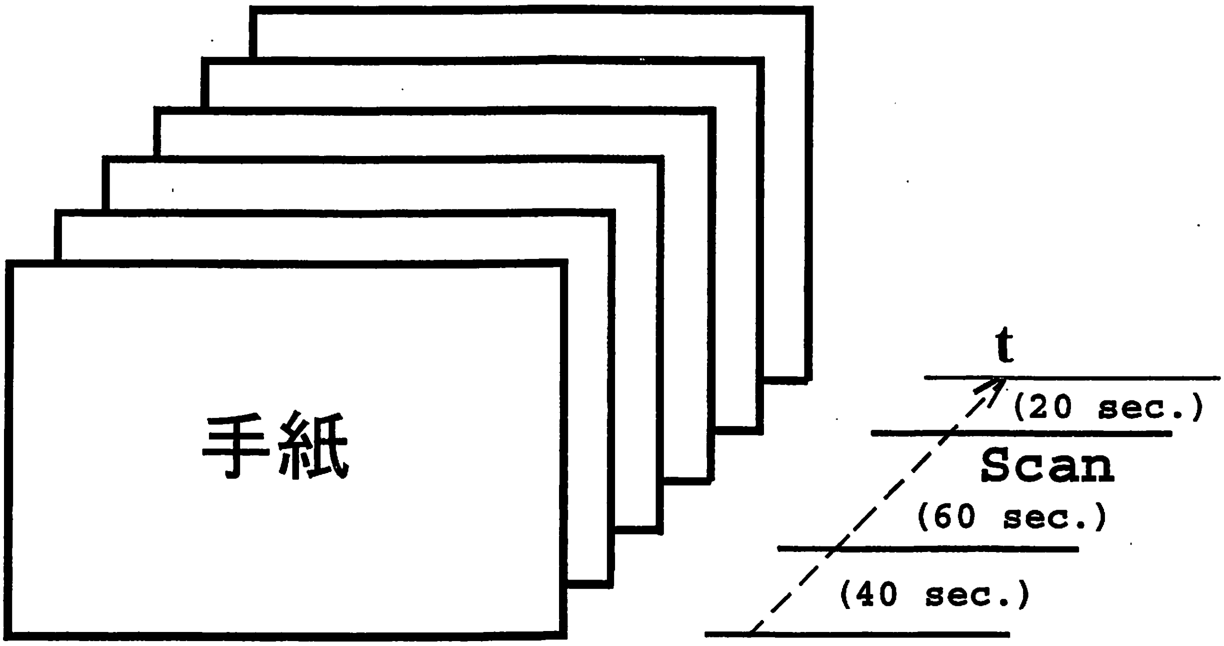

Figure 1. Behavioral task procedures. In one trial, six cue words were visually presented one by one at a rate of 20 seconds. The PET image was acquired for 60 seconds from 41 seconds after the start of the trial. After finishing a PET scan, the task was continued for 20 seconds, which corresponded to the duration of one word presentation. The same procedure was employed across all tasks including the control task.

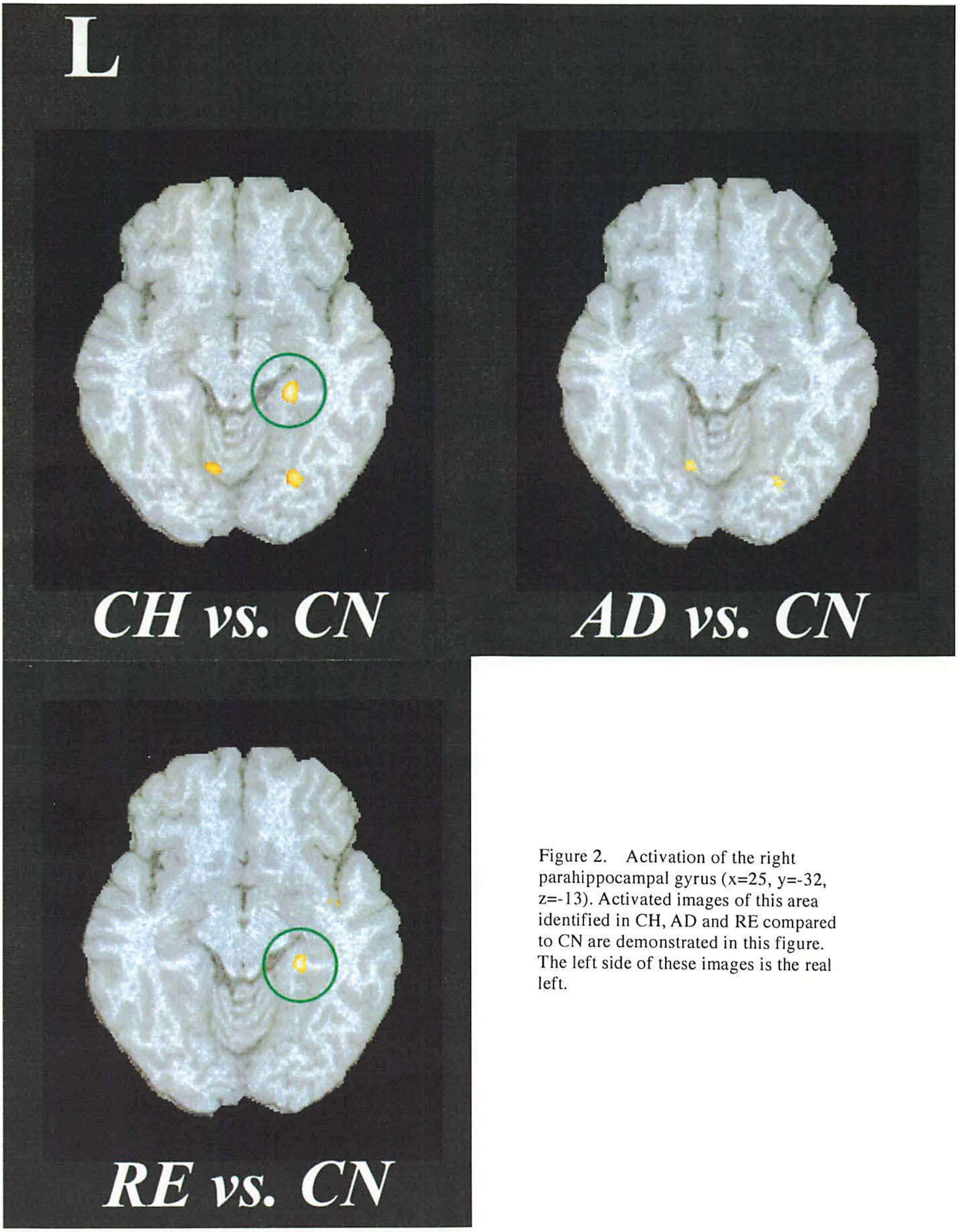

Figure 2. Activation of the right parahippocampal gyrus (x=25, y=-32, z=-13). Activated images of this area identified in CH, AD and RE compared to CN are demonstrated in this figure. The left side of these images is the real left.

# IV. 3. FDG PET in Patients with Gastric Cancer

*Yoshioka T., Yamaguchi K.*, Yamaura G., Fukuda H.**, and Ishioka C.*

*Department of Clinical Oncology, Institute of Development, Aging and Cancer, Tohoku University*
*Cyclotron and Radioisotope Center, Tohoku University **
*Department of Nuclear Medicine and Radiology, Institute of Development, Aging and Cancer*
*Tohoku University***

## INTRODUCTION

In Japan, gastric cancer continues to be the most common malignancy and associated mortality is still second highest, next to lung cancer1). This is due to the lack of the good management of advanced, metastatic, or recurrent cancers and, it is very important to develop effective treatments, especially chemotherapy.

F-18 fluoro-D-deoxy-glucose (FDG) and positron emission tomography (PET) is a noninvasive approach for determination of glycolytic status. Enhanced glycolysis is one of the most important characteristics of cancer cells2), and FDG PET has proved successful for imaging various malignant neoplasms3).

FDG PET can also serve as a diagnostic instrument for follow-up after cancer treatment because response to radiotherapy or chemotherapy is recordable earlier and more exactly in terms of FDG accumulation than by morphological changes4,5). FDG PET has been found to have wide application for treatment evaluation of malignant tumors6-9), however, information on its use for gastric cancer is limited10-13), especially regarding advanced, metastatic or recurrent cases14).

The purpose of the present study was to evaluate the clinical utility of FDG PET in a series of patients with advanced gastric cancers, and to prepare a basis for using this modality to monitor the efficacy of chemotherapy.

## MATERIALS AND METHODS

42 patients (29 men, 13 women; aged 27- 78 yr; mean age 59.2 yr) with advanced, metastatic or recurrent gastric cancers were studied with FDG PET. Thirty-six had biopsy-proven malignancies with sampling of primary lesions and six had histologically proven

malignancies from prior surgical excision of the primary tumors. Of the total, 14 had prior chemotherapy but in all cases they were studied more than 4 weeks after the prior chemotherapy when there was no residual effect of the prior chemotherapy. Patient characteristics are presented in Table 1.

All patients underwent physical examination, ultrasonography (US), double-contrast barium radiograph, upper endoscopy (GTF) and computed tomography (CT) within 2 weeks before the FDG PET. CT scans were carried out in the upper abdomen for all patients and in the range from the neck to the pelvis for those undergoing whole body PET. Bone scintigraphy (n=3) was performed when clinically indicated. Cytology was carried out when ascites or pleural effusion existed and samples could be collected. All patients were followed by physical examinations, GTF, US and CT after FDG PET for more than 4 months, every one or two months, except for one who died within one month of FDG PET.

The study protocol was approved by the Ethics Committee for Clinical Research of Tohoku University and informed consent was obtained from each patient.

All patients fasted for at least 4 hours before the PET and the blood glucose levels were measured before injection of FDG. PET scans were obtained using a PT931/04 scanner (Siemence-CTI, Knoxville, TN, USA) in 20 patients and a SET2400W scanner (Shimadzu Inc, Kyoto, Japan) in 22 patients. The mean injected dose of FDG was 222 ± 72 MBq (range, 103-400 MBq) (2.8-10.8 mCi).

In using the PT931/04 scanner, a CT scan was carried out and a line indicating the site of the targeted lesion was drawn one day before FDG PET. After transmission scanning was performed for 10-15 minutes, emission imaging was carried out in one 7.5-10 minute frame above the drawn line and one or two frames below the line, beginning 30 minutes after injection of FDG. Axial PET images were reconstructed after correction for dead time, decay, and photon attenuation.

In using the SET2400W scanner, emission scans were obtained from head to thigh for 5 minutes per frame, 45 minutes after injection of FDG and a transmission scan was performed for 5 minutes per frame after the emission scan. PET images were reconstructed using measured attenuation, dead time and decay correction factors.

Qualitative evaluation of PET scans was performed blinded and independently by three specialists for PET with images from the patients with gastric cancers but without knowledge of any other clinical information.

Most of the image data obtained by PT931/04 and all those by SET2400W were converted to the analysis format with special software packages, adjusting the cross-calibration factors between PT931/04 and SET2400W. The calibration factors were calculated on both machines twice every month, and we converted the analysis formats to the standardized uptake value (SUV, activity concentration ÷ injected dose / body weight) images with the window range of 0 to 5 for the SUV, using each calibration factor and patient's body weight. Hard copies of consecutive transaxial sections with a linear gray scale were printed out using the image data from PT931/04. The image data from SET2400W proceeded to the process of transaxial and coronary 12mm-re-slices and hard copies of consecutive transaxial and coronary sections covering from the top of the head to the thigh were printed out with a linear gray scale.

The following parameters were evaluated for the visual analysis: visibility of the primary lesion, presence of liver and lymph node metastases, and presence of ascites and peritonitis carcinomatosa in images from PT931/04 and SET2400W, and presence of lung and bone metastases and pleuritis carcinomatosa in images from SET2400W. The lesions were designated as positive (P), questionably positive (QP), negative (N) or questionably negative (QN). The accumulations were assigned QP when they were thought to be malignant but the possibility of physiological accumulations could not be ruled out, and they were assigned QN when they were thought to be physiological but the possibility of the malignancy could not be ruled out. Questionnaires involving all items and figures for the whole body were prepared. If there were other findings in addition to the items or multiple lesions for liver, lymph nodes, lung and bone metastases, each was added to the figure and evaluated.

The gold standards used for verifying lesion malignancy were as follows: GTF for primary lesions; CT and clinical course for liver, lymph node and lung metastases; CT, cytology and clinical course for ascites, peritonitis carcinomatosa and pleuritis carcinomatosa; 99mTechnetium methylene diphosphonate (99mTc MDP) bone scintigraphy and clinical course for bone metastases. "Clinical course" means all of the follow-up examinations and autopsies. Suspected lesions were compared between the initial and follow-up examinations, and decided as actual lesions chiefly based on the change of sizes. The number of lesions was counted individually. If the lesions were clumped or could not to divided, they were counted as a single lesion.

Based on the results of visual analysis, sensitivity, specificity and accuracy were calculated. QP and QN were dealt with by way of having the importance to each side of true and falseness set at half and half, and the following equations were used.

$$\text{True-Positive (TP)} = P(+) + 0.5 \times QP(+)$$
$$\text{False-Positive (FP)} = P(-) + QP(-) + 0.5 \times QN(-)$$
$$\text{False-Negative(FN)} = N(+) + QN(+) + 0.5 \times QP(+)$$
$$\text{True-Negative(TN)} = N(-) + 0.5 \times QN(-),$$

where $P(+)$ = P in the presence of a malignant lesion, $P(-)$ = P in the absence of a malignant lesion, $QP(+)$ = QP in the presence of a malignant lesion, $QP(-)$ = QP in the absence of a malignant lesion, $N(+)$ = N in the presence of a malignant lesion, $N(-)$ = N in the absence of a malignant lesion.

$$\text{Sensitivity (\%)} = TP \div (TP + FN) \times 100$$
$$\text{Specificity (\%)} = TN \div (TN + FP) \times 100$$
$$\text{Accuracy (\%)} = (TP + TN) * (TP + TN + FP + FN) \times 100$$

## RESULTS

Results of the visual analysis on FDG PET are given in Table 2. Sensitivity, specificity and accuracy were 71, 74 and 73% for the SET2400W, and 47, 79 and 62% for the PT931/04 images. They were high for the primary lesions, liver, lymph node and lung metastases, but low for the bone metastases, ascites, peritonitis and pleuritis carcinomatoses (Table 2).

## DISCUSSION

The present study demonstrated the sensitivity, specificity and accuracy of FDG PET for primary lesions, liver, lymph node and lung metastases to be high whereas values for ascites, peritonitis and pleuritis carcinomatosis, as well as bone metastases, were low. Detectability was clearly better with SET2400W than PT931/04.

The sensitivity, specificity and accuracy of FDG PET for primary lesions were high, but missed primary lesions were Borrmann type IV. Higashi et al. reported FDG uptake to reflect the number of viable tumor cells[15]. We speculate that Bormann types I, II and III are easily visible because the malignant cells are densely packed, while with the Borrmann type IV they infiltrate into the gastric wall with much intermingled stromal tissue.

The sensitivity, specificity and accuracy of FDG PET for liver, lymph node and lung metastases were here found to be high. The smallest lesion detected by FDG PET was a liver metastasis of 0.5 cm in diameter and FDG PET for metastatic lesions in nodes appears reliable. However, locoregional lymph node metastases could not be detected by FDG PET in our study. Lerut et al.[16)] reported that the regional lymph node metastases were not detected with high accuracy in line with our study. On the other hand, there were no FDG PET images revealing the existence of a malignant ascitic fluid or pleural effusion. The diagnosis of peritonitis or pleuritis carcinomatosis was possible by FDG PET only when deposits were present on the peritoneal or pleural wall and their sizes were more than 2 cm in diameter. Potter et al. earlier reported that FDG PET was not suited for screening purposes in the follow-up of treated gastric cancer because of its moderate accuracy[14)]. They pointed to incorrect PET diagnoses of recurrent gastric cancers caused by peritoneal metastases, in line with our study findings. We speculate that FDG exudes from vessels into the peritoneal or thoracic cavity and the actually concentrations may be very low. If possible, ascitic fluid or plural effusion should be taken and examined for FDG activity.

Our study group included three cases with bone metastases, suspected on the basis of hypercalcemia, hyper-alkaline-phosphatasenemia or bone pain, for which 99mTc MDP bone scintigraphies were carried out. The number of bone metastases detected with FDG PET was much less than that with the bone scanning. FDG PET appears to be superior to bone scintigraphy at detecting bone metastases from lymphomas[17)] and breast cancers[18)], but is disappointing with prostatic cancer[19)]. Cook et al. reported that FDG PET gave more accurate results than scintigraphy for osteolytic but not osteoblastic breast cancer metastases[20)]. They speculated that osteoblastic metastases might be acellular with low volumes of viable tumor. In addition, osteolytic lesions might be expected to outstrip their blood supply, which renders them hypoxic, and this might increase FDG uptake. In our cases, obviously osteolytic lesions evident with radiography were also detected by FDG PET, but the osseous lesions with no clear changes in plain bone radiographs were missed. Small numbers of malignant cells might induce an osteoblastic response to bone metastases from gastric cancers and, therefore, 99mTc MDP bone scintigraphy might be superior to FDG PET for their detection. However, since our study covered only three cases, further investigations are needed for confirmation.

In the present comparison, the SET2400W was clearly superior to the PT931/04. This is due to the differences of both machine performances, involving the special resolution. But the post-injection transmission technique also improved the results. FDG is trapped and converted to FDG-6-phosphate in the liver, dephosphorylated by a key enzyme for glucogenesis, and excreted[21]. The later the emission scan starts after FDG injection, the better the S/N ratio for liver metastasis. With the PT931/04, patients had to wait on the bed of the scanner from the start of the transmission to the end of the emission and maintain the same supine position. Because this inflicts pain on individuals suffering from severe disease, the total time of the examination must be kept as short as possible. With the SET 2400W, the use of post-injection transmission removes this limitation. Because patients can relax after the injection to the examination, the period after the injection to emission scanning can be lengthened.

To our knowledge, this study was the largest evaluation yet reported for advanced, metastatic or recurrent gastric cancers with FDG PET. Recently Response Evaluation Criteria in Solid Tumors (RECIST) have been widely applied for evaluation of cancer treatment[22]. This method is based on helical CT, but ignores the efficacy with regard to the primary lesion because it can not be measured with the approach in gastric cancer cases. Our study revealed that FDG PET can detect and evaluate primary lesions other than with Borrmann type IV disease, as well as major metastatic sites semiquantitively, and therefore could be employed as an instrument for assessing treatment, especially chemotherapy. However, the results also showed that FDG PET may fail to detect primary lesions of Borrmann type IV, peritonitis and pleuritis carcinomatosa, and bone metastases, despite those being high grade malignancy. In the application of FDG PET for gastric cancer, attention thus should be paid to the risk of missing important lesions.

Our study indicates that FDG PET is a useful diagnostic modality for advanced, metastatic or recurrent gastric cancers, but may have problems in detecting peritoneal and pleural carcinomatoses, and bone metastases. FDG uptake of primary or metastatic gastric cancers is comparatively high, but does not recessively parallel the grade of malignancy.

## ACKNOWLEDGMENTS

We would like to thank the staff of the Cyclotron and Radioisotope Center, Tohoku University. This work was supported by Grants-in-aid for scientific research (No. 13670910 and No. 10670820) from the Ministry of Education, Science, Sports, Culture, and Technology, and for Cancer Reseach (11S-3, 12S-3 and 14S-3) from the Ministry of Health, Labor, and Welfare, Japan.

## REFERENCES

1) Cancer Statistics in Japan'01. http://www.ncc.go.jp/en/statistics/2001/index.html.
2) Warburg O., Science. **123** (1956) 309.
3) Gambir S. S., Czernin J., Schwimmer J. et al., J. Nucl. Med. **42** (2001) 1S.
4) Abe Y., Matsuzawa T., Fujiwara T., et al., Eur. J. Nucl. Med. **12** (1986) 325.
5) Yoshioka T., Takahashi H., Oikawa H., et al., J. Nucl. Med. **38** (1997) 714.
6) Abe Y., Matsuzawa T., Fujiwara T., et al., Int. J. Radiat. Oncol. Biol. Phys. **19** (1990) 1005.
7) Wahl R. L., Zasadny K., Helvie M., et al., J. Clin. Oncol. **11** (1993) 2101.
8) Haberkorn U., Strauss L. G., Dimitrakopoulou A., et al., J. Nucl. Med. **34** (1993) 12.
9) Ichiya Y., Kuwabara Y., Otsuka M., et al., J. Nucl. Med. **32** (1991) 1655.
10) Couper G. W., McAteer D., Wallis F., et al., Br. J. Surg. **85** (1998) 1403.
11) MacAteer D., Wallis F., Couper G., et al., Br. J. Radiol. **72** (1999) 525.
12) Kole A. C., Plukker J. T., Nieweg O. E., Vaalburg W., Br. J. Cancer. **78** (1998) 521.
13) Stahl A., Ott K., Weber W. A., Fink U., Siewert J. R. and Schwaiger M., J. Nucl. Med. **42** (2001) 78P
14) Potter T. D., Flamen P., Cutsem E. V., et al., Eur. J. Nucl. Med. **29** (2002) 525.
15) Higashi K., Clavo A. C. and Wahl R. L., J. Nucl. Med. **34** (1993) 414.
16) Lerut T., Flamen P., Ectors N., et al., Ann. Surg. **232** (2000) 743.
17) Moog F., Kotzerke J., Reske S. N., J. Nucl. Med. **40** (1999) 1407.
18) Moon D. H., Maddahi J., Silverman D. H. S., Glaspy J. A., Phelps M. E., Hoh C. K., J. Nucl. Med. **39** (1998) 431.
19) Shreve P. D., Grossman H. B., Gross M. D. and Wahl R. L., Radiology. **199** (1996) 751.
20) Cook G. J., Houston S., Rubens R., Maisey M. N. and Fogelman I., J. Clin. Oncol. **16** (1998) 3375.
21) Gallagher B. M., Fowler J. S., Gutterson N. I., MacGregor R. R., Wan C. N. and Wolf A. P., J. Nucl. Med. **19** (1978) 1154.
22) Therasse P., Arbuck S. G., Eisenhauer E. A., et al., J. Natl. Cancer Inst. **92** (2000) 205.

Table 1. Patient characteristics.

| | Patient | Age/Sex | Primary (Borrmann) | Histology | Metastatic sites | Chemotherapy before PET | Surgery |
|---|---|---|---|---|---|---|---|
| PT931/04 | | | | | | | |
| | E01 | 72F | IV | sig | Liver, Lym (abd) | yes | |
| | E02 | 62M | III | well | Liver, Lym (abd), PC, Ascites | yes | |
| | E03 | 72M | no | poor | Liver, PC, Ascites | no | |
| | E04 | 78M | III | mod | Lym (abd) | yes | |
| | E05 | 69M | III | poor | Liver, Lym (abd) | no | |
| | E06 | 35F | IV | poor | PC | no | exp |
| | E07 | 56M | III | mod | Liver, Lym (abd), PC, Ascites | yes | |
| | E08 | 60M | no | mod | Liver | yes | |
| | E09 | 50M | III | well | Lym (abd) | yes | |
| | E10 | 63M | no | muc | Liver | yes | |
| | E11 | 78M | IV | poor | Lym (abd) | yes | |
| | E12 | 45F | II | sig | PC, Ascites | yes | |
| | E13 | 60F | IV | sig | PC, Ascites | no | exp |
| | E14 | 35M | IV | poor | PC, Ascites | no | |
| | E15 | 62F | IV | poor | no | no | |
| | E16 | 46M | IV | mod | Liver, Lym (abd) | no | |
| | E17 | 63F | III | sig | Lym (abd) | no | |
| | E18 | 66M | III | mod | Liver, Lym (abd), PC, Ascites | no | |
| | E19 | 76M | III | mod | Liver, Lym (abd) | yes | |
| | E20 | 71F | I | well | PC, Ascites | yes | |
| SET2400 | | | | | | | |
| | S01 | 68M | II | well | Liver, Lym (abd) | yes | |
| | S02 | 69M | III | poor | Lym (abd) | no | |
| | S03 | 42M | no | sig | PC | yes | ileus |
| | S04 | 66M | III | poor | Liver, Lym (abd) | no | |
| | S05 | 63M | III | well | Lung, PC, Ascites | no | |
| | S06 | 69M | II | poor | Liver, Lym (abd) | no | |
| | S07 | 49M | III | poor | Liver, Lym (abd), Bone (cost) | no | |
| | S08 | 27F | V | sig | PC, Ascites | no | |
| | S09 | 42F | no | poor | PC, Ascites, PIC | no | |
| | S10 | 64M | III | mod | Lym (abd) | no | |
| | S11 | 69M | III | poor | Liver, Lym (abd), PC | yes | bypass |
| | S12 | 72M | no | mod | PC (schnitzuler) | no | ileus |
| | S13 | 48M | I | poor | no | no | |
| | S14 | 59M | IV | sig | PC, Ascites | no | exp |
| | S15 | 34F | V | sig | Lym (abd, Virchow), PC, Ascites, PIC | no | |
| | S16 | 74M | II | poor | Liver, Lym (abd, mediastinal), Lung, PC, Ascites, PIC | no | |
| | S17 | 64F | II | well | Liver, Lym (abd) | no | bypass |
| | S18 | 61M | I | poor | no | no | |
| | S19 | 63M | II | mod | Liver, Lym (abd), PIC | no | |
| | S20 | 73M | III | poor | Liver, Lym (abd, Virchow), PC, Ascites, Bone (multipl | no | |
| | S21 | 41F | V | poor | Lym (abd), Bone (multiple) | no | |
| | S22 | 52M | III | poor | Lym (abd) | no | |

M, male; F, female; well, well differentiated adenocarcinoma; mod, moderately differentiated adenocarcinoma; poor, poorly differentiatedadenocarcinoma; sig, signet cell carcinoma; Lym, lymph node metastasis; abd, abdomen; PC, peritonitis carcinomatosa; PIC, pleuritis carcinomatosa; exp, exploratpry laparotomy; ileus, the operation to relieve the ileus status; bypass, gastrointestinal bypass.

Table 2. Sensitivity, specificity and accuracy.

| | Overall | Prim | Liver | Lym | Lung | PC | Ascites | PIC | Bone |
|---|---|---|---|---|---|---|---|---|---|
| PT931/04 | | | | | | | | | |
| Sensitivity (%) | 47 | 70 | 78 | 47 | | 9 | 2 | | |
| Specificity (%) | 79 | 78 | 82 | 62 | | 79 | 93 | | |
| Accuracy (%) | 62 | 71 | 80 | 54 | | 48 | 57 | | |
| SET2400W | | | | | | | | | |
| Sensitivity (%) | 71 | 91 | 85 | 73 | 67 | 50 | 24 | 4 | 30 |
| Specificity (%) | 74 | 100 | 74 | 78 | 88 | 63 | 76 | 100 | 82 |
| Accuracy (%) | 73 | 92 | 79 | 75 | 86 | 57 | 59 | 83 | 57 |

Overall, all lesions; Prim, primary lesions; Liver, liver metastases; Lym, lymph node metastases; Lung, lung metastases; PC, peritonitis carcinomatosa; PIC, pleuritis carcinomatosa; Bone, bone metastases. The PT931/04 scanner has a spatial resolution of 6.0 mm at full-width half-maximum (FWHM) and the sensitivity per slice of 157 kcps/MBq/ml. The SET2400W scanner has a spatial resolution of 3.9 mm at FWHM and the sensitivity per slice of 97 kcps/MBq/ml.

# V. RADIATION PROTECTION AND TRAINING OF SAFE HANDLING

# V. 1. Neutron Spectrum and $^7$Be Production of the Li(d.n) Reaction for the IFMIF

*Hagiwara M., Baba M., Kawata N., Itoga T., and Hirabayashi N.*

*Cyclotron and Radioisotope Center, Tohoku University*

The International Fusion Materials Irradiation Facility (IFMIF) project has been proposed to establish an accelerator-based D-Li neutron source designed to produce an intense fast neutron field for high fluence test irradiations of the fusion reactor candidate materials$^{1)}$.

For the design and operation of the neutron source, detailed knowledge is required on the energy-angular neutron emission spectra of the $^7$Li(d,n) reaction and the radioactivity ( $^7$Be, $^3$H etc.) accumulated in the target, whose data are indispensable for precise estimation of the neutron irradiation effects and are important for the management of the accelerator system. However, the data status is not good enough as shown by marked differences among experimental data$^{2)}$. To improve the data status, we have started experiments on the neutron emission spectra of the $^7$Li(d,n) reaction and the radioactivity induced in the target using the AVF cyclotron (K=110) at CYRIC from 2001.

In 2001, we obtained the thick target neutron yields (TTY) and production ratio of radioactive nuclide, $^7$Be from the thick lithium target for 25 MeV deuterons. We obtained almost entire energy range of the emitted neutron spectra and revealed the shape in the high energy region called 'high-energy tail' obviously$^{3-5)}$.

In 2002, the experiment was conducted for 40 MeV deuterons. Besides, we extended the measurement not only thick target but also to thin target (double differential cross section: DDX and activation cross section) to examine the accuracy of model calculations. Pair measurements of the neutron spectra such as TTY and DDX in the Li(d,n) reaction was first attempt but they are very effective for the demonstration of the neutron production mechanisms in the D-Li reaction. We prepared a thin target (~0.85 mm) and a stacked targets that consist of eight lithium plates with different thickness (~1.3, ~6.7, ~1,

~4.7, ~0.9, ~2.7, ~0.7, ~3.4 mm, total thickness ~21.4 mm) to measure not only neutron spectra but also excitation function of the $^{nat}$Li(d,x)$^{7}$Be reaction simultaneously.

The neutron spectra were measured for almost entire range (1-65 MeV) of secondary neutrons at nine laboratory angles between 0- and 110-deg with the two-gain time-of- flight (TOF) method[6] using a beam swinger system. The results are shown in Fig. 1 and Fig. 2. The pairs of the spectra show a consistency with each. In Fig. 3, The experimental results are compared with other experimental data and calculations[10]. Similarly as the previous spectra at 25 MeV[3-5], the model calculations fail to reproduce the experiment data in high energy region. We revealed the main components of 'high-energy tail' from the data of thin target, which will be helpful to develop the reaction models.

The number of $^{7}$Be accumulated in the stacked targets was measured by counting the $\gamma$-rays from $^{7}$Be using a pure Ge detector. The induced $^{7}$Be activities were determined with corrections for $\gamma$-ray detection efficiency, energy determination and deuteron attenuation using EGS 4[7], TRIM code[8] and Shen's formula[9] respectively. The results are compared with other data[11-13] as shown in Fig. 4 and Fig. 5. $^{7}$Be data in high energy region were obtained first time.

*In collaboration with National Institute for Fusion Science (NIFS).

**References**

1) IFMIF CDA TEAM, IFMIF Conceptual Design Activity Final Report edited by Marcello Martone, Report 96.11, Enea, Dipartimento Energia, Frascati (1996).
2) Lone M.A. et al., Nucl. Instrum. Methods **143** (1977) 331.
3) Baba M., Aoki T., Hagiwara M. et al., J. Nucl. Materials **307-311** (2002) 1715.
4) Aoki T. et al., CYRIC Annual Report 2001, p. 170.
5) Aoki T., Hagiwara M., Baba M. et al., J. Nucl. Sci. Tech. to be published.
6) Ibaraki M. et al., Nucl. Sci. Technol. **35** (1998) 843.
7) Nelson W., Hirayama H. and Rogers D.W.O., "The EGS4 Code System" SLAC-265, Stanford University, Stanford (1985).
8) Ziegler J.F., Biersack J.P and Littmark U., "The Stopping and Range of Ions in Solids," vol. 1 of series "Stopping and Ranges of Ions in Matter," Pergamon Press, New York (1984).
9) Shen W.Q., Wang B., Feng J., Zhan W.L., Zhu Y.T. and Feng E.P., Nucl. Phys. A **491** (1989) 130.
10) Simakov S.P., Fischer U. et al., J. Nucl. Materials **307--311** (2002) 1710.
11) Tanaka S. et al., Proc. of 8th Int. Conf. On Radiation Shielding, Arlington, Apr. 1994, Vol.2, (American Nuclear Society, 1994) pp. 965.
12) EXFOR system: OECD/NEA http://www.nea.fr.
13) Von Möllendorff U., Feuerstein H. and Giese H., Proc. 20th Symp. on Fusion Technology (Marseille, France, 7-11 Sept.1998) pp.1445.

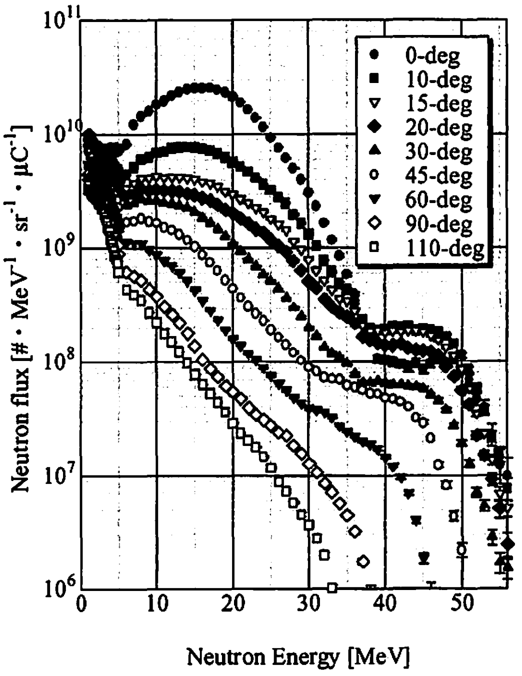

Fig .1. The neutron spectra from thick lithium target for incident deuteron energy of 40 MeV.

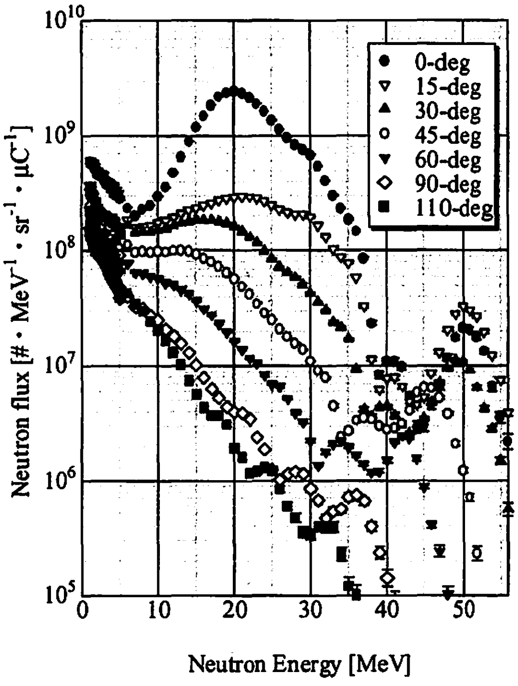

Fig. 2. The neutron spectra from thin lithium target for incident deuteron energy of 40 MeV.

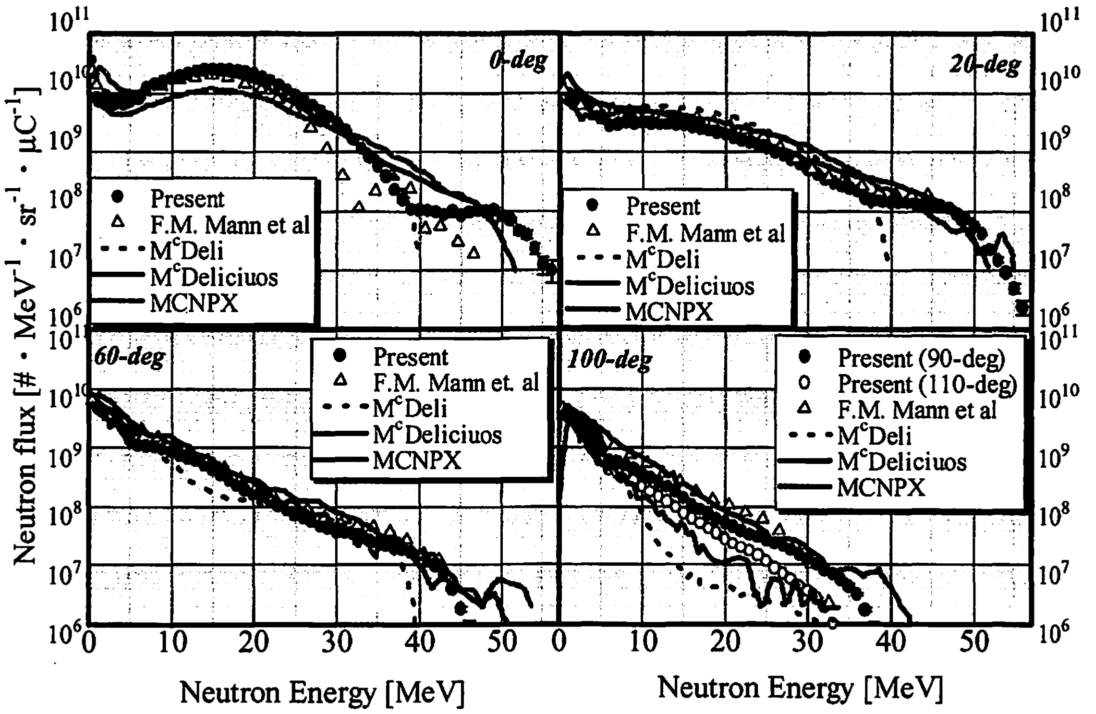

Fig. 3. Comparison of the present $^{nat}$Li(d,n) neutron spectrum with the other experimental data and calculation collected by Simakov et al[10].

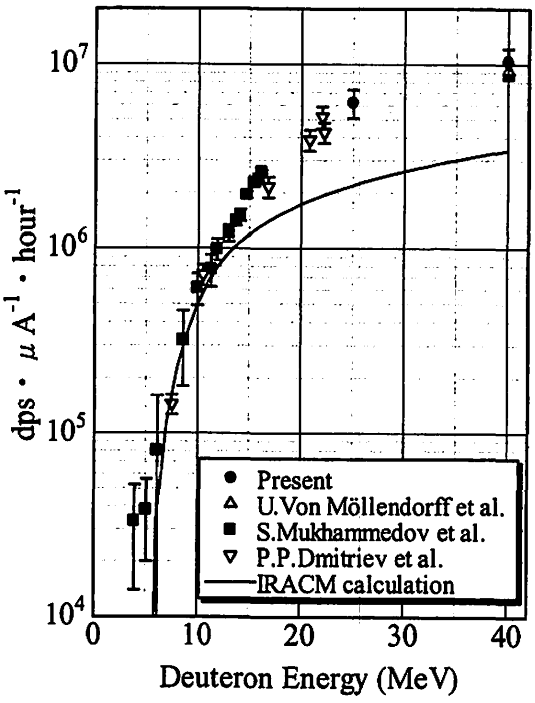

Fig. 4. $^{7}$Be production rate *via* the Li(d,x) reaction.

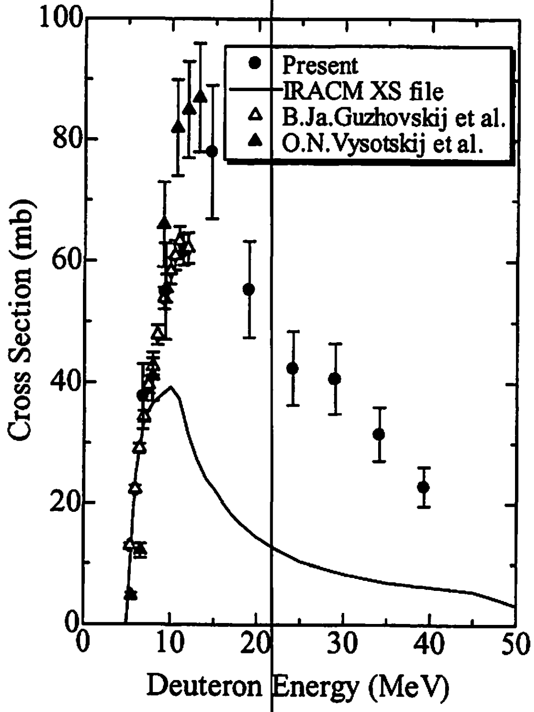

Fig. 5. $^{7}$Li(d,2n)$^{7}$Be reaction cross-section.

# V. 2. Experimental Studies of the Proton-induced Activation Cross-sections on Tantalum

*Uddin M. S., Hagiwara M., Kawata N., Itoga T., Hirabayashi N., and Baba M. Tarkanyi F.*, Ditroi F.*, and Csikai J.***

*Cyclotron and Radioisotope Center, Tohoku University, Sendai, Japan*
*Institute of Nuclear Research of the Hungarian Academy of Sciences, Debrecen, Hungary**
*Institute of Experimental Physics, University of Debrecen, Debrecen, Hungary***

## Introduction

Data on activation reaction are required for development of neutron source and accelerator-driven system (ADS) for transmutation of nuclear waste or energy-production. Measurement of medium energy activation cross-sections is most important in the estimation of the production yield, monitoring of the hot-cell procedure and an evaluation of isotopic interferences. It is required for the radiation safety and estimation of radioactive wastes. Activation cross-sections of Ta+p reactions are of interest for evaluation of radioactivity around accelerators because tantalum is used in various parts of accelerators, for production of medical radioisotopes ($^{178}$W/$^{178}$Ta, $^{172}$Hf/$^{172}$Lu, $^{177}$Lu, etc).

Despite of the importance of the Ta+p reaction only a very few cross-section measurements were published in the literature$^{1-6)}$. Besides the published data are very contradictory to each other and to the results of the theoretical calculations. The predictions of model calculations are unreliable. The data status is quiet unsatisfactory.

In view of these considerations, the present work was undertaken to obtain new and reliable excitation functions and thick target integral yields of the proton-induced reactions on tantalum target in the energy range 28-69 MeV. The cross-sections were also calculated theoretically using the Monte Carlo code, NMTC/JAM (PHITS)$^{7)}$ and compared with the experimental data.

## Experimental techniques

The excitation functions were obtained by employing a stacked target techniques. The stacked Ta foils and Cu and Al monitor foils of natural isotopic compositions were irradiated by a 70 MeV collimated proton beam using the k=110 MeV AVF Cyclotron at CYRIC. The stacks were made of aluminum, tantalum, copper, titanium, iron, platinum, palladium and zinc. Each stack consists of six different types of the above metallic target foils. Two experiments were taken place in the same experimental conditions. The stacked samples were brought instantly into the irradiation place by an automated transfer system newly designed at CYRIC. It was necessary to ensure that equal areas of the monitor and the target foils intercepted the beam. The irradiation geometry used guaranteed that practically the whole entering beam passed through every foil.

The activities of the produced radionuclides were measured nondestructively by a high resolution HPGe γ-ray detector by coupling with a 4096 multi-channel analyzer. Before the measurement, irradiated foils were sorted into polyethylene bags to avoid radioactive contamination. The efficiency versus energy curve of the detector was determined experimentally using standard gamma-ray point sources with known strength, $^{152}$Eu, $^{133}$Ba, $^{241}$Am, $^{60}$Co and $^{137}$Cs. We also calculated the detector efficiency using the EGS4 Monte Carlo Code8). The theoretically obtained efficiencies agreed with experimental values. The proton energy degradation along the stack was determined using the computer program TRIM9). We measured the beam intensity and cross-sections using the well-known activation formulae. The proton beam intensity was determined via the standard monitor reactions $^{27}$Al(p,x)$^{22,24}$Na and $^{nat}$Cu(p,x)$^{56}$Co,$^{62,65}$Zn The cross-sections were deduced for the production of $^{175,176,177,180}$Ta, $^{173,175}$Hf, $^{178}$W and $^{179}$Lu residual nucleus from 28 to 69 MeV bombarding energies. The thick target integral yields were determined from the respective thresholds of the investigated nuclear reactions using the measured cross-sections as a function of proton energy. The data were corrected for the coincidence-summing effect caused by the coincidence detection of two or more gamma rays by using the SUMECC code10).

## Results and discussion

The detector efficiency versus energy curve is the most important to give reliable cross-sections. During determination of the efficiency curve, it was found that the number of gamma-lines of the available standard sources were not sufficient in the lower energy region. Therefore, we have to use more standard gamma-ray point sources with sufficient strength to obtain the most reliable efficiency curve in the lower energy region. Two experiments took place in the same experimental conditions and resulted in reasonable agreement. The present experiment has given new data for all of the investigated reactions. The measured excitation functions only for $^{175}$Ta production along with available literature values and theoretically calculated values are shown in Fig. 1. In this case, our measured data are consistent with the experimental values reported by C.L.Rao[1], but not similar to the theoretical calculations. Besides, we have observed the contradictory results between MENDL and PHITS calculations. Therefore, our newly measured cross-sections will contribute to improve the statistical model code for reliable data calculations and allow to produce the recommended data for practical purposes. The results of this work have already been submitted to publish in the Journal of Nuclear Science and Technology[11)].

## References

1) Rao C.L. and Yaffe L., Canad. J.Chem. **41** (1963) 2516.
2) Cohen B.L., Newman E., Charpie R.A. and Handley T.H., Phys.Rev., **94** (1954) 620.
3) Zaitseva N.G., Rurarz E., Khalkin V.A., Stepailov V.I. and Popinenko L.M., J. Radiochim. Act. **64** (1994) 1.
4) Haasbroek F.J., Steyn J., Neirinckx R.D., Burdzik G.F., Cogneau M. and Wanet P., Int. J. Appl. Radiat. Isot. **28** (1977) 533.
5) Birattari C., Gadioli E., Grassi Strini A.M., Tagliafern G. and Zetta L., Nucl. Phys. **A166** (1971) 600.
6) Experimental Nuclear Reaction Data File (EXFOR), Data base last updated on Feb.**25** (2003).
7) Iwase H., Niita K. and Nakamura T., J. Nucl. Scien. Tech. **39** (2002) 1142.
8) Nelson W.R., Hirayama H. and Regers D.W.O., EGS4 code system, SLAC-265, Stanford Linear Accelerator Laboratory (1985).
9) Ziegler J.F., Biersack J. P. and Littmark U., "The stopping and range of ions in solids", Pergamon, New York (1984).
10) Torii A., Uwamino Y., Nakamura T., INS-T-468, Institute for Nuclear Study, University of Tokyo (1987).
11) Uddin M.S., Hagiwara M., Kawata N., Itoga T., Hirabayashi N., Baba M., Tarkanyi F., Ditroi F. and Csikai J., "Measurement of excitation functions of the proton – induced activation reactions on tantalum in the energy range 28-70 MeV", (2003) (submitted).

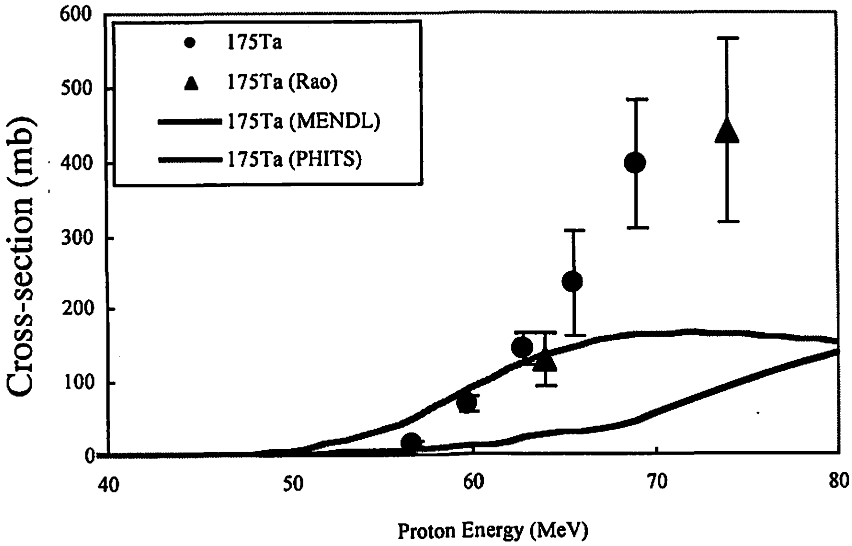

Fig. 1. Excitation functions of the $^{181}$Ta(p,x)$^{175}$Ta reaction.

# V. 3. Development of Ion Irradiation Apparatus for Simulation of Cosmic-ray Effect to Semiconductor Devices

*Hirabayashi N., Baba M., Hagiwara M., and Itoga T.*

*Cyclotron and Radioisotope Center, Tohoku University*

## Introduction

In the space environment, radiation has very severe effects on electronic components such as processors or memories in space crafts. The space radiation consists of several kinds of energetic particles: galaxy cosmic-rays, solar flare particles, particles trapped in the van Allen's belt, etc. Therefore it is required that the semiconductor parts of a satellite have high reliance against cosmic-ray radiations.

The defects which radiation causes in electronic products are classified into 1) total dose effects (TDE) and 2) single event effects (SEE). TDE is a phenomenon that degrades or destroys the structure of semiconductors gradually with the accumulation of radiation dose. SEE is a temporary soft error or a permanent latch-up of digital circuits caused by a single high energy particle.

In order to withstand such a radiation defects, the electronic products of the apparatus for the space have been developed with special specification. However, these devices have several drawbacks. For example, they are normally very expensive, need long lead times to purchase and the technology employed is several generations older than that of the most advanced commercial off-the-shelf (COTS). Therefore, the cost will be reduced if the COTS products used for PC, a cellular phone, etc. can be used in the space. In order to use COTS parts for space equipment, however, their performance in the space environment especially for radiation should be verified.

For the reasons, we have started evaluation works of SEE in the semiconductor memory using light and heavy charged particle beam from the 930 cyclotron of CYRIC in collaboration with Institute of Unmanned Space Experiment Free Flyer (USEF), and fabricated an experimental device for ion beam irradiation.

**Experimental apparatus**

For the irradiation experiments of semiconductor device, the following beam conditions are required for the case of proton:

1) Proton flux is around $5 \times 10^7$ [#/cm·sec]. (It corresponds to 8 pA of beam current)
2) Beam intensity is uniform on a device surface within about 10 % on a circle with a diameter of 2 cm.
3) Incident beam intensity can be measured in real-time.
4) The beam energy can be changed easily.
5) Devices can be irradiated in air.

The beam handling system was designed to meet these conditions. In order to uniform the beam intensity and change the energy of the beam, we decided to use copper as a diffuser which spreads the pencil beam from the accelerator and a degrader to reduce the beam energy.

The beam line was fabricated on the basis of the above requirement. Figure 1 shows schematic view of the beam line. The incident beam enters from left-hand side, and passes an aperture with a diameter of 10 mm. Next, the beam passes along the degrader or diffuser. Their thicknesses are chosen according to the beam energy. These are mounted on a ladder which can be controlled remotely.

The beam which is degraded and/or diffused travels to an aperture again. Then the narrow beam defined by the aperture goes into the secondary emission monitor (SEM: Fig.2) which reads the beam intensity during irradiation of devices. SEM is a detector of beam current by taking the secondary electrons from thin aluminum foils as a current signal. SEM needs calibration for absolute measurement because the output of the SEM depends on the beam energy as well as the intensity. Next to the SEM, a remote-controlled Faraday cup is set up, which is made of copper and serves both as a beam dump and an absolute current detector. Measurement of the beam current by the SEM is possible if the relationship of the SEM and the faraday cup is obtained prior to the irradiation experiment. The current of Faraday cup and SEM are read with a IF converter with a sensitivity of 1 pulse/1 pC (Laboratory Equipment Inc.)

Finally, the beam is extracted to the air passing through a Kapton foil (thickness around 200 $\mu$m) which separate this beam line from air.

## Prospects

We have fabricated and installed the above mentioned apparatus for simulation of cosmic-ray effect to semiconductor devices. Irradiation experiments were carried out a few times and results have been discussed in comparison with the results in other irradiation facilities. We want to establish the method of irradiation and to extend the irradiation by various heavy ion beams.

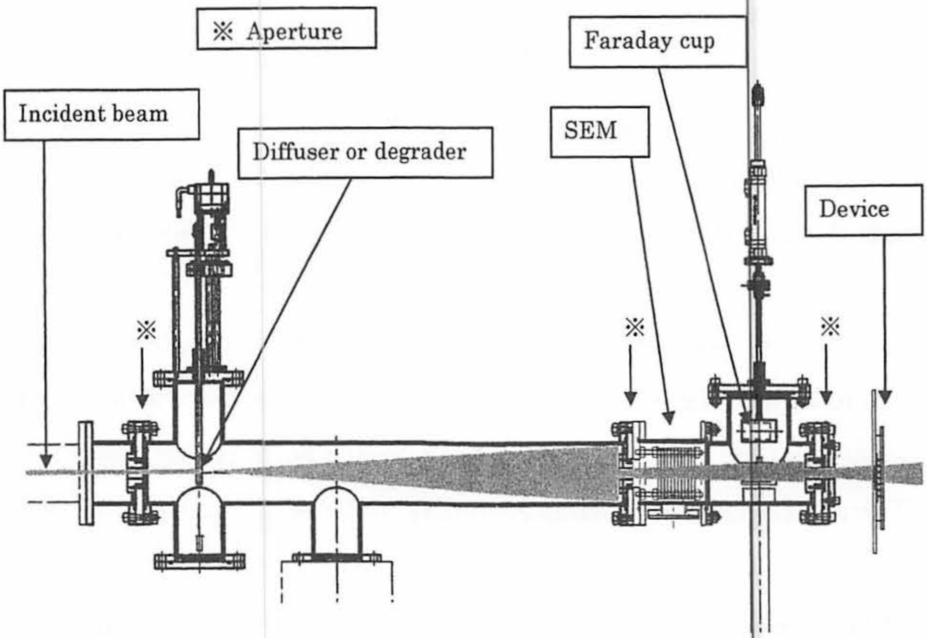

Fig. 1. Ion irradiation apparatus.

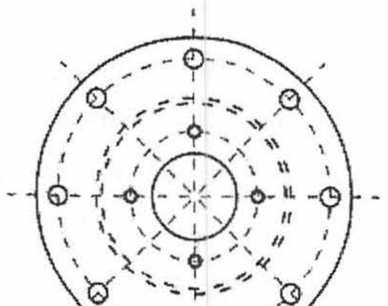
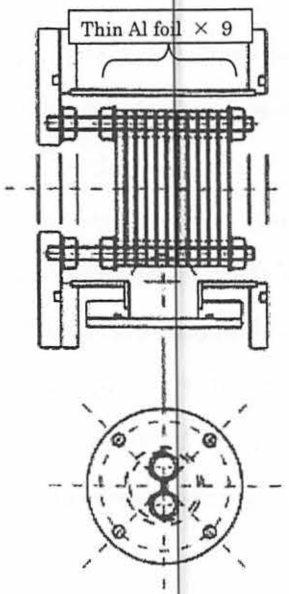

Fig. 2. Secondary emission monitor.

# V. 4. Design and Benchmark Experiment for Cyclotron-based Neutron Source for BNCT

*Yonai S., ItogaT., Nakamura T., Baba M., Yashima, H. Yokobori H.*, and Tahara Y.***

*Cyclotron and Radioisotope Center, Tohoku University*
*Advanced Reactor Technology Co., Ltd., Japan**
*Mitsubishi Heavy Industries, Ltd., Japan***

## Introduction

Boron Neutron Capture Therapy (BNCT) is a promising treatment for brain tumors such as Glioblastoma Multiforme, which are at present considered to be inoperable. BNCT relies on two components, $^{10}$B-doped pharmaceuticals and neutrons for irradiation. The $^{10}$B component, which is delivered preferentially to the tumor cells, is administered to the patient, who is subsequently irradiated with an external neutron beam. The $^{10}$B (n,α) $^{7}$Li reaction, on which BNCT is based, has a large cross section of 3837 barns for thermal neutrons and this interaction produces two particles, α and $^{7}$Li, with high Linear Energy Transfer (LET) and Relative Biological Effectiveness (RBE). The mean free path is about 10 μm and 5 μm for α particles and for $^{7}$Li, respectively. Considering that the mean cellular diameter is of the order of 10 μm, it is possible that BNCT may act selectively in killing cells.

The neutron field should exhibit an energy spectrum that delivers a therapeutic dose to tumor tissues in conjunction with a tolerable dose to normal tissues. Because of the large kerma coefficient of the $^{1}$H(n,n')$^{1}$H reaction, it is not possible to kill a cell selectively with high neutron energy. On the other hand, Gliobastoma Multiforme often locates near the center of the brain surrounding healthy tissues, and can not be killed with thermal neutrons, which have feeble penetration and stop in the skins or in other healthy tissues.

To meet the above requirements, the use of epithermal neutrons in BNCT has recently met increasing interest, taking into account that incident neutrons are moderated in the human body. For example, Yanch et al$^{1)}$ showed that epithermal neutrons in the energy range from 4 eV to 40 keV are most effective in the treatment of a brain tumor at a depth of

7cm. Many groups have investigated epithermal neutrons for BNCT with reactor- and accelerator-based neutron sources. Reactions such as $^{7}$Li(p,n) ($E_p$=1.95 MeV[2], 2.4MeV[3] and 2.5 MeV[4], $^{2}$H(d,n)$^{3}$He and $^{3}$H(d,n)$^{4}$He ($E_d$=100-400 keV)[5] are currently being investigated as accelerator-based neutron sources. However they have not been realized yet in applications, mainly because they require a very high beam current from an accelerator which introduces difficulty in target cooling.

At the Cyclotron and Radioisotope Center (CYRIC), a cyclotron accelerator has been upgraded. This upgrade allows the use of the negative ion acceleration mode, where the maximum beam intensity of the cyclotron is 300 μA for 50 MeV protons and 150 μA for 25 MeV deuterons. Such a high particle energy may not be suitable for BNCT, because it results in the emission of high energy neutrons, which increase the skin dose due to H(n,n') reactions. However, the neutron production yield of the (p,n) reaction of heavy elements ($E_p$=50 MeV) is about thausand times higher than that of the $^{7}$Li(p,n) ($E_p$= ~2.5 MeV) reaction, as can be seen from Refs.6 and 7. The beam power is 15 kW at the maximum heat load for incident 50 MeV protons of 300 μA which allows an advantage in target cooling, compared with the beam power of 48 kW for the $^{7}$Li(p,n) ($E_p$=2.4 MeV) reaction at 20 mA beam intensity in Ref. 3.

Thus it appears possible to realize epithermal neutron yields sufficient for BNCT by using protons of 50 MeV, if the neutrons produced can be effectively moderated to epithermal energy with a low contamination of high energy neutrons.

In the previous study[8], we found the feasibility of a cyclotron-based BNCT by simulations using the MCNPX code[9]. In the paper, we selected neutrons emitted at 90 degree from a thick (stopping-length) Ta target bombarded by 50 MeV protons, as the neutron source, based on the measurement of angular distributions for neutron energy spectra[10]. We also selected the assembly composed of iron, $AlF_3$/Al/$^{6}$LiF and lead as the moderator by simulations of neutron energy spectra passing through the moderator and the dose distribution in a cylindrical phantom.

## Experiment

In order to realize the cyclotron-based BNCT, we should validate the simulations. At the first step, we had a plan to measure the epithermal neutron energy spectra passing through the moderator. The measurement of epithermal neutron spectrum to be used for the treatment planning is very important for accelerator-based BNCT. However the spectrometry of neutrons in epithermal energy region, a few eV to several tens of keV, is very difficult and the measuring technique is not well established. Therefore we developed a new multi-moderator spectrometer for epithermal neutrons[11], and we applied evaluate the epithermal neutron field designed at CYRIC.

The measurements of the epithermal neutron energy spectra were performed at TOF room in CYRIC. The experimental arrangement is shown in Fig. 1. This arrangement is a little different from that in the simulations. For example, the figure of the moderator assembly was changed to rectangular due to a space limitation, while that used in the simulations was spherical. The moderators of $AlF_3$ and LiF were also thicker than that in simulations in order to make same the number of atoms between experiment and calculation, because $AlF_3$ and LiF were of powder and natural lithium was used for LiF in this experiment. Therefore the shape of the neutron energy spectrum passing through the moderator may be slightly different from simulations. However, its difference is not very serious for the aim to validate a simulation.

## Result and Discussion

Figure 2 shows the comparison of measured and calculated detector counts. The calculations agree with the measurements without the Cd absorber within ~20 %. Scattered thermal neutrons, generated by the table, wall, floor and ceiling, may give the large uncertainly to the results, especially to those obtained with the detectors which were sensitive to thermal neutrons. Therefore we also performed measurements using detectors covered with a Cd absorber in order to decrease the effect of the thermal neutrons for four detectors. As shown in Fig. 2, the calculations agree with the measurements with the Cd absorber within ~10 %.

Figure 3 shows the comparison of measured and calculated neutron energy spectra passing through the moderator. The result was obtained by unfolding the measured counts with calculated response functions. These spectra are in agreement within ~10 %.

These results indicate that we can validate the accuracy of the calculation on the neutron energy spectra passing through the moderator. At the next step to realize the BNCT at CYRIC, we have a plan to measure the thermal neutron distribution and the absorbed dose distribution in a phantom.

## References

1) Yanch J. C., Zhou X-L. and Brownell G.L., Radiat. Res. **126** (1991) 1.
2) Lee C.L., Zhou X. L.-L., Kudchadker R.J., Harmon F. and Harker Y.D., Med. Phys. **27** (2000) 192.
3) Bleuel D.L., Donahue R.J., Ludewigt B.A. and Vujic J., Med. Phys. **25** (1998) 1725.
4) Woollard J.E., Albertson B. J., Reed M.K., Blue T.E., Capala J., Gupta N. and Gahbauer R.A., Med. Phys. **28** (2001) 184.
5) Verbeke J.M., Vujic J. and Leung K.N., "Investigation of $^2$H(d,n)$^3$He and $^3$H(d,n)$^4$He Fusion Reactions as Alternative Sources for BNCT", The 8th Int. Symp. on NCT for Cancer, 13-18 September 1998, Ja Jolla CA.
6) Tesch K., Radiat. Prot. Dosim. **11** (1985) 165.
7) Bleuel D.L. and Donahue R.J., "Optimization of the $^7$Li(p,n) proton beam energy for BNCT application", LBNL Report, LBNL-37983, Rev.1, May 1996.
8) Yonai S., Aoki T., Nakamura T., Yashima H., Baba M., Yokobori H. and Tahara Y., Med. Phys. **30** (2003) 2021.
9) "MCNPX user's manual," edited by L. S. Waters, TPO-E83-G-UG-X-00001 Rev. 0, Los Alamos Natl. Lab., 14 November 1999.
10) Aoki T. et al., Nucl. Sci. Eng., in press.
11) Yonai S., "Development of a new multi-moderator spectrometer for epithermal neutrons," The second iTRS International Symposium on Radiation Safety and Detection Technology, 24-25 July 2003, Sendai., to be published in Journal of Nuclear Science and Technology.

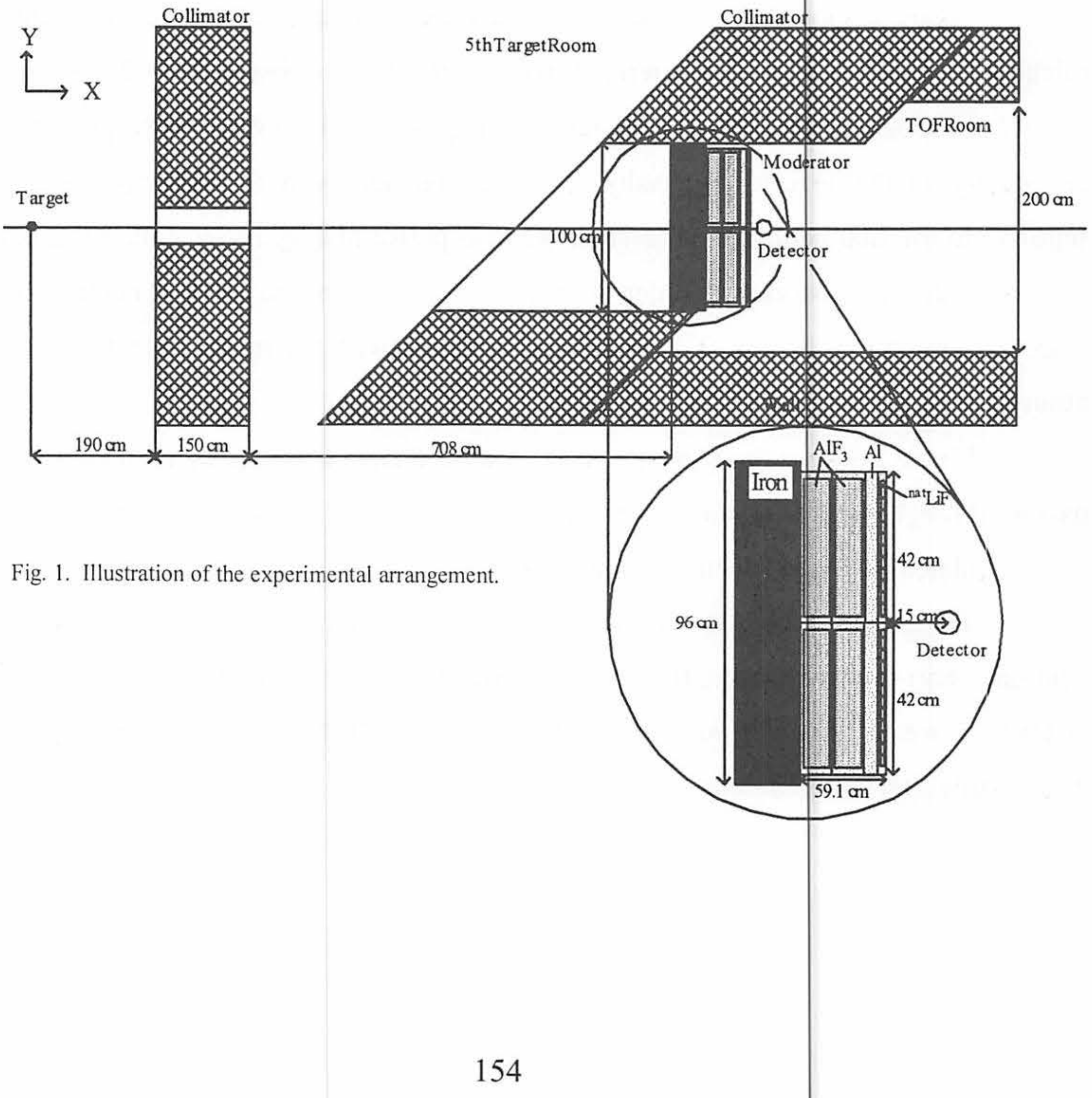

Fig. 1. Illustration of the experimental arrangement.

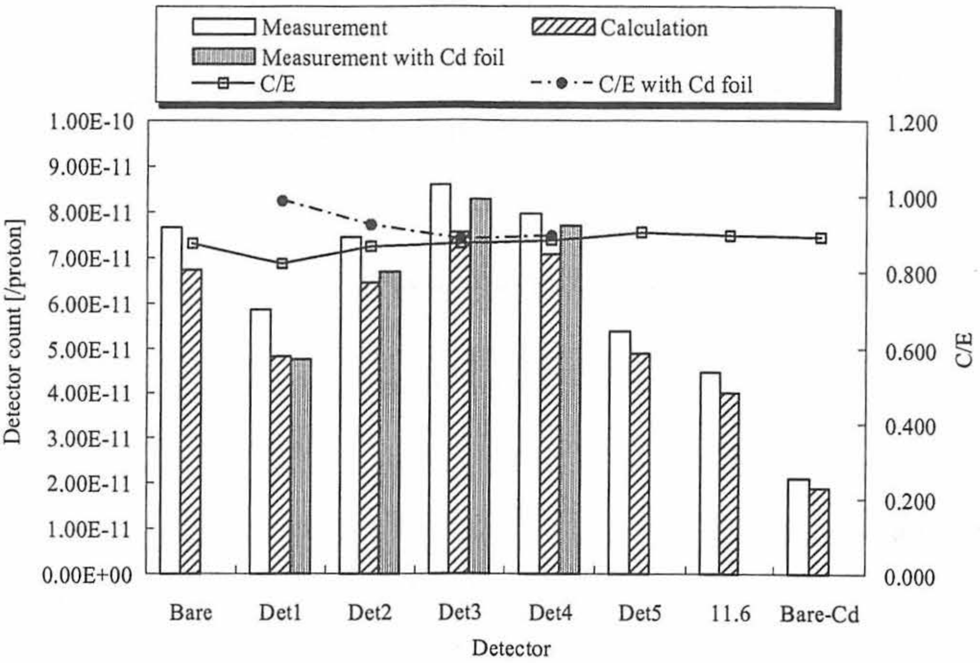

Fig. 2. Comparison of measured and calculated detector count.

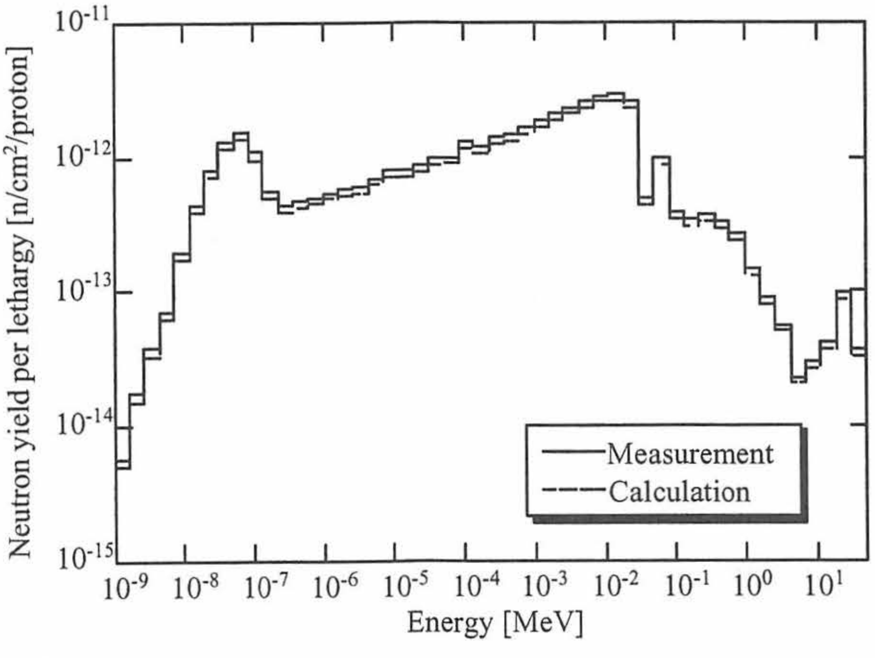

Fig. 3. Comparison of measured and calculated neutron energy spectra passing through the moderator.

# V. 5. Development of Thermal Neutron Profiling Method Using an Optical Fiber

*Itoga T., Kawata N., Hagiwara M., Hirabayashi N., Baba M., Nishitani T.*[*], Ochiai K.*[*]*

*Cyclotron and Radioisotope Center, Tohoku University,*
*Fusion Neutronics Source, Japan Atomic Energy Research Institute*[*]

## Introduction

Measurements of neutron spatial distribution are required frequently for characterization and diagnosis of neutron fields. In the case of neutron capture therapy planned in CYRIC[1)], we have to know the spatial distribution of incident neutrons in real time during irradiation without significant perturbation to the filed. Good spatial resolution is also important. Among various methods proposed for measurement of the neutron spatial distribution, the method to scan the field with a detector consisting of the ZnS(Ag) scintillator and an optical fiber developed by Mori et al[2)] is promising for our aim owing to its compact size and the ability of measurement in real time.

However, in their detector, discrimination of background components in the lower pulse height region is ambiguous because there is no clear separation between background events and true event. To eliminate the problem, we tried to improve the detector performance by employing a combination of a $^6$LiF film and a ZnS(Ag) scintillator for better light transmission. It is coupled to an optical fiber to photomultiplier tube. In the present study, we employed two types of scintillator; (1) ZnS(Ag) doped on a Mylar film and (2) an NE426 scintillator. In the case of the detector (1), backgrounds due to recoil protons from Mylar existed between neutron events and $\gamma$-ray events.

## Development of new detector

The ZnS(Ag) scintillator is plated on a Mylar film, 70 μm thick. This ZnS(Ag) film is purchased from Instrument Grade Films Co., for Nuclear Radiation Instruments. As the $^6$Li compound we employed a $^6$LiF film prepared by vacuum evaporation with a thickness of 720 μg/cm$^2$ on an aluminum foil, 12 μm thick.

We fabricated and tested a detector for neutron with various between 15 MeV and thermal energy. Fast neutrons were moderated with polyethylene blocks, 5 cm thick. We observed a valley between backgrounds and true events which means improvement of the pulse height distribution. We also did measurement for the case of cadmium plate around the detector and for $^{241}$Am α-source. We could distinguish clearly neutron events from background events.

In addition, we found that the component in low pulse height region was protons from the Mylar film from the neutron energy dependence of its pulse-height. In addition, we found that the pulse-shape discrimination technique can be applied to separate proton events from tritons and alpha particles.

We also tested a detector using an NE426 scintillator in place of ZnS(Ag)+$^6$LiF. The NE426 scintillator is a mixture of ZnS(Ag) and $^6$Li, 0.5 mm thick, placed on an aluminum plate. It is fairly stable and easy to machine.

The NE426 scintillator also provided good pulse-height distribution having valley between neutron events and backgrounds even with a fiber between the scintillator and a photomultiplier.

We applied the detector for spatial distribution measurement of thermal neutrons in the mockup experiment of a tritium breeding blanket of fusion reactors at Fusion Neutronics Source (FNS) of JAERI. The experiment is necessary to validate design calculations. Figure 1 shows the detector and mockup system.

We counted thermal neutron events continuously by moving the detector for 30 cm in the system with constant velocity using a stepping motor which is controlled remotely. We selected only thermal neutron events by the electronic circuit and counted only thermal neutron events by multi-channel-scaler (MCS). Figure 2 shows the result of the measurement. It shows the thermal neutron spatial distribution reflecting the configuration of the system. Thermal neutrons decreased in the region including $^6$Li and increased in the region of polyethylene and $^9$Be.

## Summary & Outlook

We fabricated the thermal neutron detector based on ZnS(Ag) and optical fibers and could distinguish thermal neutron events from background components unambiguously owing to improved detector performance.

The detector could be applied successfully to thermal neutron spatial distribution measurement in real time.

The detector will be applied to thermal neutron flux in the phantom for neutron field development for BNCT.

**References**

1) Yonai S., Aoki T., Nakamura T., Baba M., Yokobori H. and Tahara Y., Med. Phys. **30** (2003) 2021.
2) Mori C., Uritani A., Miyahara H., Iguchi T., Shiroya S., Kobayashi K., Takada E., Fleming R.F., Dewaraja Y.K., Stuenkel D. and Knoll G.F., Nucl. Instr. and Meth **A422** (1999) 129.

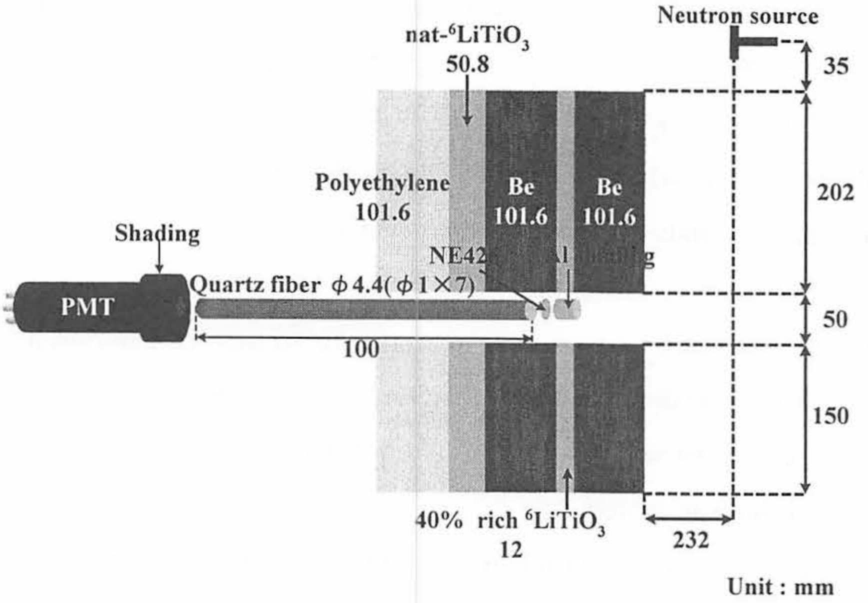

Fig. 1. Fiber detector and mockup system.

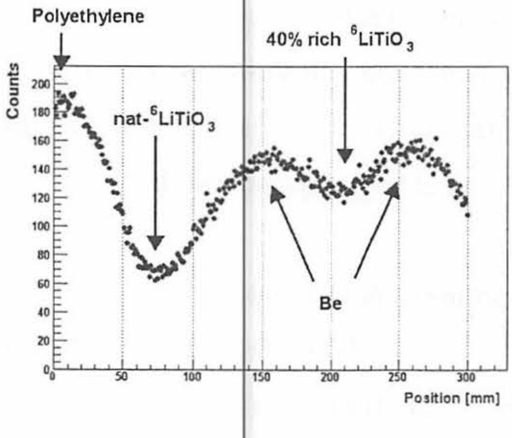

Fig. 2. Thermal neutron spatial distribution

# V. 6. Development of a New Passive Integral Dosemeter for Gamma Ray Monitoring using an Imaging Plate

*Ohuchi H., Yamadera A.* and Baba M.***

*Graduate School of Pharmaceutical Sciences, Tohoku University*
*School of Health Sciences, Hirosaki University**
*Cyclotron and Radioisotope Center, Tohoku University***

## Introduction

Since Japan's Legal Provisions for Radiation Protection was amended in April 2001, dose measurement for radiation monitoring using passive personal integral dosemeters came to be preferred. The aim of this study is to apply the imaging plate (IP) as a passive integral dosemeter for gamma rays. The thermoluminescence dosemeter (TLD), fluoroglass dosemeter (FGD), and optically stimulated luminescence dosemeter (OSLD) are already widely used as passive personal integral dosemeters. Nevertheless, the development of a quantitative evaluation method can make IP a new dosemeter with higher sensitivity, which can measure the low-level dose in the environment.

The IP is a detector of two-dimensional images and has been utilized in a number of fields. However, there are relatively few reports of applying IPs for quantitative use because of a large fading effect. Studies to measure the fading characteristics have been carried out and several results were reported1-4).

In the latest paper4), considering an IP as a one-month integral detector, the optimum conditions for quantitative measurement were evaluated by using fading correction equations. Then, the optimum condition to minimize the effect of fading on dose estimation was obtained by post-irradiation annealing BAS-MS at 80℃ for 24 hours.

In this study, an integral dose during a one-month period at 8 points inside the Cyclotron and Radioisotope Center of Tohoku University were conducted with BAS-MS from November 2001 to March 2002, under the conditions including the optimum. The results were compared with those obtained by a commercially available FGD.

## Methods

A 3.0 cm×4.0 cm piece of IP material was prepared as one IP element by cutting a sheet of BAS-MS (BAS-MS2025) fabricated by Fuji Film Co. Ltd. Measuring points 1 and 2 were located inside the radioisotope stockroom, points 3 to 7 were located around the cyclotron or at the site boundary of the controlled area, and point 8 was in an office on the upper floor. Points 4 and 7 were located outside the room, under the assumption that they might be strongly affected by temperature change. At each measuring point, four IP elements irradiated 108.9 $\mu$Sv with a $^{137}$Cs point source (108.9 $\mu$Sv/hour at 1.5 m on. July 27, 2001) and additional four non-irradiated IP elements were set 1.0m above the ground or floor, double-wrapped in black polyethylene bags as shielding from sunlight. After one month elapsed, all IP elements were collected and each set of the irradiated and non-irradiated IP elements were individually divided into two groups. One group ,including two irradiated IPs with the $^{137}$Cs source and two non-irradiated IPs, was promptly scanned and another group of same combination, was annealed at $k$℃($k$ = 60, 70, and 80) for 24 hours and then scanned. BAS-1000 readout system (Fuji Film Co.) was used for scanning. During annealing, the IPs were removed from the polyethylene bags and kept in aluminum IP cassettes inside an incubator (SANYO, MOV-112P2). The average value of each two IP elements irradiated and non-irradiated was used to determine the one-month integral dose in both case annealed and non-annealed.

The results obtained from the IPs were compared with those obtained from a commercially available FGD (Chiyoda Technol Corp.) for environmental monitoring.

## Results

The PSL density of the irradiated IPs with the $^{137}$Cs source (108.9 $\mu$Sv) can be obtained by a following equation.

$$(\mathrm{PSL})_{\mathrm{irrad.}} = (\mathrm{PSL})_{\mathrm{irrad.+A}} - (\mathrm{PSL})_{\mathrm{A}} \qquad (1)$$

where $(\mathrm{PSL})_{\mathrm{irrad.}}$ refers to the PSL density of an irradiated dose with a $^{137}$Cs source, $(\mathrm{PSL})_{\mathrm{irrad.+A}}$ is the sum of that of a $^{137}$Cs irradiated dose and a one-month integral dose, and $(\mathrm{PSL})_{\mathrm{A}}$ is that of a one-month integral dose.

The value of $(\mathrm{PSL})_{\mathrm{irrad.}}$ should be changed according to the temperature change during the month as well as the annealing temperature.

Fig. 1. is a comparison of the values of $(\mathrm{PSL})_{\mathrm{irrad.}}$ at each measuring point during

the 5 months from November 2001 to March 2002 with and without annealing. Without annealing, approximately a ±30% deviation from the average of PSL densities of each month were observed in all months, indicating the large effect of temperature change on PSL according to the measuring points. Annealing temperatures differed each month: 70℃ for Nov. 2001, 80℃ for Dec. 2001, Feb., and March 2002, and 60℃ for Jan. 2002. The deviations from the average PSL densities of each month were ±28.5% at 60℃ annealing, ±12.6% at 70℃, and ±10.0% at 80℃. The fading effect on PSL during one month becomes the smallest at 80℃. This is consistent with the result obtained by calculation and supports the conclusion that annealing at 80℃ is the optimum condition.

A one-month integral dose can be calculated from the values of $(PSL)_A$ and $(PSL)_{irrad.}$ in Eq.(1). Although the value of $(PSL)_{irrad.}$ might change according to changes in the temperature during the month and the annealing temperature as mentioned above, it corresponds to 108.9 $\mu$Sv. Based on this relationship, the value of $(PSL)_A$ can be converted to the value of Sv.

Fig. 2 shows the calculated results for each of the 5 months from November 2001 to March 2002 in comparison with of the results for annealed or non-annealed IPs and FDG.

## Discussion

Figure 2 shows that there was no big difference between the annealed and non-annealed methods at all points with some exception. Because the way of evaluation of a month-long integral dose described above corrects the fading effects by using the IP irradiated with known dose. However, at some months of points 2 and 6, there was not so good agreement between both methods and no consistency in these differences between them. The reason for this is that the differences result from errors accumulated in the indirect calculation. That is, a month-long integral dose is obtained through the PSL density irradiated with the $^{137}$Cs source, which is calculated by subtracting the PSL density of the non-irradiated IP from that of the irradiated IP.

Considering these results, an improved method that can enable calculation of a one-month dose directly from the PSL density of the annealed IP without using IP irradiated with known dose should be needed.

As shown in Fig. 2, the monthly fluctuation among the results with the three methods seems to be roughly consistent, but all the results except at point 2 show that the values with FDG are larger (sometimes double) than those with IP. The FGD is mailed to

Tohoku University in the middle of the month prior to the assigned month to be exposed. After exposure for one month, it is mailed back for the dose evaluation. It takes 1.5 to 2 months at the longest from sending and returning the FDG, thus, natural radiation accumulates during this period, although the IP exposure period is fixed at exactly one month. As for point 2 (the RI stockroom), however, the results with IP are sometimes greater than those with FDG. This indicates that some radioisotopes having energies with a big response to IP[5] might be stocked and/or taken in and out at this point.

Assuming Poisson distribution, the ratio of a counting error to a counting value can be evaluated by a following equation,

$$E=\frac{\frac{\sqrt{x}}{A}}{\frac{x}{A}} \qquad (2)$$

where x is the value of the PSL, A the readout area (mm$^2$), and $\frac{x}{A}$ the PSL density (PSL/mm$^2$). IP is a two-dimensional detector, therefore, the value of A is necessary in Eq.(2).

The readout area is fixed at 600mm$^2$ in this experiment, then, so the value of x is calculated as 0.167 PSL/mm$^2$ if a 10% error is allowed (E = 0.1 in Eq.(3)). Detection limits can be obtained by the $^{137}$Cs irradiated dose corresponding to the value of x, resulting in 0.48, 1.05 and 3.15 $\mu$Sv annealed at 60,70, and 80℃, respectively. These are considered sufficiently low in comparison with the detection limits of other passive integral dosemeters such as TLD, FGD, and OSLD; which are more than 10 $\mu$Sv[6,7].

**References**

1) Ohuchi H., Yamadera A. and Nakamura T., Nucl. Instr. and Meth. **A450** (2000) 343.
2) Ohuchi H. and Yamadera A., Rad. Meas. **35** (2002)135.
3) Ohuchi H. and Yamadera A., Nucl. Instr. and Meth. **A490** (2002) 573.
4) Ohuchi H. and Yamadera A., J. Rad.Res.43:SUPPL. **S71-S74** (2002).
5) Taniguchi S., Yamadera A., Nakamura T. and Fukuda K., Radi. Prot. Dos.**85** (1999) 7.
6) Nakamura T. and Yamaguchi T., Jap. J. Health Phys. **33** (2) (1998) 121 (in Japanese).
7) Yoder R.C., Radioisotopes **51** (2002) 133 (in Japanese).

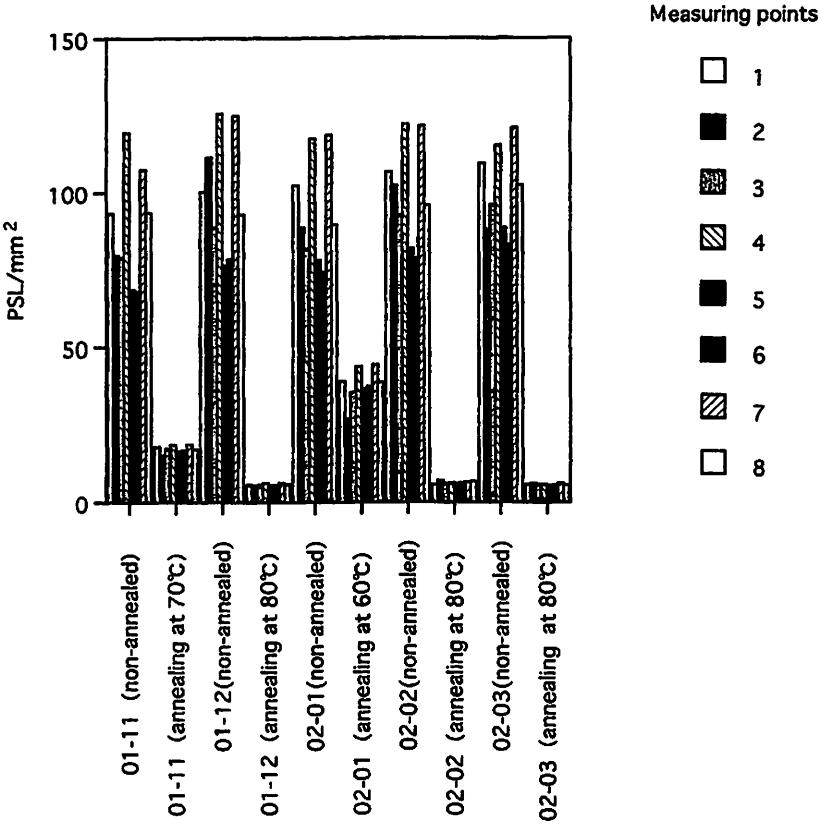

Figure 1. Comparison of PSL density irradiated with the $^{137}$Cs source between annealed IP and non-annealed IP at each measuring point.

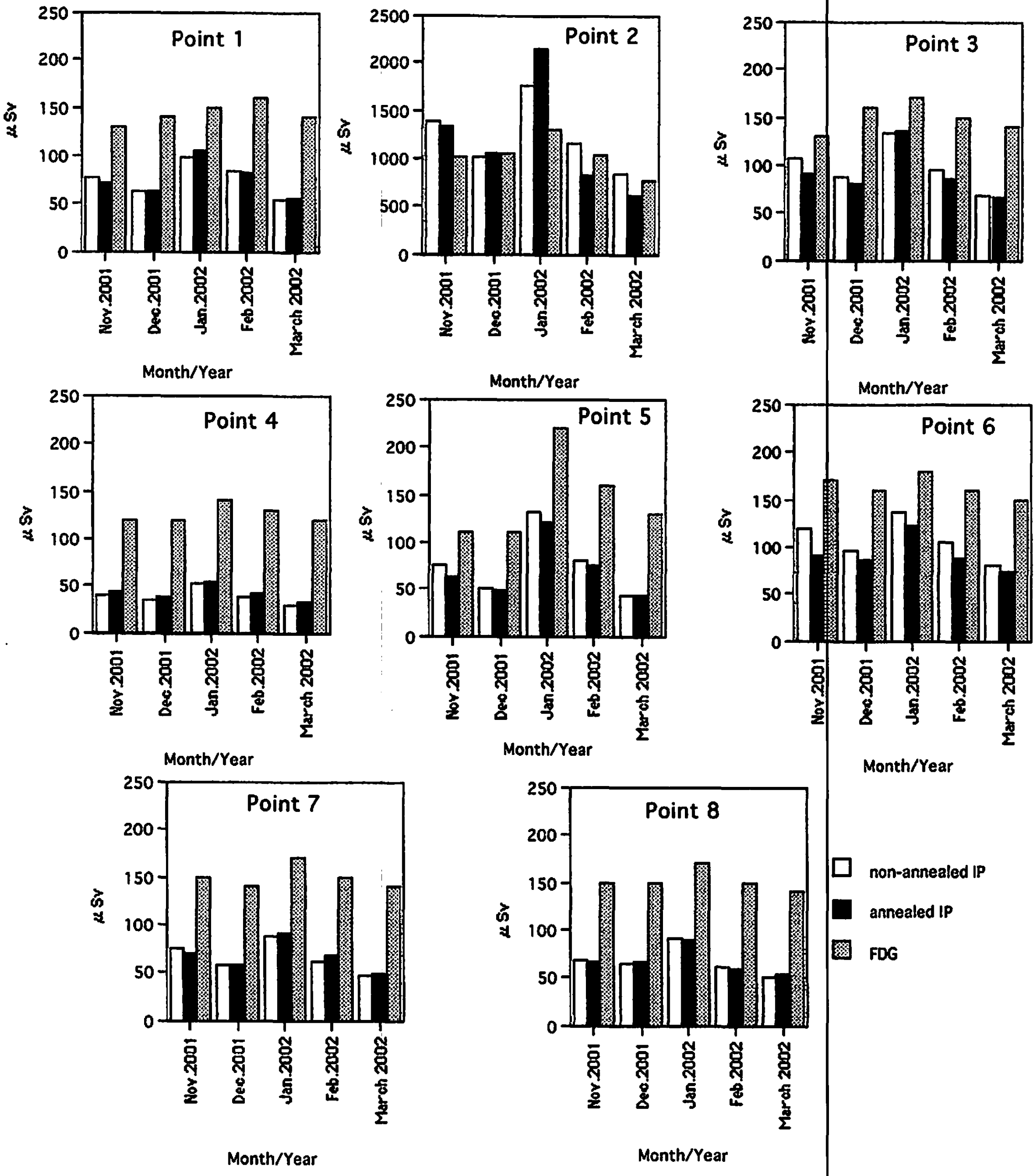

Figure 2. Comparison of integral dose of each month obtained by non-annealed IP, annealed IP, and FGD.

# V. 7. Beginners Training for Safe Handling of Radiation and Radioisotopes in Tohoku University

*Baba M., Miyata T., Iwata R., and Nakamura T.*

*Cyclotron and Radioisotope Center, Tohoku University*

During 2002, the beginners training for safe handling of radiation and radioisotopes in Tohoku University was conducted in three courses as usual; 1) Radiation and Isotopes, 2) X-ray Machines and Electron Microscope, and 3) Synchrotron Radiation (SOR). The training was held twice a year, May and November, under the help for lectures and practice from various departments and research institutes of the university.

Until 2001, the lecture was provided only in Japanese. Recently, however, the number of students and/or researchers who are not well acquainted with Japanese language is increasing. Therefore, from the training in last November, an English class was newly started for all courses, in which the lectures and texts are given in English.

The training for "Radiation and Radioisotopes" is for persons who use unshielded radioisotopes and accelerators, and has been conducted from 1977. The contents of lectures and practices are shown in Table 1. In the fiscal year of 2002, the training was performed for 557 persons (7 persons in the English class). The departments or institutes to which they belong are given in Table 2.

The training for "X-ray machines and electron microscopes" started at the end of 1983. The training is scheduled twice a year at the same time as that for "Radiation and Radioisotopes". In this course, only lectures are given with no practice. The contents of the lectures and the distributions of trainees are shown in Table 3 and Table 4, respectively. The number of trainees was 263 (6 in the English class).

The training for the "Synchrotron Radiation" began at the end of 1995. The contents of the lectures are the same as those of the radiation and radioisotopes but no practice. In 2002, the number of trainees of the SOR course was 83 (0 in the English class).

Table 1. Contents of the lectures and practices for safe handling of radiation and radioisotopes in 2002 (same for both Japanese and English class).

| Lectures (one day) | Hours |
|---|---|
| Radiation physics and measurements | 1.5 |
| Chemistry of radioisotopes | 1.0 |
| Effects of radiation to human | 1.0 |
| Radiological protection ordinance | 1.5 |
| Safe handling of radioisotopes | 1.5 |

| Practice (one day) | Hours |
|---|---|
| Treatment of unsealed radioactive solution | 4.0 |
| Measurement of surface contamination and decontamination | 1.0 |
| Measurement of gamma-rays and beta-rays | 2.0 |

Table 2. Distribution of trainees for "radiation and radioisotopes" in 2002.

| Department | Staff | Student | Total | | English class |
|---|---|---|---|---|---|
| Medicine | 13 | 105 | 118 | | 1 |
| Dentistry | 1 | 18 | 19 | | |
| Pharmacy | 0 | 49 | 49 | | 1 |
| Science | 1 | 56 | 57 | | 1 |
| Engineering | 1 | 74 | 75 | | |
| Agriculture | 0 | 103 | 103 | | |
| Research Institutes | 7 | 74 | 81 | | 4 |
| The others* | 3 | 52 | 55 | | |
| Total | 26 | 531 | 557 | | 7 |

* Graduate schools independent from faculties

Table 3. Contents of the lectures for "X-ray machines and electron microscopes" in 2002 for both Japanese (same for both Japanese and English class).

| Lectures (one day) | Hours |
|---|---|
| Safe handling of X-ray machines | 1.5 |
| Radiological protection ordinance | 0.5 |
| VTR for safe handling of radiation and radioisotopes | 0.5 |

Table 4. Distribution of trainees for "X-ray machines and electron microscopes" in 2002.

| Department | Staff | Student | Total | | English class |
|---|---|---|---|---|---|
| Medicine | 0 | 2 | 2 | | |
| Dentistry | 2 | 1 | 3 | | |
| Science | 1 | 17 | 18 | | |
| Engineering | 5 | 110 | 115 | | |
| Research Institutes | 8 | 110 | 118 | | 6 |
| The others | 2 | 5 | 7 | | |
| Total | 18 | 245 | 263 | | 6 |

Table 5. Distribution of trainees for "synchrotron radiation" in 2002.

| Department | Staff | Student | Total |
|---|---|---|---|
| Medicine | 0 | 1 | 1 |
| Dentistry | 0 | 2 | 2 |
| Pharmacy | 1 | 6 | 7 |
| Science | 0 | 18 | 18 |
| Engineering | 0 | 35 | 35 |
| Research Institutes | 1 | 19 | 20 |
| Total | 2 | 81 | 83 |

# V. 8. Radiation Protection and Management

*Miyata T., Baba M., and Watanabe N.**

*Cyclotron and Radioisotope Center, Tohoku University*
*Japan Radiation Protection Co., Ltd.**

## (1) Overview

During the fiscal year of 2002, research and education in the center were conducted as active as usual.

During the year, a special fund was provided by "Monbu-kagakusho" (the Ministry of Education and Culture, Sports, Science and Technology) for replacement of the online radiation protection and management system of CYRIC. The system was about eight years old and suffered from malfunctions and rather slow system response. The system consists of two parts; one is an online radiation monitoring system and the other one is an admission management system to the controlled area. Both systems are composed of hard wares, mechanical or physical parts, and a computer system with software.

In the occasion, the computer system and software were entirely replaced with modern ones while the hardware parts were left unchanged because the fund was rather limited and hardware parts looked still OK. After replacement in March to May, the response time of the admission system was markedly improved and system reliability was also improved certainly.

## (2) Unsealed radio nuclides used in CYRIC

The species and amounts of unsealed radio nuclides handled in CYRIC during the fiscal year of 2002 are summarized in Table 1. The table includes the isotopes produced by the cyclotron as well as those purchased from the Japan Radio Isotope Association or taken over from other radioisotope institutes.

## (3) Monitoring of individual worker

The exposure doses of the workers in CYRIC during 2002 are given in Table 2.

They were sufficiently less than the legal dose limit.

## (4) Monitoring of the workplace

Radiation dose rates inside and outside of the controlled areas in CYRIC were monitored periodically and occasionally when needed. They were generally below the legal dose limit. Surface contamination levels of the floors inside the controlled areas were measured with a smear method and a survey meter method. They were below the legal regulation levels.

## (5) Wastes management

The radioactive wastes delivered to the Japan Radio Isotope Association in 2002 are shown in Table 3. The concentration of radioisotopes in the air released from the stack after filtration was monitored with stack gas monitors. The values on concentration of radioactive nucleides were lower than the legal regulation levels. The radioactive water was stocked in the tanks at least for 3 days and then released to the sewerage after confirming that the concentration was lower than the legal regulation levels. Radioactive organic scintillator waste of 450 litter was treated by incinerator provided by Fuji-kogyo Co.Ltd.

Table 1. Unsealed radioisotopes used in each building of CYRIC during 2002.
(a) Cyclotron Building (kBq)

| Group 1,2 | | Group 3 | | Group 4 | |
|---|---|---|---|---|---|
| | | $^{11}$C | 266,710,800.000 | $^{14}$C | 370.000 |
| | | $^{13}$N | 1,000.000 | $^{18}$F | 993,993,900.000 |
| | | | | $^{3}$H | 178,464.400 |
| Total | 0 | Total | 266,711,800.000 | Total | 994,172,734.400 |

(b) Radio-isotope Building (kBq)

| Group 1,2 | | Group 3 | | Group 4 | |
|---|---|---|---|---|---|
| $^{90}$Sr | 421.080 | $^{11}$C | 4,058,900.000 | $^{14}$C | 48,784.500 |
| $^{60}$Co | 706.250 | $^{32}$P | 1,159,677.926 | $^{18}$F | 285,272,065.000 |
| $^{137}$Cs | 6,848.200 | $^{99m}$Tc* | 1,673,300.000 | $^{3}$H | 2,273,639.019 |
| $^{55}$Fe | 30,128.000 | | | | |
| $^{68}$Ge | 134,554.000 | | | | |
| $^{125}$I | 232,454.200 | | | | |
| Total | 405,111,650.000 | Total | 5,218,577.926 | Total | 287,594,488.2519 |

* In the " $\beta$ -ray analysis" room

(c) Research Building (kBq)

| Group 1,2 | | Group 3 | | Group 4 | |
|---|---|---|---|---|---|
| | | $^{15}$O | 28,712,000.000 | $^{18}$F | 1,998,000.000 |
| Total | 0 | Total | 28,712,000.000 | Total | 1,998,000.000 |

Table 2. Occupational radiation exposures at CYRIC during the fiscal year of 2002.

| Dose range (mSv) | Number of individuals |
|---|---|
| No measurable exposure | 38 |
| Less than 1.0 | 9 |
| 1.0 to 2.0 | 1 |
| 2.0 to 3.2 | 1 |
| Total number of persons monitored | 49 |

Table 3. Radioactive wastes delivered to the Japan Radioisotope Association in 2002.

| Wastes type | Wastes Container | Number |
|---|---|---|
| Solids | | |
| Combustible type Ⅰ | 50 ℓ drum | 21 |
| Combustible type Ⅱ | 50 ℓ drum | 15 |
| Incombustible (compressible) | 50 ℓ drum | 6 |
| Animal carcasses | 50 ℓ drum | 12 |
| Liquids | | |
| Inorganic liquids | 25 ℓ PE bottle | 8 |

Type Ⅰ :Cloths and papers made of natural cellulose.

Type Ⅱ :Combustion plastics such as polyethylene and polypropylene.

# VI. PUBLICATIONS

# VI. PUBLICATIONS

*(January 2002 ~ December 2002)*

[543] Imaging of Ischemic but Viable Myocardium Using a New $^{18}$F-Labeled 2-Nitroimidazole Analog, $^{18}$F-FRP170.
Tomohiro Kaneta, Yoshihiro Takai, Yutaka Kagaya, Yuriko Yamane, Hiroaki Wada, Masahiro Yuki, Ren Iwata, Michihiko Tsujitani, Shoki Takahashi, Shogo Yamada.
*J. Nucl. Med.*, **43** (2002) 109-116.

[544] A case of dementia with Lewy bodies: a clinico-pathological study.
H. Arai, S. Higuchi, M. Higuchi, N. Okamura, S. Hara. M. Itoh, R. W. Shin, J. Q. Trojanowski, H. Sasaki.
*Review Series DEMENTIA*, **1** (2002) 14-15.

[545] Design of an all-permanent-magnet ECR ion source at the Cyclotron and Radioisotope Center.
A. Yamazaki, M. Fujita, E. Tanaka, T. Shinozuka, T. Yokoi, T. Ozawa, H. Tanaka.
*Review of Scientific Instruments*, **73** (2002) 589-591.

[546] The Role of the Basal Forebrain in Episodic Memory Retrieval: A Positron Emission Tomography study.
Toshikatsu Fujii, Jiro Okuda, Takashi Tsukiura, Hiroya Ohtake, Rina Miura, Reiko Fukatsu, Kyoko Suzuki Ryuta Kawashima, Masatoshi Itoh, Hiroshi Fukuda, Atsushi Yamadori.
*NeuroImage*, **15** (2002) 501-508.

[547] A combined loop-SPE method for the automated preparation of [$^{11}$C]doxepin.
R. Iwata, C. Pascali, A. Bogni, K. Yanai, M. Kato, T. Ido, K. Ishiwata.
*J. Label. Compd. Radiopharm.*, **45** (2002) 271-280.

[548] [$^{18}$F]Fluoromethyl triflate, a novel and reactive [$^{18}$F]fluoromethylating agent: preparation and application to the on-column preparation of [$^{18}$F]fluorocholine.
Ren Iwata, Claudio Pascali, Anna Bogni, Shozo Furumoto, Kazunori Terasaki, Kazuhiko Yanai.
*Appl. Radiat. Isot.*, **57** (2002) 347-352.

[549] Design and synthesis of fluorine-18 labeled matrix metalloproteinase inhibitors for cancer imaging.
Shozo Furumoto, Ren Iwata, Tatsuo Ido.
*J. Label. Compd. Radiopharm.*, **45** (2002) 975-986.

[550] Gamow-Teller matrix elements in light nuclei and $(p, n)$ cross sections at $Ep = 35$ MeV.
H. Orihara, A. Terakawa, K. Itoh, H. Suzuki, K. Kumagai, Y. Kikuchi, G. C. Jon, K. Ishii, T. Niizeki, H. Sagawa, H. Ohnuma.
*Physics Letters*, **B 539** (2002) 40-45.

[551] New fast-neutron time-of-flight facilities at CYRIC.
A. Terakawa, H. Suzuki, K. Kumagai, Y. Kikuchi, T. Uekusa, T. Uemori, H. Fujisawa, N. Sugimoto, K. Itoh, M. Baba, H. Orihara, K. Maeda.
*Nuclear Instruments and Methods in Physics Research*, **A 491** (2002) 419-425.

**[552]** Effect of angiotensin converting enzyme inhibition on myocardial phosphoinositide metabolism visualised with 1-[1-$^{11}$C]-butyryl-2-palmitoyl -*rac*-glycerol in myocardial infarction in the rat..
Yutaka Kagaya, Masanobu Chida, Yoshio Imahori, Ryou Fujii, Shigeto Namiuchi, Morihiko Takeda, Yuriko Yamane, Hiroki Otani, Jun Watanabe, Mitsumasa Fukuchi, Fumiaki Tezuka, Tatsuo Ido, Kunio Shirato.
*Eur. J Nucl. Med.*, **29** (2002) 1516-1522.

**[553]** Excitation functions of proton induced nuclear reactions on $^{nat}$Rb from 30 to 70 MeV. Implication for the production of $^{82}$Sr and other medically important Rb and Sr radioisotopes.
Tatsuo Ido, Alex Hermanne, Ferenc Ditrói, Zoltán Szücs, Imre Mahunka, Ferenc Tárkányi.
*Nuclear Instruments and Methods in Physics Research*, B **194** (2002) 369-388.

**[554]** Proton single-particle strength in $^{19}$F measured via (d, n) reaction.
A. Terakawa, H. Orihara, M. Oura, M. Hosaka, T. Tohei, T. Nakagawa, J. Takamatsu, A. Narita, K. Hosomi, K. Ishii, G. C. Jon, K. Miura, and H. Ohnuma.
*Physical Review C* **66**, 0064313 (2002).

**[555]** PIXE elemental analysis of drinking water supplies.
H. Yamazaki, K. Ishii, Y. Takahashi, Ts. Amartaivan, S. Matsuyama, T. Sato, S. Sugihara, K. Sera and G. C. Jon.
*International Journal of PIXE*, **12** (3&4), 2002,209-216.

**[556]** PIXE analysis of trace heavy metals in river and tap waters using an ion-exchange cellulose filter paper.
Ts.Amartaivan, K.Ishii, H.Yamazaki, Y.Takahashi, S.Matsuyama, T.Satoh, S.Sugihara K.Katoh Y.Komori and H.Orihara.
*International Journal of PIXE*, **12** (3&4), 2002, 217-224.

**[557]** Rreliminary Measurement of the low energy detection efficiency of a Si(Li) detector for PIXE Application.
M. Rodriguez, T. Yonezawa, K. Ishii, S. Matsuyama, H. Yamazaki, T. Saoto, Ts. Amartaivan, S. Sugihara, A. Tanaka, K. Kato, Y. Komori.
*International Journal of PIXE*, **12** (2002) 71-78.

**[558]** Analysis of Trace Level thorium and Uranium in Drainage from a Radioisotope Laboratory by Particle-Induced X-ray Emission.
Hiromichi Yamazaki, Keizo Ishii, Yoshinori Takahashi, Shigeo Matsuyama, Takahiro Satoh and Hikonojoh Orihara.
*Journal of Nuclear Science and Technology, supplement 3*, (2002) 560-563.

**[559]** Se-atom incorporation in fullerene by using nuclear recoil and Ab initio MD simulations.
T. Ohtsuki, K. Ohno, K. Shiga, Y. Kawazoe, H. Yuki.
*Physical Review B* **65**, 073402-(1-4) (2002).

**560]** Charged-particle activation analysis of oxygen in fluoride and chalcogenide glasses used for fiber-amplifiers.
K.Shikano, Y.Nishida, K.Kobayashi, T.Kanamori, M.Shimizu, K.Masumoto, T. Ohtsuki.
*J. Radioanal. Nucl. Chem.*, **253** (2002) 25-29.

**[561]** Insertion of foreign-atoms in fullerenes by nuclear recoil and their MD simulation.
T. Ohtsuki, K. Ohno.
*The Bulletin of the Cluster Science and Technology*, **5** (2002) 23-29.

**[562]** Combined analysis of CSF Tau levels and [$^{123}$I] Iodoamphetamine SPECT in mild cognitive impairment: Implications for a novel predictor of Alzheimer's disease.
Okamura N, Arai H, Maruyama M, Higuchi M, Matsui T, Tanji H, Seki T, Hirai H, Chiba H, Itoh M, Sasaki H.
*Am. J. Pshchiat.*, **159** (2002) 474-476.

**[563]** The Role of the Basal Forebrain in Episodic Memory Retrieval: A Positron Emission Tomography Study.
Fujii T., Okuda J., Tsukiura T., Ohtake H., Miura R., Fukatsu R., Suzuki K., Kawashima R., Itoh M., Fukuda H., Yamadori A.
*Neuroimage*, **15** (2002) 501-508.

**[564]** Endoding-related brain activity during deep processing of verbal materials: a PET study.
Fujii T., Okuda J., Tsukiura T., Ohtake H., Suzuki M., Kawashima R., Itoh M., Fukuda H., Yamadori A.
*Neurosci Res.*, **44** (2002) 429-438.

**[565]** Differential cognitive effects of ebastine and (+)-chlorpheniramine in healthy subjects: correlation between cognitive impairment and plasma drug concentration.
Tagawa M., Kano M., Okamura N., Higuchi M., Matsuda M., Mizuki Y., Arai H., Fujii T., Komemushi S., Itoh M., Sasaki H. Watanabe T., Yanai K.
*Br. J. Clin. Pharmacol.*, **53** (2002) 296-304.

**[566]** Brain mapping of muscle-brain interaction during chewing by SPM analysis: A FDG-PET study.
Rikimaru H., Itoh M., Tashiro M., Watanabe M.
*Brain Imagin Using PET*: edited by Senda M. Kimura Y, Herscovitch P. Academic Press New York, 2002, pp. 269-275.

**[567]** How does Yoga affect the brain.
Itoh M., Singh L. N., Yamaguchi K., Miyake M., Watanuki S., Jeong M.
*J Int. Soc. Life Inform. Sci.*, **20** (2002) 473-479.

**[568]** Neuroanatomical correlates of low body weight in Alzheimer's disease: a PET study.
Hu X., Okamura N., Arai H., Higuchi M., Maruyama M., Itoh M., Yamaguchi K., Sasaki H.
*Prog. Neuropsychopharmacol. Biol. Psychiatry*, **26** (2002) 1285-1289.

**[569]** Time-dependent contribution of the hippocampal complex when remembering the past: a PET study.
Tsukiura T., Fujii T., Okuda J., Ohtake H., Kawashima R., Itoh M., Fukuda H., Yamadori A.
*Neuroreport.*, **13** (2002) 2319-2323.

**[570]** Roles of histamine in regulation of arousal and cognition: functional neuroimaging of histamine $H_1$ receptors in human brain.
Tashiro M., Mochizuki H., Iwabuchi K., Sakurada Y., Itoh M., Watanabe T., Yanai K.
*Life Sci.*, **72** (2002) 409-4014.

# VII. MEMBERS OF COMMITTEE

# VII. MEMBERS OF COMMITTEE (as of Jan. 1, 2003)

## General

| | | | |
|---|---|---|---|
| (Chairman) | Hikonojo | Orihara | (CYRIC) |
| | Katsuto | Nakatsuka | (Vise President) |
| | Osamu | Hashimoto | (Graduate School of Science) |
| | Hiroshi | Kudo | (Graduate School of Science) |
| | Akira | Takahashi | (Graduate School of Medicine) |
| | Nobuhiro | Takahashi | (Graduate School of Dentistry) |
| | Yasushi | Ohizumi | (Faculty of Pharmaceutical Sciences) |
| | Katsunori | Abe | (Graduate School of Engineering) |
| | Teruo | Miyazawa | (Graduate School of Agricultural Science) |
| | Kazuhiko | Nishitani | (Graduate School of Life Science) |
| | Isamu | Sato | (Institute for Materials Research) |
| | Hiroshi | Fukuda | (Institute for Development, Aging and Cancer) |
| | Yukio | Noda | (Institute of Multidisciplinary Research for advanced Materials) |
| | Syogo | Yamada | (University Hospital) |
| | Jirohta | Kasagi | (Laboratory of Nuclear Science) |
| | Tatsuo | Ido | (CYRIC) |
| | Masatoshi | Itoh | (CYRIC) |
| | Mamoru | Baba | (CYRIC) |
| | Ren | Iwata | (CYRIC) |
| | Tsutomu | Shinozuka | (CYRIC) |
| | Keizo | Ishii | (Graduate School of Engineering) |
| | Takashi | Nakamura | (Graduate School of Engineering)<br>(Radiation Safety Committee, Research Promotion Council) |
| | Tetsuya | Ono | (Radiation Safety Committee, Research Promotion Council) |

| | | | |
|---|---|---|---|
| | Masatoshi | Itoh | (CYRIC) |
| | Hiroyasu | Hasegawa | (Director-General, Administration Bureau) |
| | Makoto | Sugawara | (Head of Administration Office, Graduate School of Information Science:Observer) |

**Research Program**

| | | | |
|---|---|---|---|
| (Chairman) | Takashi | Nakamura | (Graduate School of Engineering) |
| | Tatsuo | Ido | (CYRIC) |
| | Masatoshi | Itoh | (CYRIC) |
| | Mamoru | Baba | (CYRIC) |
| | Ren | Iwata | (CYRIC) |
| | Tsutomu | Shinozuka | (CYRIC) |
| | Osamu | Hashimoto | (Graduate School of Science) |
| | Tsutomu | Sekine | (Graduate School of Science) |
| | Kazuhiko | Yanai | (Graduate School of Medicine) |
| | Akira | Takahashi | (Graduate School of Medicine) |
| | Katsunori | Abe | (Graduate School of Engineering) |
| | Keizo | Ishii | (Graduate School of Engineering) |
| | Isamu | Sato | (Institute for Materials Research) |
| | Kazuo | Kubota | (Institute for Development, Aging and Cancer) |
| | Syoki | Takahashi | (University Hospital) |
| | Jirohta | Kasagi | (Laboratory of Nuclear Science) |

**Cyclotron**

| | | | |
|---|---|---|---|
| (Chairman) | Osamu | Hashimoto | (Graduate School of Science) |
| | Toshio | Kobayashi | (Graduate School of Science) |
| | Satoru | Kunii | (Graduate School of Science) |
| | Tsutomu | Sekine | (Graduate School of Science) |
| | Kazushige | Maeda | (Graduate School of Science) |
| | Hirokazu | Tamura | (Graduate School of Science) |
| | Keizo | Ishii | (Graduate School of Engineering) |

| | | |
|---|---|---|
| Takashi | Nakamura | (Graduate School of Engineering) |
| Akira | Hasegawa | (Graduate School of Engineering) |
| Isamu | Sato | (Institute for Materials Research) |
| Minoru | Issiki | (Institute of Multidisciplinary Research for advanced Materials) |
| Tsutomu | Otsuki | (Laboratory of Nuclear Science) |
| Tatsuo | Ido | (CYRIC) |
| Masatoshi | Itoh | (CYRIC) |
| Ren | Iwata | (CYRIC) |
| Mamoru | Baba | (CYRIC) |
| Tsutomu | Shinozuka | (CYRIC) |
| Atsuki | Terakawa | (CYRIC) |
| Mashiro | Fijita | (CYRIC) |
| Masayasu | Miyake | (CYRIC) |

## Radiation Protection and Training of Safe Handling

| | | | |
|---|---|---|---|
| (Chairman) | Takashi | Nakamura | (Graduate School of Engineering) |
| | Hiroshi | Kudo | (Graduate School of Science) |
| | Yoshihiko | Uehara | (Graduate School of Medicine) |
| | Tsutomu | Araki | (Graduate School of Pharmaceutical Sciences) |
| | Keizo | Ishii | (Graduate School of Engineering) |
| | Toshiyasu | Yamaguchi | (Graduate School of Agricultural Science) |
| | Kazuhiro | Togawa | (Graduate School of Agricultural Science) |
| | Masayuki | Hasegawa | (Institute for Materials Research) |
| | Hiroshi | Fukuda | (Institute for Development, Aging and Cancer) |
| | Yoshihiro | Takai | (University Hospital) |
| | Tatsuo | Ido | (CYRIC) |
| | Mamoru | Baba | (CYRIC) |

## Life Science

| | | | |
|---|---|---|---|
| (Chairman) | Tatsuo | Ido | (CYRIC) |
| | Yasuhito | Itoyama | (Graduate School of Medicine) |
| | Kazuie | Iinuma | (Graduate School of Medicine) |
| | Syogo | Yamada | (Graduate School of Medicine) |
| | Reizo | Shirane | (Graduate School of Medicine) |
| | Masahiko | Yamamoto | (Graduate School of Medicine) |
| | Makoto | Watanabe | (Graduate School of Dentistry) |
| | Norimichi | Nakahata | (Graduate School, Division of Pharmaceutical Sciences) |
| | Keizo | Ishii | (Graduate School of Engineering) |
| | Takashi | Nakamura | (Graduate School of Engineering) |
| | Satoshi | Yokota | (Graduate School of Agricultural Science) |
| | Kazuo | Yamamoto | (Graduate School of Life Science) |
| | Hiroshi | Fukuda | (Institute for Development, Aging and Cancer) |
| | Kazuo | Kubota | (Institute for Development, Aging and Cancer) |
| | Junichi | Gotoh | (University Hospital) |
| | Shin | Maruoka | (College of Medical Sciences) |
| | Masatoshi | Itoh | (CYRIC) |
| | Kei-ichiro | Yamaguchi | (CYRIC) |
| | Yoshihito | Funaki | (CYRIC) |

## Prevention of Radiation Hazards

| | | | |
|---|---|---|---|
| (Chairman) | Takashi | Nakamura | (Graduate School of Engineering) |
| | Osamu | Hashimoto | (Graduate School of Science) |
| | Tsutomu | Sekine | (Graduate School of Science) |
| | Keizo | Ishii | (Graduate School of Engineering) |
| | Tatsuo | Ido | (CYRIC) |
| | Mamoru | Baba | (CYRIC) |
| | Tsutomu | Shinozuka | (CYRIC) |
| | Tadashi | Sasaki | (CYRIC) |
| | Takamoto | Miyata | (CYRIC) |

# VIII. STAFF

# VIII. STAFF (as of Jan. 1, 2003)

**Director** Hikonojo Orihara

## Division of Accelerator

| | |
|---|---|
| Osamu | Hashimoto[1] |
| Tsutomu | Shinozuka |
| Takuya | Endo |
| Toru | Miyake |
| Masahiro | Fujita |
| Eiji | Tanaka |
| Shizuo | Kan[6] |
| Shizuo | Chiba[6] |
| Yasuaki | Ohmiya[6] |
| Naoto | Takahashi[6] |

## Division of Instrumentations

| | |
|---|---|
| Hikonojo | Orihara |
| Keizo | Ishii[2] |
| Atsuki | Terakawa |
| Hiroshi | Suzuki |
| Sho-ichi | Watanuki |
| Yukihiro | Oishi |

## Division of Radiopharmaceutical Chemistry

| | |
|---|---|
| Tatsuo | Ido |
| Ren | Iwata |
| Yoshihito | Funaki |
| Valdes, Gonzales | Tania |
| Syozou | Furumoto |
| Hideo | Takahashi |

| | |
|---|---|
| Yo-ichi | Ishikawa7) |

## Division of Cyclotron Nuclear Medicine

| | |
|---|---|
| Masatoshi | Itoh |
| Kazuhiko | Yanai4) |
| Keiichiro | Yamaguchi |
| Shintaro | Itoh |
| Masayasu | Miyake |

## Division of Radiation Protection and Safety Control

| | |
|---|---|
| Mamoru | Baba |
| Takashi | Nakamura2) |
| Takamoto | Miyata |
| Noboru | Watanabe7) |

## Graduate Student and Researcher

| | | |
|---|---|---|
| Tetsu | Sonoda | (Graduate School of Science) |
| Tomokazu | Suzuki | (Graduate School of Science) |
| Gotoh | Atsushi | (Graduate School of Science) |
| Kazuaki | Kumagai | (Graduate School of Science) |
| Yu-ji | Kikuchi | (Graduate School of Science) |
| Naoya | Sugimoto | (Graduate School of Science) |
| Naoto | Nakagawa | (Graduate School, Division of Pharmaceutical Sciences) |
| Hiroshi | Kitagawa | (Graduate School, Division of Pharmaceutical Sciences) |
| Katsuyuki | Tanaka | (Graduate School, Division of Pharmaceutical Sciences) |
| Aiko | Ono | (Graduate School, Division of Pharmaceutical Sciences) |
| Megumi | Maeda | (Graduate School, Division of Pharmaceutical Sciences) |
| Md. Mehedi Masud | | (Graduate School, Division of Medicine) |
| Laxmi N. Singh | | (Graduate School, Division of Medicine) |
| Manami | Suzuki | (Graduate School, Division of Medicine) |
| Sabina Khond Kar | | (Graduate School, Division of Medicine) |
| Yoshiriro | Chida | (Graduate School, Division of Medicine) |
| Honda | Goh | (Graduate School, Division of Medicine) |

| | | |
|---|---|---|
| Naoki | Kawata | (Graduate School of Engineering) |
| Masayuki | Hagiwara | (Graduate School of Engineering) |
| Naoya | Hirabayashi | (Graduate School of Engineering) |
| Toshiro | Itoga | (Graduate School of Engineering) |
| Hiroshi | Yashima | (Graduate School of Engineering) |
| Syunsuke | Yonai | (Graduate School of Engineering) |

**Office Staff**

| | |
|---|---|
| Makoto | Sugawara |
| Tadashi | Sasaki |
| Akihiro | Matsuya |
| Kyoko | Fujisawa |
| Junko | Matsuno |
| Fumiko | Mayama |
| Mitsuko | Endo |
| Yu-ko | Yamashita |
| Keietsu | Aizawa |
| Kietu | Takahashi |
| Yuri | Okumura |
| Noriko | Suzuki |
| Kimiko | Abe |
| Toshiyuki | Watanabe(7) |

1) Graduate School of Science
2) Graduate School of Engineering
3) Institute for Materials Research
4) Graduate School of Medicine
5) Institute for Development, Aging and Cancer
6) SUMI-JU Accelerator Service Ltd.
7) Japan Radiation Protection Co., Ltd.